Studies of Aggregation Pathways for Amyloidogenic Peptides by Dielectric Relaxation Spectroscopy

Donald E. Barry, Jr.

A Dissertation
Submitted to the Faculty of
Worcester Polytechnic Institute
in partial fulfillment of the requirements for the
Degree of Doctor of Philosophy
in
Physics

April 2013

APPROVED:

Izabela R.C. Stroe, Assistant Professor of Physics, WPI, PhD Advisor

---

Germano S. Iannacchione, Department Head & Associate Professor of Physics, WPI

David C. Medich, Assistant Professor of Physics, WPI

Florin Despa, Assistant Professor, Dept. of Pharmacology, Univ. of California, Davis

© Copyright by Donald E. Barry, Jr., 2013.

All rights reserved.

Abstract

Diseases associated with amyloid aggregation have been a growing focus of medical research in recent years. Altered conformations of amyloidogenic peptides assemble to form soluble aggregates that deposit into the brain and spleen causing disorders such as Alzheimer's disease and Type II diabetes. Emergent theories predict that fibrils may not be the toxic form of amyloidogenic structures and that smaller oligomer and protofibril aggregates may be the primary source of cellular function damage.

Studies show that these amyloidogenic aggregates are characterized by an increased number of poorly dehydrated hydrogen backbones and large surface densities of patches of bulk like water which favor protein association. When proteins aggregate to form larger structures, there is a redistribution of water surrounding these proteins. The water dynamics of amyloidogenic aggregation is different than the monomeric form and has a decrease in the number of patches occupied by molecules with bulk-like water behavior. We demonstrate that the redistribution of water during amyloid aggregation is reflected in a change in the dielectric relaxation signal of protein-solvent mixtures.

We use dielectric relaxation spectroscopy (DRS) as a tool for studying the dynamics of amyloidogenic peptides—amyloid beta ($A\beta_{1-42}$) and human islet amyloid polypeptide (hIAPP)—during self-assembly and aggregation. Non-amyloidogenic analogs—scrambled $A\beta_{42-1}$ and rat islet amyloid polypeptide (rIAPP)—were used as controls. We first present studies of amyloidogenic peptides in a deionized water buffer at room temperature as a function of concentration and incubation time. From this we were able to determine differences in amyloidogenic and non-amyloidogenic peptides through the dielectric modulus. We next present the same analytes in a deionized water-glycerol buffer to facilitate the study of the dielectric permittivity at sub-freezing temperatures and model the kinetics of the α-and β-relaxation processes. We conclude our work by studying the peptides in a bovine serum albumin

(BSA) and glycerol buffer to demonstrate dielectric spectroscopy as a sensitive tool for measuring amyloidogenic peptides in an *in vivo*-like condition.

Acknowledgements

First and foremost I would like to thank my family. To my parents, Donald and Susan Barry who who have always supported and inspired me to pursue a career in science. To my wife, Romiya who has been crucial in my successes through her love, encouragement, and unwavering support. I am so very lucky to have you in my life.

I give very special thanks to Dr. W. Peter Hansen and Dr. Petra Krauledat. Not only have you been employers and mentors, you have also been great friends. I tremendously appreciate the support you have given me throughout my graduate studies. Your guidance over the last ten years has helped mold me into the researcher and leader that I am today.

I would like to thank my advisor, Dr. Izabela Stroe for her enthusiasm and mentoring throughout my dissertation work. The origins of this project lies in your profound interest to make a meaningful contribution to public health through physics and I thank you for this opportunity. I thank the WPI Physics Department for supporting me through fellowships and teaching assistantships during the final years of my studies. I am thankful to Professors Germano Iannacchione, David Medich, and Florin Despa for serving on my committee and for their guidance.

I would like to thank WPI students Fioleda Prifti, Shaun Marshal, Shane Waterman, Shelby Hunt, Yusuke Hirai, and Reem Assiri that have assisted me over the years with the work contained in this thesis. I enjoyed working with each of you and I am grateful for your time, efforts, and collaboration.

Dedicated to my parents...

Contents

Abstract iii

Acknowledgements v

List of Tables x

List of Figures xii

1 Introduction **1**

1.1 Motivation for the Studies of Amyloidogenic Peptides 1

1.1.1 Pathogenesis of amyloidogenic diseases 3

1.2 Protein Structure and Amyloidogenic Disease 7

1.2.1 Protein composition and structure 7

1.2.2 Protein folding and aggregation 10

1.3 Amyloids and Amyloidogenic Diseases 13

1.4 The Role of Biological Water 16

1.5 Dielectric Spectroscopy as a Tool for Studying Amyloidogenic Peptides 18

1.6 A Review of Methods for Studying Amyloidogenic Peptides 20

1.7 Thesis Scope and Outline 23

2 Materials and Methods **25**

2.1 Introduction to Dielectric Relaxation Spectroscopy 25

2.1.1 Polarization and the static field 27

2.1.2 Time-dependent fields 28

2.1.3 Non-Debye relaxation processes 30
2.1.4 Dielectric modulus 32
2.1.5 Relaxation kinetics 35
2.2 Broadband Dielectric Spectroscopy 36
2.2.1 Instrumentation 36
2.2.2 Sample cells 40
2.3 Data Analysis Methods 42
2.4 Peptides 45
2.4.1 β-amyloid 45
2.4.2 Islet Amyloid Polypeptide (IAPP) 46
2.5 Buffers 47

3 Dielectric Studies of Amyloidogenic Peptides at Room Temperature as a Function of Concentration and Incubation Time 48

3.1 Overview 48
3.2 Sample Preparation and Data Collection 49
3.3 Results and Discussions 50
3.3.1 Studies of $A\beta_{1-42}$ and Scrambled $A\beta_{42-1}$ 50
3.3.2 Studies of Human and Rat Islet Amyloid Polypeptide 62
3.4 Conclusions 73

4 Dielectric Studies of Amyloidogenic Peptides in Deionized Water Buffer at Low Temperature 75

4.1 Overview 75
4.2 Sample Preparation and Data Collection 76
4.3 Results and Discussions 77
4.3.1 Studies of $A\beta_{1-42}$ and Scrambled $A\beta_{42-1}$ 77
4.3.2 Studies of Human and Rat Islet Amyloid Polypeptide 102

4.4 Conclusions 127

5 Dielectric Studies of Amyloidogenic Peptides in BSA Buffer at Low Temperature 131

5.1 Overview 131

5.2 Sample Preparation and Data Collection 132

5.3 Results and Discussions 133

  5.3.1 Studies of $A\beta_{1-42}$ and Scrambled $A\beta_{42-1}$ 133

  5.3.2 Human and Rat Islet Amyloid Polypeptide 158

5.4 Conclusions 184

6 Conclusion 186

6.1 General Conclusions 186

6.2 Future Direction 189

  6.2.1 Expansion of DRS Methods 189

  6.2.2 Miniaturized sample cell 190

  6.2.3 Amyloid fibril inhibitors 190

  6.2.4 Complementary analysis tools 191

  6.2.5 Serum studies 191

Bibliography 192

List of Tables

1.1 Various diseases caused by amyloid formation and their associated pathogenic peptide 13

1.2 Summary of methods used in the studies of amyloid structure and aggregation. 22

3.1 Parameters of the power law fits to the f_{max} versus time for M'' in the form $f(t) = C + At^k$ at concentrations $X_M = 5\mu$M, 50μM, and 100μM for $A\beta_{1-42}$ and $A\beta_{42-1}$. 60

3.2 Parameters of the power law fits to the f_{max} versus time for M'' in the form $f(t) = C + At^k$ at concentrations $X_M = 5\mu$M, 50μM, and 100μM for hIAPP and rIAPP. 72

4.1 Parameters of the linear fits to the β-relaxation measurements of $\log(f_{max}(T))$ of the form $A + BT$. 98

4.2 Parameters of the VFT fits to the α-relaxation measurements of $f_{max}(T)$ of the form $\log(f_{max}) = \log(f_\infty(T)) - \frac{DT_0}{T-T_0}$ 98

4.3 Parameters of the linear fits to the β-relaxation measurements of $\log(f_{max}(T))$ of the form $A + BT$. 125

4.4 Parameters of the VFT fits to the α-relaxation measurements of $f_{max}(T)$ of the form $\log(f_{max}) = \log(f_\infty(T)) - \frac{DT_0}{T-T_0}$ 125

4.5 Activation energies for various small, aggregating peptides 130

5.1 Parameters of the linear fits to the β-relaxation measurements of $\log(f_{max}(T))$ of the form $A + BT$. 153

5.2 Parameters of the VFT fits to the α-relaxation measurements of $f_{max}(T)$ of the form $\log(f_{max}) = \log(f_{\infty}(T)) - \frac{DT_0}{T-T_0}$ 153

5.3 Parameters of the linear fits to the β-relaxation measurements of $\log(f_{max}(T))$ of the form $A + BT$. 181

5.4 Parameters of the VFT fits to the α-relaxation measurements of $f_{max}(T)$ of the form $\log(f_{max}) = \log(f_{\infty}(T)) - \frac{DT_0}{T-T_0}$ 181

List of Figures

1.1 Non-pathogenic (a) and pathogenic (b) proteolytic processing of APP by α- or β-secretase, followed by γ-secretase cleavage. 5

1.2 The linear structure of a polypeptide chain showing the links between carboxyl and amino groups of sequential amino acids. 8

1.3 Amino acids and consequently, the polypeptide backbone consists of one positively charged and one negatively charged end. This produces a permanent dipole moment. 9

1.4 The two forms of protein secondary structure are shown here: the α-helix and the β-strand. An atomic model as well as a shorthand cartoon model for each conformation is depicted. 10

1.5 Hydrophobic tails bury in the interior during micelle formation as hydrophilic regions interact with polar solvents. 11

1.6 β-strands may stack in parallel or anti-parallel β-sheets. Hydrogen bonds form between the NH and CO groups of adjacent strands. . . . 12

1.7 Nucleation starts with oligomer formation of β-amyloid fragments. Monomers then attach longitudinally to the oligomeric nucleus. . . . 14

1.8 Ribbon representation viewed down the fibril axis showing protofilament structure. Each $A\beta$ polypeptide molecule contains two β-strands (red and blue) that form parallel stacked β-sheets. 15

1.9 Representation of the hydration profile for $A\beta_{1-42}$ shows the three types of biological water at various regions in and around the protein. The confinement of water by a protein causes restricted rotations and other motions of water molecules resulting in attenuated relaxation times. The blue portions of the ribbon are hydrophilic and the red are hydrophobic. The $A\beta_{1-42}$ structure was obtained from PDB ID: 1IYT 17

2.1 Schematic representation of the polarization processes in a broadband dielectric spectrum for the real and imaginary parts of the permittivity. 27
2.2 Time-dependence of the polarization P of a dielectric material when an E field is applied. 29
2.3 Schematic representation of the Cole-Cole plot for a Havriliak-Negami function where β, γ, and $\Delta\varepsilon$ are the shape parameters of the H-N function. 34
2.4 Model of a double-minimum potential (a) in a steady-state and (b) in the presence of an applied electric field. The application of an electric field causes a shift in the potentials such that an energy barrier is created. 35
2.5 The fragility of glass forming materials can be visualized diagrammatically by the deviation from Arrhenius-type behavior. 36
2.6 Material dipoles are typically in a random orientation. When placed inside an electric field, the dipoles align between the capacitive plates. 37
2.7 In dielectric relaxation spectroscopy (DRS), complex impedance is calculated from the ratio of the applied voltage and induced current with a phase shift. 38
2.8 A schematic diagram of DRS gain phase measurement. Two probing voltages are used to compute the complex permittivity. 39

2.9 Block diagram of the Novocontrol Broadband Dielectric/Impedance Spectrometer apparatus with the Alpha-A analyzer and Quatro Cryosystem. 40

2.10 Cross-section views of the two sample cells used for collecting permittivity data. (a) The BDS 1309 sample cell was used for room temperature data. The approximate volume is 0.5mL.(b) The BDS 1307 sample cell was used for low temperature data. The approximate volume is 1.8mL. 41

2.11 Fits to the real (ε') and imaginary (ε'') part of the dielectric permittivity using two Havriliak-Negami functions and conductivity. The low frequency rise in ε' that lies outside of the fit function is most likely due to electrode polarization. 44

2.12 Fits to maximum relaxation frequency, f_{max} inverse temperature, 1000/T for two relaxation processes. The linear Arrhenius and curved VFT behaviors are depicted. 44

2.13 Amino acid sequences of (a) $A\beta_{1-42}$ and (b) scrambled $A\beta_{42-1}$. The hydrophobic amino acids are shown in red. The sequence found in native $A\beta_{1-42}$ possesses a hydrophilic head, hydrophobic tail, and a hydrophobic region in the middle that causes the β turn in the secondary structure. 45

2.14 Amino acid sequences of (a) human hIAPP$_{22-27}$ and (b) rat rIAPP$_{20-29}$. The hydrophobic amino acids are shown in red. The arrow points to a proline substitution at amino acid position 25 that prevents β-sheet formation in rat amylin. 46

3.1 The relationship between M'', ε', and ε'' for $A\beta_{1-42}$, $A\beta_{42-1}$, and the solvent. The intersection of ε' and ε'' occurs at the peak loss modulus, M'' for the conductivity process. Regions of ε' with slope, m=0 is the conductivity process and slope m<0 are polarization effects. 51

3.2 **Dielectric modulus (M'') as a function of frequency for $A\beta_{1-42}$ and $A\beta_{42-1}$ at concentrations of 5μM, 50μM and 100μM after 1 hour and 4 hours of incubation time.** There is an immediate shift in peak frequency for $A\beta_{1-42}$ for all concentrations after just 1 hour. The peak shift for $A\beta_{42-1}$ is only a half decade or less for both 1 and 4 hours for all concentrations. Note that after 4 hours of incubation, the shift for 5μM $A\beta_{1-42}$ is more than twice the shift for any concentration of $A\beta_{42-1}$. 52

3.3 **Dielectric modulus (M'') as a function of frequency for $A\beta_{1-42}$ and $A\beta_{42-1}$ at concentrations of 5μM, 50μM and 100μM after 8 hours and 24 hours of incubation time.** The shift for $A\beta_{42-1}$ is approximately twice the shift of $A\beta_{42-1}$ for each concentration at 8 and 24 hours of incubation. The frequency shifts for $A\beta_{1-42}$ and $A\beta_{42-1}$ indicates that there is some aggregation with both peptides, but the process is composition and concentration dependent. We note a large increase in the magnitude of M'' for only 50μM $A\beta_{1-42}$ at 24 hours, though the peak frequency follows the trend. 53

3.4 **Dielectric modulus (M'') as a function of frequency for $A\beta_{1-42}$ and $A\beta_{42-1}$ at concentrations of 5μM, 50μM and 100μM after 72 hours and 144 hours of incubation time.** The shift for $A\beta_{42-1}$ is approximately 1.5 times the shift of $A\beta_{42-1}$ for each concentration at 72 and 144 hours of incubation. We note a large increase in the magnitude of M'' for 100μM $A\beta_{1-42}$ at 72 hours, though the peak frequency follows the trend to higher frequency. Data was not collected beyond 72 hours for $A\beta_{1-42}$. 54

3.5 **Time evolution for 5 μM $A\beta_{1-42}$ and $A\beta_{42-1}$ for 0-8 hours and 1-168 hours (7 days).** The $A\beta_{1-42}$ has an initial jump in peak frequency of approximately 1 decade at the first measurement, then continues for another half decade. There is no shift in $A\beta_{24-1}$ for the first two hours, then steady shift throughout 168 hours. The peak frequencies of $A\beta_{1-42}$ and $A\beta_{42-1}$ are very close after 168 hours of incubation. 56

3.6 **Time evolution for 50 μM $A\beta_{1-42}$ and $A\beta_{42-1}$ for 0-8 hours and 1-168 hours (7 days).** The $A\beta_{1-42}$ has an initial jump in peak frequency of approximately 1.5 decades at the first measurement, then continues with small increases. There is a small shift in $A\beta_{24-1}$ of a half decade, then steady shift throughout 168 hours. The peak frequency of $A\beta_{1-42}$ is approximately a half decade above $A\beta_{42-1}$ after 168 hours of incubation. The large increase in the magnitude of $A\beta_{1-42}$ at 0 and 24 hours could be the result of an evolving surface landscape during fibril formation. 57

3.7 **Time evolution for 100 μM $A\beta_{1-42}$ and $A\beta_{42-1}$ for 0-8 hours and 1-168 hours (7 days).** No data was collected for $A\beta_{1-42}$ after 72 hours. The $A\beta_{1-42}$ has an initial jump in peak frequency of approximately 2 decades at the first measurement, then continues with small increases. Data was not collected beyond 72 hours. There is a small shift in $A\beta_{24-1}$ of a half decade, then steady shift to 1.5 decades throughout 168 hours. The peak frequency of $A\beta_{1-42}$ is more than a half decade above $A\beta_{42-1}$ for all time points. The large increase in the magnitude of $A\beta_{1-42}$ at 72 hours could be the result of an evolving surface landscape during fibril formation. 58

3.8 Example of the curve fitting analysis performed for the determination of f_{max} in the modulus M" versus frequency plots for the solvent, $A\beta_{1-42}$, and $A\beta_{42-1}$. 59

3.9 **Plots of f_{max} of M" versus time for $A\beta_{1-42}$ and $A\beta_{42-1}$ at 5μM, 50μM, and 100μM concentrations.** For each concentration, f_{max} has two distinct regions (0-8 hours and 24-168 hours). Modulus peak determination for the $A\beta_{1-42}$ after 6 hours was not possible because the peaks have shifted to frequencies above the measurement limits. . 61

3.10 The relationship between M'', ε', and ε'' for hIAPP, rIAPP, and the solvent. The intersection of ε' and ε'' occurs at the peak loss modulus, M'' for the conductivity process. Regions of ε' with slope, m=0 is the conductivity process and slope m<0 are polarization effects. 62

3.11 **Dielectric modulus (M'') as a function of frequency for hIAPP and rIAPP at concentrations of 5μM, 50μM and 100μM after 1 hour and 4 hours of incubation time.** Both hIAPP and rIAPP show an initial shift to lower frequency for low concentrations of protein (5μM). The peak frequency increases with increasing concentration for both hIAPP and rIAPP from 5-100μM. After 4 hours of incubation, only hIAPP shows a positive shift in peak frequency at 5μM. Also, there is an increase in peak magnitude. The jump in peak magnitude at 1 hour for 50μM and 4 hours for 5μM hIAPP is indicative of a changing surface landscape of charges. This may have occurred with 100μM prior to our first measurement. We note that after 4 hours, hIAPP 100μM has shifted to lower frequency than 50μM. 63

3.12 **Dielectric modulus (M'') as a function of frequency for hIAPP and rIAPP at concentrations of 5μM, 50μM and 100μM after 6 hours and 24 hours of incubation time.** After 24 hours of incubation, the rIAPP 5μM shows a small positive shift in frequency for the first time, but is less than half that of the hIAPP. The hIAPP and rIAPP 50μM solutions display similar peak frequency shifts. The increase in magnitude of 50μM and decrease in magnitude of 100μM at 6 hours indicates surface changes due to fibril formation. We note that the hIAPP 100μM is at lower frequency than 50μM. 64

3.13 **Dielectric modulus (M'') as a function of frequency for hIAPP and rIAPP at concentrations of 5μM, 50μM and 100μM after 72 hours and 144 hours of incubation time.** After 72 hours of incubation, the hIAPP and rIAPP 5μM and 50μM solutions display similar peak frequency shifts. The increase in magnitude of hIAPP 50μM at 72 hours indicates surface changes due to fibril formation. A decrease in magnitude of rIAPP 100μM at 72 hours and rIAPP at 50μM at 144 hours is observed. We note that the hIAPP 100μM is at lower frequency than 50μM for both time points and similarly for rIAPP at 144 hours. Trends of rIAPP appear to follow hIAPP after much longer timescales indicating that aggregation occurs for both peptides, but at different rates. 65

3.14 **Time evolution for 5μM rIAPP and hIAPP for 0-24 hours and 1-144 hours (6 days).** The hIAPP solution displays a larger frequency shift than rIAPP in the first 24 hours and a spike in the magnitude of M'' at 4 hours. Both hIAPP and rIAPP display similar behavior beyond 24 hours. 67

3.15 **Time evolution for 50μM rIAPP and hIAPP for 0-24 hours and 1-144 hours (6 days).** The hIAPP and rIAPP solutions display similar frequency shifts for both incubation time scales. However, the hIAPP shows a spike in magnitude at 1 and 6 hours. A smaller, yet significant spike is seen with rIAPP at 4 and 72 hours. 68

3.16 **Time evolution for 100μM hIAPP and rIAPP for 0-24 hours and 1-144 hours (6 days).** The hIAPP frequency shift is less than that of the rIAPP in the first 24 hours of incubation. The hIAPP shifts to lower frequency in the first 24 hours with a spike in magnitude at 24 hours. The rIAPP does not significantly change in the first 24 hours with a spike in magnitude at 4 hours. There is little change over time for the peak frequency for both hIAPP and rIAPP at 100μM. 69

3.17 Example of the curve fitting analysis performed for the determination of f_{max} in the modulus M" versus frequency plots for the solvent, hIAPP, and rIAPP. 70

3.18 **Plots of f_{max} of M" versus time for hIAPP and rIAPP at 5μM, 50μM, and 100μM concentrations.** Each concentration is fit to two power law fits: one from 0-8 hours and one from 24-168. . . 71

4.1 **Temperature evolution of the real and imaginary parts of the dielectric permittivity for the solvent, $A\beta_{1-42}$, and $A\beta_{42-1}$ from 228K to 213K.** Two relaxation processes for the real (ε') and imaginary (ε'') parts of the permittivity for the solvent, $A\beta_{1-42}$, and scrambled $A\beta_{42-1}$ are observed. 78

4.2 **Temperature evolution of the real and imaginary parts of the dielectric permittivity for the solvent, $A\beta_{1-42}$, and $A\beta_{42-1}$ from 198K to 168K.** The α-relaxation process rapidly shifts to lower frequency with decreasing temperature. In the range of 198K to 188K the two processes cross where the α-relaxation is at lower frequency than the β-relaxation process at temperatures of 183K and below. . . 79

4.3 **Temperature evolution of the real and imaginary parts of the dielectric permittivity for the solvent, Aβ(1-42), and Aβ(42-1) from 163K to 133K.** The β-relaxation process dominates below the crossing temperature and continues to slow to under 1 Hz. The DC conductivity has reduced in magnitude to outside the measured range below 158K. 80

4.4 **Dielectric loss ε'' as a function of frequency for $A\beta_{1-42}$ in the range of 228K-213K and incubation periods of 0, 8, and 24 hours.** The arrows depict trends of the conductivity, σ to lower magnitude. Mixing between σ and the β-process make it difficult to determine the time-evolution of β in this temperature range. The α-process displays a small shift to lower frequency over time. 83

4.5 **Dielectric loss ε'' as a function of frequency for scrambled $A\beta_{42-1}$ in the range of 228K-213K and incubation periods of 0, 8, and 24 hours.** The arrows depict trends of the conductivity, σ to higher magnitude and the α-process to slightly frequency and magnitude. The conductivity shift is opposite that of $A\beta_{1-42}$ in the same temperature range. The shift of the α-process is the same. Mixing between σ and the β-process make it difficult to determine the time-evolution of β in this temperature range. 84

4.6 **Dielectric loss ε'' as a function of frequency for $A\beta_{1-42}$ in the range of 208K-193K and incubation periods of 0, 8, and 24 hours.** Deconvolution of the peaks from curve fitting analysis shows that at 193K, the α-process occurs at near the same frequency as the β-process but with lower magnitude. The conductivity, σ shifts to lower magnitude over time. 85

4.7 **Dielectric loss ε'' as a function of frequency for scrambled $A\beta_{42-1}$ in the range of 208K-193K and incubation periods of 0, 8, and 24 hours.** At 193K, the α-process occurs at near the same frequency as the β-process but with lower magnitude. The arrows depict trends of the conductivity, σ to higher magnitude. This opposite the behavior of $A\beta_{1-42}$ in the same temperature range. The apparent peak increase at the β-process is the result of the change in conductivity and not a process change. 86

4.8 **Dielectric loss ε'' as a function of frequency for $A\beta_{1-42}$ in the range of 188K-173K and incubation periods of 0, 8, and 24 hours.** The α-process has shifted to a lower frequency than the β-process. The arrows depict trends of the conductivity, σ to lower magnitude. There is significant mixing between σ and α at 173K and 178K. 87

4.9 **Dielectric loss ε'' as a function of frequency for scrambled $A\beta_{42-1}$ in the range of 188K-173K and incubation periods of 0, 8, and 24 hours.** The α-process has shifted to a lower frequency than the β-process. The arrows depict trends of the conductivity, σ to higher magnitude. This opposite the behavior of $A\beta_{1-42}$ in the same temperature range. There is significant mixing between σ and α at 173K and 178K. 88

4.10 **Dielectric loss ε'' as a function of frequency for $A\beta_{1-42}$ in the range of 168K-153K and incubation periods of 0, 8, and 24 hours.** At 168K, the α-process has shifted to frequency below the measured range. At 163K and below, the conductivity has been reduced to a point where the β-process is clearly discerned. The arrows depict the shifts of the β-process first to lower magnitude and higher frequency, then to an increase in magnitude and decrease in frequency. 89

4.11 **Dielectric loss ε'' as a function of frequency for scrambled $A\beta_{42-1}$ in the range of 168K-153K and incubation periods of 0, 8, and 24 hours.** At 168K, the α-process has shifted to frequency below the measured range. At 163K and below, the conductivity has been reduced to a point where the β-process is clearly discerned. The arrows depict the shifts of the β-process first to higher magnitude and lower frequency, then to a decrease in magnitude and increase in frequency. This opposite the behavior of $A\beta_{1-42}$ in the same temperature range. 90

4.12 **Dielectric loss ε'' as a function of frequency for $A\beta_{1-42}$ in the range of 148K-133K and incubation periods of 0, 8, and 24 hours.** The arrows depict the shifts of the β-process first to lower magnitude and higher frequency, then to an increase in magnitude and decrease in frequency. 91

4.13 **Dielectric loss ε'' as a function of frequency for scrambled $A\beta_{42-1}$ in the range of 148K-133K and incubation periods of 0, 8, and 24 hours.** The arrows depict the shifts of the β-process first to higher magnitude and lower frequency, then to an decrease in magnitude and increase in frequency. This opposite the behavior of $A\beta_{1-42}$ in the same temperature range. 92

4.14 **Curve fitting of imaginary part of the permittivity data using the WinFIT program of the solvent, $A\beta_{1-42}$, and $A\beta_{42-1}$ at 223K.** A large, low frequency DC conductivity is fit with a power law. The β-relaxation process at around 10^4 Hz is fit with a Cole-Davidson function and the α-relaxation process at around 10^7 Hz is fit with a Havriliak-Negami function. The root-mean-square deviation (RMSD) of the fits are 0.018, 0.012, and 0.013, respectively. 94

4.15 **Curve fitting of imaginary part of the permittivity data using the WinFIT program of the solvent, $A\beta_{1-42}$, and $A\beta_{42-1}$ at 208K.** A large, low frequency DC conductivity is fit with a power law. The β-relaxation process at around 10^3 Hz is fit with a Cole-Davidson function and the α-relaxation process at around 10^5 Hz is fit with a Havriliak-Negami function. The RMSD of the fits are 0.045, 0.009, and 0.013, respectively. 95

4.16 **Curve fitting of imaginary part of the permittivity data using the WinFIT program of the solvent, $A\beta_{1-42}$, and $A\beta_{42-1}$ at 188K.** A large, low frequency DC conductivity is fit with a power law. The β-relaxation process at around 10^3 Hz is fit with a Cole-Davidson function and the α-relaxation process at around 10^1 Hz is fit with a Havriliak-Negami function. Here, the α process has crossed over to slower than β relaxation times. The RMSD of the fits are 0.008, 0.011, and 0.013, respectively. 96

4.17 **Curve fitting of the imaginary part of the permittivity data using the WinFIT program of the solvent, $A\beta_{1-42}$, and $A\beta_{42-1}$ at 133K.** A small, very low frequency DC conductivity is fit with a power law. The β-relaxation process at around 1 Hz is fit with a Cole-Davidson function and the α-relaxation process is not observed. The RMSD of the fits are 0.092, 0.123, and 0.082, respectively. 97

4.18 **Arrhenius plots of f_{max} versus inverse temperature for $A\beta_{1-42}$ over time.** The α-relaxation process follows a VFT behavior whereas the β-relaxation process follows an Arrhenius, or linear behavior. The α-process departs from the VFT curvature at low temperature. 99

4.19 **Arrhenius plots of f_{max} versus inverse temperature for scrambled $A\beta_{42-1}$ over time.** The α-relaxation process follows a VFT behavior whereas the β-relaxation process follows an Arrhenius, or linear behavior. The α-process departs from the VFT curvature at low temperature. 100

4.20 **Dielectric strength, $\Delta\varepsilon$ of the β-relaxation for $A\beta_{1-42}$ and $A\beta_{42-1}$ versus inverse temperature.** The dielectric strength for the $A\beta_{1-42}$ solution first increases, then deceases to values less than the solvent. The dielectric strength of $A\beta_{42-1}$ continued to increase over time. The decrease in dielectric strength indicates that the $A\beta_{1-42}$ displays an anti-parallel β-sheet conformation. 102

4.21 **Temperature evolution of the real and imaginary parts of the dielectric permittivity for the solvent, hIAPP, and rIAPP from 228K to 203K.** Two relaxation processes for the real (ε') and imaginary (ε'') parts of the permittivity for the solvent, hIAPP, and rIAPP are observed. 103

4.22 **Temperature evolution of the real and imaginary parts of the dielectric permittivity for the solvent, hIAPP, and rIAPP from 198K to 168K.** The α-relaxation process rapidly shifts to lower frequency with decreasing temperature. In the range of 198K to 188K the two processes cross to where the α-relaxation is at lower frequency than the β-relaxation process at temperatures of 183K and below. . . 104

4.23 **Temperature evolution of the real and imaginary parts of the dielectric permittivity for the solvent, hIAPP, and rIAPP from 163K to 133K.** The β-relaxation process dominates below the crossing temperature and continues to slow to under 1 Hz. The DC conductivity has reduced in magnitude to outside the measured range below 158K. 105

4.24 **Dielectric loss ε'' as a function of frequency for hIAPP in the range of 228K-213K and incubation periods of 0, 24, 48, and 120 hours.** The arrows depict shifts of the the α-process to slightly lower frequency by approximately a half decade. The conductivity and β-process does show a different behavior for the 0 hour time point, but there is no consistency within this temperature range. 107

4.25 **Dielectric loss ε'' as a function of frequency for rIAPP in the range of 228K-213K and incubation periods of 0, 24, 48, and 120 hours.** The arrows show the trend of increasing conductivity over time. This was not observed with hIAPP. The apparent peak increase at the β-process is most likely the result of the change in conductivity and not a process change. There are changes observed in the α-process at 228K and 223K, but without a trend. 108

4.26 **Dielectric loss ε'' as a function of frequency for hIAPP in the range of 208K-193K and incubation periods of 0, 24, 48, and 120 hours.** At 193K, the α-process occurs at near the same frequency as the β-process but with lower magnitude. The conductivity, α-, and β-processes show a different behavior for the 0 hour time point, but it is difficult to determine a time-dependent trend. 109

4.27 **Dielectric loss ε'' as a function of frequency for rIAPP in the range of 208K-193K and incubation periods of 0, 24, 48, and 120 hours.** At 193K, the α-process occurs at near the same frequency as the β-process but with lower magnitude. The arrows show the trend of increasing conductivity over time. This was not observed with hIAPP. 110

4.28 **Dielectric loss ε'' as a function of frequency for hIAPP in the range of 183K-168K and incubation periods of 0, 24, 48, and 120 hours.** The α-process has shifted to a lower frequency than the β-process. At 183K and below, the conductivity has been reduced to a point where there is little or no mixing with the processes. 111

4.29 **Dielectric loss ε'' as a function of frequency for rIAPP in the range of 188K-173K and incubation periods of 0, 24, 48, and 120 hours.** The α-process has shifted to a lower frequency than the β-process. The arrows show the trend of increasing conductivity over time. This was not observed with hIAPP. 112

4.30 **Dielectric loss ε'' as a function of frequency for hIAPP in the range of 168K-153K and incubation periods of 0, 24, 48, and 120 hours.** Only the β-process is observed at temperatures below 168K. The peaks of hIAPP have increased in frequency by more than a decade as compared to the solvent. The peaks have shifted to lower magnitude and frequency over time. 113

4.31 **Dielectric loss ε'' as a function of frequency for rIAPP in the range of 168K-153K and incubation periods of 0, 24, 48, and 120 hours.** Only the β-process is observed at temperatures below 158K. The arrows show that the conductivity increases and the β-process peaks shift to higher magnitude over time. This opposite the behavior of hIAPP in the same temperature range. There is no increase in frequency at t = 0hr, where hIAPP displayed a decade shift. The shift in peak position at 168K and 163K may be due to conductivity. 114

4.32 **Dielectric loss ε'' as a function of frequency for hIAPP in the range of 148K-133K and incubation periods of 0, 24, 48, and 120 hours.** The arrows depict that the β-process of hIAPP shifts to lower frequency and lower magnitude over time. 115

4.33 **Dielectric loss ε'' as a function of frequency for rIAPP in the range of 148K-133K and incubation periods of 0, 24, 48, and 120 hours.** The arrows depict that the β-process of rIAPP shifts to lower frequency and higher magnitude over time. This opposite the behavior of hIAPP in the same temperature range. 116

4.34 **Curve fitting of imaginary part of the permittivity data using the WinFIT program of the solvent, hIAPP, and rIAPP at 223K.** A large, low frequency DC conductivity is fit with a power law. The α-relaxation process at around 10^7 Hz is fit with a Havriliak-Negami function and the β-relaxation function is not observed. The RMSD of the fits are 0.015, 0.005, and 0.016, respectively. 118

4.35 **Curve fitting of imaginary part of the permittivity data using the WinFIT program of the solvent, hIAPP, and rIAPP at 208K.** A large, low frequency DC conductivity is fit with a power law. The β-relaxation process at around 10^3 Hz is fit with a Cole-Davidson function and the α-relaxation process at around 10^5 Hz is fit with a Havriliak-Negami function. The RMSD of the fits are 0.027, 0.013, and 0.010, respectively. 119

4.36 **Curve fitting of imaginary part of the permittivity data using the WinFIT program of the solvent, hIAPP, and rIAPP at 188K.** A large, low frequency DC conductivity is fit with a power law. The β-relaxation process at around 10^3 Hz is fit with a Cole-Davidson function and the α-relaxation process at around 10^1 Hz is fit with a Havriliak-Negami function. Here, the α process has crossed over to slower than β relaxation times. The RMSD of the fits are 0.012, 0.004, and 0.043, respectively. 120

4.37 **Curve fitting of the imaginary part of the permittivity data using the WinFIT program of the solvent, hIAPP, rIAPP at 133K.** A small, very low frequency DC conductivity is fit with a power law. The β-relaxation process at around 1 Hz is fit with a Cole-Davidson function and the α-relaxation process is not observed. The RMSD of the fits are 0.169, 0.080, and 0.054, respectively. 121

4.38 **Arrhenius plots of f_{max} versus inverse temperature for solvent over time.** The α-relaxation process follows a VFT behavior whereas the β-relaxation process follows an Arrhenius, or linear behavior. . . . 122

4.39 **Arrhenius plots of f_{max} versus inverse temperature for hIAPP from 0-120 hours.** The α-relaxation process follows a VFT behavior whereas the β-relaxation process follows an Arrhenius, or linear behavior. The α-process departs from the VFT curvature at low temperature. 123

4.40 **Arrhenius plots of f_{max} versus inverse temperature for rIAPP from 0-120 hours.** The α-relaxation process follows a VFT behavior whereas the β-relaxation process follows an Arrhenius, or linear behavior. The α-process departs from the VFT curvature at low temperature. 124

4.41 **Dielectric strength, $\Delta\varepsilon$ of the β-relaxation for hIAPP and rIAPP versus inverse temperature.** The dielectric strength for the hIAPP solution first increases, then deceases to values less than the solvent. The dielectric strength of rIAPP continued to increase over time. This indicates a mixed grouping of parallel and anti-parallel β-sheets in hIAPP and random-coil aggregation in rIAPP. 126

4.42 Plots of the β-relaxation peak shift at 143K for $A\beta_{1-42}/A\beta_{42-1}$ and hIAPP/rIAPP as compared to the solvent. 128

4.43 **Arrhenius plots of f_{max} versus inverse temperature for pure glycerol and glycerol-water mixtures of approximately 50-50% by weight [63, 158, 142, 78].** The glycerol-water mixtures display both α- and β-relaxation processes. Only the α process appears in pure glycerol. 129

5.1 **Temperature evolution of the real and imaginary parts of the dielectric permittivity for the solvent, $A\beta_{1-42}$, and $A\beta_{42-1}$ from 223K to 198K.** Two relaxation processes for the real (ε') and imaginary (ε'') parts of the permittivity for the solvent, $A\beta_{1-42}$, and scrambled $A\beta_{42-1}$ are observed. 134

5.2 **Temperature evolution of the real and imaginary parts of the dielectric permittivity for the solvent,$A\beta_{1-42}$, and $A\beta_{42-1}$ from 193K to 168K.** The α-relaxation process rapidly shifts to lower frequency with decreasing temperature. In the range of 193K to 188K the two processes cross where the α-relaxation is at lower frequency than the β-relaxation process at temperatures of 183K and below. . . 135

5.3 **Temperature evolution of the real and imaginary parts of the dielectric permittivity for the solvent, $A\beta_{1-42}$, and $A\beta_{42-1}$ from 163K to 133K.** The β-relaxation process dominates below the crossing temperature and continues to slow to under 1 Hz. The DC conductivity has reduced in magnitude to outside the measured range below 158K. 136

5.4 D**ielectric loss ε'' as a function of frequency for $A\beta_{1-42}$ in the range of 223K-208K and incubation periods of 0, 8, and 24 hours.** At temperatures above 208K, the β-relaxation process is masked by the conductivity, σ. The arrows depict a decrease in magnitude of ε'', due to the decrease in σ over time. The spectra shows a shift towards higher frequency at 223K, but does not appear to follow a trend. 138

5.5 **Dielectric loss ε'' as a function of frequency for scrambled $A\beta_{42-1}$ in the range of 223K-208K and incubation periods of 0, 8, and 24 hours.** At temperatures above 208K, the β-relaxation process is masked by the conductivity, σ. The arrows depict a small decrease in magnitude of ε'', due to the decrease in σ over time. As with $A\beta_{1-42}$, the spectra shows a shift towards higher frequency at 223K, but does not appear to follow a trend. 139

5.6 **Dielectric loss ε'' as a function of frequency for $A\beta_{1-42}$ in the range of 203K-188K and incubation periods of 0, 8, and 24 hours.** At 193K, the α-process occurs at near the same frequency as the β-process but with lower magnitude. The arrows show a shift in magnitude of ε'' across the spectra due to the conductivity, σ. 140

5.7 **Dielectric loss ε'' as a function of frequency for scrambled $A\beta_{42-1}$ in the range of 203K-188K and incubation periods of 0, 8, and 24 hours.** At 193K, the α-process occurs at near the same frequency as the β-process but with lower magnitude. The arrows show a shift in magnitude of ε'' across the spectra due to the conductivity, σ. 141

5.8 **Dielectric loss ε'' as a function of frequency for $A\beta_{1-42}$ in the range of 183K-168K and incubation periods of 0, 8, and 24 hours.** In the range of 183K-168K, there is significant mixing between σ, α-, and β-processes. 142

5.9 **Dielectric loss ε'' as a function of frequency for scrambled $A\beta_{42-1}$ in the range of 183K-168K and incubation periods of 0, 8, and 24 hours.** In the range of 183K-168K, there is significant mixing between σ, α-, and β-processes. Trends in this range are due to changes in conductivity, σ. 143

5.10 **Dielectric loss ε'' as a function of frequency for $A\beta_{1-42}$ in the range of 163K-148K and incubation periods of 0, 8, and 24 hours.** At 158K, the conductivity, σ and the α-process are substantially separated from the β process. At 158K and below, the β-relaxation peak in ε'' trends to lower magnitude and lower frequency over time. 144

5.11 **Dielectric loss ε'' as a function of frequency for scrambled $A\beta_{42-1}$ in the range of 163K-148K and incubation periods of 0, 8, and 24 hours.** At 163K, the conductivity, σ and the α-process are substantially separated from the β process. At 158K and below, the β-relaxation peak in ε'' trends to lower magnitude but unlike $A\beta_{1-42}$, the peak shifts towards higher frequency over time. 145

5.12 **Dielectric loss ε'' as a function of frequency for $A\beta_{1-42}$ in the range of 143K-133K and incubation periods of 0, 8, and 24 hours.** The β-relaxation peak in ε'' trends to lower magnitude and lower frequency over time. 146

5.13 **Dielectric loss ε'' as a function of frequency for scrambled $A\beta_{42-1}$ in the range of 143K-133K and incubation periods of 0, 8, and 24 hours.** The β-relaxation peak in ε'' trends to lower magnitude but unlike $A\beta_{1-42}$, the peak shifts towards higher frequency over time. 147

5.14 **Curve fitting of imaginary part of the permittivity data using the WinFIT program of the solvent, $A\beta_{1-42}$, and $A\beta_{42-1}$ at 223K.** A large, low frequency DC conductivity is fit with a power law. The α-relaxation process at around 10^7 Hz is fit with a Havriliak-Negami function. The β-relaxation function is not observed. The root-mean-square deviation (RMSD) of the fits are 0.015, 0.030, and 0.088, respectively. 149

5.15 **Curve fitting of imaginary part of the permittivity data using the WinFIT program of the solvent, $A\beta_{1-42}$, and $A\beta_{42-1}$ at 208K.** A large, low frequency DC conductivity is fit with a power law. The β-relaxation process at around 10^3 Hz is fit with a Cole-Davidson function and the α-relaxation process at around 10^5 Hz is fit with a Havriliak-Negami function. The RMSD of the fits are 0.018, 0.005, and 0.012, respectively. 150

5.16 **Curve fitting of imaginary part of the permittivity data using the WinFIT program of the solvent, $A\beta_{1-42}$, and $A\beta_{42-1}$ at 188K.** A large, low frequency DC conductivity is fit with a power law. The β-relaxation process at around 10^3 Hz is fit with a Cole-Davidson function and the α-relaxation process at around 10^1 Hz is fit with a Havriliak-Negami function. Here, the α process has crossed over to slower than β relaxation times. The RMSD of the fits are 0.001, 0.019, and 0.017, respectively. 151

5.17 **Curve fitting of the imaginary part of the permittivity data using the WinFIT program of the solvent, $A\beta_{1-42}$, and $A\beta_{42-1}$ at 133K.** A small, very low frequency DC conductivity is fit with a power law. The β-relaxation process at around 1 Hz is fit with a Cole-Davidson function and the α-relaxation process is not observed. The RMSD of the fits are 0.073, 0.042, and 0.006, respectively. 152

5.18 **Arrhenius plots of f_{max} versus inverse temperature for $A\beta_{1-42}$ over time.** The α-relaxation process follows a VFT behavior whereas the β-relaxation process follows an Arrhenius, or linear behavior. The α-process departs from the VFT curvature at low temperature. 154

5.19 **Arrhenius plots of f_{max} versus inverse temperature for scrambled $A\beta_{42-1}$ over time.** The α-relaxation process follows a VFT behavior whereas the β-relaxation process follows an Arrhenius, or linear behavior. The α-process departs from the VFT curvature at low temperature. 155

5.20 **Dielectric strength, $\Delta\varepsilon$ of the β-relaxation for $A\beta_{1-42}$ and $A\beta_{42-1}$ versus inverse temperature.** The dielectric strength for the $A\beta_{1-42}$ solution deceases to values less than the solvent over time. The decrease in dielectric strength indicates an anti-parallel β-sheet confirmation. The dielectric strength of $A\beta_{42-1}$ does not change and remains similar to the profile of the solvent. 157

5.21 **Temperature evolution of the real and imaginary parts of the dielectric permittivity for the solvent, hIAPP, and rIAPP from 223K to 198K.** Two relaxation processes for the real (ε') and imaginary (ε'') parts of the permittivity for the solvent, hIAPP, and rIAPP are observed. 159

5.22 **Temperature evolution of the real and imaginary parts of the dielectric permittivity for the solvent, hIAPP, and rIAPP from 193K to 168K.** The α-relaxation process rapidly shifts to lower frequency with decreasing temperature. In the range of 193K to 188K the two processes cross to where the α-relaxation is at lower frequency than the β-relaxation process at temperatures of 183K and below. . . 160

5.23 **Temperature evolution of the real and imaginary parts of the dielectric permittivity for the solvent, hIAPP, and rIAPP from 163K to 133K.** The β-relaxation process dominates below the crossing temperature and continues to slow to under 1 Hz. The DC conductivity has reduced in magnitude to outside the measured range below 158K. 161

5.24 **Dielectric loss ε'' as a function of frequency for hIAPP in the range of 223K-208K and incubation periods of 0, 24, 48, and 120 hours.** At temperatures above 208K, the β-relaxation process is masked by the conductivity, σ. The arrows depict a decrease in magnitude of ε'', due to the decrease in σ over time. The α-relaxation peak shows a shift at 223K and 218K at 0 hours, but does not appear to follow a trend. 163

5.25 **Dielectric loss ε'' as a function of frequency for rIAPP in the range of 223K-208K and incubation periods of 0, 24, 48, and 120 hours.** At temperatures above 208K, the β-relaxation process is masked by the conductivity, σ. The arrows depict an apparent shift in the α-relaxation process first to lower magnitude and frequency, then higher magnitude and frequency. This differs in behavior to hIAPP in the same temperature range. 164

5.26 **Dielectric loss ε'' as a function of frequency for hIAPP in the range of 203K-188K and incubation periods of 0, 24, 48, and 120 hours.** At 193K, the α-process occurs at near the same frequency as the β-process but with lower magnitude. The arrows depict trends of the conductivity, σ to lower magnitude at 203K and 198K, however trends in the permittivity at 193K and 188K appear to be due to relaxation processes. 165

5.27 **Dielectric loss ε'' as a function of frequency for rIAPP in the range of 203K-188K and incubation periods of 0, 24, 48, and 120 hours.** At 193K, the α-process occurs at near the same frequency as the β-process but with lower magnitude. At 193K and 188K, there are some shifts in the the conductivity, σ, but it does not appear to follow a trend over time. 166

5.28 **Dielectric loss ε'' as a function of frequency for hIAPP in the range of 183K-168K and incubation periods of 0, 24, 48, and 120 hours.** In the range of 183K-168K, there is significant mixing between σ, α-, and β-processes. Trends in this range are indeterminate. 167

5.29 **Dielectric loss ε'' as a function of frequency for rIAPP in the range of 183K-168K and incubation periods of 0, 24, 48, and 120 hours.** In the range of 183K-168K, there is significant mixing between σ, α-, and β-processes. Trends in this range are indeterminate. 168

5.30 **Dielectric loss ε'' as a function of frequency for hIAPP in the range of 163K-148K and incubation periods of 0, 24, 48, and 120 hours.** At 158K, the conductivity, σ and the α-process are substantially separated from the β process. At 158K and below, the β-relaxation peak in ε'' trends to higher magnitude and lower frequency over time. 169

5.31 **Dielectric loss ε'' as a function of frequency for rIAPP in the range of 163K-148K and incubation periods of 0, 24, 48, and 120 hours.** At 158K, the conductivity, σ and the α-process are substantially separated from the β process. At 158K and below, the β-relaxation peak first shifts to lower frequency and higher magnitude, then shifts to higher frequency and lower magnitude towards the spectra of the solvent. This differs in behavior from that of hIAPP in the same temperature range. 170

5.32 **Dielectric loss ε'' as a function of frequency for hIAPP in the range of 143K-133K and incubation periods of 0, 24, 48, and 120 hours.** The β-relaxation peak in ε'' trends to higher magnitude and lower frequency over time. 171

5.33 **Dielectric loss ε'' as a function of frequency for rIAPP in the range of 143K-133K and incubation periods of 0, 24, 48, and 120 hours.** The β-relaxation peak first shifts to lower frequency and higher magnitude, then shifts to higher frequency and lower magnitude towards the spectra of the solvent. This differs in behavior from that of hIAPP in the same temperature range. 172

5.34 **Curve fitting of imaginary part of the permittivity data using the WinFIT program of the solvent, hIAPP, and rIAPP at 223K.** A large, low frequency DC conductivity is fit with a power law. The α-relaxation process at around 10^7 Hz is fit with a Havriliak-Negami function. The β-relaxation function is not observed. The RMSD of the fits are 0.015, 0.016, and 0.034, respectively. 174

5.35 **Curve fitting of imaginary part of the permittivity data using the WinFIT program of the solvent, hIAPP, and rIAPP at 208K.** A large, low frequency DC conductivity is fit with a power law. The β-relaxation process at around 10^3 Hz is fit with a Cole-Davidson function and the α-relaxation process at around 10^5 Hz is fit with a Havriliak-Negami function. The RMSD of the fits are 0.018, 0.007, and 0.020, respectively. 175

5.36 **Curve fitting of imaginary part of the permittivity data using the WinFIT program of the solvent, hIAPP, and rIAPP at 188K.** A large, low frequency DC conductivity is fit with a power law. The β-relaxation process at around 10^3 Hz is fit with a Cole-Davidson function and the α-relaxation process at around 10^1 Hz is fit with a Havriliak-Negami function. Here, the α process has crossed over to slower than β relaxation times. The RMSD of the fits are 0.001, 0.006, and 0.008, respectively. 176

5.37 **Curve fitting of the imaginary part of the permittivity data using the WinFIT program of the solvent, hIAPP, rIAPP at 133K.** A small, very low frequency DC conductivity is fit with a power law. The β-relaxation process at around 1 Hz is fit with a Cole-Davidson function and the α-relaxation process is not observed. The RMSD of the fits are 0.073, 0.090, and 0.035, respectively. 177

5.38 **Arrhenius plots of f_{max} versus inverse temperature for solvent over time.** The α-relaxation process follows a VFT behavior whereas the β-relaxation process follows an Arrhenius, or linear behavior. . . . 178

5.39 **Arrhenius plots of f_{max} versus inverse temperature for hIAPP from 0-120 hours.** The α-relaxation process follows a VFT behavior whereas the β-relaxation process follows an Arrhenius, or linear behavior. The α-process departs from the VFT curvature at low temperature. 179

5.40 **Arrhenius plots of f_{max} versus inverse temperature for rIAPP from 0-120 hours.** The α-relaxation process follows a VFT behavior whereas the β-relaxation process follows an Arrhenius, or linear behavior. The α-process departs from the VFT curvature at low temperature. 180

5.41 **Dielectric strength, $\Delta\varepsilon$ of the β-relaxation for hIAPP and rIAPP versus inverse temperature.** The dielectric strength for the hIAPP solution remains relatively constant for the first 48 hours, then deceases to values less than the solvent after 120 hours of incubation. This may be an indication that the final aggregated state of hIAPP in serum is an anti-parallel β-sheet. The dielectric strength of rIAPP was similar to the solvent for all time points. This is a similar $\Delta\varepsilon$ behavior of $A\beta_{1-42}$ and $A\beta 42-1$ observed for the same solvent. 183

5.42 **Plots of the β-relaxation peak shift at 143K for $A\beta_{1-42}/A\beta_{42-1}$ and hIAPP/rIAPP as compared to the solvent.** The amyloidogenic peptides demonstrate a characteristic "red- shift" towards tower frequencies, indicating an increase in structured water. 185

Chapter 1

Introduction

1.1 Motivation for the Studies of Amyloidogenic Peptides

Improved patient care coupled with higher standards of living has nearly doubled the average life span of a person over the past century [1]. Furthermore, the leading edge of the "baby boom" generation is now approaching the midlife mark causing an influx of aged persons. The result of an increasingly older population is a record high incidence of aging-related diseases that is projected to triple over the next 40 years [2].

Many of these diseases are attributed to misfolded, aggregated proteins known as amyloids. Amyloids collect in the tissues and organs such as the brain, pancreas, and spleen causing debilitating diseases such as Alzheimer's and Type II Diabetes Mellitus. Each disease is associated with a particular protein responsible for the pathologic effects of amyloidogenic diseases, or amyloidoses. Although there have been several attempts to develop diagnostic methods based on the detection of amyloidogenic oligomers, there is an absence of a widely-accepted and deterministic approach.

Alzheimer's disease

Alzheimer's Disease (AD) is the most common cause of senile dementia. AD is an age-associated neurodegenerative disorder that causes loss of memory and language skills, damaged cognitive function, and altered behavior. AD typically affects people over the age of 65, but can start as early as people in their 30s [3].

It is estimated that 5.4 million Americans are living with AD, including approximately 200,000 age 65 years or younger with the aging of the baby boom generation projected to result in an additional 10 million people with AD in the near future. By 2050, there is expected to be nearly a million new cases per year, and AD prevalence is projected to be 11 to 16 million [4].

AD is the sixth leading cause of death in the United States and the fifth leading cause of death in Americans age $\geq$65 years. Although the proportions of deaths due to other major causes of death have decreased in the last several years, the proportion of deaths due to AD has risen significantly by a staggering 66% [4].

In 2011, more than 15 million family members and other unpaid caregivers provided an estimated 17.4 billion hours of care to people with AD and other dementias. In 2012, payments for health care, long-term care, and hospice services for people age $\geq$65 years with AD and other dementias are expected to be $200 billion. An estimated 800,000 people with AD (one in seven) live alone, and up to half of them do not have an identifiable caregiver [4].

Diabetes mellitus

Diabetes mellitus is the most common endocrine disease, characterized by high glucose levels, or hyperglycemia. The source of hyperglycemia may be due to either reduced insulin secretion or inaction by the body to properly use insulin. Common symptoms of diabetes are polyuria, polydypsia, polyphagia, weight loss, fatigue, blurred vision, and numbness [5].

There are four main types of diabetic disorders: Type I, Type II, gestational, and diabetes induced from other illnesses, such as pancreatic cancer or liver disfunction. Type I diabetes is also known as insulin-dependent or juvenile onset diabetes and occurs due to a loss of insulin-producing pancreatic β-cells. Type II diabetes is also known as non-insulin depended or adult onset diabetes. Type II diabetes occurs due to an insulin resistance and decreased production of insulin by pancreatic β-cells. In Type II diabetic patients, the muscles, liver, and fat cells cannot use the insulin produced in the body which leads to high levels of insulin [5].

Diabetes mellitus affects 25.8 million people of all ages-approximately 8.3 % of the U.S. population. Among U.S. residents ages 65 years and older, 10.9 million, or 26.9 %, had diabetes in 2010. About 1.9 million people ages 20 years or older were newly diagnosed with diabetes in 2010 in the United States. A study in 2005-2008 found that 35 % of U.S. adults ages 20 years or older and 50 % of adults ages 65 years or older had signs of prediabetes [6].

Diabetes is the leading cause of kidney failure, nontraumatic lower-limb amputations, and new cases of blindness among adults in the United States. It is also one of the major causes of heart disease and stroke and the seventh leading cause of death in the United States [6].

Direct medical costs are estimated at $116 billion in 2010. Average medical expenditures among people with diagnosed diabetes were 2.3 times higher than what expenditures would be in the absence of diabetes. Indirect costs such as disability, work loss, premature mortality are estimated at $58 billion [6].

1.1.1 Pathogenesis of amyloidogenic diseases

Amyloidosis is a pathological condition that refers to a number of diseases characterized by the formation of insoluble amyloid deposits in tissues and organs, such as liver, spleen, kidneys, and brain [7]. The deposits are caused by the misfolding and aggregation of amyloidogenic peptides into organized, fibrillar structures. Examples of the most common amyloid-related diseases are Alzheimer's disease, Type II diabetes, Huntington's disease, Parkinson's disease, Creutzfeldt-Jakob disease, and even transmissible diseases, such as spongiform encephalopathies [8]. Each disease has its own characteristic amyloidogenic peptide responsible for tissue and organ destruction. Although the etiology is varied (Genetic, sporadic, and infectious) [9], all present the characteristic amyloid plaque deposits in tissues that can be imaged *ex vivo* via histopathologic staining.

Historically, the amyloid hypothesis implicated amyloid plaques as the primary cause of amyloidogenic diseases [10, 11]. Recent evidence shows that organ and tissue disruption begins with aggregation of soluble, pre-fibrillar oligomers [12, 13, 14, 15]. Soluble amyloidogenic peptides have been found in cerebral spinal fluid (CSF) [16], urine [17], and blood [18], but currently there is no diagnostic method. Early detection of pre-fibrillar oligomers in any of these media is the motivation of our research.

Pathology of Alzheimer's disease

Alois Alzheimer first observed fibrils in the port-mortem brains of patients who suffered from a form of dementia now known as Alzheimer's disease (AD) [19]. Two physiological abnormalities are present in the brains of patients whom suffered from AD: intracellular neurofibrillary tangles (NFT) and extracellular amyloid desposits [20]. NFTs are paired helical filaments of hyperphosphorylated tau protein aggregates that are commonly found in the brains of patients with neurological disorders [20]. The amyloid deposits between neurons consist mainly of the polypeptides β-amyloid $A\beta_{1-40}$ and $A\beta_{1-42}$ and contrary to NFTs, are only found in patients with AD. Amyloid plaques and NFTs collect in the cerebral cortex and hippocampus regions of the brain[21]. Recent discovery of a pathogenic mutation in the amyloid precursor protein (APP) suggest that β-amyloid deposition is the primary cause of AD and may cascade the formation of hyperphosphorylated tau tangles and eventual neuronal death [22].

The β-amyloids originate from proteolytic cleavage (hydrolysis of the peptide bond) of the transmembrane amyloid precursor protein (APP). In a healthy brain, APP is cleaved by α- then γ-secretase between the lysine (16) and leucine (17) residues located in the hydrophobic KLVFF (16-20) region [11]. Cleavage of the hydrophobic region inhibits β-amyloid aggregation and the resulting chain is $A\beta_{17-40}$ or $A\beta_{17-42}$, also known as $3p$ [23, 11]. In pathogenic proteolytic processing of APP, the chain is first cleaved by β-secretase, not α-, which results in a longer chain of $A\beta_{1-40}$ or $A\beta_{1-42}$, as depicted in Figure 1.1. Enzymatic processes regulate and destroy pathogenic $A\beta$, preventing fibril formation in non-Alzheimer's patients [24].

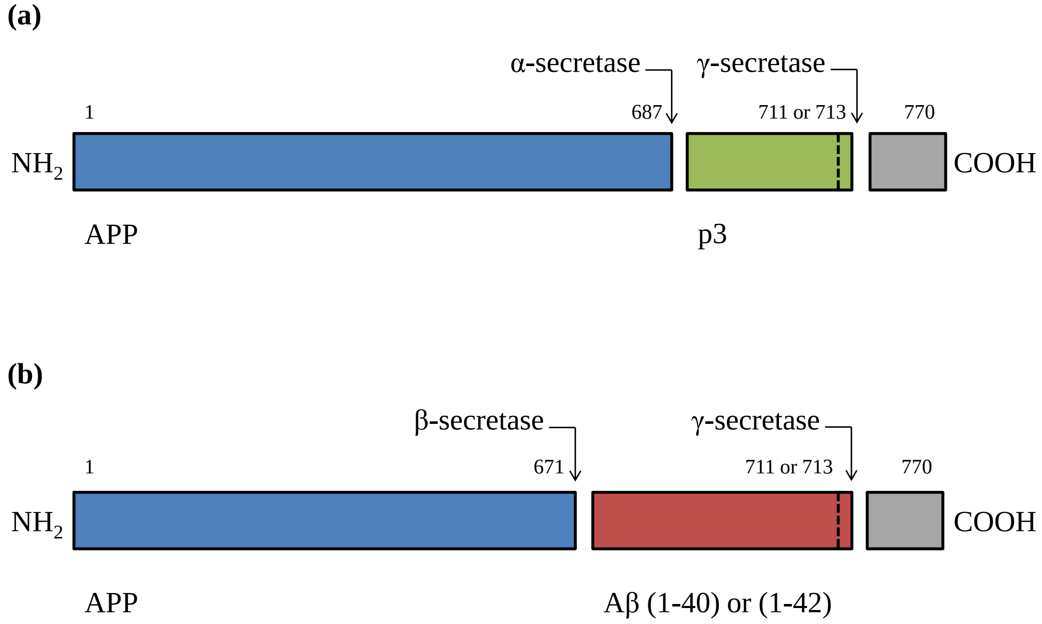

Figure 1.1: Non-pathogenic (a) and pathogenic (b) proteolytic processing of APP by α- or β-secretase, followed by γ-secretase cleavage. Adapted from [11].

Early theories about the pathogenesis of β-amyloid suggested that amyloid fibrils and plaques caused cell damage and death [25]. It is now believed that the oligomer and protofibril conformations are in fact more toxic because of their pore-forming capabilities [26, 16]. The molecular mechanism for toxicity is believed due to amyloid-

β disruption of the calcium channels at the membrane lipid bilayer through pore formation [26, 27].

Forms of soluble β-amyloid has been found in a number of fluids in both clinical AD and non-clinical AD individuals, including cerebral spinal fluid (CSF), blood plasma, and urine [18, 28]. Therefore, the development of a novel detection method of the soluble, intermediate oligomeric forms of β-amyloid in one or all of these fluids is a central focus of our studies.

Pathology of Type II diabetes

Amyloid deposits of human Islet Amyloid Polypeptide (IAPP), also known as amylin, have been found post-mortem in the pancreatic beta cells of more than 90% of patients with Type II diabetes [29]. Amylin is co-secreted with insulin by the pancreatic β-cells in the islets of Langerhans as a regulator of glucose uptake and gastric emptying. The 37 residue polypeptide amylin is soluble and non-toxic in its natural form. Environmental conditions and genetic predisposition cause amylin to aggregate and form toxic amyloid fibrils [30]. The amyloid deposits cause death of the pancreatic β-cells leading to reduced production of insulin and eventually Type II diabetes [31].

Amylin has been found to be amyloidogenic in humans, monkeys, and cats but not amyloidogenic in hamsters, mice, and rats [32, 33]. The variations in amino acid sequencies between species points to a theory that specific hydrophobic regions are responsible for amyloid formation. For example, in human IAPP, sequence 20-29 has been shown *in vivo* as a source for amyloid fibril formation [33, 31].

Recent theory suggest that cell membrane toxicity by IAPP is caused by pore-like disruption by oligomer and protofibril species [12]. The oligomers form ion channels in the lipid bilayers on the pancreatic β-cell membrane. These small pores allow cell contents to pass through, causing destabilization and cell death [34]. A cascading effect then follows where amylin aggregation destroys β-cells leading to decreased insulin. The remaining β-cells try to compensate by releasing more insulin and thus, more amylin which leads to further destruction of β-cells [35]. It is known that resulting basal amylin serum concentration is abnormal in patients with Type II diabetes [36], though the structure of the amylin (i.e. monomers, dimers, oligomers, etc.) is not classified. Novel detection of the oligomer and protofibril forms of amylin in blood serum is a central focus of our studies.

1.2 Protein Structure and Amyloidogenic Disease

1.2.1 Protein composition and structure

Proteins are a class of biological polymers responsible for a variety of essential biological functions in living systems; they act as reaction catalysts, transport and storage mechanisms, support immune function, transmit nerve impulses, and control growth and differentiation[37]. Each protein has a unique structure tailored to serve a specific biological role [38].

Proteins are comprised of primary building blocks called amino acids. Amino acids consist of a central carbon atom (α-carbon), amino group, carboxylic acid group, hydrogen atom, and a side chain (R group). The properties of proteins are mainly dependent on the characteristics of their composing animo acids, such as capacity to polymerize, acid-base properties, structure and chirality, and chemical functionality. Nearly all proteins found in all living organisms are constructed from the same 20 amino acids [37].

Proteins are linear chains of amino acids formed by linking the carboxyl group of one amino acid to the amine group of the next by a covalent link called a peptide bond (Figure 1.2). The bond releases a water molecule with the carboxyl group supplying the oxygen and the amine group supplying the two hydrogens. A series of amino acid comprising of less than 50 residues is referred to as a *polypeptide* and is named in the order from amine-terminal (N-terminal) to the carboxyl-terminal (C-terminal) [37][1]. The repeating sequence of $N - C_\alpha - C_O$ called the main chain or backbone, where the N is the amide nitrogen, the C_α is the α-carbon of the amino acid, and the C_O is the carbonyl carbon [38].

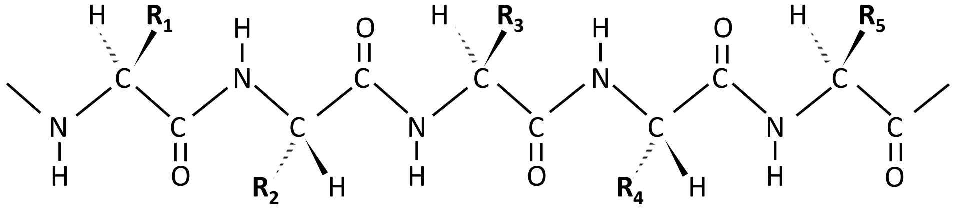

Figure 1.2: The linear structure of a polypeptide chain showing the links between carboxyl and amino groups of sequential amino acids.

The structure of the peptide bond prevents rotation about the $N - C_O$ atoms and is thus considered to have double-bond strength [38]. Since the resulting peptide bond is uncharged, this allows for tight packing of globular structures [37]. Conversely, the intra-amino acid covalent bonds between $N - C_\alpha$, $C_\alpha - C_O$, and side chains allow for the rigid peptide units to rotate and fold across these points in the chain. These two important features of the polypeptide chain provide the basis for higher order protein structure and function [38]

The polypeptide backbone is inherently polar. The amide nitrogen presents a protonated (positive) charged form and the carbonyl oxygen becomes deprotonated (negatively) charged [38]. The result at normal pH is that the backbone possesses a permanent dipole, represented in Figure 1.3.

Proteins are one or more polypeptide chains, typically on the order of 50-2000 residues. They usually take either a fibreous, globular, or membrane conformations. Fibreous proteins have a simple, linear structure, characteristically insoluble in water, and often serve a structural role, such as fibrinogen and collagen. Globular proteins

---

[1] a peptide or polypeptide may also refer to synthetically prepared proteins, unnatural chain lengths, or mutations

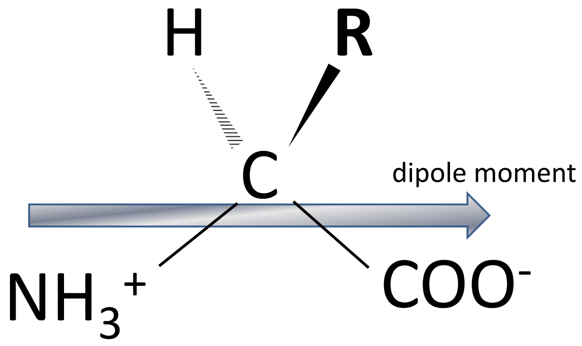

Figure 1.3: Amino acids and consequently, the polypeptide backbone consists of one positively charged and one negatively charged end. This produces a permanent dipole moment.

take an approximate spherical shape and are soluble in water. Most enzymes and myoglobin are examples of globular proteins. Membrane proteins have hydrophobic side chains oriented outward so that they can interact with the non-polar phase within membranes. Membrane proteins are insoluble in water but often soluble in detergents and other non-polar compounds. The light-absorbing proton pump, bacteriorhodopsin is an example of a typical membrane protein [38].

Proteins are classified into a structural hierarchy by their composition and conformation. The simplest form is the *primary structure*, or linear polypeptide chain. The *secondary structure* of proteins represents a three-dimensional arrangement of polypeptides formed by hydrogen bonding between amino acids that are in spatial proximity, but not necessarily neighboring. Secondary structure proteins may take the form of either a twisted α-helix or pleated β-strand that extends along one-dimension. Diagrammatic representations of both conformations are shown in Figure 1.4. The *tertiary structure* is characterized by a compact three-dimensional arrangement by bending or folding of the polypeptide chains. Globular proteins are organized by a tertiary structure. The tertiary structure may be stabilized by the formation of covalent bonds, such as ionic, disulfide and salt bridges, or non-covalent bonds, such as van der Waals forces and hydrogen bonds. The *quaternary structure* is a combination of two or more interacting tertiary structures. Each subunit of the quaternary structure acts cooperatively in the protein's function [37, 38].

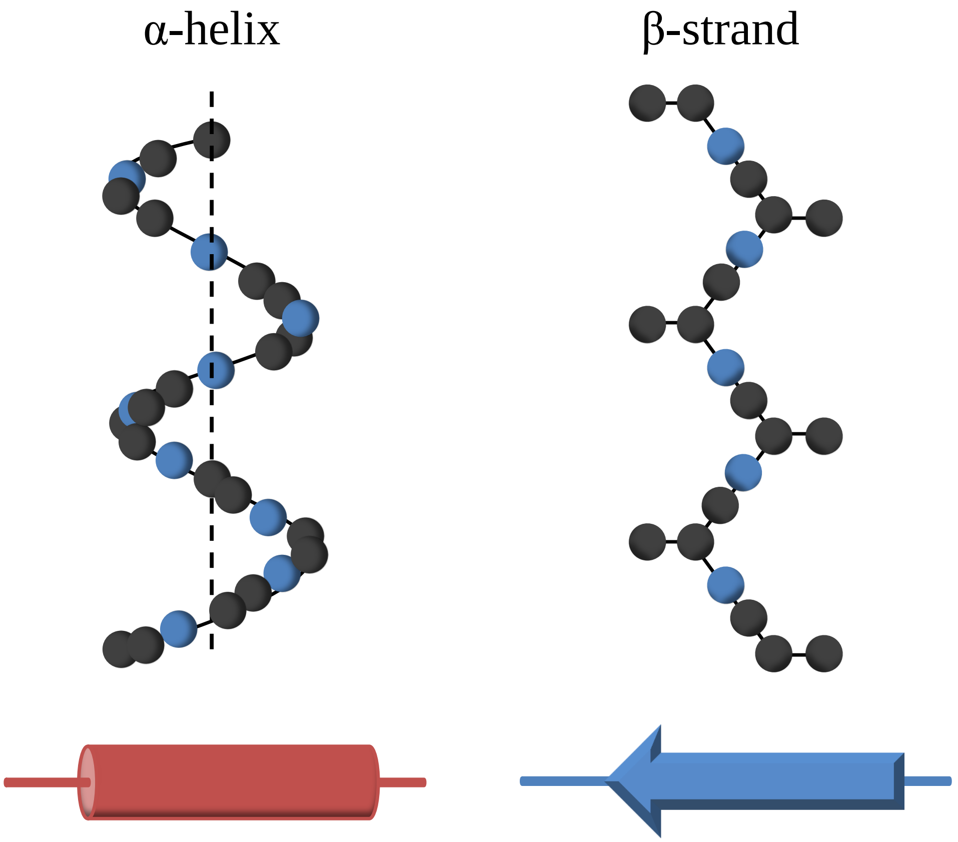

Figure 1.4: The two forms of protein secondary structure are shown here: the α-helix and the β-strand. An atomic model as well as a shorthand cartoon model for each conformation is depicted. Adapted from [37]

1.2.2 Protein folding and aggregation

When proteins are exposed to aqueous environments, they cluster to form tightly-packed structures with non-polar cores. The ordering of solvent, known as the hydrophobic effect, is an important driving force in protein aggregation and folding. The hydrophobic effect is a process in which non-polar groups cluster in order to minimize surface interactions with water [39]. Amphiphilic molecules, such as β-amyloid, consisting of strongly polar and non-polar groups exhibit, this behavior. Amphiphilic molecules form micelles in which the non-polar ends combine to form a hydrophobic domain of hydrocarbon tails while polar ends have ionic interactions with the solvent [37]. Figure 1.5 shows the burying of internal hydrophobic regions in micelle formation.

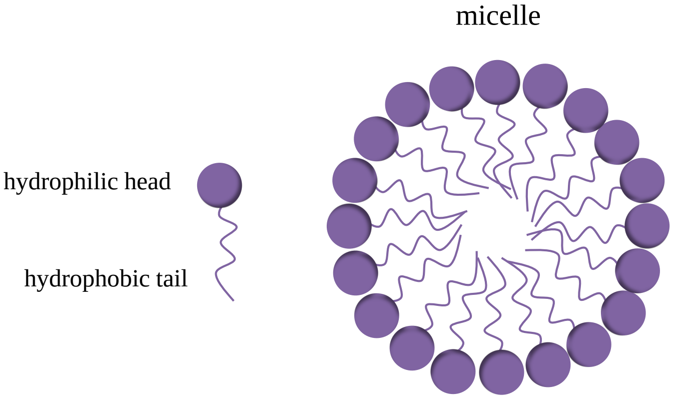

Figure 1.5: Hydrophobic tails bury in the interior during micelle formation as hydrophilic regions interact with polar solvents.

The immediate layers of water molecules surrounding the protein is known as the hydration shell. When a protein is placed in water, the hydration shell is disturbed. The water competes with the hydrogen bonding in the hydrophobic domain of the protein causing a reordering of the bound water. The bound water is then released and the hydrophobic regions begin to cluster. This is driven by a thermodynamically favorable event where the movement of bound, ordered water, moves to free, bulk-like water in the direction of increased entropy [37]. When a protein folds, the hydrophobic and hydrophilic regions combine via non-covalent interactions to form secondary structures, such as α-helices and β-sheets. The α-helix is formed by hydrogen bonds between NH and CO groups of the main chain. Figure 1.6 shows the β-sheet conformation is formed by either parallel or anti-parallel stacking between polypeptide strands [37, 38].

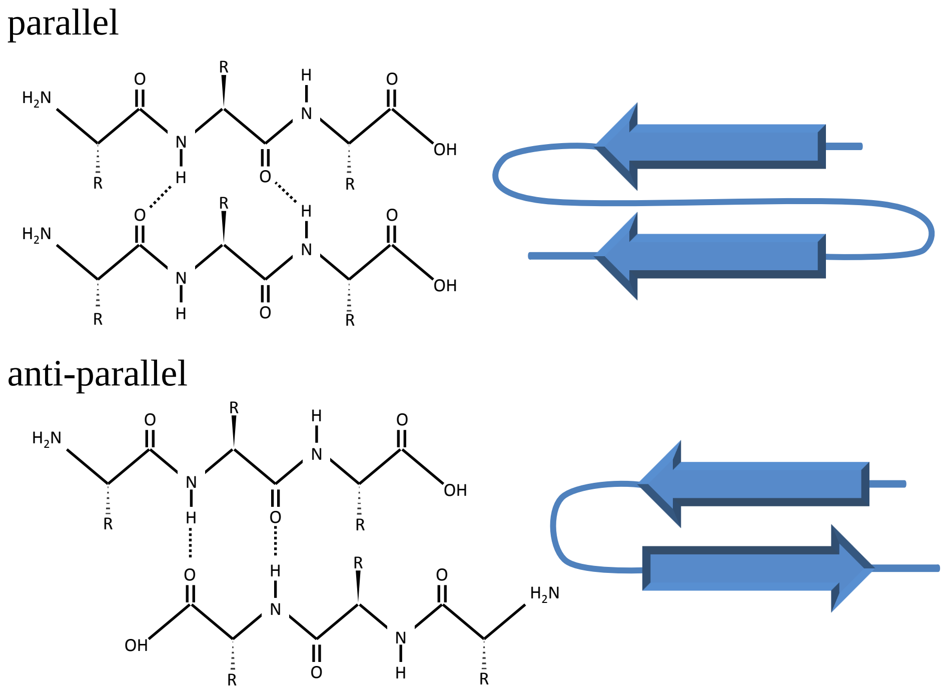
parallel
anti-parallel

Figure 1.6: β-strands may stack in parallel or anti-parallel β-sheets. Hydrogen bonds form between the NH and CO groups of adjacent strands. Adapted from [37]

1.3 Amyloids and Amyloidogenic Diseases

Although proper protein folding is necessary for biological function, alterations from standard conformations of proteins are attributed as the source for a number of diseases. A summary of the most common pathologies is outlined in Table 1.1 [8, 15, 40, 41, 42, 43]. Protein misfolding is commonly formed into β-sheets [44, 45, 46, 47]. If correctly folded, amino acids with hydrophobic side chains, such as valine, leucine, and isoleucine, are buried within the core yielding a soluble structure. Commonly, sequence errors or mutations cause a polypeptide to become misfolded. The hydrophobic regions are then exposed and will combine with structures of similar surfaces forming highly-ordered, insoluble structures [48, 49, 50]. The formation of fibrilar aggregates from misfolded hydrophobic combinations are known as amyloids.

Disease	**Peptide Responsible**
Alzheimer's disease	β-amyloid
Type II diabetes	amylin (IAPP)
Huntington's disease	huntingtin
Amyotrophic Lateral Sclerosis (ALS)	superoxide dismutase
Parkinson's disease	α-synuclein
Creutzfeldt-Jakob disease	prion protein
familial amyloidoses	transthyretin

Table 1.1: Various diseases caused by amyloid formation and their associated pathogenic peptide

All amyloids, though different in composition, share common structural characteristics. The terminal state of amyloidogenic peptide aggregates is an amyloid fibril; a long fibrillar structure with a diameter 6-10 nm and may have length of many microns [51, 52]. The amyloid fibril is formed by parallel or anti-parallel stacking of β-sheets perpendicular to the fibril axis [37].

Amyloid self-assembly and aggregation by the hydrophobic effect is linked to specific sequences of amino acids [53]. The specific size and location of hydrophobic amino acid regions determine whether a misfolded or mutated polypeptide will aggregate to form the β-sheet structure and ultimately, amyloid fibrils. Hydrophobic regions that are normally hidden in a properly folded protein are exposed to favor fibril formation by the surrounding solvent. Electrostatic and hydrophobic interactions cause these hydrophobic regions to combine into higher ordered structures.

Fibril formation begins with monomers, dimers, and small oligomers combining to form a pre-fibrilar oligomer nucleus. Once the nucleus is formed, monomers attach longitudinally to the core to create elongated protofibril strands (Figure 1.7) [54, 55]. Hydrogen bonds between elongated protofibrils then stack together laterally in parallel combinations to form fibril strands, as shown in Figure 1.8 [56]. The hydrogen bond network of the cross-β spine between β-strands creates insoluble and extremely stable fibrils [55].

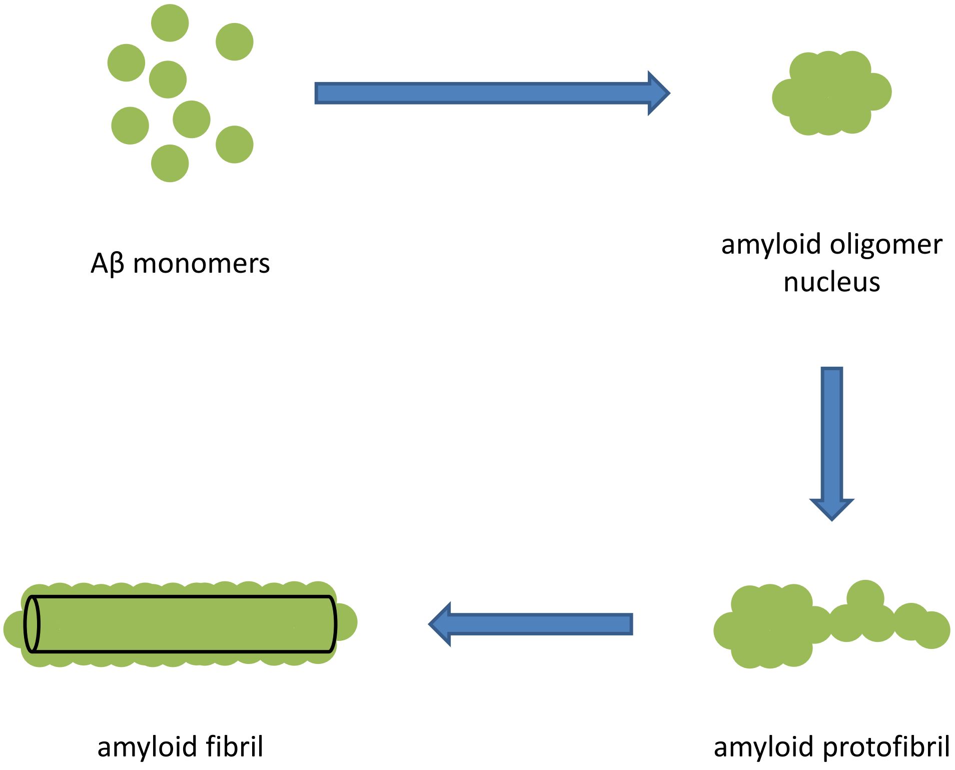

Figure 1.7: Nucleation starts with oligomer formation of β-amyloid fragments. Monomers then attach longitudinally to the oligomeric nucleus.

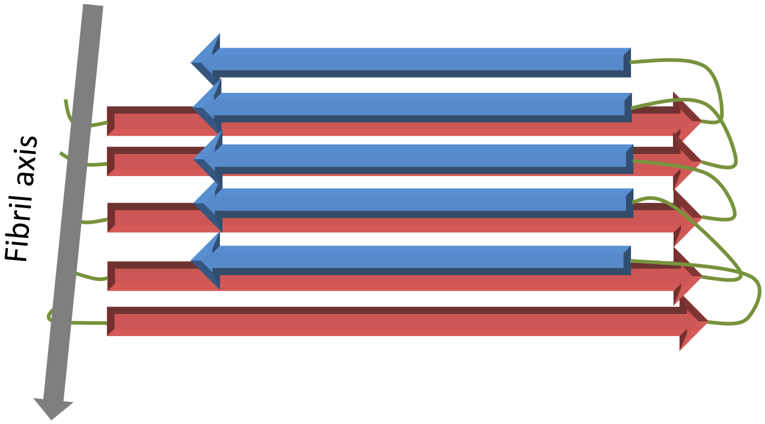

Figure 1.8: Ribbon representation viewed down the fibril axis showing protofilament structure. Each $A\beta$ polypeptide molecule contains two β-strands (red and blue) that form parallel stacked β-sheets. Adapted from [56].

1.4 The Role of Biological Water

Water plays a crucial role in protein hydration dynamics. Proteins are not static structures, but rather undergo a variety of fluctuations such as vibrations and rotations [57]. Recent theories suggest that water controls large-scale motions and shape changes as well as control internal motions necessary for function [58, 59, 57, 60, 61, 62]. Water mediated motions in proteins can be studied by modeling the α and β fluctuations that are traditionally observed in glass-forming materials [63, 59].

The dynamics of water interactions vary in regards to the location with respect to a protein. Biological water can be classified into three main groups: bulk-like or free water, surface or bound water, and internal or caged water [64]. Figure 1.9 shows the distribution of the three types of biological water at the protein-water interface using $A\beta_{1-42}$ structure as an example (obtained from Protein Data Bank ID: 1IYT [65]). Each classification of biological water plays a role in the dynamics and function of proteins.

Bulk-like water is located in the region beyond the first few molecules of the protein surface. It resembles pure water in structure, properties, and function. Bulk water plays a role in large-scale motions and shape changing as described by the α fluctuations of a hydrated protein solution [59]. We hypothesize that during amyloid aggregation, changes to the α fluctuations can be observed in the dielectric spectra.

Bound water is located at the surface of proteins where their hydrogen bond networks can interact with amino acid side chains and other surface water molecules [66]. The diversity of protein composition and structure present varying and unique forms of bound water. Chemical composition, hydrophobicity, size, and shape of a protein will determine the behavior of bound water. Bound water at the hydration layer of proteins is described by internal motions and protein function, known as β fluctuations [59]. Our hypothesis is that changes to the surface properties of pro-

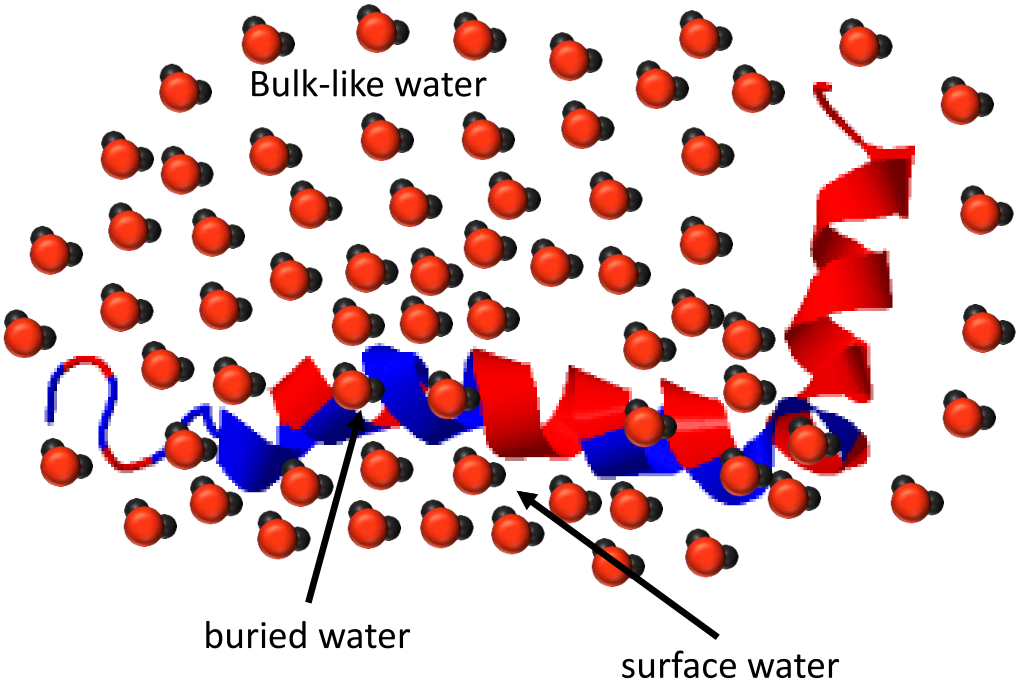

Figure 1.9: Representation of the hydration profile for $A\beta_{1-42}$ shows the three types of biological water at various regions in and around the protein. The confinement of water by a protein causes restricted rotations and other motions of water molecules resulting in attenuated relaxation times. The blue portions of the ribbon are hydrophilic and the red are hydrophobic. The $A\beta_{1-42}$ structure was obtained from PDB ID: 1IYT

teins through aggregation can be observed through changes of the β fluctuations in dielectric spectra.

Internal water is located in the interior of proteins [67]. Internal packing of the caged form of water greatly limits the molecular movements, yet it is crucial for protein stability and function [68]. Internal water hydrophobically interacts with the buried amino acid side chains, contributing to the protein's overall structure. Any change to the amino acid packing within a protein changes the structure and ultimately function of the protein. Internal water is not observable by dielectric spectroscopy but has been well studied by x-ray diffraction and NMR [67, 69].

1.5 Dielectric Spectroscopy as a Tool for Studying Amyloidogenic Peptides

Dielectric relaxation spectroscopy (DRS) is an effective technique for the study and characterization of biological materials and systems. The non-invasive nature of the technique allows for *in situ* monitoring of processes in a variety of environments. For decades, DRS has been using to study the dynamics of water at protein interfaces [70, 71, 72, 73]. Water structure near the surfaces of proteins is subject to hydrogen bonding of water molecules to proteins and electrostatic interactions due to the large dipole moment [74]. Studies of relaxation processes give us insight into structural and dynamical properties of biomaterials.

DRS allows the study of thermal fluctuations of supercooled liquids and glasses by relaxation measurements. Fluctuations and relaxations are interconnected by the fluctuation-dissipation theorem, which states that the same phenomena, observed under small perturbations, must also occur at equilibrium. Meaning that, observations of relaxation dynamics are representative of equilibrium fluctuations. Since protein structure and function are slaved to solvent behavior [58], this has great significance in the study of protein dynamics [75]. Application of an external electric field to a material provides the thermodynamical disturbance that can then be studying by relaxation spectroscopy.

The studies presented in this thesis probe the dynamics of proteins over a wide range of temperatures. The glass-forming cryoprotectant, glycerol is used as a buffer to study processes at supercooled temperatures. In many glass forming materials, a number of relaxation processes will present as peaks in dielectric loss, ε'' over a broadband of frequencies. They are typically termed in order of increasing frequency, α-, β-, δ-, and γ-relaxations [63]. It is important to note that the observed relaxation processes do not originate in the protein itself, but in the bulk solvent and the hydration shell [59].

α-relaxation

The α-relaxation occurs at low frequency, $10^1 - 10^5$ Hz. The α process describes structural fluctuations, as described by the mechanical Maxwell relation [59],

$$k_\alpha(T) = G_0/\eta(T) \tag{1.1}$$

where $k_\alpha(T)$ is the rate coefficient for the α fluctuations to the viscosity $\eta(T)$ and the infinite-frequency shear modulus G_0. At low temperature where the material acts as a solid, the viscosity is extremely large and therefore the α-fluctuations are essentially absent. The rate coefficient of α fluctuations typically follow the Vogel-Fulcher-Tammann relation [63].

β-relaxation

The β-relaxation occurs in the radio frequency, $10^5 - 10^7$ Hz. β processes in supercooled liquids and glasses are essentially independent of viscosity and will exist even at glassy states where we expect α fluctuations to disappear [76, 77, 59]. The β fluctuations take two forms in molecular liquids [78, 79, 80]. The Johari-Goldstein fluctuations are intertwined with the α fluctuations, and at high temperature (>300K), they merge[81]. Another form of β fluctuations occur as a non-cooperative process that does not merge with the α process. In contrast, this β process is at lower frequency than the α process above a crossing temperature [59]. This later form of the β_h relaxation, where h denotes hydration is observed in our studies of protein-solvent interactions. The rate coefficient of β fluctuations typically follow an Arrhenius relation [63].

δ-relaxation

The δ-relaxation occurs in the radio-microwave frequency, $10^8 - 10^{10}$ Hz. The δ process may possibly be representative of the dynamics of water near a biomolecule as an exchange between free and bound water states [82, 83, 74]. This process is out of the range of our measurement apparatus and will not be explored in this thesis.

γ-relaxation

The γ-relaxation occurs in the microwave frequency, $10^{10} - 10^{12}$ Hz. This frequency is typical of the relaxation of bulk or free water [74, 84] at distances of many molecules from the protein surface. This process is out of the range of our measurement apparatus and will not be explored in this thesis.

1.6 A Review of Methods for Studying Amyloidogenic Peptides

Studies of amyloids *in vitro* have been effective models for *in vivo* phenomena [85, 18]. Researchers have been able to observe mechanisms of fibril formation, structure, and kinetics though a variety of approaches, each with their own advantages and limitations. Table 1.2 outlines a summary of methods used in the studies of amyloid structure and aggregation that have provided a baseline for our work. Our goal is to show that dielectric spectroscopy is an effective tool for early detection of pre-amyloid structures.

Broadband dielectric relaxation spectroscopy (BDS or DRS) has not been extensively used in the studies of amyloidogenic peptides. One published study on amyloid fibril formation by DRS was done in non-*in vivo*-like conditions and lacks a non-amyloidogenic peptide control [86]. The full capabilities of DRS as an analysis tool of amyloidogenic structures has yet to be explored. The α and β fluctuations due to the protein and the solvent can be observed through modulation of the dielectric signal.

Method	Characteristics	Limitations	References
Microscopy	Oldest method for studying amyloids in tissue. Congo red binds to all amyloid structures and displays birefringence under cross polarized light. More recently, fluorescent microscopy and thioflavin T has been used to study kinetics.	Limited to fibrils: cannot be used to quantitatively determine the presence of smaller structures or observe fibril formation at the molecular level	[87, 88, 89, 90, 91, 92]
Dynamic light scattering (DLS)	Study the kinetics of fibril formation, similar to methods using thioflavin T.	No insight on structure or detection. Signal is greatly affected by structures found in blood and plasma and thus is an unrealistic choice for a diagnostic tool	[93, 94, 95, 96]
Electron microscopy (SEM/STM)	First method for direct imaging of amyloid fibril ultrastructure and their morphology. Information about the size and 3D shape of amyloid aggregates at different stages of fibril formation	Limited to *ex situ* studies of dried samples at cryogenic temperatures.	[97, 98, 99, 100]
X-ray diffraction	Directly image fibril structure and the cross-β spine of amyloidogenic structures	Limited to protein crystals and therefore can not be used to monitor fibril formation or as a quantitative measurement of oligomers.	[51, 101, 102, 103, 104]
Atomic force microscopy (AFM)	*in situ* monitoring of fibril formation and thermal and chemical stability. Probe the mechanical and structural properties of amyloids at the molecular level	Samples must be adsorbed to a surface: measurements in bulk fluid are not possible. Hardware not suitable in a medical diagnostics environment.	[105, 106, 107, 108]
Nuclear magnetic resonance (NMR)	*in situ* monitoring of fibril formation. 3D structure of amyloids	limited to measurements at specific relaxation times of solvent molecules. Lacks information about hydration layers and β fluctuations	[109, 110, 111]

Table 1.2: Summary of methods used in the studies of amyloid structure and aggregation.

1.7 Thesis Scope and Outline

Recent theories suggest that protein function and dynamics are connected to solvent interaction and hydration [59]. Protein structure and the hydration profile can be observed by measuring α and β fluctuations of the solvent-protein solution. Our hypothesis is that changes in the dielectric permittivity of protein-solvent relaxations can be observed during amyloid aggregation and fibril formation using the method of dielectric relaxation spectroscopy (DRS). We expect that the oligomeric form of amyloid aggregates will display a unique dielectric profile from that of monomers and fibrils. Characteristics such as space-charge polarization, dipole moment, and dielectric loss are used to profile the aggregation stages of the peptides.

We discuss the experimental portion in Chapter 3 with the studies of amyloidogenic peptides in a deionized water buffer at room temperature. The amyloidogenic human IAPP and β-amyloid and their non-amyloidogenic analogs, rat IAPP and scrambled β-amyloid are measured by DRS over time and with three concentrations. The dielectric modulus representation is used to present the conductivity and space-charge polarization effects measured over seven days of incubation.

We continue in Chapter 4 by studying the same peptides in a 50-50% by weight deionized water and glycerol buffer. The use of glycerol allows us to study the dielectric signal at sub-freezing temperatures and model the temperature evolution of the various peptides at different incubation times. Each time point represents a different fraction of monomers, oligomers, and fibrils. Analysis of the dielectric spectra provides information about activation energies (enthalpy) and glass-forming fragility for each time point in an effort to characterize the phase of aggregation. The dielectric strength for each time and temperature point give information about the dipole moment of the protein-solvent solutions to determine the structure, whether parallel or anti-parallel β-sheets.

We conclude the experimental portion in Chapter 5 by measuring the peptides in an *in vivo*-like condition using serum. The peptides are first diluted in a bovine serum albumin (BSA) buffer and then diluted in 50-50% by weight glycerol mixture. Again, the peptide solutions are measured at low temperature and as a function of time. Activation energies and fragilities are determined and an attempt to classify the conformations of the peptides is made. The dielectric strength is used to determine the structural nature of the peptides in the BSA buffer.

We summarize in Chapter 6 the general conclusions of these studies of amyloidogenic peptides by dielectric relaxation spectroscopy. A direction for future work is presented for continuation beyond the scope of this thesis.

Chapter 2

Materials and Methods

2.1 Introduction to Dielectric Relaxation Spectroscopy

The study of the propagation of electric fields in matter is of great interest to physicists, chemists, biologist, and engineers. Not all matter responds to electric fields in a consistent manner, yet most can be classified into two groups–conductors and insulators (or dielectrics). Conductors can be considered as possessing an unlimited amount of charge carriers that are free to move about a material. The electrons in a conductor are not bound to a particular nucleus but will transfer between molecules of the substance. By contrast, the electrons of an insulator or dielectric will remain with the nucleus as a bound ensemble within an atom or molecule [112]. However, when placed in an electric field the atom or molecule may deform or reorient based on a mechanism known as polarization. In the dynamic regime, there exists a lag phase between when the electric field is switched on and when the polarization attains a steady-state value. The time for a material to reach the maximum polarization is denoted the *relaxation time* in the physical phenomena, *dielectric relaxation.* We observe a number of polarization mechanisms in dielectric relaxation over a broadband of frequencies, each of which are summarized below [113] and can be seen in Figure 2.1.

Electron polarization

Electron polarization is the deformation of the atomic electrons in the presence of an electric field. This process occurs at high (optical) frequencies, near 10^{15} Hz.

Atomic polarization

Atomic polarization is the displacement of atoms or groups of atoms relative to one another within a molecule in the presence of an electric field. This process occurs at high (microwave to optical) frequencies, at approximately 10^{12} - 10^{14} Hz.

Orientation polarization

Orientation polarization, also known as dipole relaxation, is the rotation and orientation of a molecule in the presence of an electric field. Only polar molecules with permanent dipole moments will exhibit orientation polarization. This rotation is impeded by thermal motion and viscosity and this, the relaxation time is highly dependent on the frequency of the applied electric field, temperature, and pressure. The frequency range is typically in the radio frequencies (MHz) and below.

Ionic polarization

Ionic polarization is the displacement of positive ions in the direction of an applied electric field with negative electrons in the opposing direction in an ionic lattice. The result is a net dipole moment to the entire structure. Ionic polarization is predominately at very low (DC) frequencies and only has a weak temperature dependence. Commonly referred to as DC conductivity, it only presents dielectric losses to the system.

Electrode polarization

Electrode polarization is an impedance of the mobility of charge carriers at the interface of ionic materials and a metal conductor [114]. Electrode polarization may introduce a large dielectric response at low frequencies.

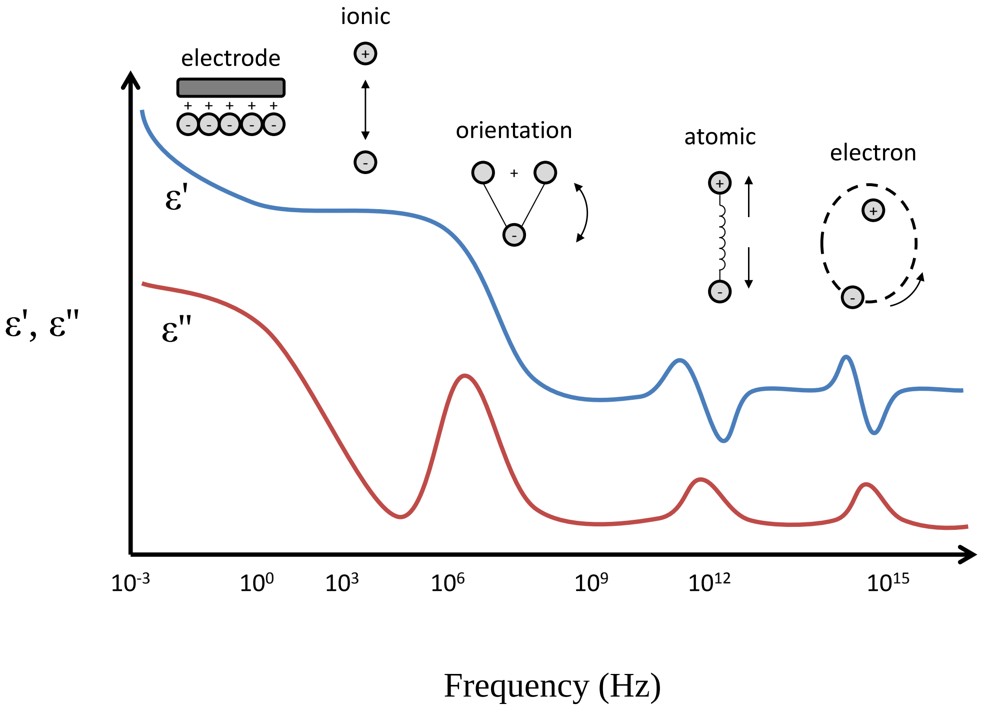
ionic
electrode
orientation
atomic
electron
ε'
ε''
ε', ε''
10^{-3}
10^{0}
10^{3}
10^{6}
10^{9}
10^{12}
10^{15}
Frequency (Hz)

Figure 2.1: Schematic representation of the polarization processes in a broadband dielectric spectrum for the real (ε') and imaginary (ε'') parts of the permittivity. Adapted from [115].

2.1.1 Polarization and the static field

Polarization occurs when dielectric materials are placed in and electric field. The molecular and atomic dipoles align in proportion with the strength of that field. In the presence of a constant (DC) electric field, the polarization, $\mathbf{P}$ of a material can be represented in terms of the electric susceptibility, χ_e and the electric field, **E** by

$$\mathbf{P} = \varepsilon_0 \chi_e \mathbf{E} \tag{2.1}$$

where $\varepsilon_0 = 8.854 \times 10^{-12}$ $\mathrm{C^2/N{\cdot}m^2}$ is the permittivity of free space.

Gauss's law in linear media facilitates the description of dielectric materials by means of the free charge density, $\rho free$

$$\nabla \cdot (\varepsilon_0 \mathbf{E} + \mathbf{P}) = \rho_{free} \tag{2.2}$$

The separation of electric charges in a dielectric can be represented as the electric displacement, **D** defined as

$$\mathbf{D} \equiv \varepsilon_0 \mathbf{E} + \mathbf{P} \tag{2.3}$$

Using the definition of polarization we introduce ε as the permittivity of a material.

$$\mathbf{D} = \varepsilon \mathbf{E} \tag{2.4}$$

$$\varepsilon \equiv \varepsilon_0 (1 + \chi_e) \tag{2.5}$$

2.1.2 Time-dependent fields

In the case of a time-dependent (AC) electric field applied to a dielectric material, frequency-dependent charge displacements are observed. The polarization of the material will not reach the static value immediately, but will approach it gradually with a lag phase from when the electric field is applied and when the dipoles orient (see Figure 2.2). The rate at which the media is polarized can be represented as the exponential law [116]

$$P(t) = P_0 (1 - e^{-t/\tau}) \tag{2.6}$$

Analogous to the static case, a time-dependent complex polarization **P*** can be

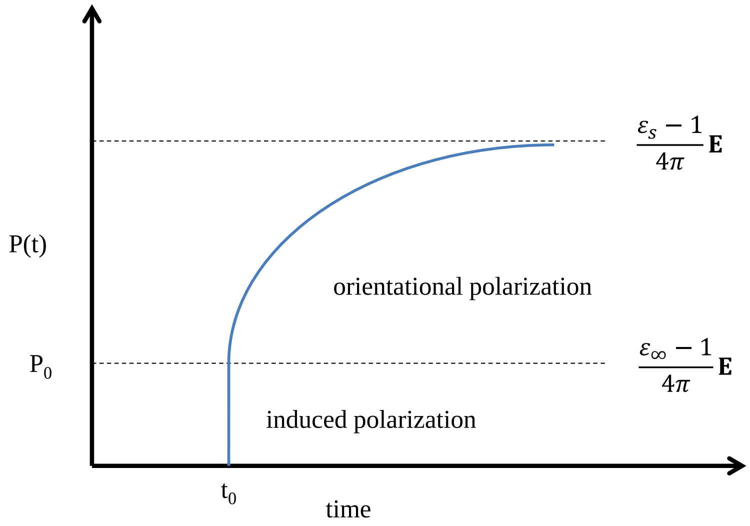

$\frac{\varepsilon_s - 1}{4\pi}\mathbf{E}$
P(t)
orientational polarization
P$_0$
$\frac{\varepsilon_\infty - 1}{4\pi}\mathbf{E}$
induced polarization
t$_0$
time

Figure 2.2: Time-dependence of the polarization P of a dielectric material when an electric field is applied. Adapted from [63].

expressed in terms of the complex electric susceptibility and the electric field,

$$\mathbf{P}^* = \varepsilon_0 \chi_e^* \mathbf{E}^* \tag{2.7}$$

or

$$\mathbf{P}^*(\omega) = \varepsilon_0(\varepsilon^* - 1)\mathbf{E}^*(\omega) \tag{2.8}$$

where

$$\varepsilon^*(\omega) = \varepsilon'(\omega) - i\varepsilon''(\omega) \tag{2.9}$$

is the complex dielectric function in the presence of a time-dependant electric field,

$$\mathbf{E}(t) = E_0 e^{-i\omega t} \tag{2.10}$$

The real part of the dielectric function $\varepsilon'(\omega)$ is proportional to the energy stored in the system and is commonly referred to as the absorption. The imaginary part $\varepsilon''(\omega)$ is proportional to the energy dissipated in the system and is commonly referred to as the dielectric dispersion or loss [63]. The real and imaginary parts of the dielectric function are related by the Kramers-Kronig relations [117, 63] such that

$$\varepsilon'(\omega) = \varepsilon_\infty + \frac{2}{\pi}\int_0^\infty \frac{\xi\varepsilon''(\xi)}{\xi^2 - \omega^2} d\xi \tag{2.11}$$

$$\varepsilon''(\omega) = -\frac{2\omega}{\pi}\int_0^\infty \frac{\varepsilon'(\xi) - \varepsilon_\infty}{\xi^2 - \omega^2} d\xi \tag{2.12}$$

where ξ is a dummy variable of integration. This relation has great significance in practice in that the absorbtion process can be derived by observation of the dispersion phenomena. Application of a Laplace transformation of the polarization decay function yields the Debye relations for dielectric relaxation [118]

$$\varepsilon'(\omega) = \varepsilon_\infty + \frac{\Delta\varepsilon}{1 + \omega^2\tau^2} \tag{2.13}$$

$$\varepsilon''(\omega) = \frac{\Delta\varepsilon\omega\tau}{1 + \omega^2\tau^2} \tag{2.14}$$

$$\varepsilon^*(\omega) = \varepsilon_\infty + \frac{\Delta\varepsilon}{1 + i\omega\tau} \tag{2.15}$$

where τ is the relaxation time found in $P(t) = P_0(1 - e^{-t/\tau})$. The dielectric strength $\Delta\varepsilon = \varepsilon_s - \varepsilon_\infty$ is introduced with the boundary conditions ε_s as the static permittivity and ε_∞ as the permittivity high high frequency such that

$$\varepsilon_s = \varepsilon'(0) \tag{2.16}$$

$$\varepsilon_\infty = \varepsilon'(\infty) \tag{2.17}$$

2.1.3 Non-Debye relaxation processes

The Debye relaxation equations assume the dielectric material is isotropic and the decay of the polarization follows the model exponential function. Often in the case of polymers and biological materials, the relaxation time is better modeled by a non-Debye distribution. Kenneth S. Cole and Robert H. Cole first introduced a modification of the Debye distribution with symmetric broadening of the dielectric loss peak [119]

$$\varepsilon^*_{CC}(\omega) = \varepsilon_\infty + \frac{\Delta\varepsilon}{1 + (i\omega\tau_{CC})^\beta} \tag{2.18}$$

where β is the broadening parameter from $0< \beta \leq 1$ and τ_{CC} is the Cole-Cole relaxation time. Note that when β=1, the Debye function is recovered. The maximal dielectric loss occurs at ω_{max}=$2\pi\nu_{max}$=$1/\tau_{CC}$.

Liquids and low molecular glass-forming materials typically exhibit dielectric spectra with asymmetric broadening [63]. The asymmetric broadening parameter γ, $0< \gamma \leq 1$ arises in the Davidson-Cole formalism [120, 121]

$$\varepsilon^*_{DC}(\omega) = \varepsilon_\infty + \frac{\Delta\varepsilon}{(1 + i\omega\tau_{DC})^\gamma} \tag{2.19}$$

with τ_{DC} as the Davidson-Cole relaxation time and again, with γ=1 the Debye equations are recovered. Since the Davidson-Cole function is asymmetrical, the relaxation time τ_{DC} is not at the frequency of maximal dielectric loss, but rather dependent on the shape parameters, given by [63]

$$\omega_{max} = \frac{1}{\tau_{DC}} \tan\left[\frac{\pi}{2\gamma + 2}\right] \tag{2.20}$$

Havriliak and Negami introduced a more general, empirical form for the relaxation distribution to account for both symmetric and asymmetric broadening of the dielectric loss [122, 123]

$$\varepsilon^*_{HN}(\omega) = \varepsilon_\infty + \frac{\Delta\varepsilon}{(1 + (i\omega\tau_{HN})^\beta)^\gamma} \tag{2.21}$$

with τ_{HN} as the Havriliak-Negami relaxation time. The versatility of the Havriliak-Negami function proves to be quite useful in the analysis of anisotropic systems such as polymers and biopolymers. Similar to the Davidson-Cole function, since the Havriliak-Negami function is asymmetrical, the relaxation time $\tau_{_{HN}}$ is dependent on the shape parameters, given by [63, 124]

$$\omega_{max} = \frac{1}{\tau_{_{HN}}} \left[sin\frac{\beta\pi}{2\gamma+2} \right]^{1/\beta} \left[sin\frac{\beta\gamma\pi}{2\gamma+2} \right]^{-1/\beta} \tag{2.22}$$

At low frequency, dielectric spectra are often dominated by DC conductivity due to free ions in the solution. The conductivity only introduces dielectric loss and is modeled by the power law

$$\sigma(\omega) = -i\left(\frac{\sigma_0}{\varepsilon_0\omega}\right)^N \tag{2.23}$$

where σ_0 is the DC conductivity and N is the exponent of the frequency dependence of the conductivity. In the analysis of dielectric spectra, the conductivity term is added to a number (n) of relaxation processes such that the total dielectric function is

$$\varepsilon^*(\omega) = -i\left(\frac{\sigma_0}{\varepsilon_0\omega}\right)^N + \sum_{k=1}^{n}\left[\varepsilon_{\infty,k} + \frac{\Delta\varepsilon_k}{(1+(i\omega\tau_k)^{\beta_k})^{\gamma_k}}\right] \tag{2.24}$$

2.1.4 Dielectric modulus

Ionic materials, such as the case of protein-solvent mixtures, often display a highly conductive component. In low frequency domain is often dominated by the conductivity in the region where dipole relaxation processes would be typically observed. The dielectric modulus, M^* is a useful parameter for analyzing the dielectric spectra when ionic conductors are present [125, 126, 127, 128]. The complex modulus is defined as:

$$M^* = M' + iM'' = \frac{1}{\varepsilon^*} = \frac{\varepsilon'}{\varepsilon'^2 + \varepsilon''^2} + i\frac{\varepsilon''}{\varepsilon'^2 + \varepsilon''^2} \tag{2.25}$$

where analogous to the permittivity, M' is the dielectric modulus absorbtion and M'' is the loss. One advantage of the dielectric modulus is that it transforms the conductivity into a relaxation peak, which allows low frequency orientational relaxation modes to be more easily studied [129].

Cole and Cole suggested a model-free method of analyzing dielectric data by plotting ε'' vs. ε' in the complex plane [119]. Not to be confused with the Cole-Cole dielectric function, a Cole-Cole plot can be used in the analysis of any dielectric spectra. In the case of Debye relaxation, a perfect semicircle is obtained. Deformations of the semicircle can be best modeled by the Havriliak-Negami function as seen in Figure 2.3 where the angles of tilt are defined by the shape parameters of the Havriliak-Negami function [63]. Each relaxation process will contribute its own semicircle in a Cole-Cole plot and often the semicircles will overlap. Similarly in the modulus formalism, a modulus Cole-Cole plot can be created by plotting M'' vs. M'. The modulus Cole-Cole plot is particularly useful in the case of ionic liquids [126, 127, 130] where the conductivity will dominate at low frequencies. Since the conductivity appears in both M'' and M', a new semicircle for the conductivity appears in the modulus Cole-Cole plot that is not present in the permittivity.

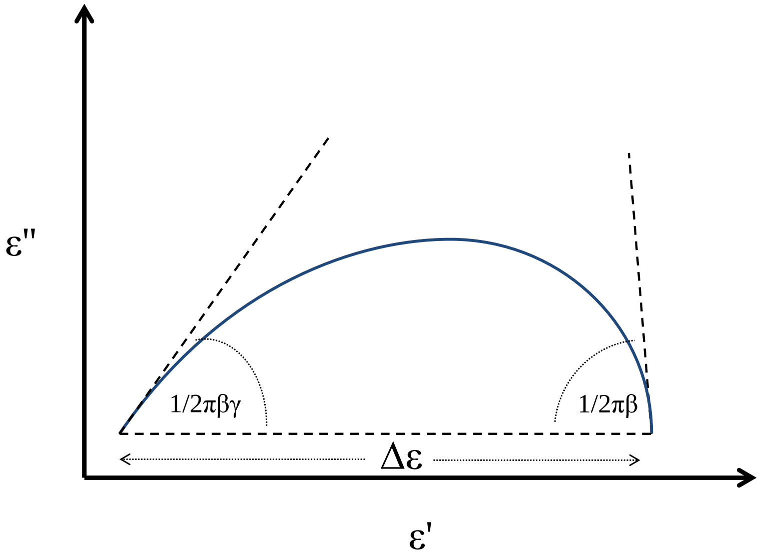

Figure 2.3: Schematic representation of the Cole-Cole plot for a Havriliak-Negami function where β, γ, and $\Delta\varepsilon$ are the shape parameters of the H-N function.

2.1.5 Relaxation kinetics

As previously stated, thermal motions of dipole orientation are highly dependent on temperature and viscosity. Energy barriers between initial and final states in relaxation processes follow similar behavior to empirical formulas developed for reaction rate theory. The Arrhenius law [131] describes the temperature dependence of a reaction rate, $k(T)$ in terms of the activation energy E_a and Boltzmann constant $k_B = 1.381 \times 10^{-23} J/K$

$$k(T) = Ae^{\left(\frac{-E_a}{k_B T}\right)} \tag{2.26}$$

In the analysis of dipole relaxation rates, A denotes the relaxation rate at the high temperature limit. The physical representation of the activation energy can be seen in Figure 2.4; a model system of double-minimum potential. In the steady-state, thermal fluctuations will allow equal transitions between the two potentials. When an external electric field is applied, the dipoles orient in a manner that differentiates the potentials [63]. The minimum energy required to transfer from the lower to higher energy level is the activation energy of the process.

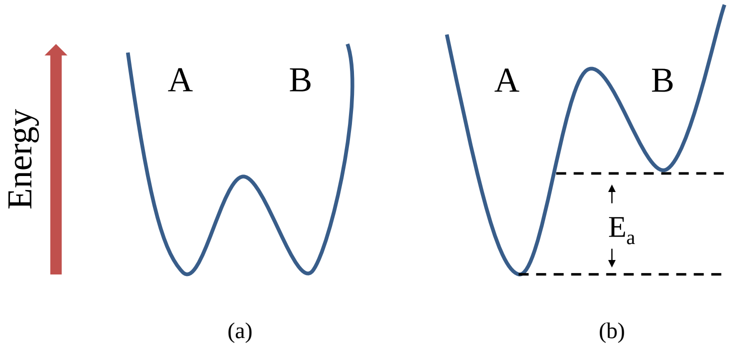

Figure 2.4: Model of a double-minimum potential (a) in a steady-state and (b) in the presence of an applied electric field. The application of an electric field causes a shift in the potentials such that an energy barrier is created.

The relaxation rates of supercooled liquids and glasses can not always be best-described by Arrhenius behavior. The Vogel-Fulcher-Tammann (VFT) equation [132, 133, 134] is a useful empirical formula that demonstrates a deviation from the Arrhenius behavior. Similar to the Arrhenius equation but with the addition of T_V, the VFT temperature or ideal glass transition temperature [63]

$$\nu(T) = \nu_\infty e^{\frac{-DT_V}{T-T_V}} \tag{2.27}$$

The VFT parameter D, quantitatively characterizes the fragility of glass forming materials. Materials that deviate greatly from Arrhenius-type behavior are called "fragile" glass formers [135, 136] as seen in Figure 2.5.

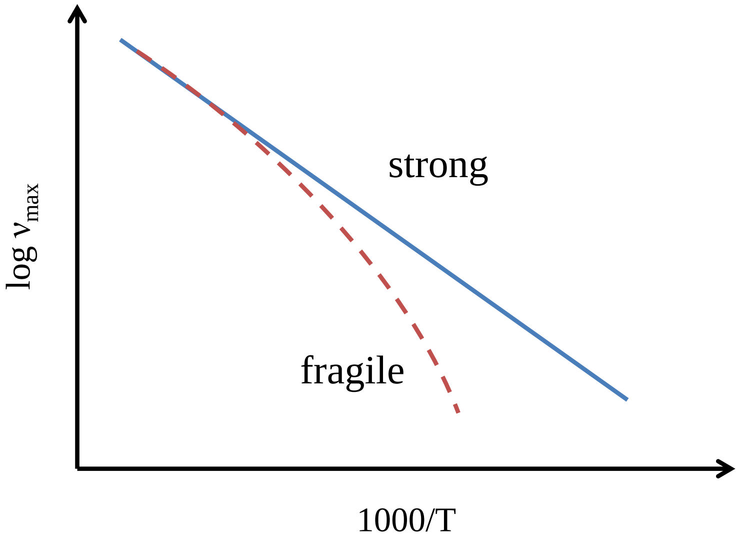

Figure 2.5: The fragility of glass forming materials can be visualized diagrammatically by the deviation from Arrhenius-type behavior.

2.2 Broadband Dielectric Spectroscopy

2.2.1 Instrumentation

The complex dielectric function, ε^* can be experimentally measured using the broadband dielectric relaxation spectroscopy (BDS or DRS) technique. DRS may span frequencies of $10^{-6} - 10^{12}$ Hz, using a combination of electrical impedance $(10^{-6} - 10^{7})$

and optical measurement $10^7 - 10^{12}$ techniques [63]. Our measurements are limited to electrical impedance in which the sample is treated as a parallel or serial circuit of an ideal capacitor and ohmic resistor.

In DRS, a capacitive sample cell made of two conducting parallel plates is place under a probing AC field with a fixed frequency, V_0. When a dielectric sample is placed between the two plates, the capacitance increases over that of the empty cell. The dielectric permittivity can be directly measured by relating the empty cell capacitance to the capacitance in the presence of a sample. When a voltage is applied to a dielectric sample, the dipoles will align as in Figure 2.6.

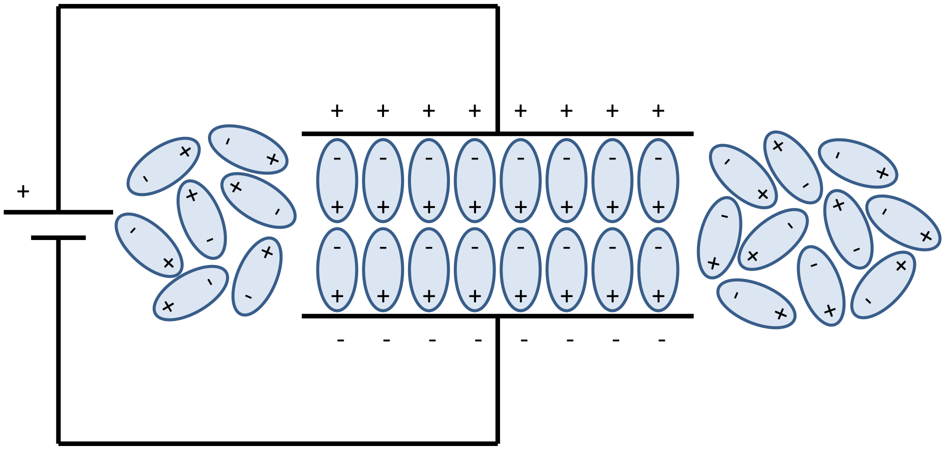

Figure 2.6: Material dipoles are typically in a random orientation. When placed inside an electric field, the dipoles align between the capacitive plates.

The applied voltage results in an induced current, I_0 at the same frequency with a phase shift, φ shown in Figure 2.7.

For a capacitor filled with a sample, the complex dielectric permittivity, ε^* is defined as the ratio,

$$\varepsilon^* = \varepsilon'(\omega) - i\varepsilon''(\omega) = \frac{C^*}{C_0} \tag{2.28}$$

where $C^*(\omega)$ is the complex capacitance and C_0 is the empty cell (vacuum) capacitance [63]. When an oscillating AC field, $V^*(\omega) = V_0 e^{i\omega t}$, the dielectric function can

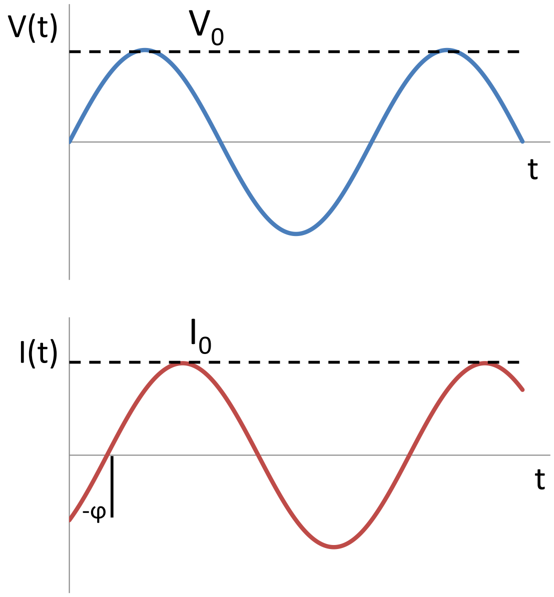

Figure 2.7: In dielectric relaxation spectroscopy (DRS), complex impedance is calculated from the ratio of the applied voltage and induced current with a phase shift.

be determined by measuring the complex impedance of the sample

$$Z^*(\omega) = Z' + iZ'' = \frac{V^*(\omega)}{I^*(\omega)} \tag{2.29}$$

which is connected to the complex permittivity by [63]

$$\varepsilon^*(\omega) = \frac{1}{i\omega\varepsilon_0 Z^*(\omega) C_0} \tag{2.30}$$

Our DRS analyzer is setup to collect data in *gain phase measurement* mode in which two voltage channels are used to compute the permittivity. The input voltage (V_1) amplitude and phase is measured directly from the analyzer through Channel 1. The output current, I_s is first converted to a voltage using a variable resistor and operational amplifier and collected via Channel 2 as pictured in Figure 2.8. The value of R_x is chosen so that V_2 is in a measurable range. A protective resistor, R_0 is used to limit the current if the sample impedance Z_s is too low [137]. Ideally, the sample current is defined by

$$I_s = \frac{-V_2}{R_x} \tag{2.31}$$

such that the sample impedance is

$$Z_s = \frac{V_1}{I_s} = \frac{-V_1}{V_2} R_x \tag{2.32}$$

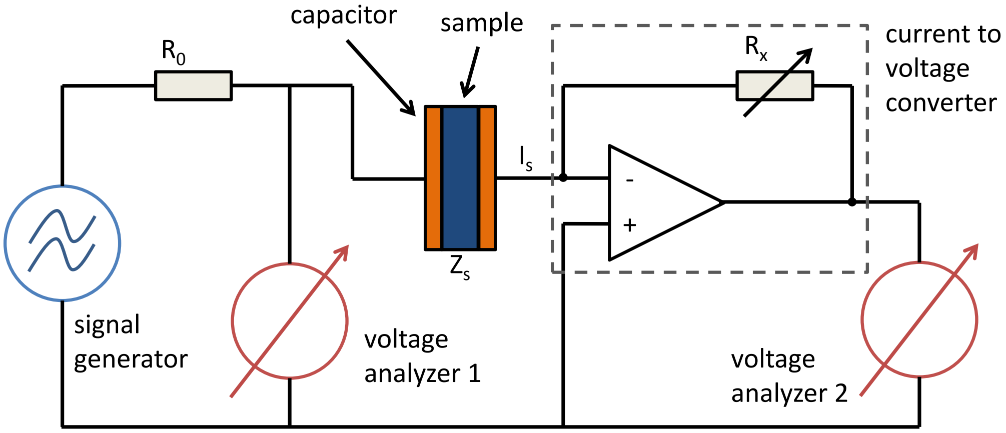

Figure 2.8: A schematic diagram of DRS gain phase measurement. Two probing voltages are used to compute the complex permittivity.

Dielectric relaxation measurements were taken using Alpha-A Analyzer and Quatro Cryosystem turnkey systems from Novocontrol Technologies. A block diagram of the complete DRS setup is depicted in Figure 2.9.

The Alpha-A mainframe contains a frequency response analyzer with a sine wave and DC-bias generator and two AC voltage input channels. The analyzer can measure samples in the frequency range from $3 \cdot 10^{-5}$ to $4 \cdot 10^{7}$ Hz, impedance from 10^{-3} to 10^{15} Ω, and capacitance down to 1 fF (10^{-15}). In addition, the mainframe contains the power supplies, analog and digital control lines and the firmware for operation of the test interfaces.

The Quatro Cryosystem provides fully automatic temperature control for DRS measurements. The main parts of the system are the cryostat, gas heating mod-

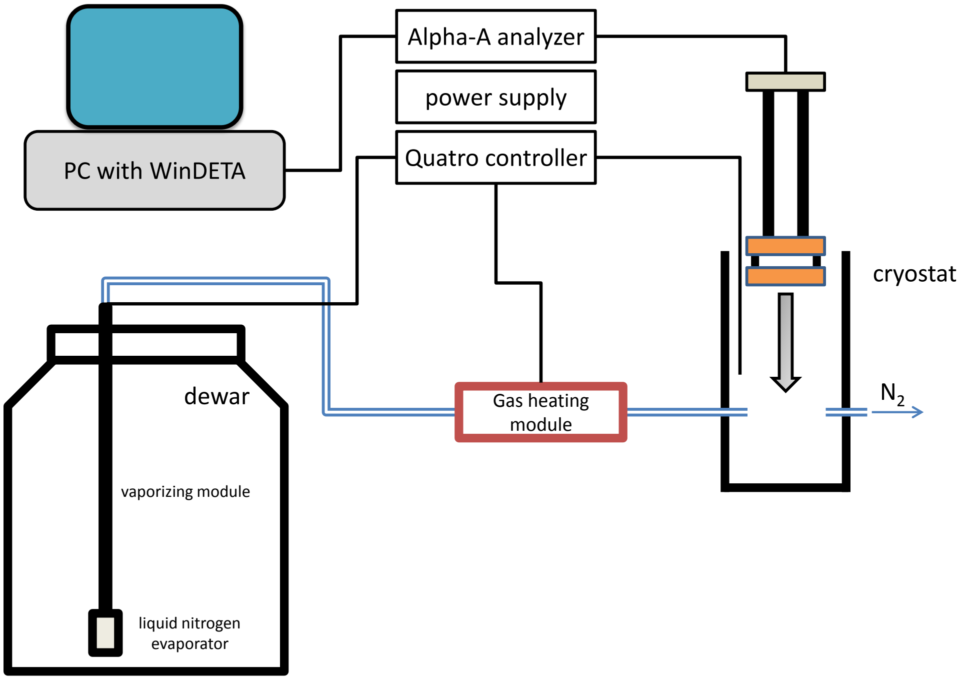
Alpha-A analyzer
power supply
Quatro controller
PC with WinDETA
cryostat
dewar
Gas heating module
N_2
vaporizing module
liquid nitrogen evaporator

Figure 2.9: Block diagram of the Novocontrol Broadband Dielectric/Impedance Spectrometer apparatus with the Alpha-A analyzer and Quatro Cryosystem.

ule, pressurizer module, vacuum system, liquid nitrogen dewar, controller and power supply. The Quatro controller has four circuits controlling sample temperature, gas temperature, liquid nitrogen temperature in the dewar, and pressure in the dewar. The temperature control range is from −160°C to 400°C with 0.01°C temperature stability.

2.2.2 Sample cells

The Novocontrol BDS 1309 and 1307 sample cells were used to obtain DRS measurements. The BDS 1309 cylindrical gold-plated cell is optimal for use with liquids of high permittivity and ion DC conductivity. The cell geometry is designed such that electrode spacing is unusually wide and approximately equal to the electrode diameter. This seeks to combat high sample capacity and low frequency electrode polarization. The BDS 1309 was used for the collection of room temperature data. The BDS 1307 cylindrical stainless steel sample cell was used for collection of low temperature data. This particular cell is advantageous when analyzing dielectric spectra of liquids at subfreezing temperatures. The design is such that the cell does not need to be completely full and thus reduces the effects of thermal expansion and fluid leakage [138]. This geometry keeps the same amount of fluid between the capacitive plates over a wide range of temperatures. A schematic of both sample cells can be seen in Figure 2.10.

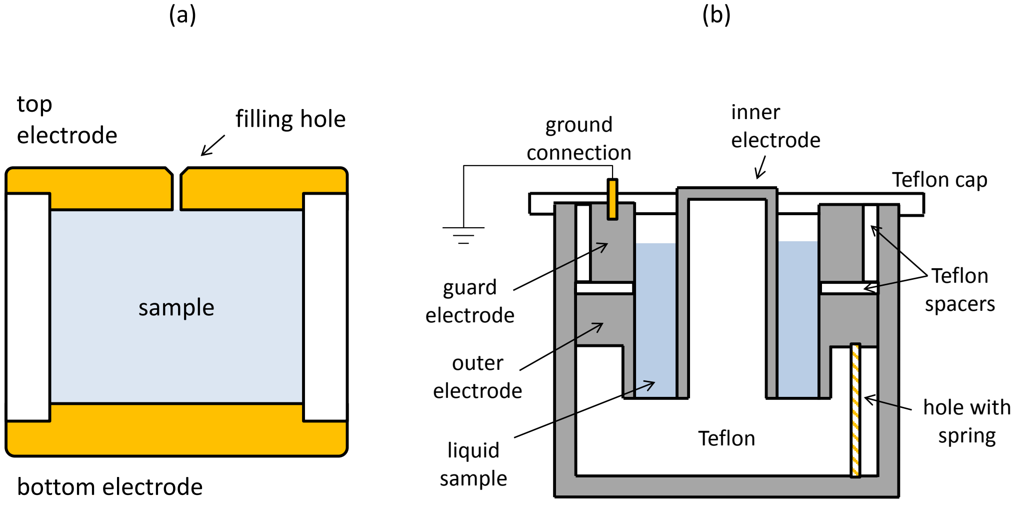
(a)
(b)
top electrode
filling hole
sample
bottom electrode
ground connection
inner electrode
Teflon cap
guard electrode
outer electrode
liquid sample
Teflon
Teflon spacers
hole with spring

Figure 2.10: Cross-section views of the two sample cells used for collecting permittivity data. (a) The BDS 1309 sample cell was used for room temperature data. The approximate volume is 0.5mL.(b) The BDS 1307 sample cell was used for low temperature data. The approximate volume is 1.8mL.

Extensive cleaning to the sample cell is needed prior to each analysis. Any previous sample must first be flushed out of the cell using deionized water. The sample cell components are then set in a bath of acetone and placed in an ultrasonic cleaner for three minutes. The components are then flushed with deionized water, placed in a both of isopropyl alcohol and again placed in an ultrasonic cleaner for three minutes. The isopropyl alcohol is then rinsed off using deionized water and the components are subjected to a final sonication in a deionized water bath. The components are rinsed a final time in deionized water. The stainless steel pieces are placed in an oven at 350°F for approximately five minutes and the Teflon pieces are set on the bench to air dry. The parts are allowed to cool to room temperature prior to placing any sample in the cell.

2.3 Data Analysis Methods

The data was collected using a PC and the Novocontrol WinDETA software package. WinDETA is a system control package for experimental setup, data evaluation and graphical representation in two or three dimensional diagrams. The measured impedance data is used to calculate basic dielectric and impedance parameters, such as complex dielectric function, modulus, and conductivity. The calibration procedure for the sample cells is done automatically using a set of input parameters provided by Novocontrol. Worklists are created to collect data as a function of frequency and temperature. ASCII files for each measurement can be exported for external analysis of the impedance data.

Data analysis and curve fitting was done using the WinFIT program from Novocontrol. In the frequency domain, WinFIT is used to optimize best-fit curves of dielectric data using Debye, Cole-Cole, Cole-Davidson, and Havriliak-Negami functions and conductivity. Up to three relaxation processes can be simultaneously optimized. In the temperature domain, the peak relaxation times can be modeled using the Vogel-Fulcher-Tammann (VFT) function and displayed in an Arrhenius plot. Activation energies and glass-forming fragilities for each relaxation process are determined by fits to the VFT or Arrhenius plots.

Further curve fitting and plotting was done using Igor Pro 6 from WaveMetrics. Igor Pro can perform mean square deviation (MSD) minimization of user-defined curve fitting functions. General text files of dielectric data was exported using WinDETA, then imported into Igor Pro for additional analysis and plotting.

Fitting procedure

Curve fitting of the dielectric permittivity data was done in the frequency domain using the WinFIT program. Two Havriliak-Negami functions with a conductivity tail were chosen as fit functions to analyze the imaginary part of the permittivity, ε'' in a log-log representation. Figure 2.11 shows an example total fit with the deconvolution of the three fit functions and experimental data.

The fitting procedure begins with a visual estimate of the conductivity, τ, and $\Delta\varepsilon$ parameters. A least squares fit is then done by WinFIT to optimize the conductivity, then τ and $\Delta\varepsilon$ for both Havriliak-Negami functions, simultaneously. Often the onductivity must then be re-optimized once the τ and $\Delta\varepsilon$ have been fixed. The spread parameters of the Havriliak-Negami function, β and γ are then optimized, if symmetric or asymmetric broadening are observed. The high frequency permittivity limit, ε_∞ can then be optimized by analyzing the real part of the permittivity, ε', though this parameter is not needed for further analysis. This process is repeated to fit dielectric spectra for each temperature point. At temperatures below approximately 200K, a linear-log plot of ε'' versus frequency is also used for optimization of Havriliak-Negami parameters.

The activation energies and glass-forming fragilities can be modeled by utilizing the fits to the permittivity data over a broad range of temperatures. The maximum frequency for each relaxation process, f_{max} is plotted versus inverse temperature, 1000/T as shown in Figure 2.12. The maximum frequency of each relaxation process is related to the relaxation time by $\tau_{max} = 1/(2\pi f_{max})$. The log f_{max} vs. 1000/T plot for each relaxation process is then fitted using either an Arrhenius (linear) or VFT (curved) fit function.

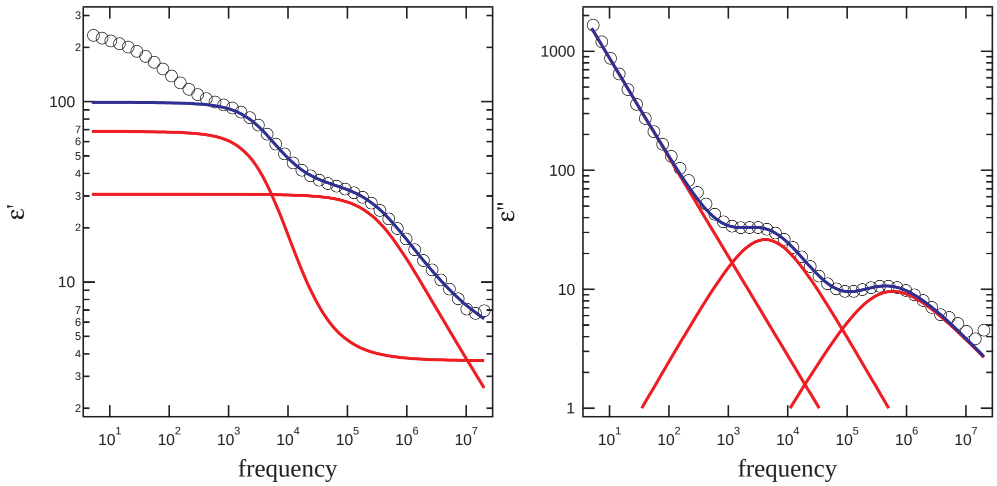

Figure 2.11: Fits to the real (ε') and imaginary (ε'') part of the dielectric permittivity using two Havriliak-Negami functions and conductivity. The low frequency rise in ε' that lies outside of the fit function is most likely due to electrode polarization.

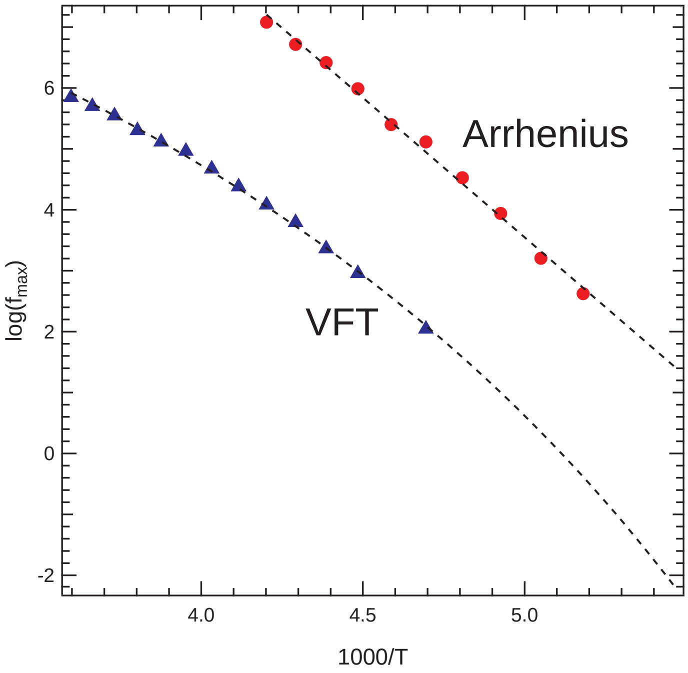

Figure 2.12: Fits to maximum relaxation frequency, f_{max} inverse temperature, 1000/T for two relaxation processes. The linear Arrhenius and curved VFT behaviors are depicted.

2.4 Peptides

2.4.1 β-amyloid

Amyloid deposits of polypeptides β-amyloid $A\beta_{1-42}$ and $A\beta_{1-40}$ are hallmark characteristics of patients who have suffered from Alzheimer's disease [11, 10]. Approximately 90% of β-amyloid peptides are $A\beta_{1-40}$ and 10% is $A\beta_{1-42}$, but the $A\beta_{1-42}$ chain is the faster amyloid aggregate former and comprises of the majority of amyloid deposits in the brain [139]. Both β-amyloid chains are amphiphilic molecules containing a hydrophilic N- and hydrophobic C-terminus with a hydrophobic region at residues KLVFF (16-20) [16].

We selected the amyloidogenic polypeptide, β-amyloid $A\beta_{1-42}$ and scrambled $A\beta_{42-1}$ as a non-amyloidogenic analog. The synthesized peptides were supplied from Anaspec, Inc. as a lyophilized powder and kept frozen until use. Both $A\beta_{1-42}$ and scrambled $A\beta_{42-1}$) are identical in amino acid composition and molecular weight of 4514.1 Da, but with different sequence order as shown in Figure 2.13. The scrambled sequence was developed such that amyloid-forming hydrophobic clustering interactions should not occur.

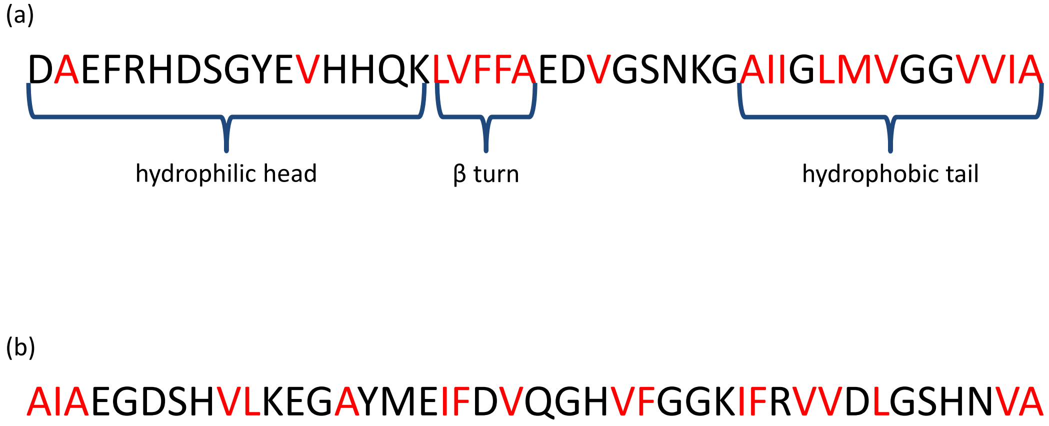
(a)
DAEFRHDSGYEVHHQKLVFFAEDVGSNKGAIIGLMVGGVVIA
hydrophilic head
β turn
hydrophobic tail
(b)
AIAEGDSHVLKEGAYMEIFDVQGHVFGGKIFRVVDLGSHNVA

Figure 2.13: Amino acid sequences of (a) $A\beta_{1-42}$ and (b) scrambled $A\beta_{42-1}$. The hydrophobic amino acids are shown in red. The sequence found in native $A\beta_{1-42}$ possesses a hydrophilic head, hydrophobic tail, and a hydrophobic region in the middle that causes the β turn in the secondary structure.

2.4.2 Islet Amyloid Polypeptide (IAPP)

Amyloid deposits of human Islet Amyloid Polypeptide (hIAPP) or amylin have been found post-mortem in the pancreatic beta cells of more than 90% of patients with Type II diabetes [29]. The 37 residue polypeptide amylin is soluble and non-toxic in its natural form but environmental conditions and genetic predisposition cause amylin to aggregate and form toxic amyloid fibrils [30]. In human IAPP, sequence 20-29 has been shown as a source for amyloid fibril formation [33, 31]. The sequence and composition of IAPP varies between species resulting in a chain that may or may not aggregate to form amyloid fibrils. For example, in the 37 residue sequence, only six amino acids differ between rat and human, five of which are located in sequence 20-29 [140].

We selected the amyloidogenic polypeptide, human hIAPP_{22-27} and rat rIAPP_{20-29} as a non-amyloidogenic analog. The synthesized peptides were supplied from Anaspec, Inc. as a lyophilized powder and kept frozen until use. The hIAPP_{22-27} has a molecular weight of 633.8 Da and the rIAPP_{20-29} has a weight of 1007.2 Da. The proline substitutions in rIAPP (see Figure 2.14) almost completely inhibits hydrophobic clustering and amyloid fibril formation [140].

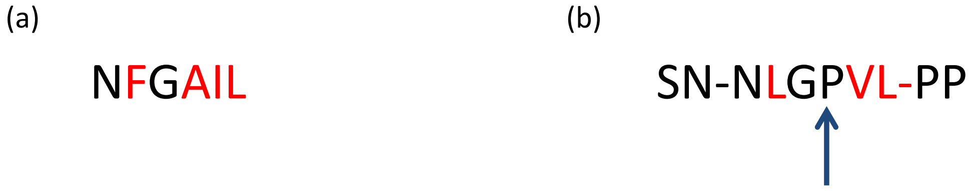

Figure 2.14: Amino acid sequences of (a) human hIAPP_{22-27} and (b) rat rIAPP_{20-29}. The hydrophobic amino acids are shown in red. The arrow points to a proline substitution at amino acid position 25 that prevents β-sheet formation in rat amylin.

2.5 Buffers

Experiments were performed using a deionized water or bovine serum albumin (BSA) buffer. The deionized water, 18.2MΩ·cm minimum, was supplied using a Millipore Direct-Q water purification system. The BSA was purchased from Sigma, catalogue #B8655 with a protein concentration of 45-75 mg/mL and containing 0.01% thimerosal as a preservative. The serum was kept frozen until use. Glycerol, 99% minimum (Sigma, #G5516) was used as a cryoprotectant for experiments under subfreezing temperatures.

Chapter 3

Dielectric Studies of Amyloidogenic Peptides at Room Temperature as a Function of Concentration and Incubation Time

3.1 Overview

Amyloidogenic peptides characteristically aggregate to form higher-ordered structures from dimers, trimers, and oliogomers, to protofibrils and fibrillar plaques [44, 45, 46, 47]. Aggregation and changes to the surface landscape of amyloid structures produces a redistribution of mobile charge carriers and molecular dipoles. This redistribution is reflected in a changing dielectric response over time during the fibrillation process.

The aim of our work was to characterize the dielectric relaxation response for two amyloidogenic peptides and their non-amyloidogenic analogs. Amyloidogenic peptides $A\beta_{1-42}$ and human islet amyloid polypeptide, hIAPP$_{22-27}$ were used as models for studying protein aggregation and beta sheet formation at room temperature. Their non-amyloidogenic analogs, scrambled $A\beta_{42-1}$ and rat islet amyloid polypeptide, rIAPP$_{20-29}$ were selected as control materials. Dielectric measurements at room temperature of conductive, heterogeneous materials, such as proteins, are dominated by conductivity and polarization effects [127, 126]. Here, we explore changes to conductivity and space-charge polarization as amyloidogenic peptides combine to form higher-ordered structures.

3.2 Sample Preparation and Data Collection

Lyophilized peptides of $A\beta_{1-42}$, scrambled $A\beta_{42-1}$, hIAPP$_{22-27}$, rIAPP$_{20-29}$ were obtained from AnaSpec, Inc in quantities of 0.5 mg and 1.0 mg. The vials were stored at approximately -20°C until the time of reconstitution. The $A\beta_{1-42}$ was first rehydrated using 35μL 1% NH_4OH added to 0.5mg of protein to ensure that the solution was first driven to a monomeric state. Deionized water, 18.2M$\Omega\cdot$cm minimum, was used to dilute and rehydrate the peptides to concentrations of 5μM, 50μM, and 100μM. Each solution was stored in sterile vials. The samples were then mixed by repeated inversion of the vials and set to incubate for 0-168 hours at room temperature. The same sample preparation was used for each time point. The samples were again mixed by repeated inversion of the vials, then placed in the Novocontrol BDS 1309 cylindrical gold-plated sample cell.

Data were collected using the Novocontrol Alpha-A Analyzer and Quatro Cryosystem in gain phase measurement mode with an AC probing voltage of 1.000 V$_{RMS}$. Measurements were taken at room temperature of approximately 295 K. We selected 60 data points in a frequency range from $1.00 \times 10^{7} - 4.78 \times 10^{-2}$ Hz, spaced evenly in a logarithmic scale.

3.3 Results and Discussions

3.3.1 Studies of $A\beta_{1-42}$ and Scrambled $A\beta_{42-1}$

The dielectric spectra of $A\beta_{1-42}$ and scrambled $A\beta_{42-1}$ at concentrations of 5μM, 50μM, and 100μM are presented at various incubation times in Figures 3.2 - 3.4. Dielectric spectra are typically represented using the permittivity formalism, however interfacial polarization and DC conductivity dominate the spectra in the case of highly conductive materials. The interfacial polarization occurs due to the space-charge accumulation at macroscopic interfaces as a result of the differences in conductivities and permittivities in heterogenous materials [126]. The dielectric modulus is an alternative formalism used to study the conductivity and relaxation spectra of materials in the presence of interfacial polarization [125, 126, 127, 128]. Figure 3.1 shows the relationship between M'', ε', and ε''. When plotted together, the intersection of ε' and ε'' occurs at the peak loss modulus, M'' for the conductivity. The region of ε' with zero slope is the conductivity and the region of negative slope is polarization effects. In the following, we present the dielectric spectra using the dielectric loss modulus, M'' as a function of frequency to show the changes in the conductivity process throughout fibril formation.

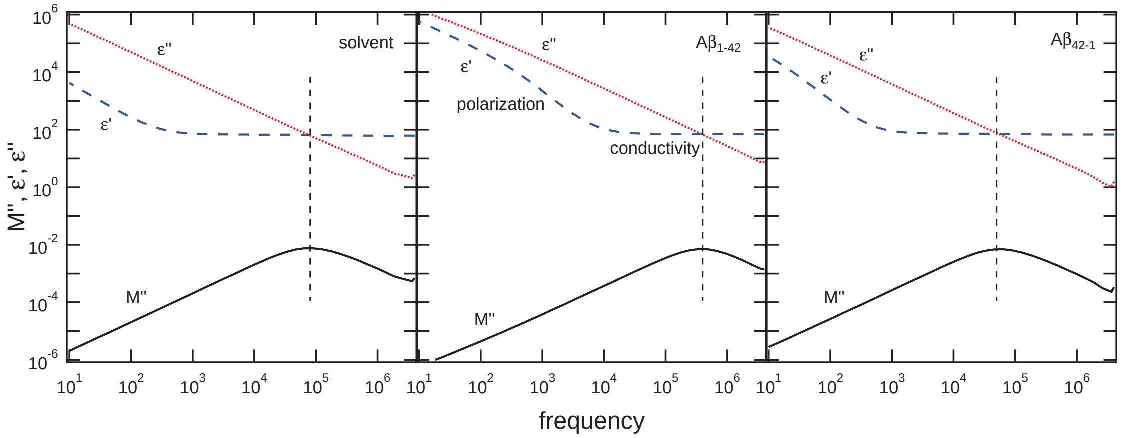

Figure 3.1: The relationship between M'', ε', and ε'' for $A\beta_{1-42}$, $A\beta_{42-1}$, and the solvent. The intersection of ε' and ε'' occurs at the peak loss modulus, M'' for the conductivity process. Regions of ε' with slope, m=0 is the conductivity process and slope m<0 are polarization effects.

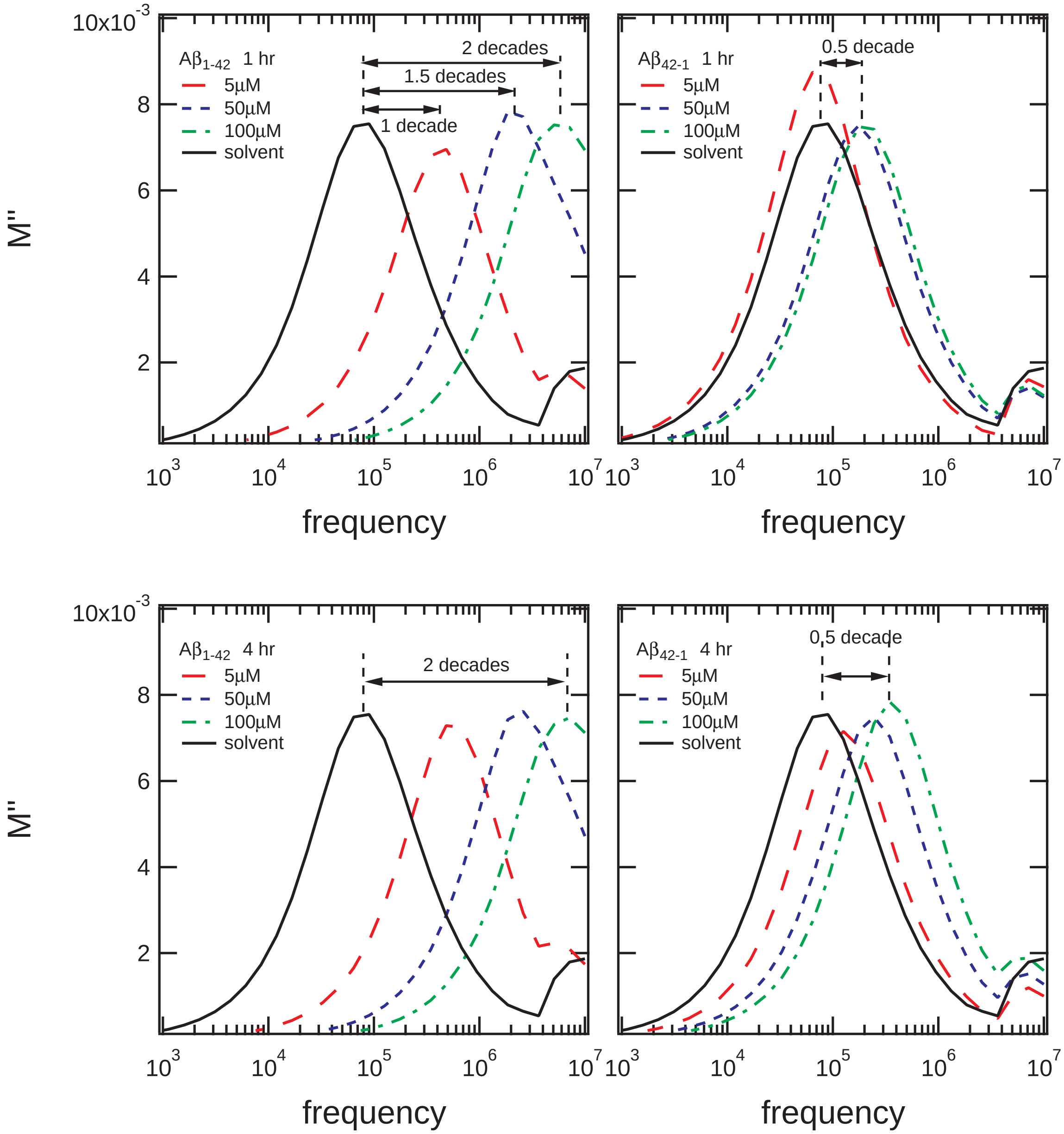

Figure 3.2: **Dielectric modulus (M'') as a function of frequency for $A\beta_{1-42}$ and $A\beta_{42-1}$ at concentrations of 5μM, 50μM and 100μM after 1 hour and 4 hours of incubation time.** There is an immediate shift in peak frequency for $A\beta_{1-42}$ for all concentrations after just 1 hour. The peak shift for $A\beta_{42-1}$ is only a half decade or less for both 1 and 4 hours for all concentrations. Note that after 4 hours of incubation, the shift for 5μM $A\beta_{1-42}$ is more than twice the shift for any concentration of $A\beta_{42-1}$.

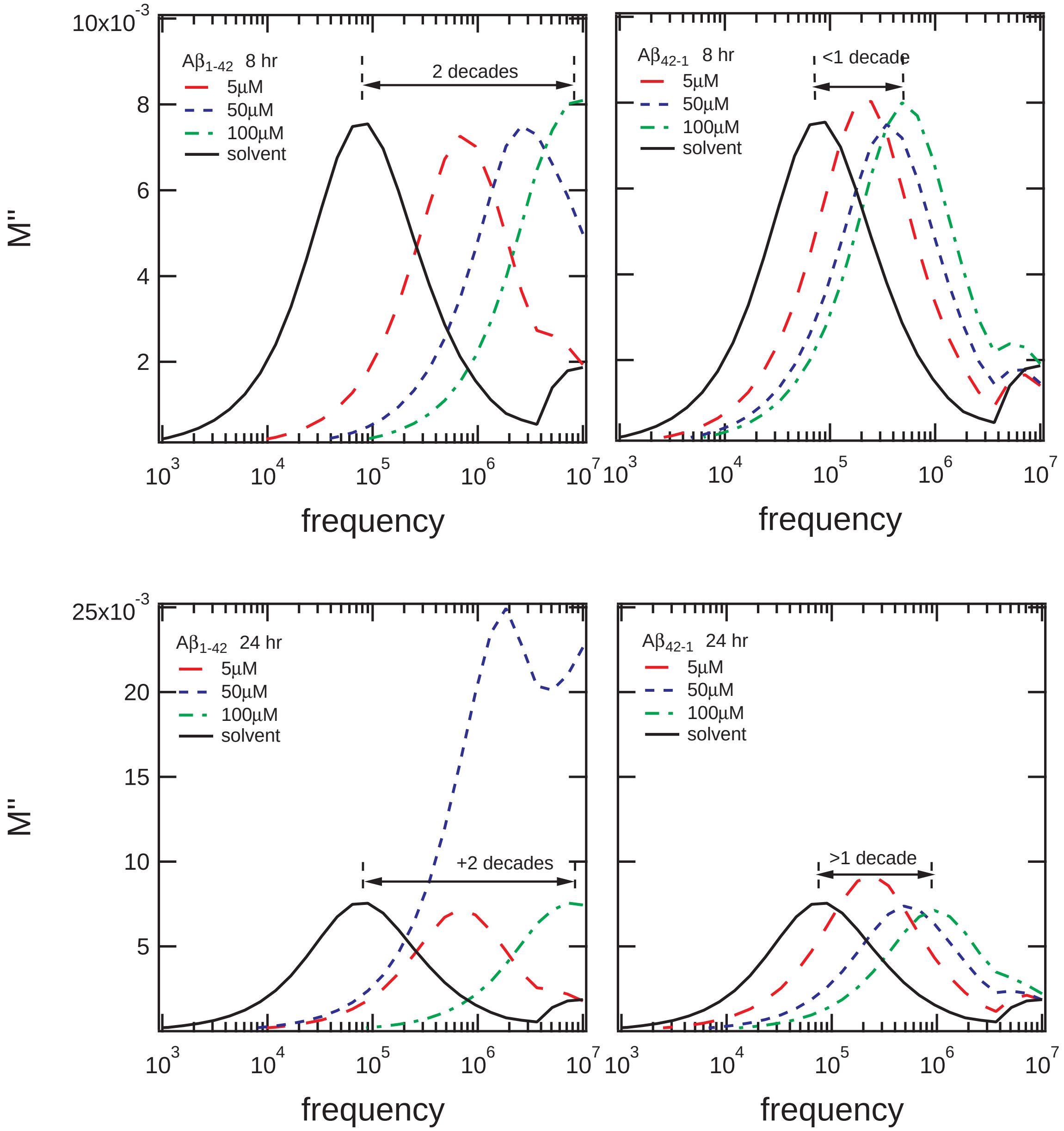

Figure 3.3: **Dielectric modulus (M'') as a function of frequency for $A\beta_{1-42}$ and $A\beta_{42-1}$ at concentrations of 5μM, 50μM and 100μM after 8 hours and 24 hours of incubation time.** The shift for $A\beta_{42-1}$ is approximately twice the shift of $A\beta_{42-1}$ for each concentration at 8 and 24 hours of incubation. The frequency shifts for $A\beta_{1-42}$ and $A\beta_{42-1}$ indicates that there is some aggregation with both peptides, but the process is composition and concentration dependent. We note a large increase in the magnitude of M'' for only 50μM $A\beta_{1-42}$ at 24 hours, though the peak frequency follows the trend.

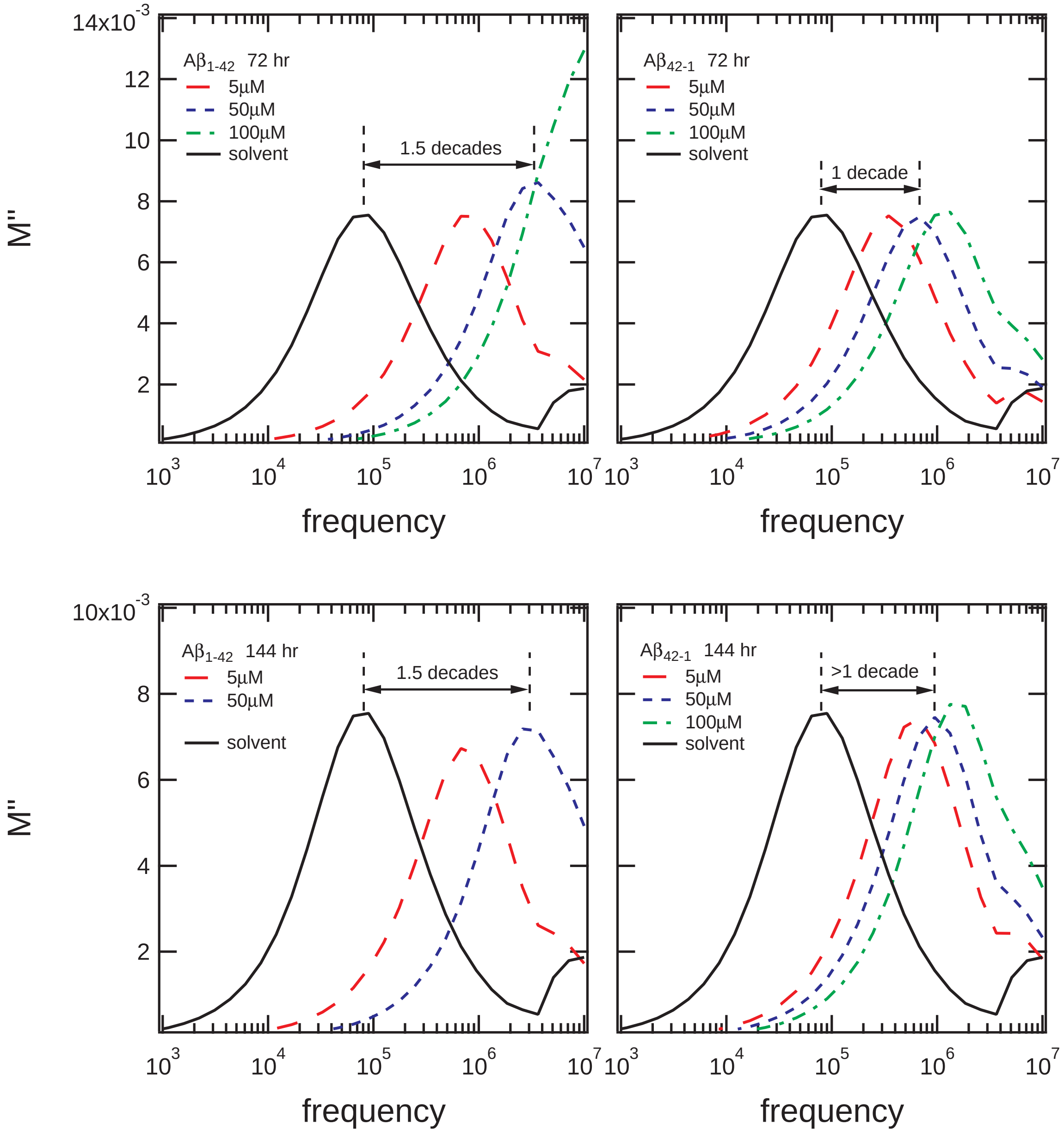

Figure 3.4: **Dielectric modulus (M'') as a function of frequency for $A\beta_{1-42}$ and $A\beta_{42-1}$ at concentrations of 5μM, 50μM and 100μM after 72 hours and 144 hours of incubation time.** The shift for $A\beta_{42-1}$ is approximately 1.5 times the shift of $A\beta_{42-1}$ for each concentration at 72 and 144 hours of incubation. We note a large increase in the magnitude of M'' for 100μM $A\beta_{1-42}$ at 72 hours, though the peak frequency follows the trend to higher frequency. Data was not collected beyond 72 hours for $A\beta_{1-42}$.

The time evolution of $A\beta_{1-42}$ and scrambled $A\beta_{42-1}$ shows that both shift towards higher frequency with increasing concentrations of 5μM, 50μM, and 100μM at each time point. The frequency shift for $A\beta_{1-42}$ is approximately twice that of $A\beta_{42-1}$ for each concentration and time point. Figures 3.5 - 3.7 show the progression of dielectric modulus shifts for each concentration of $A\beta_{1-42}$ and $A\beta_{42-1}$ as compared to the solvent on two different time scales.

The 5μM $A\beta_{1-42}$ has an initial shift towards high frequency of half of a decade and continues to shift up to a decade at 8 hours. Beyond 8 hours, there is only a small shift towards high frequency. The 5μM $A\beta_{42-1}$ does not shift for the first two hours, then up to half of a decade at 8 hours. The shift continues gradually up to a decade after 7 days.

The 50μM $A\beta_{1-42}$ has an initial shift towards high frequency of +1.4 decades and continues to shift up to +1.5 decades at 8 hours. Beyond 8 hours, there is a continuing shift of up to +1.7 decades. The 50μM $A\beta_{42-1}$ has a small initial shift of +0.4 decade, then up to +0.7 decade at 8 hours. The shift continues gradually up to +1.5 decades after 7 days.

The 100μM $A\beta_{1-42}$ has an initial shift towards high frequency of +2 decades and continues to shift up to +2.5 decades at 8 hours. Beyond 8 hours, there is a continuing shift of more than +2 decades, but it is above the measured frequency. The 100μM $A\beta_{42-1}$ has a small initial shift of +0.4 decade, then up to +1.5 decades at 8 hours. The shift continues gradually up to +1.5 decades after 7 days.

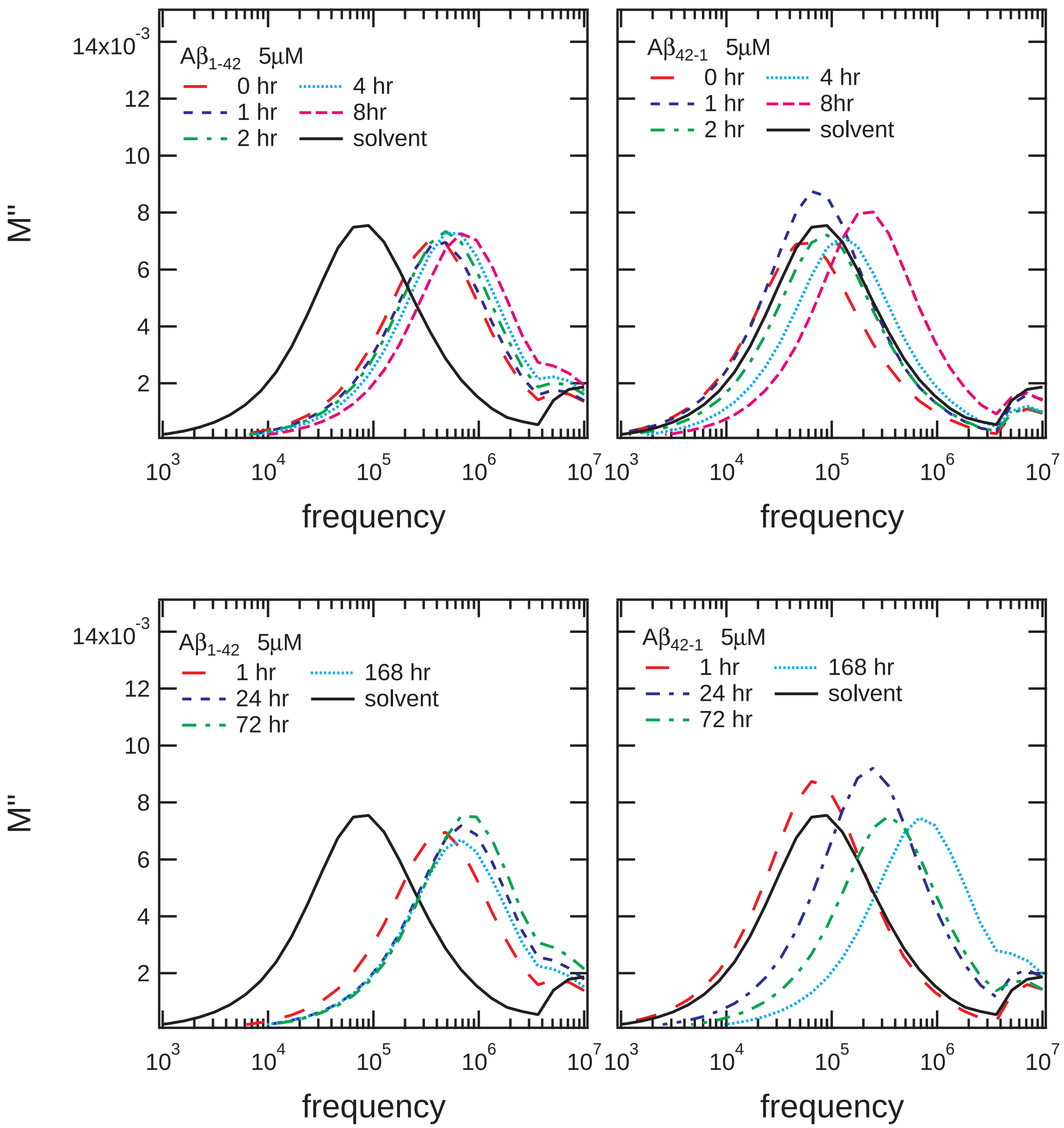

Figure 3.5: **Time evolution for 5 μM $A\beta_{1-42}$ and $A\beta_{42-1}$ for 0-8 hours and 1-168 hours (7 days).** The $A\beta_{1-42}$ has an initial jump in peak frequency of approximately 1 decade at the first measurement, then continues for another half decade. There is no shift in $A\beta_{24-1}$ for the first two hours, then steady shift throughout 168 hours. The peak frequencies of $A\beta_{1-42}$ and $A\beta_{42-1}$ are very close after 168 hours of incubation.

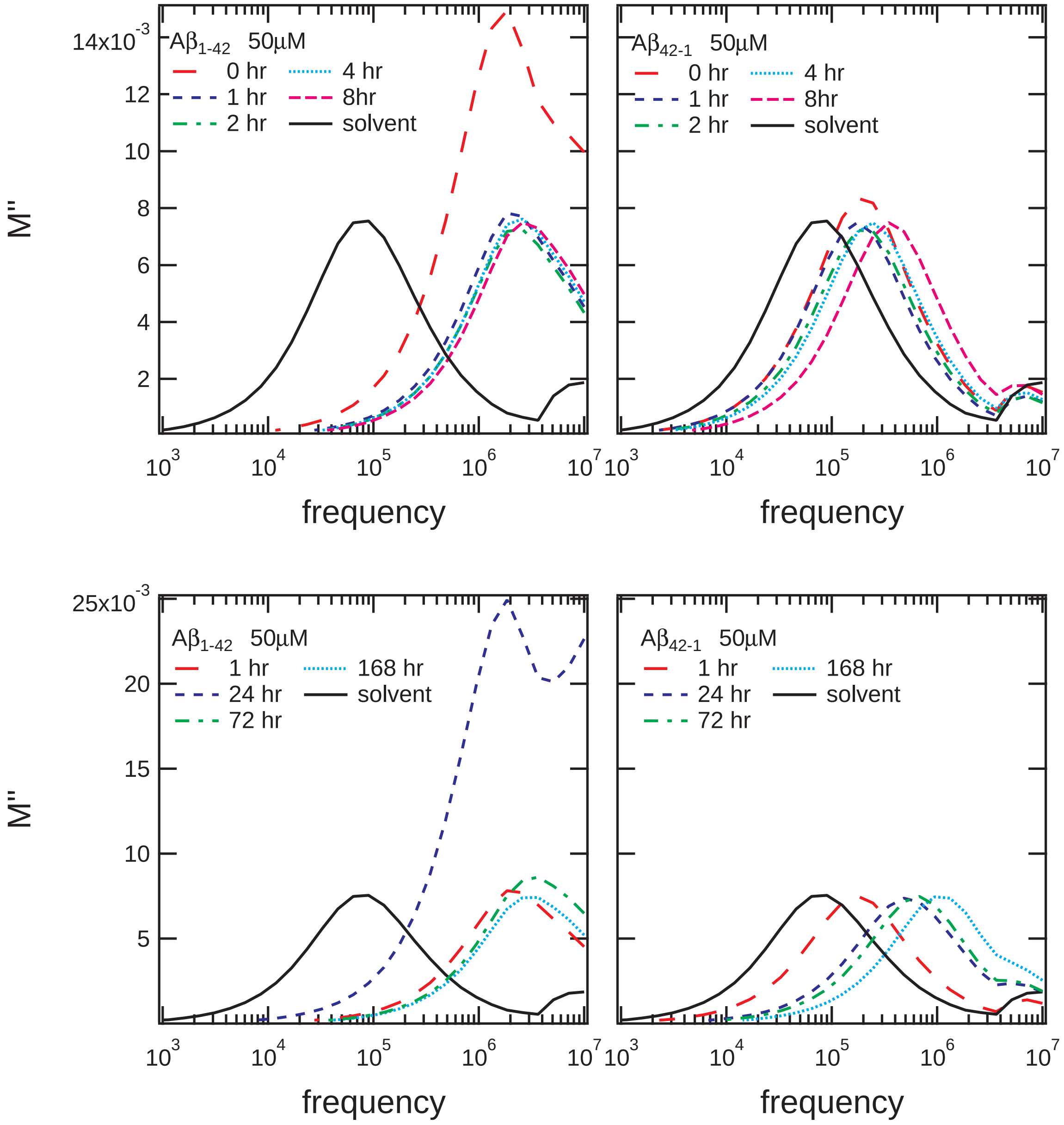

Figure 3.6: **Time evolution for 50 μM $A\beta_{1-42}$ and $A\beta_{42-1}$ for 0-8 hours and 1-168 hours (7 days).** The $A\beta_{1-42}$ has an initial jump in peak frequency of approximately 1.5 decades at the first measurement, then continues with small increases. There is a small shift in $A\beta_{24-1}$ of a half decade, then steady shift throughout 168 hours. The peak frequency of $A\beta_{1-42}$ is approximately a half decade above $A\beta_{42-1}$ after 168 hours of incubation. The large increase in the magnitude of $A\beta_{1-42}$ at 0 and 24 hours could be the result of an evolving surface landscape during fibril formation.

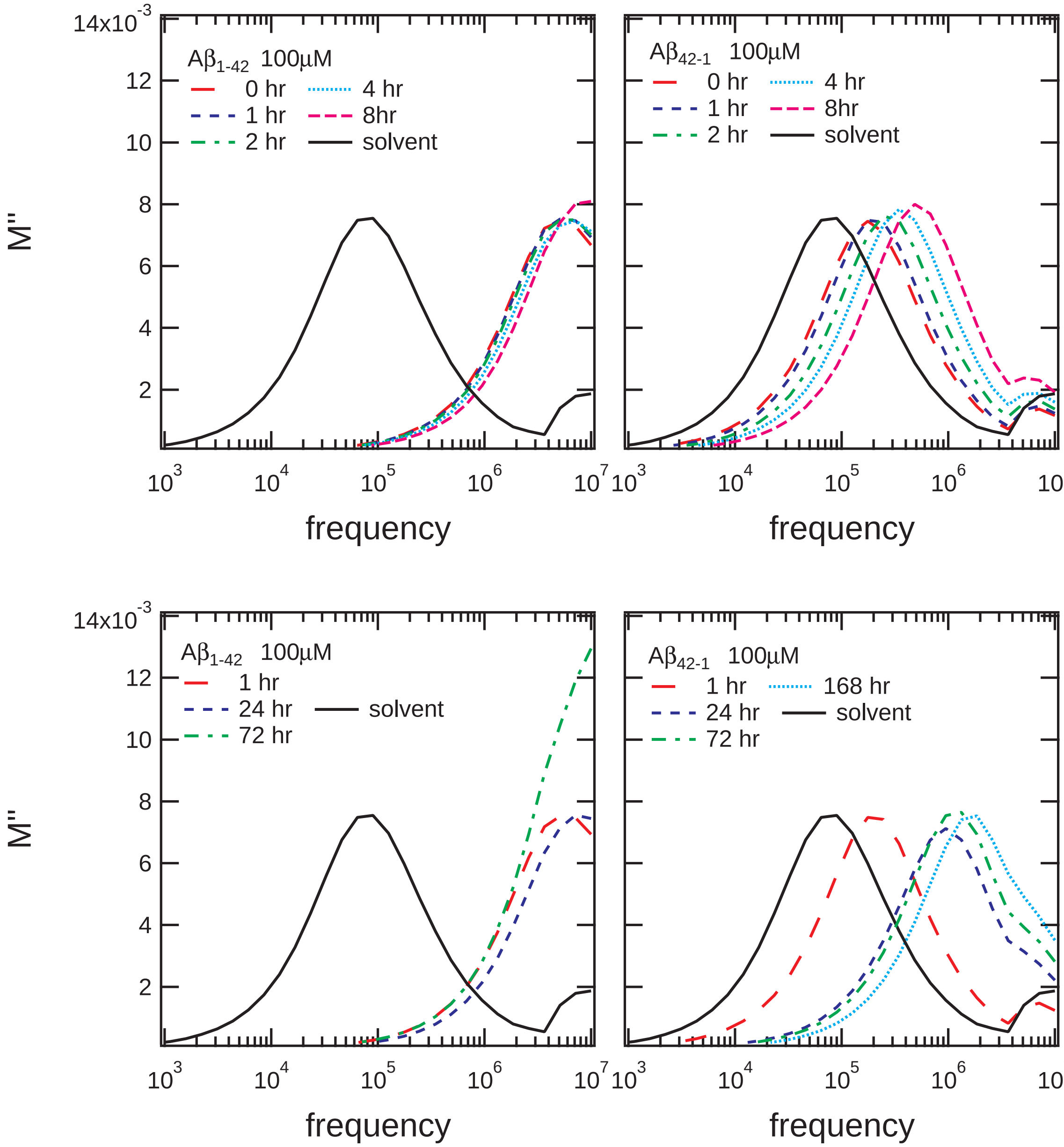

Figure 3.7: **Time evolution for 100 μM $A\beta_{1-42}$ and $A\beta_{42-1}$ for 0-8 hours and 1-168 hours (7 days).** No data was collected for $A\beta_{1-42}$ after 72 hours. The $A\beta_{1-42}$ has an initial jump in peak frequency of approximately 2 decades at the first measurement, then continues with small increases. Data was not collected beyond 72 hours. There is a small shift in $A\beta_{24-1}$ of a half decade, then steady shift to 1.5 decades throughout 168 hours. The peak frequency of $A\beta_{1-42}$ is more than a half decade above $A\beta_{42-1}$ for all time points. The large increase in the magnitude of $A\beta_{1-42}$ at 72 hours could be the result of an evolving surface landscape during fibril formation.

The dielectric loss modulus, M'' was fit in the frequency domain using a generalized susceptibility model function in the form [141, 142]

$$M''(\omega) = \frac{M''_p}{\frac{(1-C)}{a+b}[b(\omega/\omega_p)^{-a} + a(\omega/\omega_p)^{b}] + C} \tag{3.1}$$

where $\omega = 2\pi f$ is the angular frequency. The parameters M''_p and ω_p describe the height and position of the modulus loss peak at its maximum. The parameters a and b are the slopes of the low and high frequency side of the peak and the C parameter describes the broadening. Sample fits using this susceptibility model for the solvent, $A\beta_{1-42}$, and scrambled $A\beta_{42-1}$ are shown in Figure 3.8.

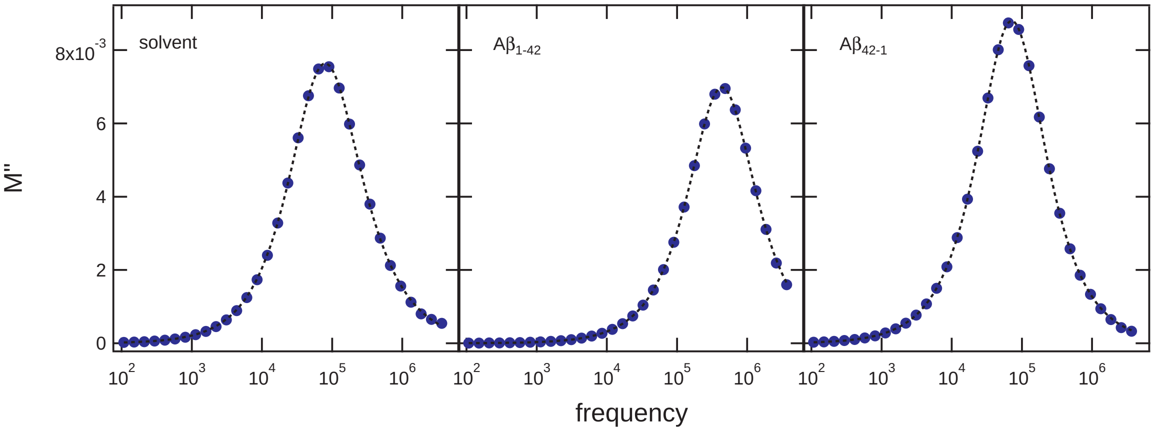

Figure 3.8: Example of the curve fitting analysis performed for the determination of f_{max} in the modulus M" versus frequency plots for the solvent, $A\beta_{1-42}$, and $A\beta_{42-1}$.

Plots of f_{max} versus time for $A\beta_{1-42}$ and scrambled $A\beta_{42-1}$ display distinct behavior in two regimes: 0-8 hours and 24-168 hours for each concentration. Each regime was empirically fit to a power law in the form

$$f(t) = C + At^{k} \tag{3.2}$$

and are shown in Figure 3.9 and tabulated in Table 3.1. It is interesting to note that two clearly different behaviors for the short-term and long-term were observed for each concentration. Both $A\beta_{1-42}$ and $A\beta_{42-1}$ show a rapid shift towards higher frequency for each concentration in the time frame from 0-8 hours. The $A\beta_{1-42}$ then appears to not shift after little change beyond 24 hours. Peak modulus determination for the 100μM $A\beta_{1-42}$ because it has shifted above the measured frequency range. The scrambled $A\beta_{42-1}$ however continues a steady shift towards higher frequency throughout the 168 hour testing period.

The dielectric modulus loss peaks displayed in the spectra are dominated by interfacial polarization effects. Changes in the magnitude of M'' and the peak frequency may be an indication of peptide conformational changes. As the peptides aggregate, charged and uncharged amino acids will reorganize and produce a differentiated space-charge organization, depicted as the change in modulus signal. The observation that $A\beta_{1-42}$ experiences a rapid shift in frequency in the first 8 hours, then virtually no shift afterwards may be an indication of organized aggregation and beta sheet formation. It is possible that fibril formation has completed after the 8 hours with no further assembly for $A\beta_{1-42}$. The scrambled $A\beta_{42-1}$ may also be aggregating, but possibly not as fast or towards a final, organized state.

	$A\beta_{1-42}$				$A\beta_{42-1}$			
	X_M	C (10^5)	A (10^4)	k	X_M	C (10^5)	A (10^4)	k
0-8 hours	5μM	3.92	4.79	0.93	5μM	0.70	0.54	1.57
	50μM	23.4	11.5	0.86	50μM	1.53	2.27	1.08
	100μM	55.6	14.4	1.38	100μM	1.13	9.49	0.68
24-168 hours	5μM	0.13	74.5	0.01	5μM	1.75	0.10	1.23
	50μM	3.93	181	0.18	50μM	4.84	0.03	1.50
	100μM	–	–	–	100μM	8.70	0.14	1.24

Table 3.1: Parameters of the power law fits to the f_{max} versus time for M'' in the form $f(t) = C + At^k$ at concentrations X_M = 5μM, 50μM, and 100μM for $A\beta_{1-42}$ and $A\beta_{42-1}$.

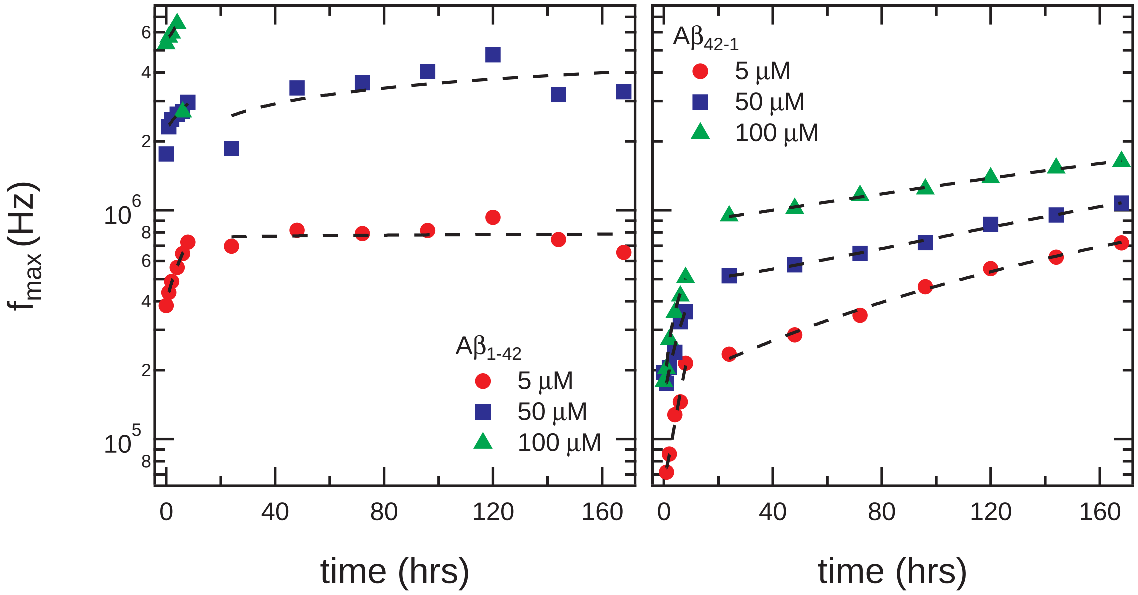

Figure 3.9: **Plots of f_{max} of M" versus time for $A\beta_{1-42}$ and $A\beta_{42-1}$ at 5μM, 50μM, and 100μM concentrations.** For each concentration, f_{max} has two distinct regions (0-8 hours and 24-168 hours). Modulus peak determination for the $A\beta_{1-42}$ after 6 hours was not possible because the peaks have shifted to frequencies above the measurement limits.

3.3.2 Studies of Human and Rat Islet Amyloid Polypeptide

The dielectric spectra of human (hIAPP) and rat (rIAPP) islet amyloid polypeptide at concentrations of 5μM, 50μM, and 100μM are presented at various incubation times in Figures 3.11 - 3.13. Similar to the measurements performed on $A\beta_{1-42}$, the dielectric spectra is dominated by interfacial polarization and DC conductivity due to the heterogeneity and highly conductive nature of the peptides. Figure 3.10 shows the relationship between M'', ε', and ε'' for hIAPP, rIAPP, and the solvent. When plotted together, the intersection of ε' and ε'' occurs at the peak loss modulus, M'' for the conductivity. The region of ε' with zero slope represents the conductivity and the region of slope of approximately -1 is polarization effects. Here, we present the data using the dielectric loss modulus, M'' as a function of frequency to show the changes in the conductivity process throughout fibril formation.

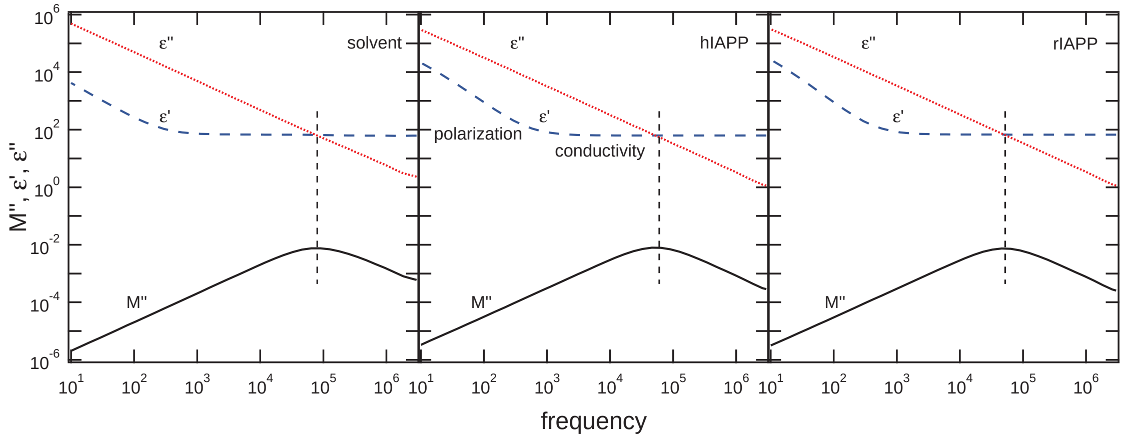

Figure 3.10: The relationship between M'', ε', and ε'' for hIAPP, rIAPP, and the solvent. The intersection of ε' and ε'' occurs at the peak loss modulus, M'' for the conductivity process. Regions of ε' with slope, m=0 is the conductivity process and slope m<0 are polarization effects.

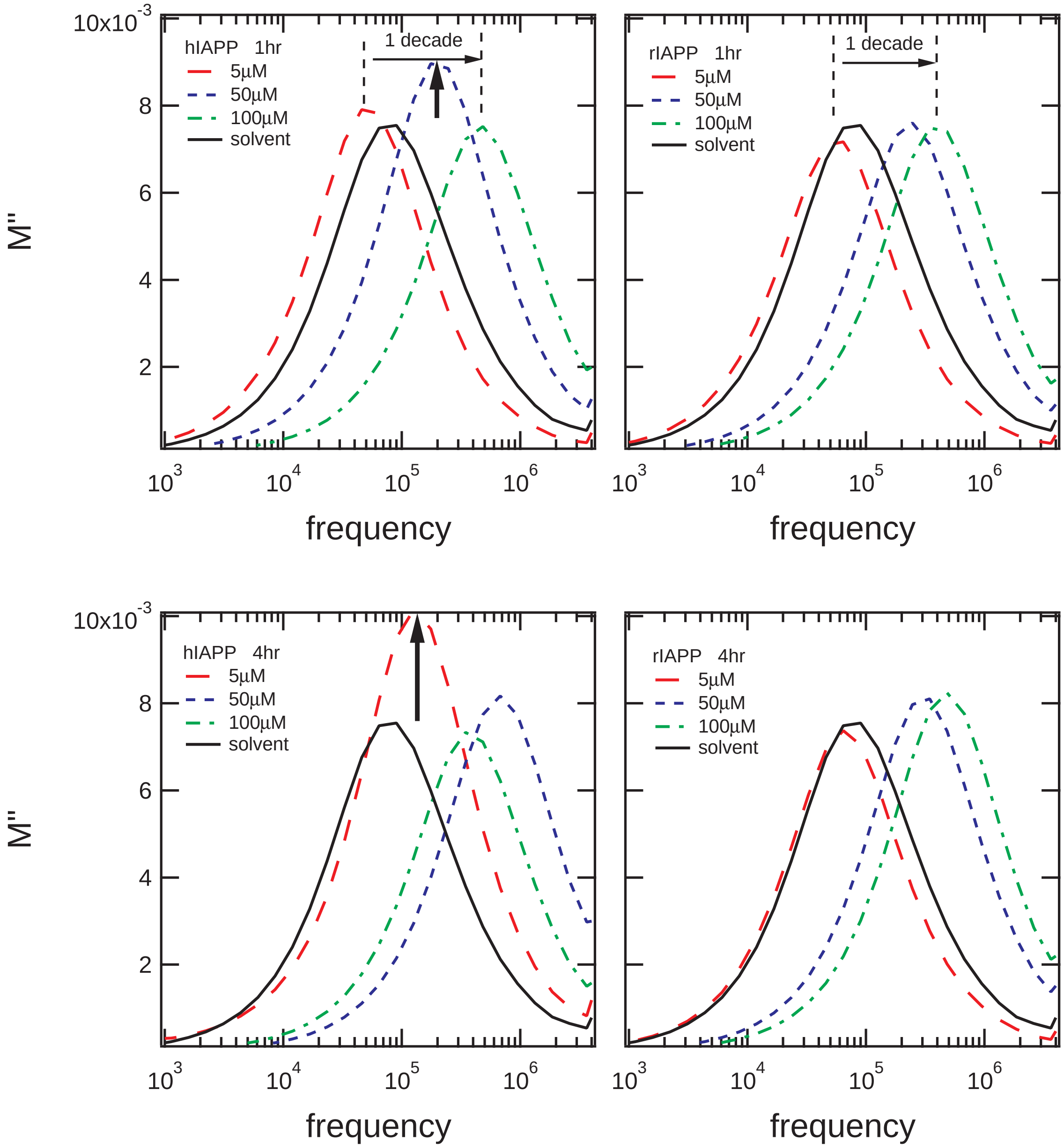

Figure 3.11: **Dielectric modulus (M'') as a function of frequency for hIAPP and rIAPP at concentrations of 5μM, 50μM and 100μM after 1 hour and 4 hours of incubation time.** Both hIAPP and rIAPP show an initial shift to lower frequency for low concentrations of protein (5μM). The peak frequency increases with increasing concentration for both hIAPP and rIAPP from 5-100μM. After 4 hours of incubation, only hIAPP shows a positive shift in peak frequency at 5μM. Also, there is an increase in peak magnitude. The jump in peak magnitude at 1 hour for 50μM and 4 hours for 5μM hIAPP is indicative of a changing surface landscape of charges. This may have occurred with 100μM prior to our first measurement. We note that after 4 hours, hIAPP 100μM has shifted to lower frequency than 50μM.

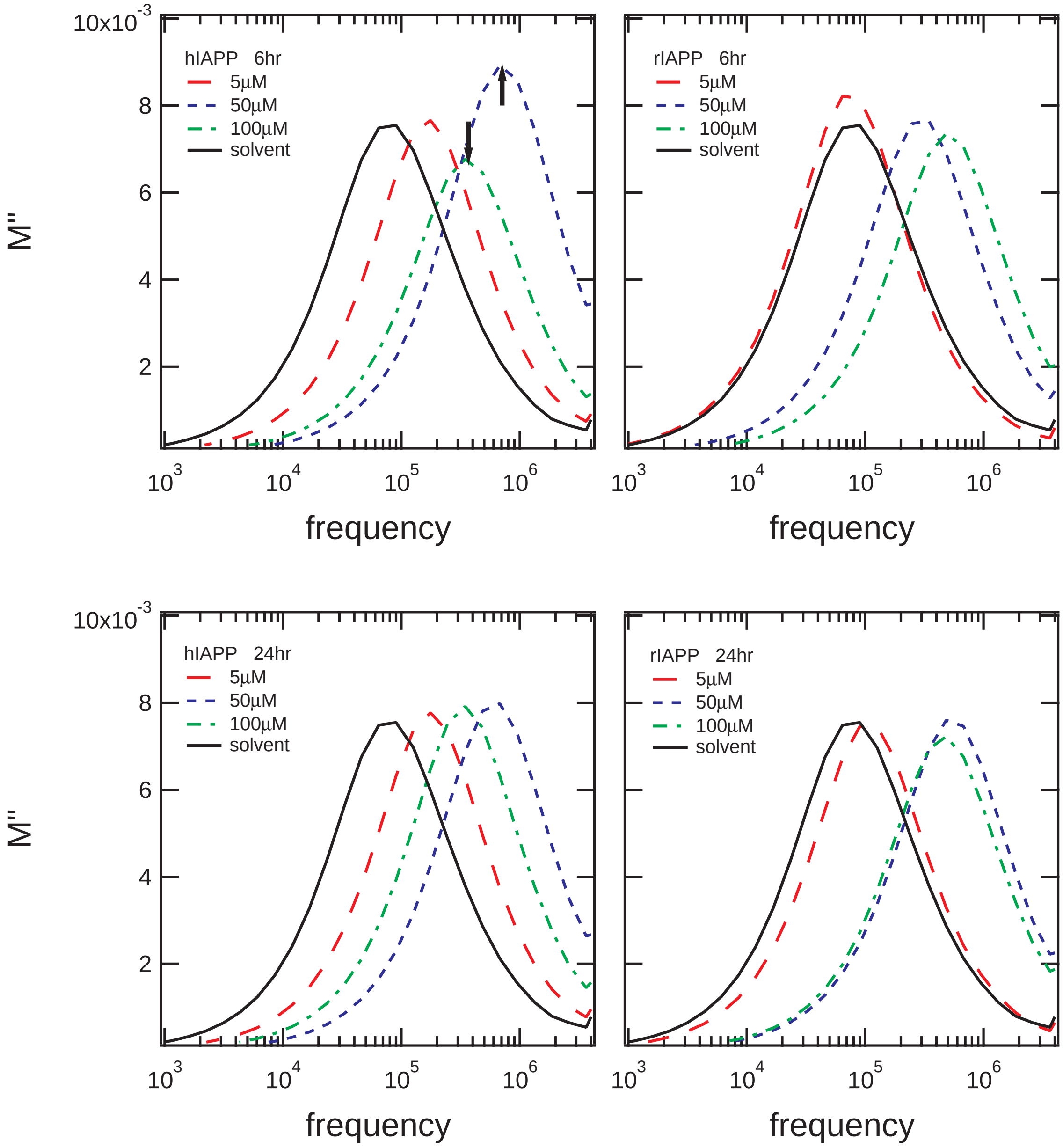

Figure 3.12: **Dielectric modulus (M'') as a function of frequency for hIAPP and rIAPP at concentrations of 5μM, 50μM and 100μM after 6 hours and 24 hours of incubation time.** After 24 hours of incubation, the rIAPP 5μM shows a small positive shift in frequency for the first time, but is less than half that of the hIAPP. The hIAPP and rIAPP 50μM solutions display similar peak frequency shifts. The increase in magnitude of 50μM and decrease in magnitude of 100μM at 6 hours indicates surface changes due to fibril formation. We note that the hIAPP 100μM is at lower frequency than 50μM.

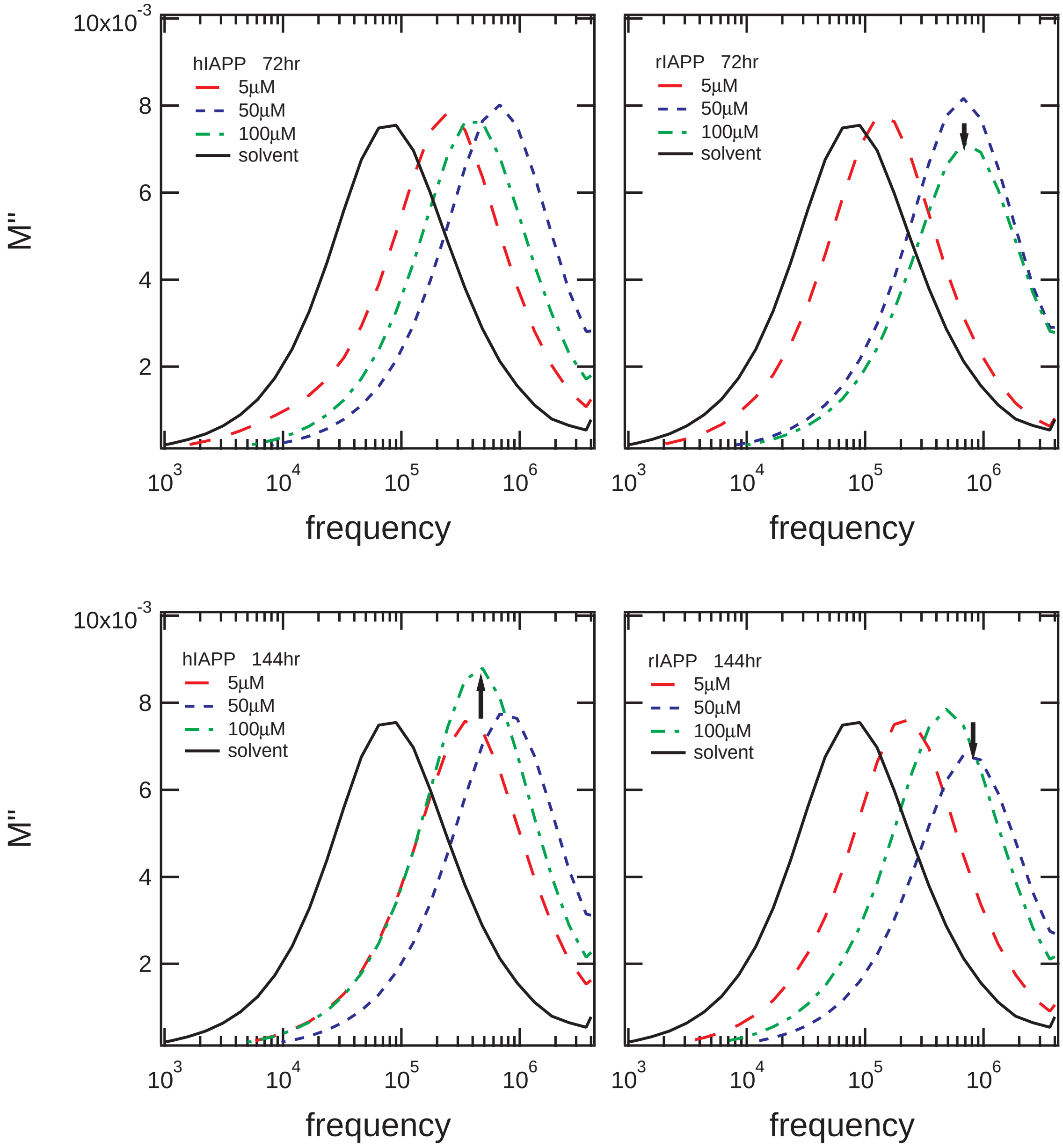

Figure 3.13: **Dielectric modulus (M'') as a function of frequency for hIAPP and rIAPP at concentrations of 5μM, 50μM and 100μM after 72 hours and 144 hours of incubation time.** After 72 hours of incubation, the hIAPP and rIAPP 5μM and 50μM solutions display similar peak frequency shifts. The increase in magnitude of hIAPP 50μM at 72 hours indicates surface changes due to fibril formation. A decrease in magnitude of rIAPP 100μM at 72 hours and rIAPP at 50μM at 144 hours is observed. We note that the hIAPP 100μM is at lower frequency than 50μM for both time points and similarly for rIAPP at 144 hours. Trends of rIAPP appear to follow hIAPP after much longer timescales indicating that aggregation occurs for both peptides, but at different rates.

The time evolution of both hIAPP and rIAPP shows a shift towards higher frequency with increasing concentrations of 5μM, 50μM, and 100μM at each time point. Figures 3.14 - 3.16 show the progression of dielectric modulus shifts for 5μM, 50μM, and 100μM hIAPP and rIAPP as compared to the solvent on two different time scales.

The 5μM hIAPP has an initial shift towards lower frequency of -0.2 decade and then continues to shift up to +0.3 decade at 6 hours. Beyond 6 hours, there is a continuing shift up to +0.7 decade after 144 hours. The rIAPP also has an initial shift towards lower frequency of -0.2 decade, then continues to shift towards the same frequency as the solvent after 6 hours. The shift continues gradually up to +0.4 decade after 144 hours.

The 50μM hIAPP has an initial shift towards high frequency of half of a decade and continues to shift up to a decade at 6 hours. At 144 hours, there is only a small shift. The 50μM rIAPP has a small initial shift of half of a decade, then up to +0.6 decade at 6 hours, and continues gradually up to a decade after 144 hours.

The 100μM hIAPP has an initial shift towards high frequency of +0.8 decade, then a shift towards lower frequency at +0.6 decade after 6 hours. The peak then continues to shift back towards higher frequency of +0.8 decade after 144 hours. The 100μM rIAPP has a similar initial shift of +0.7 decade, then continues to shift to +0.8 decade for 6 hours and beyond.

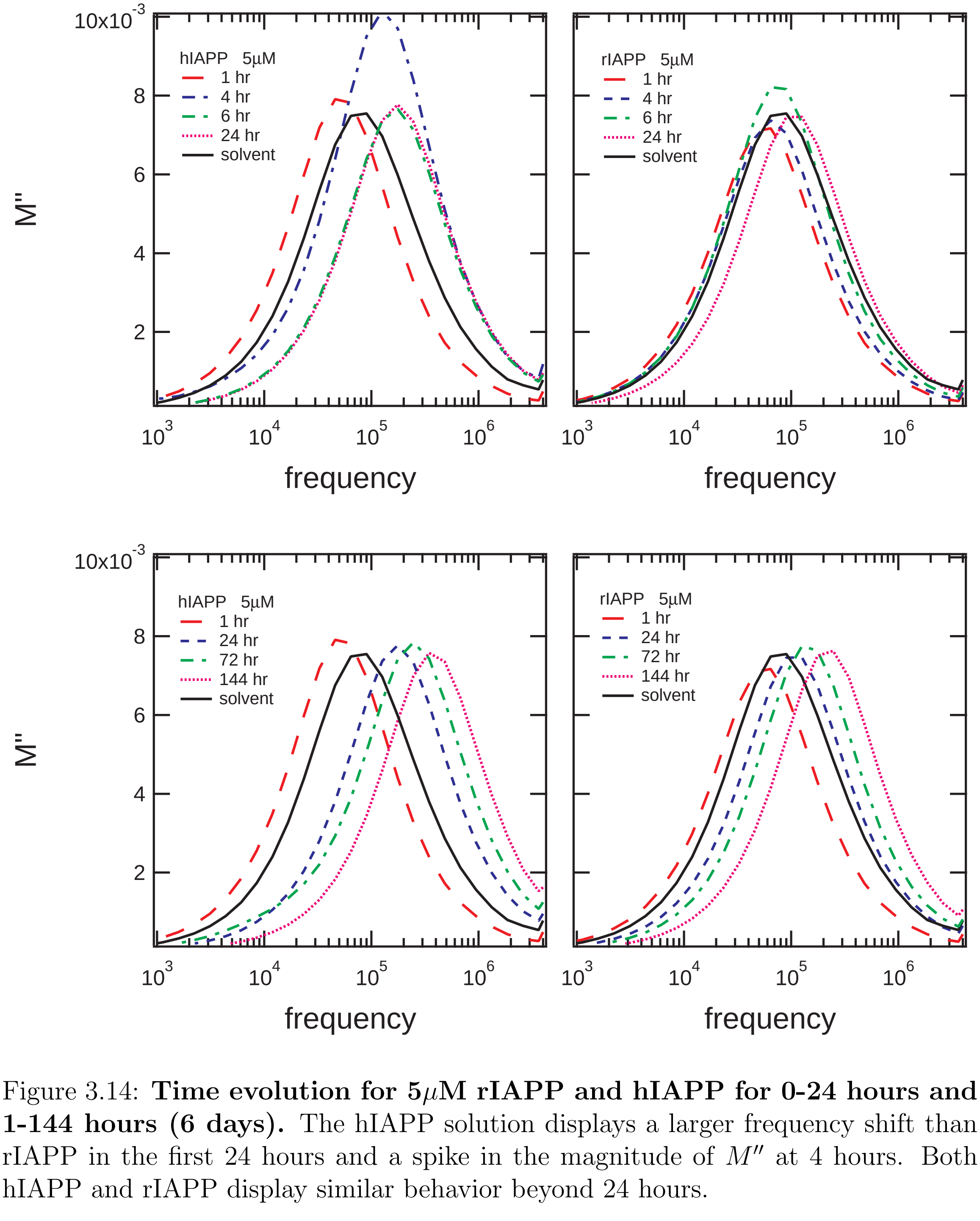

Figure 3.14: **Time evolution for 5μM rIAPP and hIAPP for 0-24 hours and 1-144 hours (6 days).** The hIAPP solution displays a larger frequency shift than rIAPP in the first 24 hours and a spike in the magnitude of M'' at 4 hours. Both hIAPP and rIAPP display similar behavior beyond 24 hours.

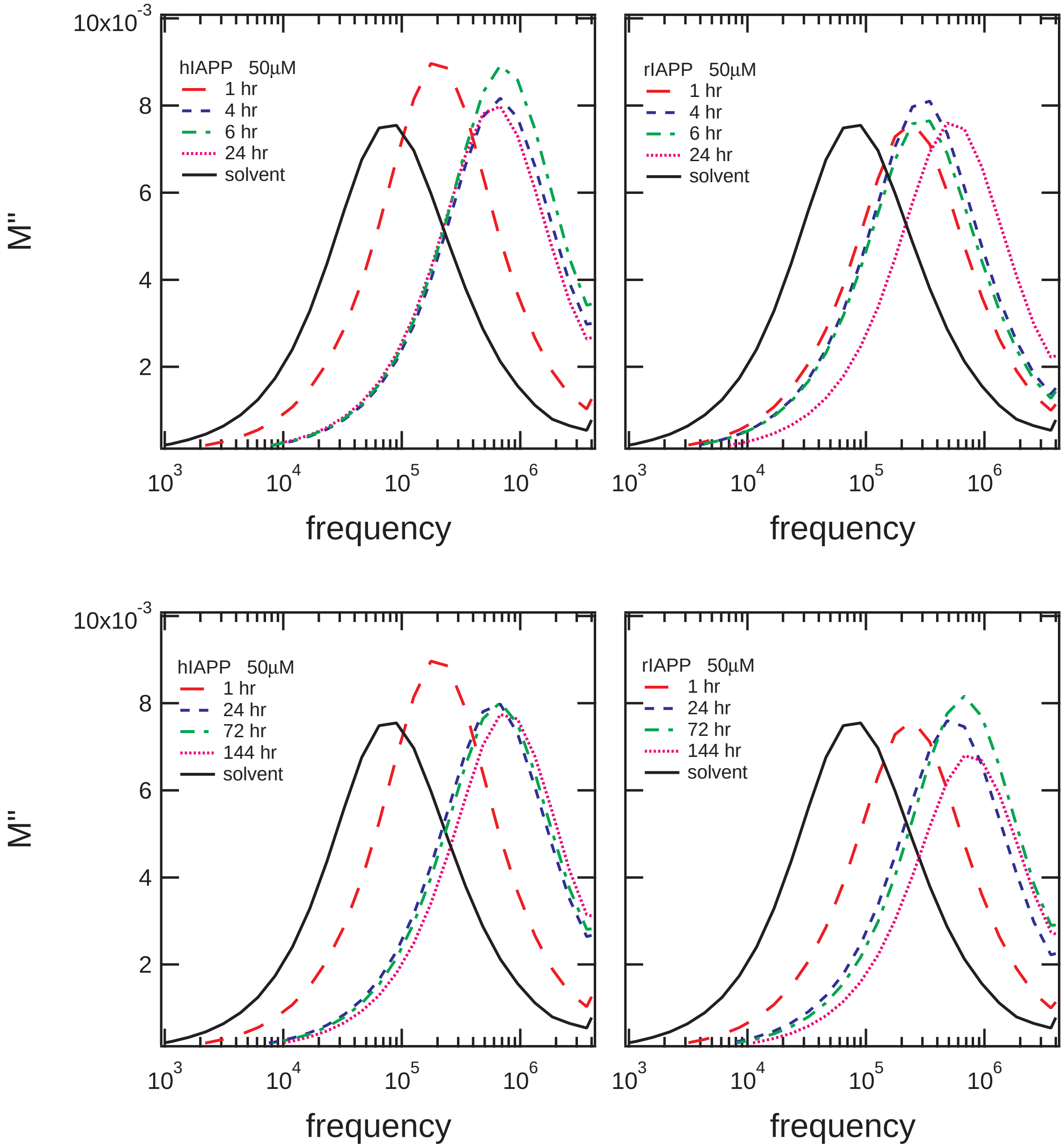

Figure 3.15: **Time evolution for 50μM rIAPP and hIAPP for 0-24 hours and 1-144 hours (6 days).** The hIAPP and rIAPP solutions display similar frequency shifts for both incubation time scales. However, the hIAPP shows a spike in magnitude at 1 and 6 hours. A smaller, yet significant spike is seen with rIAPP at 4 and 72 hours.

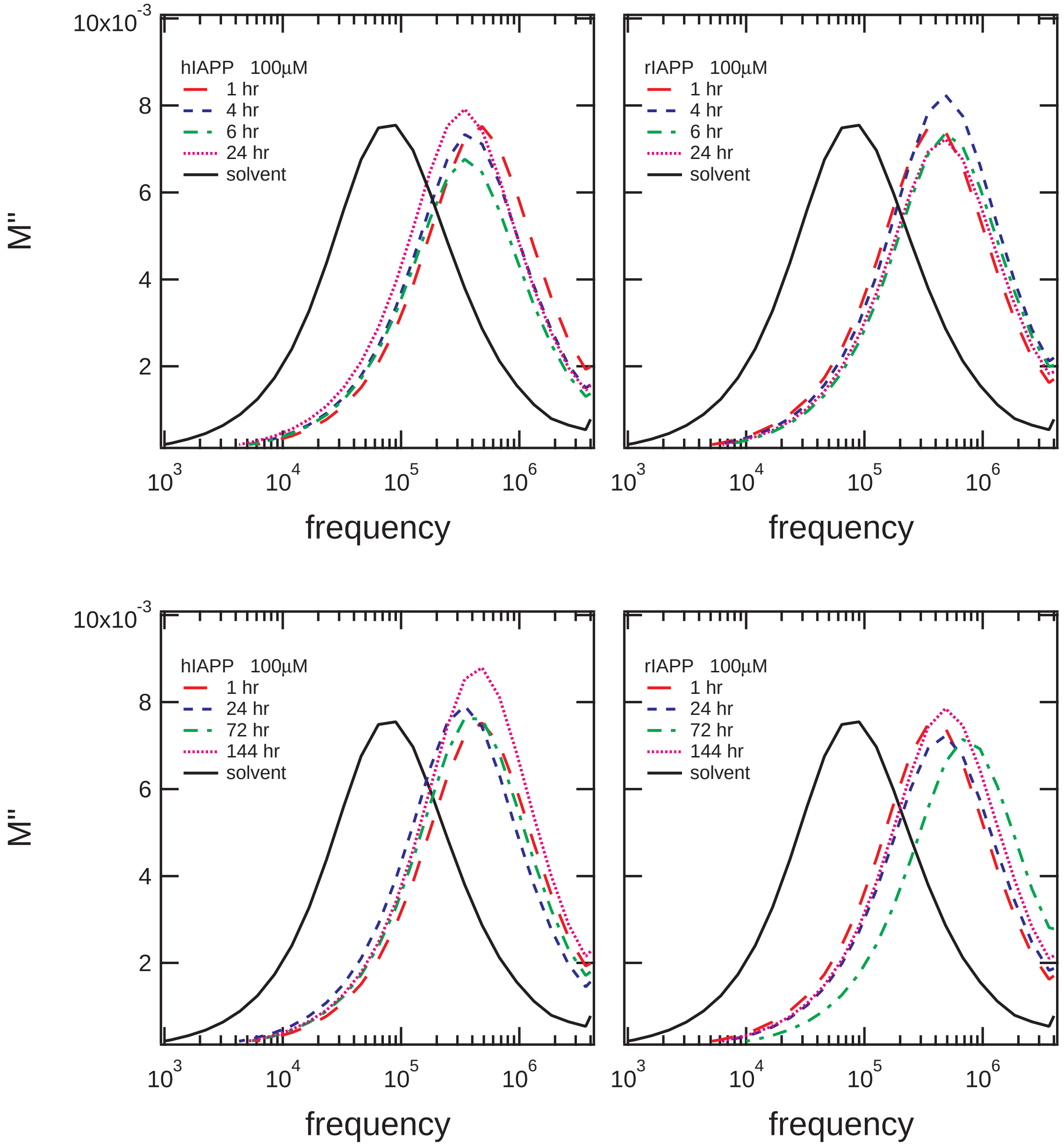

Figure 3.16: **Time evolution for 100μM hIAPP and rIAPP for 0-24 hours and 1-144 hours (6 days).** The hIAPP frequency shift is less than that of the rIAPP in the first 24 hours of incubation. The hIAPP shifts to lower frequency in the first 24 hours with a spike in magnitude at 24 hours. The rIAPP does not significantly change in the first 24 hours with a spike in magnitude at 4 hours. There is little change over time for the peak frequency for both hIAPP and rIAPP at 100μM.

The dielectric loss modulus, M'' was fit in the frequency domain using the same generalized susceptibility model function noted in the fits for $A\beta$. Sample fits for the solvent, hIAPP, and rIAPP are shown in Figure 3.17.

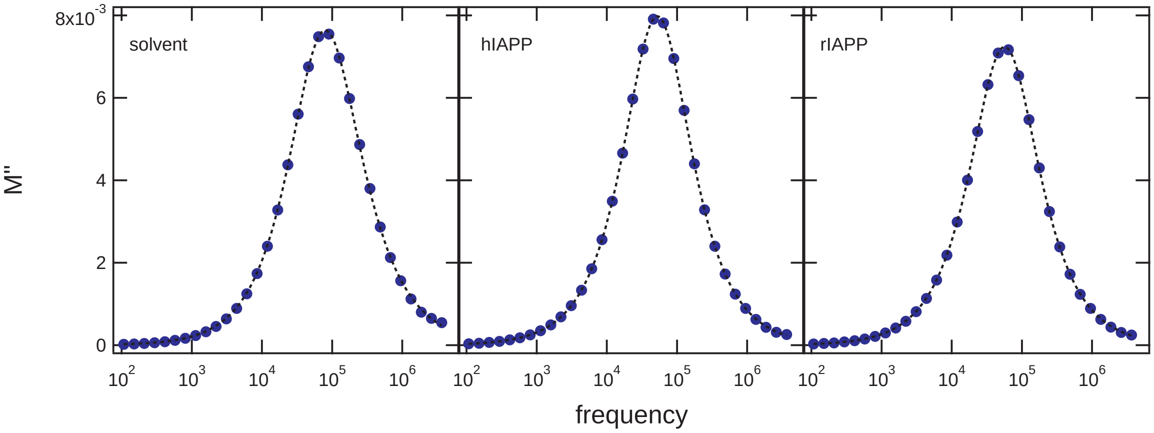

Figure 3.17: Example of the curve fitting analysis performed for the determination of f_{max} in the modulus M" versus frequency plots for the solvent, hIAPP, and rIAPP.

Plots of f_{max} versus time for hIAPP and rIAPP display distinct behavior in two regimes: 0-8 hours and 24-168 hours for each concentration. Each regime was empirically fit to a power law and is shown in Figure 3.18 and tabulated in Table 3.2. As with $A\beta_{1-42}$ and $A\beta_{42-1}$, we observe two clearly different trends for each time scale and concentration. Both hIAPP and rIAPP show a rapid shift towards higher frequency for each concentration in the time frame from 0-8 hours, except for hIAPP 100 μM which has an initial shift, then trends downward. Both hIAPP and rIAPP at 5μM concentrations continue to shift towards higher frequencies over the entire measured time period with the hIAPP always at higher frequency at every time point. The hIAPP 50μM, rIAPP 50μM, and rIAPP 100μM all display a similar behavior beyond 24 hours with virtually no shift and at approximately the same frequency. We note that the hIAPP 100μM has a slight trend towards high frequency, but occurs at lower frequency than 50μM.

As with $A\beta$, the dielectric modulus loss peaks displayed in the IAPP spectra are dominated by interfacial polarization effects. The observation that the behavior of rIAPP and hIAPP follow similar trends at low concentration (5μM) may be due to a critical concentration required for beta sheet formation. At 100μM, the shift of hIAPP to a lower frequency than that of 50μM hIAPP may be an indication that the beta sheet formation at high concentrations has caused a shift in the interfacial polarization signal that is not observed in rIAPP at the same concentrations.

The time evolution of the modulus loss peak in the first 24 hours is of particular interest. A closer look at the 50μM and 100μM shows that hIAPP first shifts to high frequency, then towards lower frequency after 24 hours. Conversely, rIAPP at the same concentrations continues with a slight increase in frequency. The back-and-forth shifting of the hIAPP interfacial polarization is expected due to protein surface modulation during oligomerization and fibril formation.

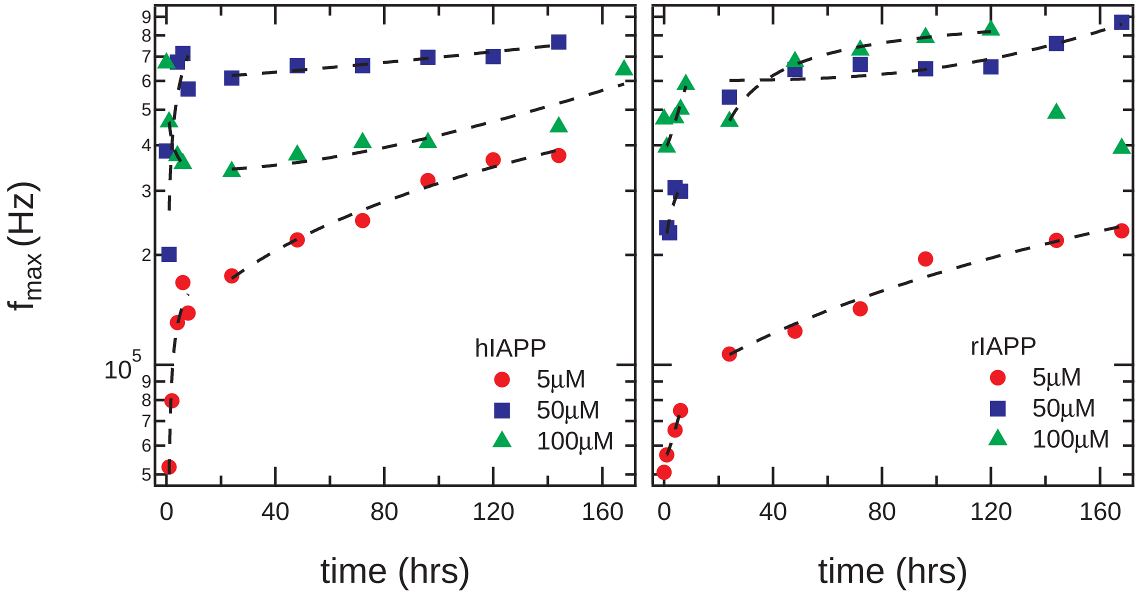

Figure 3.18: **Plots of f_{max} of M" versus time for hIAPP and rIAPP at 5μM, 50μM, and 100μM concentrations.** Each concentration is fit to two power law fits: one from 0-8 hours and one from 24-168.

	hIAPP				rIAPP			
	X_M	C (10^5)	A (10^5)	k	X_M	C (10^5)	A (10^5)	k
0-8 hours	5μM	2.79	-23.0	-0.30	5μM	0.55	0.15	1.43
	50μM	-25.2	278	0.02	50μM	1.77	5.22	0.52
	100μM	2.59	20.5	-0.41	100μM	3.87	1.16	1.36
24-168 hours	5μM	1.12	0.41	0.85	5μM	0.83	0.11	0.97
	50μM	6.08	0.02	1.32	50μM	6.02	0.00	3.16
	100μM	3.39	0.00	2.04	100μM	10.1	-438	-0.66

Table 3.2: Parameters of the power law fits to the f_{max} versus time for M'' in the form $f(t) = C + At^k$ at concentrations $X_M = 5\mu$M, 50μM, and 100μM for hIAPP and rIAPP.

3.4 Conclusions

Studies of these peptides at room temperature reveal that there is a large contribution to the conductivity and space-charge polarization due to the heterogeneity of the peptide-solvent mixture. In the presence of strong space-charge polarization effects, the dielectric modulus is often the preferred parameter for probing dielectric properties. The dielectric modulus reveals a conductivity relaxation peak that changes with concentration and incubation time.

Both the $A\beta_{1-42}$ and scrambled $A\beta_{42-1}$ display a positive shift in frequency of the conductivity relaxation peak. However, the $A\beta_{1-42}$ displays an instant shift and a much more rapid change in the first 8 hours of measurement than that of the scrambled $A\beta_{42-1}$. The shifts are larger and faster with increasing concentration from 5μM to 100μM. The Aβ_{1-42} appears to reach a final state after the first day of measurements, where the scrambled $A\beta_{42-1}$ continues to gradually shift over the 7 days. This may be an indication that both the $A\beta_{1-42}$ and scrambled $A\beta_{42-1}$ undergo some form of aggregation, but the process with the $A\beta_{1-42}$ is faster and with a larger frequency shift. The conformation differences in $A\beta_{1-42}$ versus $A\beta_{42-1}$ is observed in the conductivity relaxation. A higher organized, tightly packed β-sheet should give rise to more ordering in the space-charge polarization.

Measurements of the hIAPP and rIAPP also show a positive shift in frequency for all concentrations, except the hIAPP at 100μM which shifts to lower frequency. The trends observed in the measurements of IAPP indicates that the aggregation behavior may be dependant on the peptide concentration. At 5μM, the hIAPP and rIAPP follow similar trends, though a fast and larger shift is observed with hIAPP. At 50μM, the hIAPP against shifts faster and to higher frequency, but does not shift after 24 hours, where rIAPP continues to shift. At 100μM, hIAPP shifts to lower frequency in the first 24 hours, then does not shift for the remaining incubation time. The rIAPP shifts to higher frequencies and continues to shift over time. It is also notable that the hIAPP 100μM shifts to lower frequency than hIAPP 50 μM, where rIAPP is similar for 50μM and 100μM. One possibility is that 5μM is below some critical concentration necessary for fibril formation, or it requires a much longer incubation time, hence the continuation of the frequency shift. The 50μM follows a similar trend observed for $A\beta_{1-42}$ and scrambled $A\beta_{42-1}$. The behavior of hIAPP and rIAPP at 100μM would be interesting for further examination.

Trends in the maximum amplitude of the dielectric loss modulus, M'', are noted in Figures 3.2 - 3.4 and 3.11 - 3.13. The amyloidogenic peptides $A\beta_{1-42}$ and hIAPP demonstrate spikes of increased magnitude of M'' at several timepoints and concentrations. No spikes were observed for the non-amyloidogenic analogs. The intermittent spikes in M'' are representative of a high fraction of oligomer structures in the ensemble. During nucleation and oligomer formation, hydrophobic and hydrophilic regions of amyloidogenic peptides reorganize in conformations that favor β-sheet formation [48, 49, 50]. This results in an increase to the number of accessible mobile charge carriers in the solution, as reflected in an increase of the magnitude of M''. The charges carriers are then restricted upon the formation of fibrils, resulting in a change in magnitude of M'' towards that of the solvent. The non-amyloidogenic peptides do not display these spikes because they are not expected to form intermediary oligomeric structures and fibrils. However, they may aggregate in other conformations that would explain the increase in frequency of M'', but not magnitude.

Chapter 4

Dielectric Studies of Amyloidogenic Peptides in Deionized Water Buffer at Low Temperature

4.1 Overview

Protein association and aggregation causes a redistribution of biological water molecules at the protein-water interface [143, 144]. Studies show that amyloidogenic aggregates are characterized by an increased number of poorly dehydrated hydrogen backbones and large surface densities of patches of bulk like water which favor protein association [145, 144]. The water dynamics in the vicinity of the amyloidogenic aggregates is different than the monomeric form and thus there is an increase of patches which are occupied by molecules with bulk-like water behavior (i.e. no translations or rotations). The change on the surface depends on how many patches of structural defects remain after the formation of dimers, tetramers, oligomers, and protofibrils

[143]. We hypothesize that this change in the long-lived water structures provides the change in the dielectric relaxation signal of the structure. Our theoretical model suggests that measurement over a wide range of frequencies produces a differentiated signal for the different configurations of protein-water interface.

In this chapter, dielectric spectroscopy data and analysis are presented for two amyloidogenic peptides and their non-amyloidogenic analogs. Amyloidogenic peptides $A\beta_{1-42}$ and human islet amyloid polypeptide, hIAPP_{22-27} were used as models for studying protein aggregation in a deionized water buffer. Deionized water was chosen as a buffer to first study the peptides in the absence of any other biological fluids and proteins. Their non-amyloidogenic analogs, scrambled $A\beta_{42-1}$ and rat islet amyloid polypeptide, rIAPP_{20-29} were selected as control materials. Measurements were performed from room temperature down to cryogenic temperature in order to study the relaxation kinetics. Trends of dielectric spectra as a function of incubation time and temperature are explored within.

4.2 Sample Preparation and Data Collection

Lyophilized peptides were obtained from AnaSpec, Inc in quantities of 0.5 mg and 1.0 mg. The vials were stored at approximately -20°C until the time of reconstitution. Both the $A\beta_{1-42}$ and $A\beta_{42-1}$ were first rehydrated using 35μL 1% NH_4OH added to 0.5mg of protein to ensure that the solution was first driven to a monomeric state. Deionized water, 18.2MΩ·cm minimum, was used to dilute and rehydrate the peptides to a concentration of approximately 100μM and stored in a sterile vial. A separate sample was prepared for each time point. The samples were then mixed by repeated inversion of the vials and set to incubate for 0, 8, 24, 48, or 120 hours at room temperature. Using turbidimetric measurements, Jarrett et al. showed that $A\beta_{1-42}$ in a concentration of 20μM began immediate oligomerization and reached a final state at approximately 20 hours [146]. Rhodes et al. showed that hIAPP in a concentration of 20μM began oligomerization after approximately 40 hours of incubation and reached a final state at approximately 100 hours [147]. Glycerol, 99% minimum from Sigma was then added to a final concentration of 50μM peptide in 50%-50% by weight DI H_2O-glycerol solvent. The samples were again mixed by repeated inversion of the vials. The samples were then placed in the Novocontrol BDS 1307 stainless steel sample cell.

Data were collected using the Novocontrol Alpha-A Analyzer and Quatro Cryosystem in gain phase measurement mode with an AC probing voltage of 1.000 V_{RMS}. A liquid nitrogen cryostat was used to control temperature from 283K down to 133K at 5K intervals. We selected 60 data points in a frequency range from $2.00 \times 10^7 - 4.78 \times 10^{-2}$ Hz, spaced evenly in a logarithmic scale. Data for each temperature point was collected in duplicate. The first of the duplicates were during temperature stabilization and were discarded from analysis.

4.3 Results and Discussions

4.3.1 Studies of $A\beta_{1-42}$ and Scrambled $A\beta_{42-1}$

The dielectric spectra of $A\beta_{1-42}$, scrambled $A\beta_{42-1}$, and the solvent shows two relaxation processes (α and β) and low-frequency DC conductivity below 228K, depicted in Figure 4.1. At temperatures above 228K, the relaxation processes are either at frequencies above the range of the Alpha-A Analyzer or the conductivity dominates the spectra. The fast, α-relaxation process is clearly observed at 228K at a frequency of approximately 10^7 Hz in both the real and imaginary parts of the permittivity. The slower β-relaxation process is clearly observed at approximately 10^4 Hz at 228K.

With decreasing temperature the peaks of the α- and β-relaxation processes shift towards lower frequency. The α-process shifts faster than the β-process causing the

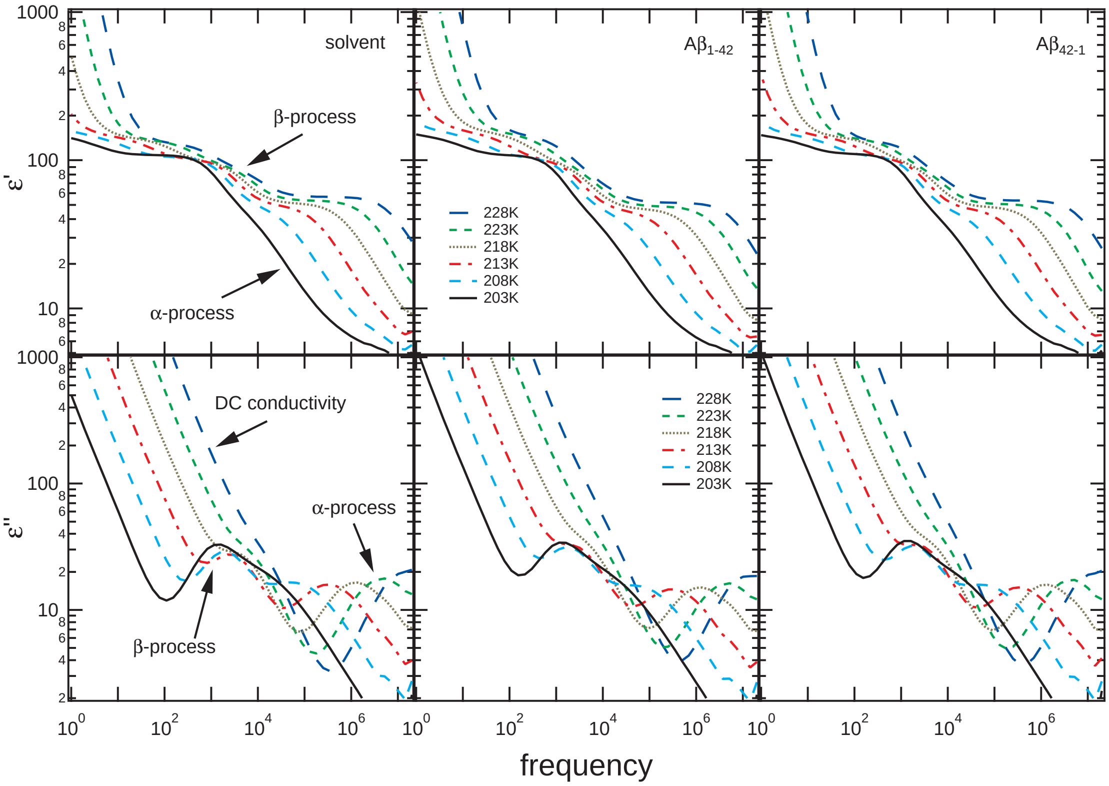

Figure 4.1: **Temperature evolution of the real and imaginary parts of the dielectric permittivity for the solvent, $A\beta_{1-42}$, and $A\beta_{42-1}$ from 228K to 213K.** Two relaxation processes for the real (ε') and imaginary (ε'') parts of the permittivity for the solvent, $A\beta_{1-42}$, and scrambled $A\beta_{42-1}$ are observed.

two processes to merge below 203K and eventually cross at approximately 193K as shown in Figure 4.2. The α-process continues to shift to very low frequencies with decreasing temperature. At around 163K the α-process shifts to frequency out of our measured frequency range. After the crossing of the two processes, the β-relaxation process dominates the dielectric spectra and shifts to approximately 10^{-1} Hz at 133K (Figure 4.3). Below 153K, the DC conductivity has decreased in magnitude and also shifted to frequency below the measured range.

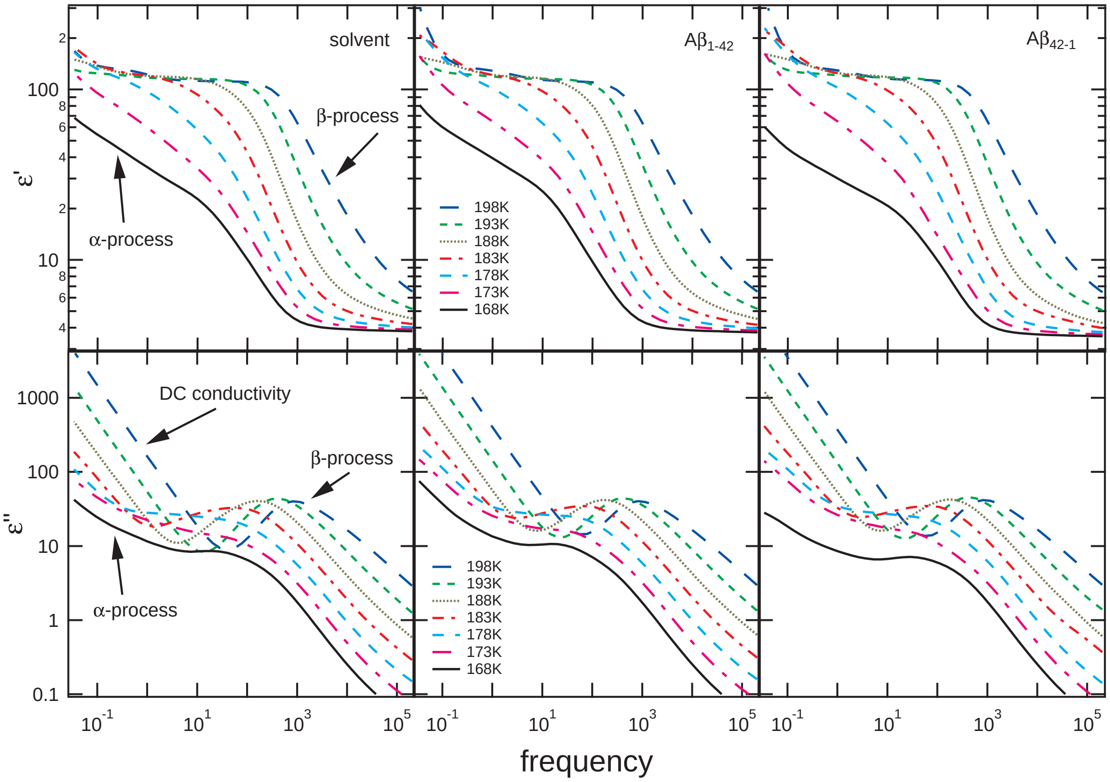

Figure 4.2: **Temperature evolution of the real and imaginary parts of the dielectric permittivity for the solvent, $A\beta_{1-42}$, and $A\beta_{42-1}$ from 198K to 168K.** The α-relaxation process rapidly shifts to lower frequency with decreasing temperature. In the range of 198K to 188K the two processes cross where the α-relaxation is at lower frequency than the β-relaxation process at temperatures of 183K and below.

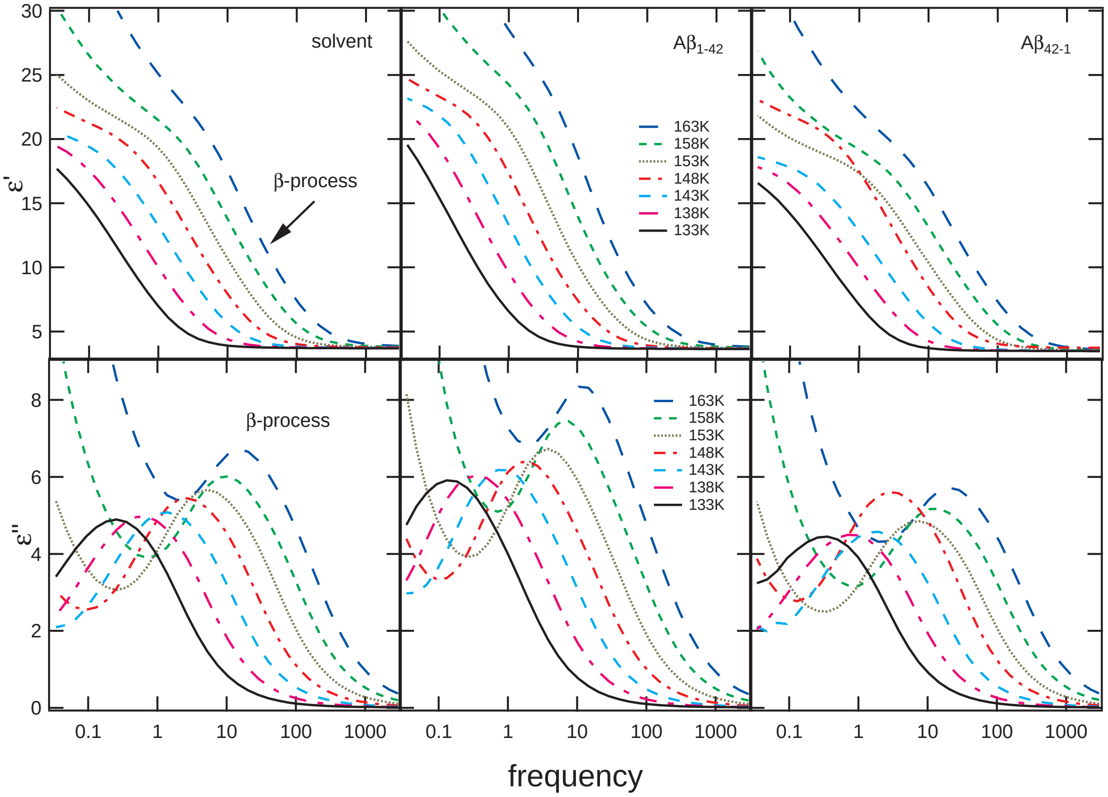

Figure 4.3: **Temperature evolution of the real and imaginary parts of the dielectric permittivity for the solvent, Aβ(1-42), and Aβ(42-1) from 163K to 133K.** The β-relaxation process dominates below the crossing temperature and continues to slow to under 1 Hz. The DC conductivity has reduced in magnitude to outside the measured range below 158K.

Permittivity data for $A\beta_{1-42}$ and scrambled $A\beta_{42-1}$ were plotted against the solvent to compare the time-evolution of dielectric signal. Data were collected after 0, 8, and 24 hours of incubation at room temperature. The dielectric loss of $A\beta_{1-42}$ and $A\beta_{42-1}$ as compared to the solvent over the observable temperature range 228K-133K is shown in Figures 4.4 - 4.13.

The magnitude of the dielectric loss peaks of the scrambled $A\beta_{42-1}$ shifts over time towards the signal of the solvent. Figure 4.5 above the α-β relaxation crossing temperature of 193K, we observe that the magnitude of α-process peak of $A\beta_{42-1}$ is similar to the solvent after 0 and 8 hours but is lower than the solvent after 24 hours. The β-relaxation process in the same temperature range is the same for 0 and 24 hours, but is the same as the solvent after 8 hours. In the crossing region of 193K - 183K where the processes occur at similar frequency, Figures 4.7 and 4.9 show that the dielectric signal of $A\beta_{42-1}$ in both frequency and magnitude are nearly overlapping with the solvent for all time points. At temperatures of 168K and below where the β-process dominates the spectra, the magnitude of $A\beta_{42-1}$ begins lower than that of the solvent at 0 hours, then above for 8 and 24 hours as seen in Figures 4.11 - 4.13. In that same region, the peak frequency of the beta process of $A\beta_{42-1}$ begins higher than the solvent at 0 hours, then steadily decreases and lies below the solvent for 8 and 24 hours.

The magnitude of the dielectric loss peaks of the $A\beta_{1-42}$ follows a different trend than the $A\beta_{42-1}$. Above the α-β relaxation crossing temperature of 193K, the magnitude of α-relaxation peak of $A\beta_{1-42}$ is slightly below the solvent and does not change much from 0-24 hours, as seen in Figure 4.4. The β-relaxation process in the same temperature range is higher in magnitude than the solvent at 0 hours and trends downward towards the solvent at 8 and 24 hours. This follows the trend of the decrease in DC conductivity over time. In the crossing region of 193K - 183K where the processes occur at similar frequency, Figures 4.6 and 4.8 show that the relaxation processes of $A\beta_{1-42}$ nearly overlaps with the solvent and the DC conductivity decreased in magnitude towards that of the solvent. At temperatures of 168K and below where the β-process dominates the spectra, the magnitude of $A\beta_{1-42}$ first decreases after 8 hours and then increases after 24 hours, but always remains larger than the solvent as shown in Figures 4.10 - 4.12. Additionally, the peak frequency of the beta process of $A\beta_{1-42}$ starts below the solvent, then shifts above the solvent after 8 hours, then back to lower frequency than the solvent after 24 hours.

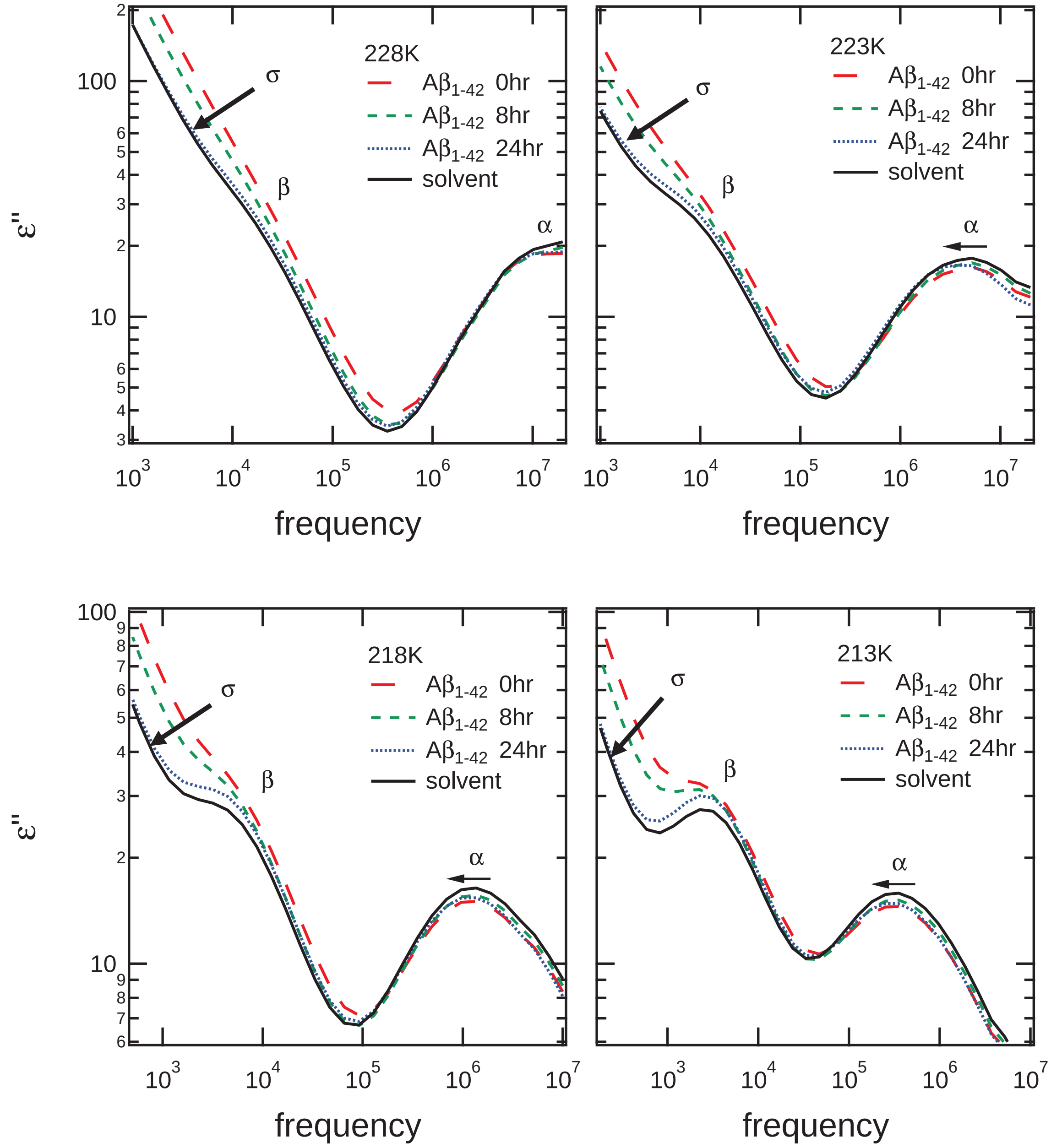

Figure 4.4: **Dielectric loss ε'' as a function of frequency for $A\beta_{1-42}$ in the range of 228K-213K and incubation periods of 0, 8, and 24 hours.** The arrows depict trends of the conductivity, σ to lower magnitude. Mixing between σ and the β-process make it difficult to determine the time-evolution of β in this temperature range. The α-process displays a small shift to lower frequency over time.

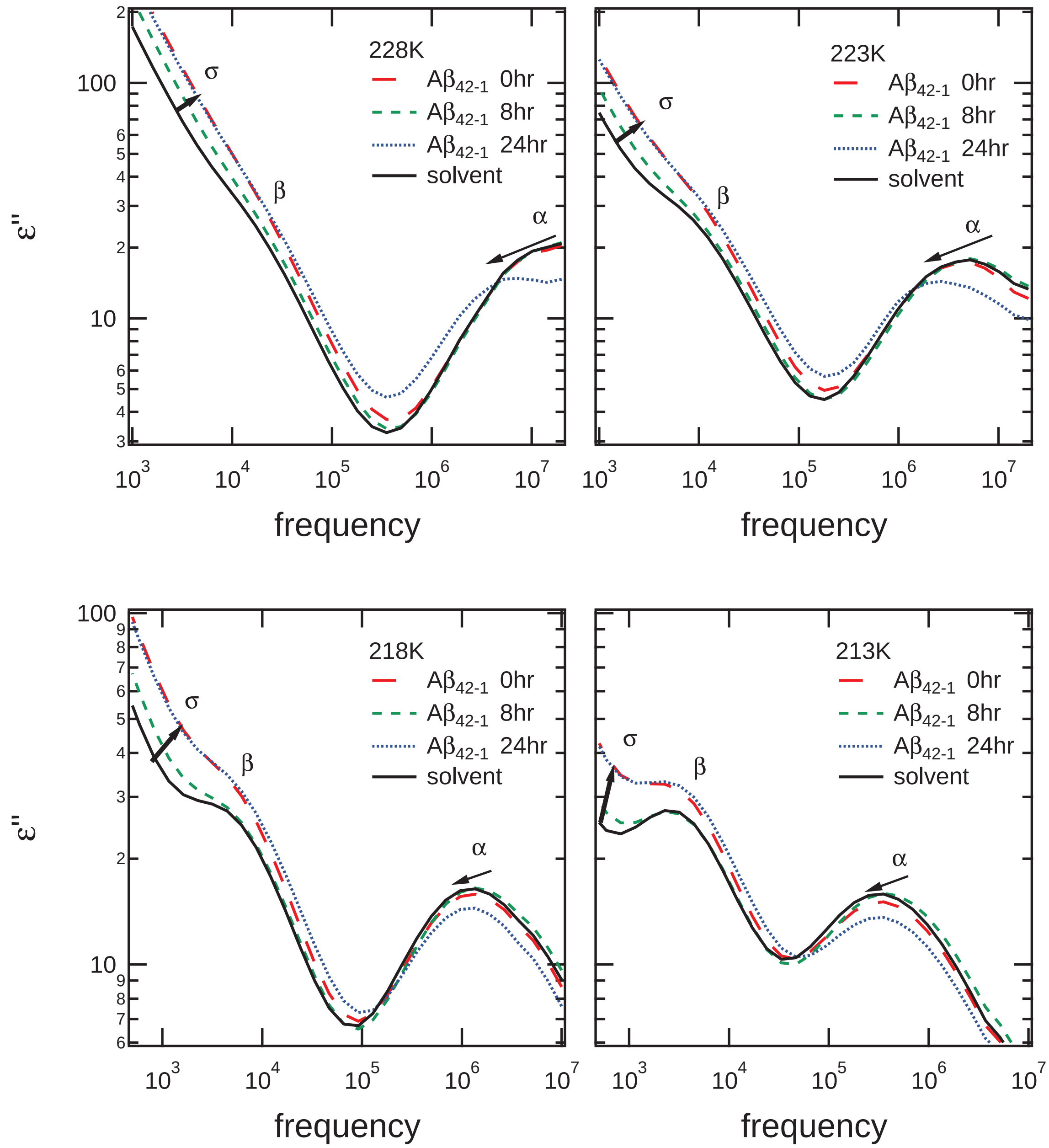

Figure 4.5: **Dielectric loss ε'' as a function of frequency for scrambled** $A\beta_{42-1}$ **in the range of 228K-213K and incubation periods of 0, 8, and 24 hours.** The arrows depict trends of the conductivity, σ to higher magnitude and the α-process to slightly frequency and magnitude. The conductivity shift is opposite that of $A\beta_{1-42}$ in the same temperature range. The shift of the α-process is the same. Mixing between σ and the β-process make it difficult to determine the time-evolution of β in this temperature range.

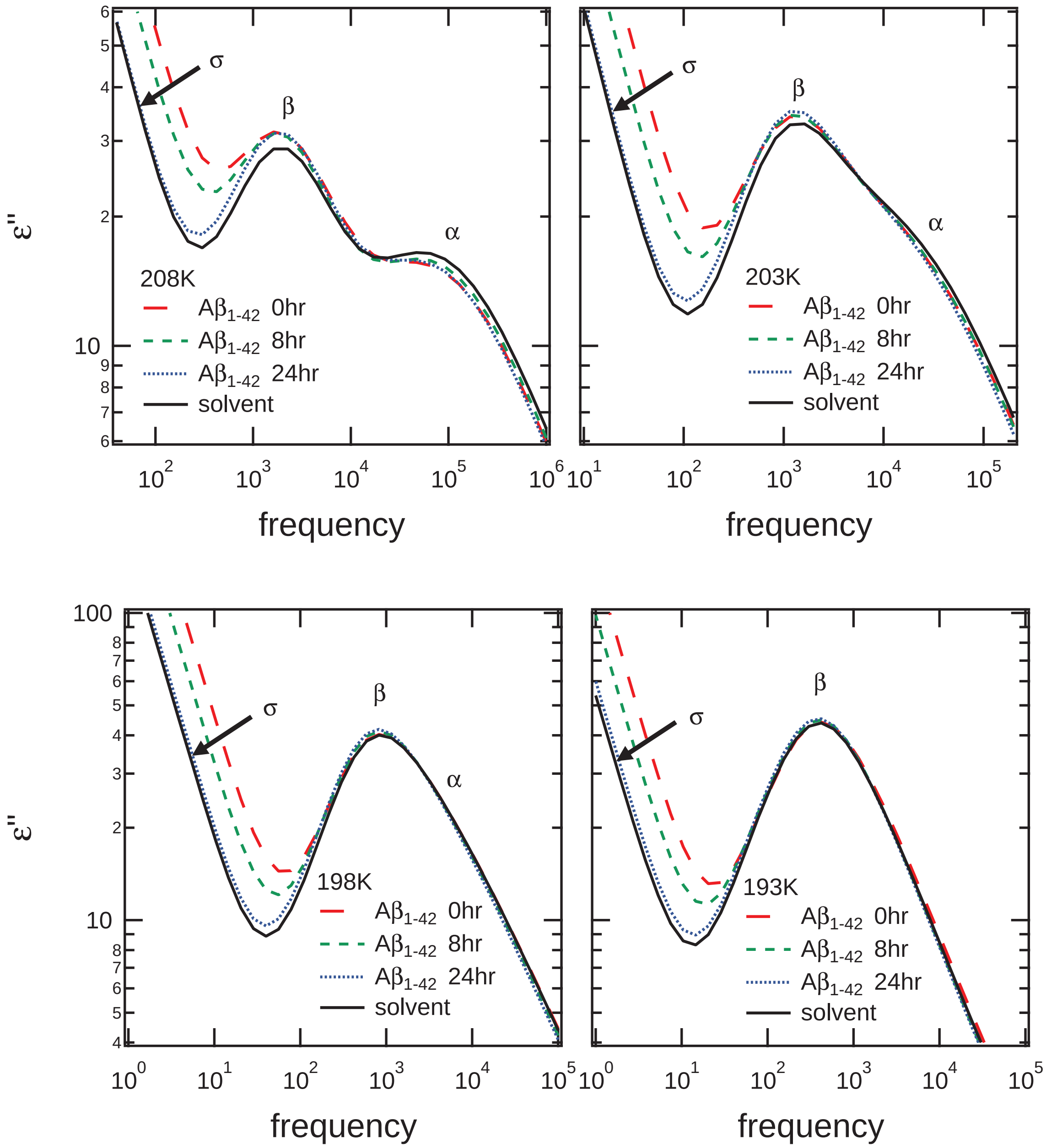

Figure 4.6: **Dielectric loss ε'' as a function of frequency for $A\beta_{1-42}$ in the range of 208K-193K and incubation periods of 0, 8, and 24 hours.** Deconvolution of the peaks from curve fitting analysis shows that at 193K, the α-process occurs at near the same frequency as the β-process but with lower magnitude. The conductivity, σ shifts to lower magnitude over time.

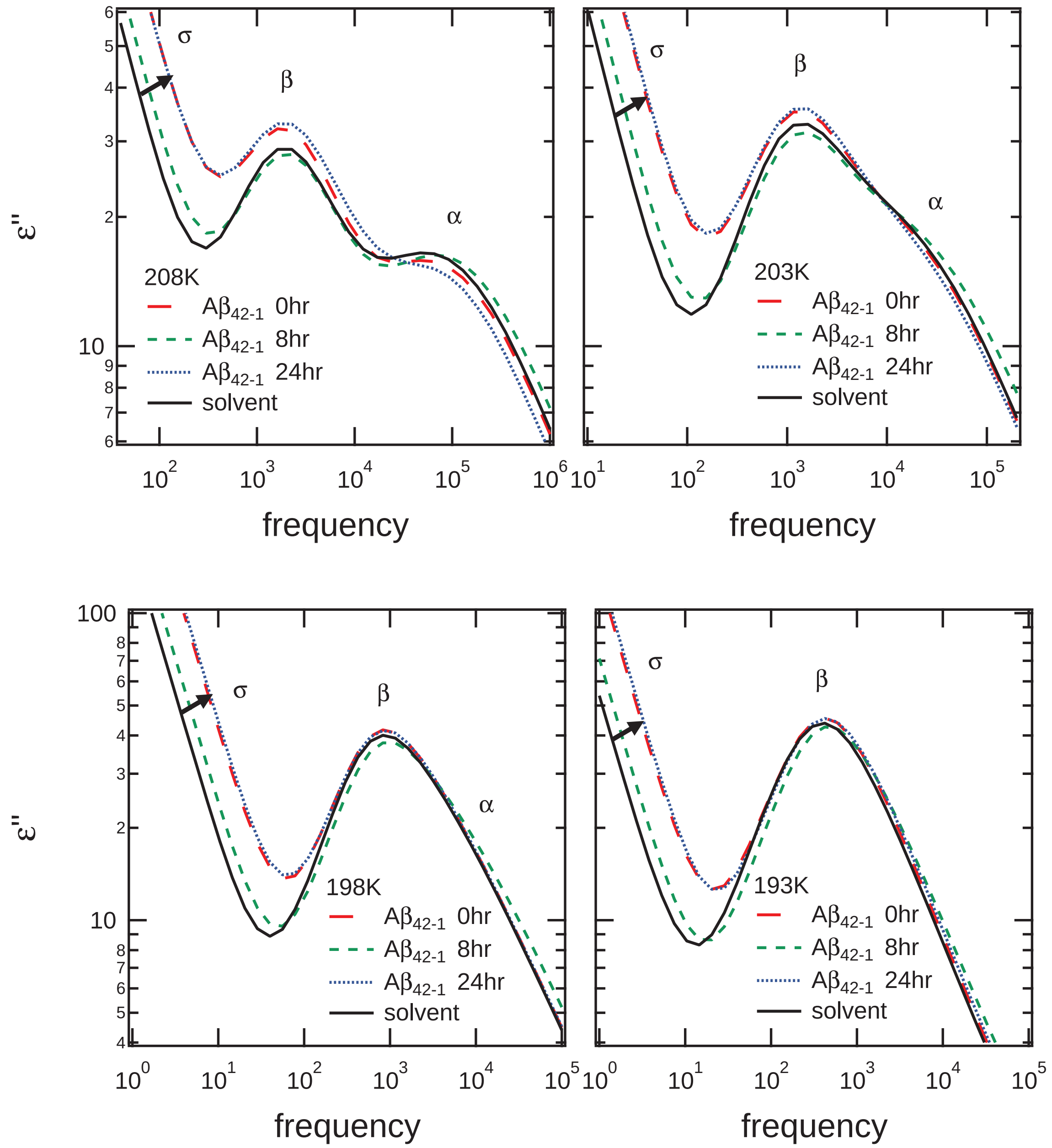

Figure 4.7: **Dielectric loss ε'' as a function of frequency for scrambled $A\beta_{42-1}$ in the range of 208K-193K and incubation periods of 0, 8, and 24 hours.** At 193K, the α-process occurs at near the same frequency as the β-process but with lower magnitude. The arrows depict trends of the conductivity, σ to higher magnitude. This opposite the behavior of $A\beta_{1-42}$ in the same temperature range. The apparent peak increase at the β-process is the result of the change in conductivity and not a process change.

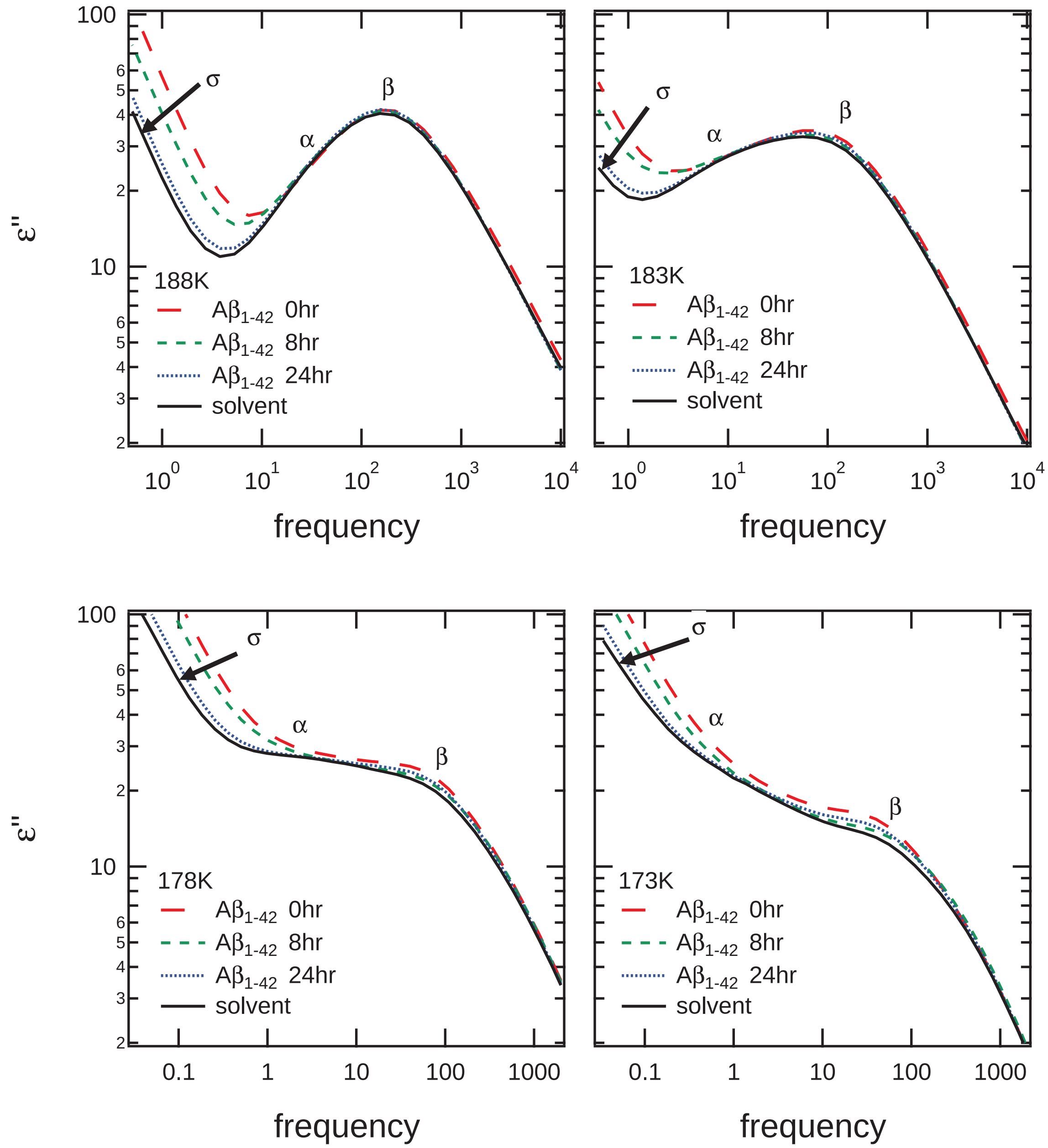

Figure 4.8: **Dielectric loss ε'' as a function of frequency for $A\beta_{1-42}$ in the range of 188K-173K and incubation periods of 0, 8, and 24 hours.** The α-process has shifted to a lower frequency than the β-process. The arrows depict trends of the conductivity, σ to lower magnitude. There is significant mixing between σ and α at 173K and 178K.

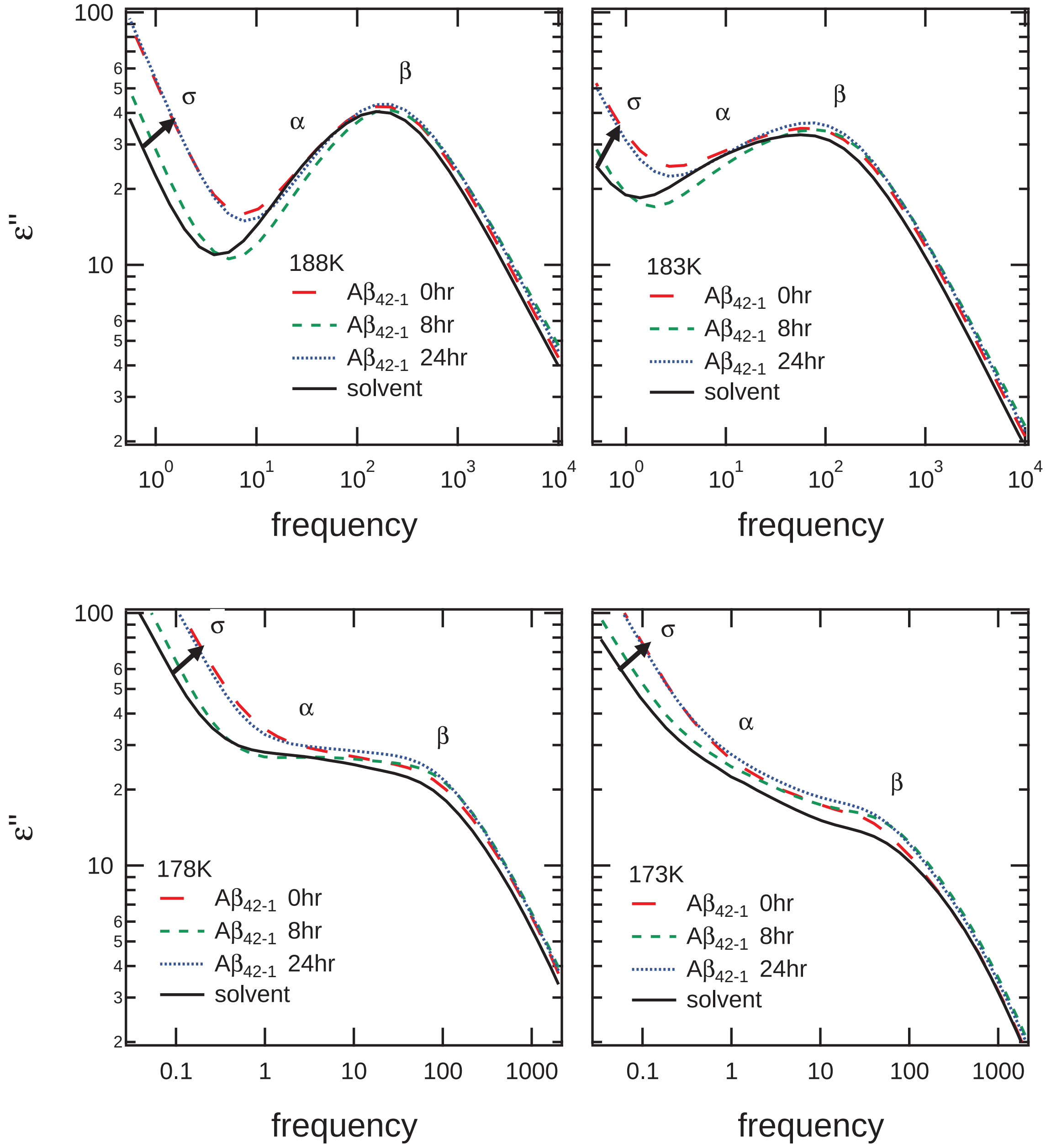

Figure 4.9: **Dielectric loss ε'' as a function of frequency for scrambled $A\beta_{42-1}$ in the range of 188K-173K and incubation periods of 0, 8, and 24 hours.** The α-process has shifted to a lower frequency than the β-process. The arrows depict trends of the conductivity, σ to higher magnitude. This opposite the behavior of $A\beta_{1-42}$ in the same temperature range. There is significant mixing between σ and α at 173K and 178K.

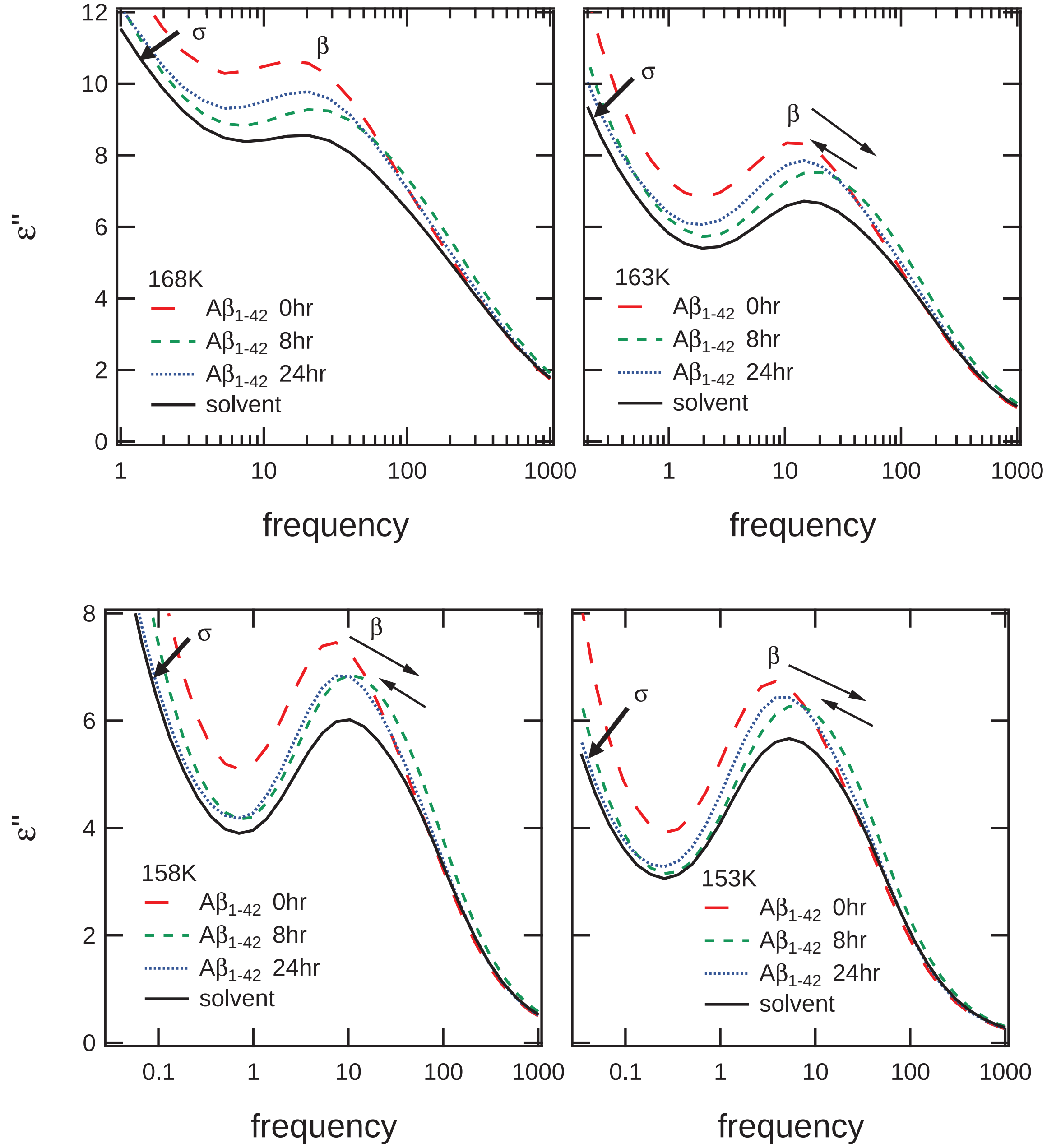

Figure 4.10: **Dielectric loss ε'' as a function of frequency for $A\beta_{1-42}$ in the range of 168K-153K and incubation periods of 0, 8, and 24 hours.** At 168K, the α-process has shifted to frequency below the measured range. At 163K and below, the conductivity has been reduced to a point where the β-process is clearly discerned. The arrows depict the shifts of the β-process first to lower magnitude and higher frequency, then to an increase in magnitude and decrease in frequency.

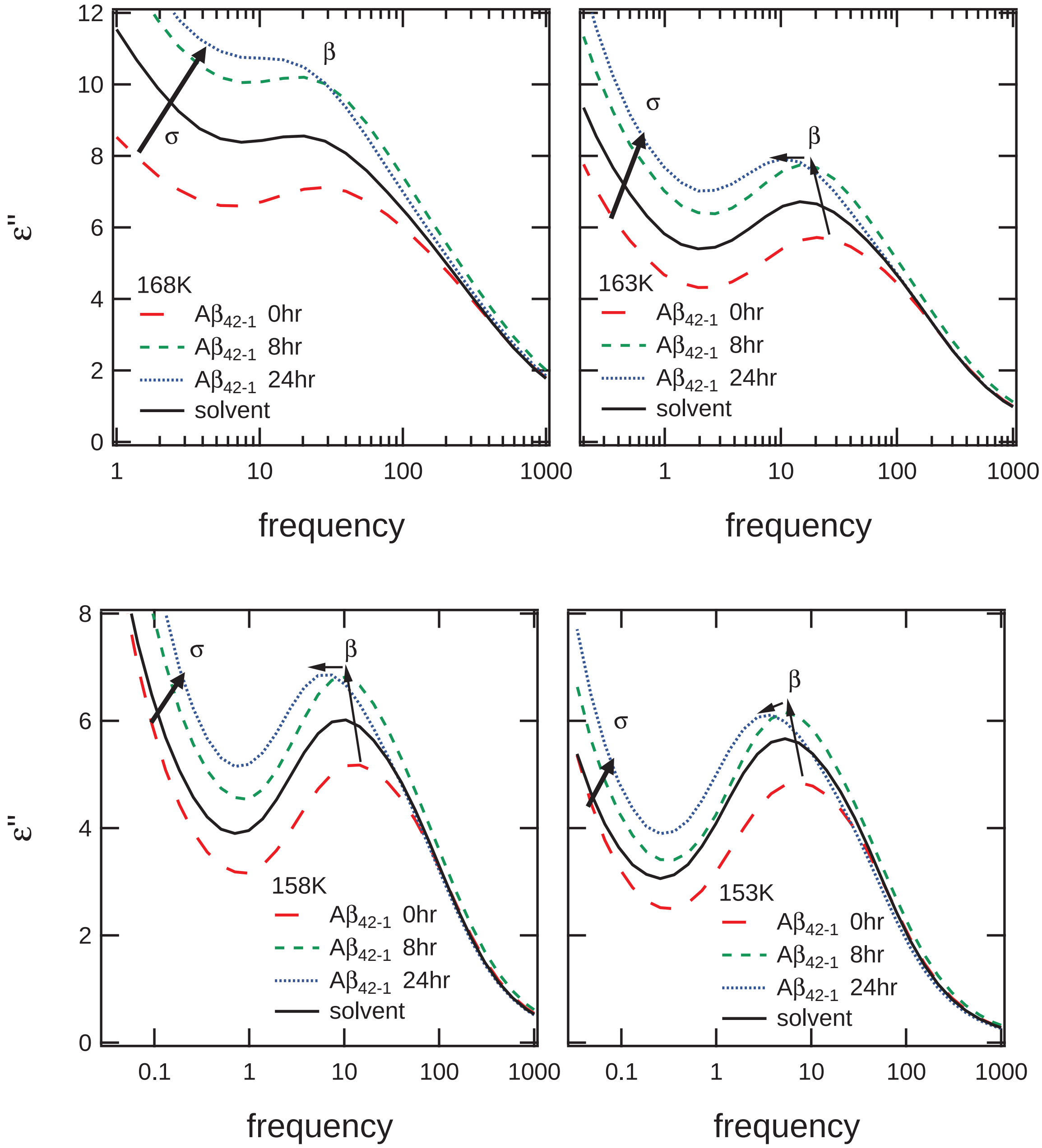

Figure 4.11: **Dielectric loss ε'' as a function of frequency for scrambled $A\beta_{42-1}$ in the range of 168K-153K and incubation periods of 0, 8, and 24 hours.** At 168K, the α-process has shifted to frequency below the measured range. At 163K and below, the conductivity has been reduced to a point where the β-process is clearly discerned. The arrows depict the shifts of the β-process first to higher magnitude and lower frequency, then to a decrease in magnitude and increase in frequency. This opposite the behavior of $A\beta_{1-42}$ in the same temperature range.

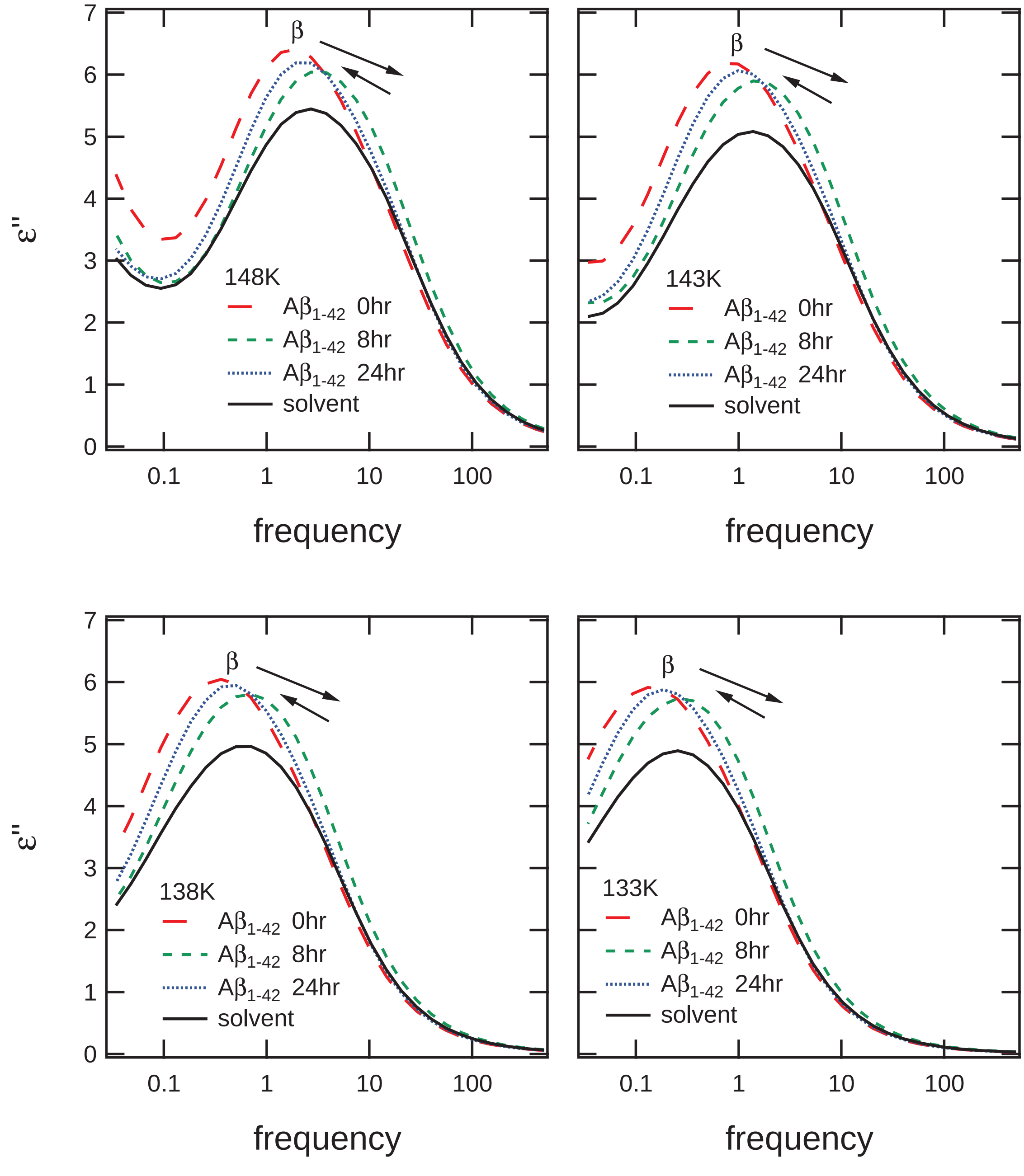

Figure 4.12: **Dielectric loss ε'' as a function of frequency for $A\beta_{1-42}$ in the range of 148K-133K and incubation periods of 0, 8, and 24 hours.** The arrows depict the shifts of the β-process first to lower magnitude and higher frequency, then to an increase in magnitude and decrease in frequency.

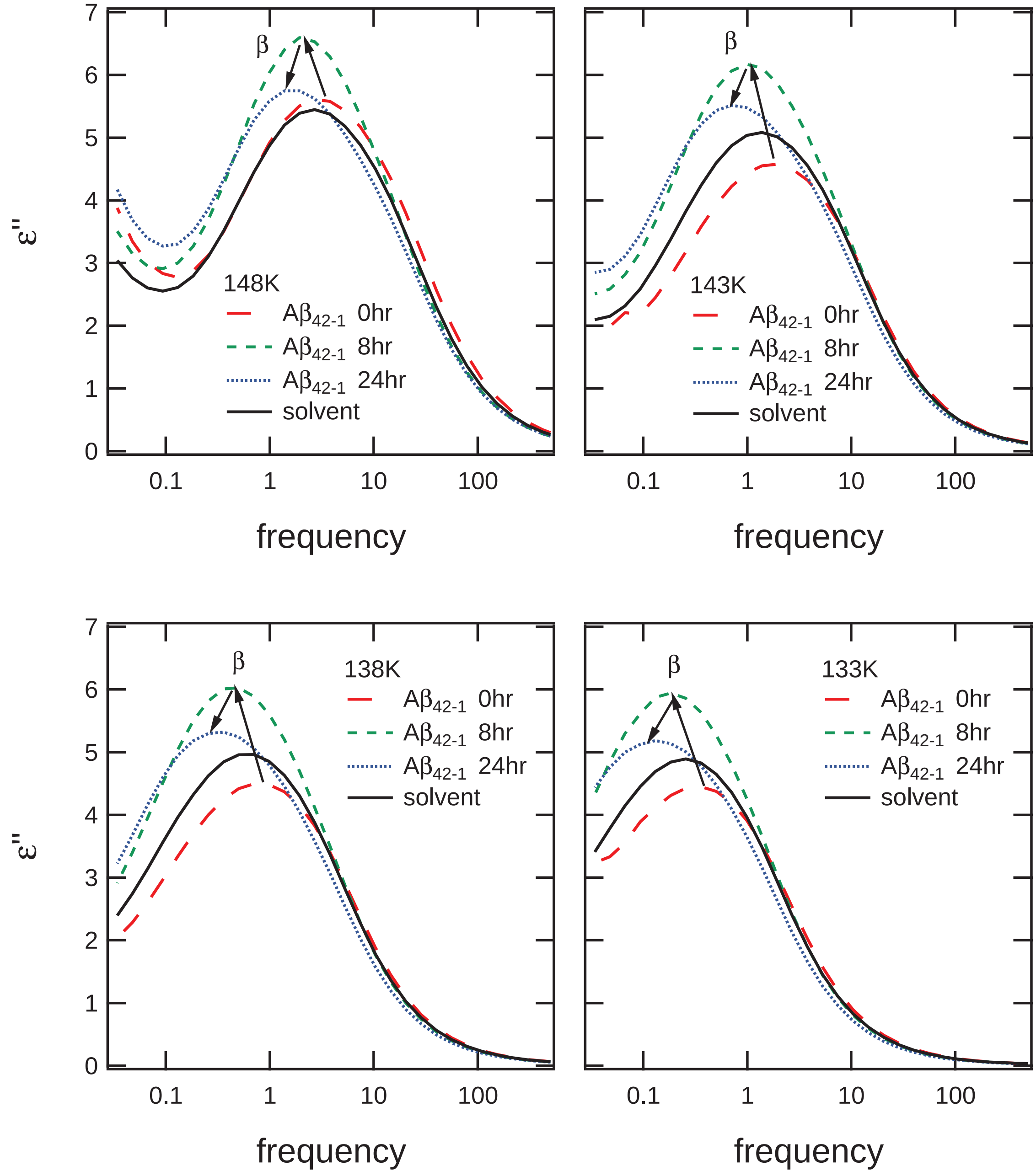

Figure 4.13: **Dielectric loss ε'' as a function of frequency for scrambled $A\beta_{42-1}$ in the range of 148K-133K and incubation periods of 0, 8, and 24 hours.** The arrows depict the shifts of the β-process first to higher magnitude and lower frequency, then to an decrease in magnitude and increase in frequency. This opposite the behavior of $A\beta_{1-42}$ in the same temperature range.

Dielectric permittivity data for $A\beta_{1-42}$, and $A\beta_{42-1}$, and the solvent were modeled using the WinFIT program for each temperature from 223K to 133K and at incubation time points 0, 8, and 24 hours. The model functions include a power law for conductivity and the Havriliak-Negami function for each relaxation process given by

$$\varepsilon^*(\omega) = -i\left(\frac{\sigma_0}{\varepsilon_0\omega}\right)^N + \sum_{k=1}^{2}\left[\varepsilon_{\infty,k} + \frac{\Delta\varepsilon_k}{(1+(i\omega\tau_k)^{\beta_k})^{\gamma_k}}\right] \tag{4.1}$$

The β-relaxation process demonstrates symmetric broadening but no asymmetric broadening over the measured temperature range. This reduces the Havriliak-Negami function to a Cole-Davidson with $\gamma = 1$ and $\beta < 1$. The symmetric broadening parameter, β remains relatively constant over the entire temperature range at approximately 0.8. The α-relaxation process demonstrates both symmetric and asymmetric broadening over the observed temperature range. Both β and γ spreading parameters change with temperature. Data were fit using a least-squares minimization and the root-mean-squared-deviation (RMSD) is reported for goodness of fit.

The α-relaxation process is observed from 228K to 168K, though in the crossing temperatures of 198K to 183K, it overlaps with the β-process. During this temperature range, the β-relaxation process dominates. The β-relaxation process is observed between approximately 228K down to the lowest temperature, 133K. At temperatures above 208K, the DC conductivity dominates the spectra in the region of the β-relaxation. Examples of curve fitting performed at representative temperatures are shown in Figures 4.14 - 4.17.

Figure 4.17 shows a clear β-relaxation process with a high-frequency excess wing. The excess wing is known to exist in certain glass-forming liquids such as glycerol [63]. The wing may exist at all temperatures but is most pronounced at low temperatures, particularly below the glass transition. Despite efforts to characterize the excess wing, there is no common explanation to its physical origin and thus it is treated as an empirical phenomenon [63, 148]. It is possible to fit the wing with another empirical function, but this is not necessary in determining the peak position and shape parameters for the β-relaxation process.

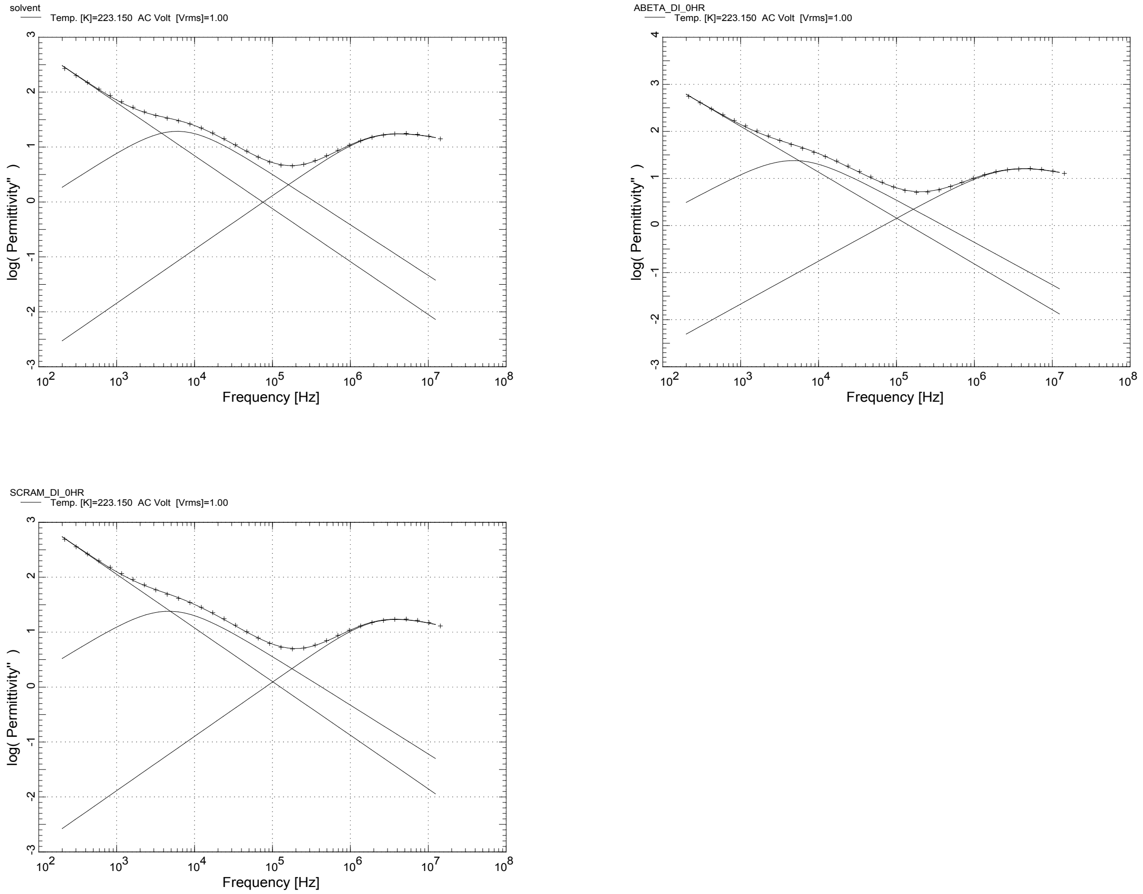

Figure 4.14: **Curve fitting of imaginary part of the permittivity data using the WinFIT program of the solvent, $A\beta_{1-42}$, and $A\beta_{42-1}$ at 223K.** A large, low frequency DC conductivity is fit with a power law. The β-relaxation process at around 10^4 Hz is fit with a Cole-Davidson function and the α-relaxation process at around 10^7 Hz is fit with a Havriliak-Negami function. The root-mean-square deviation (RMSD) of the fits are 0.018, 0.012, and 0.013, respectively.

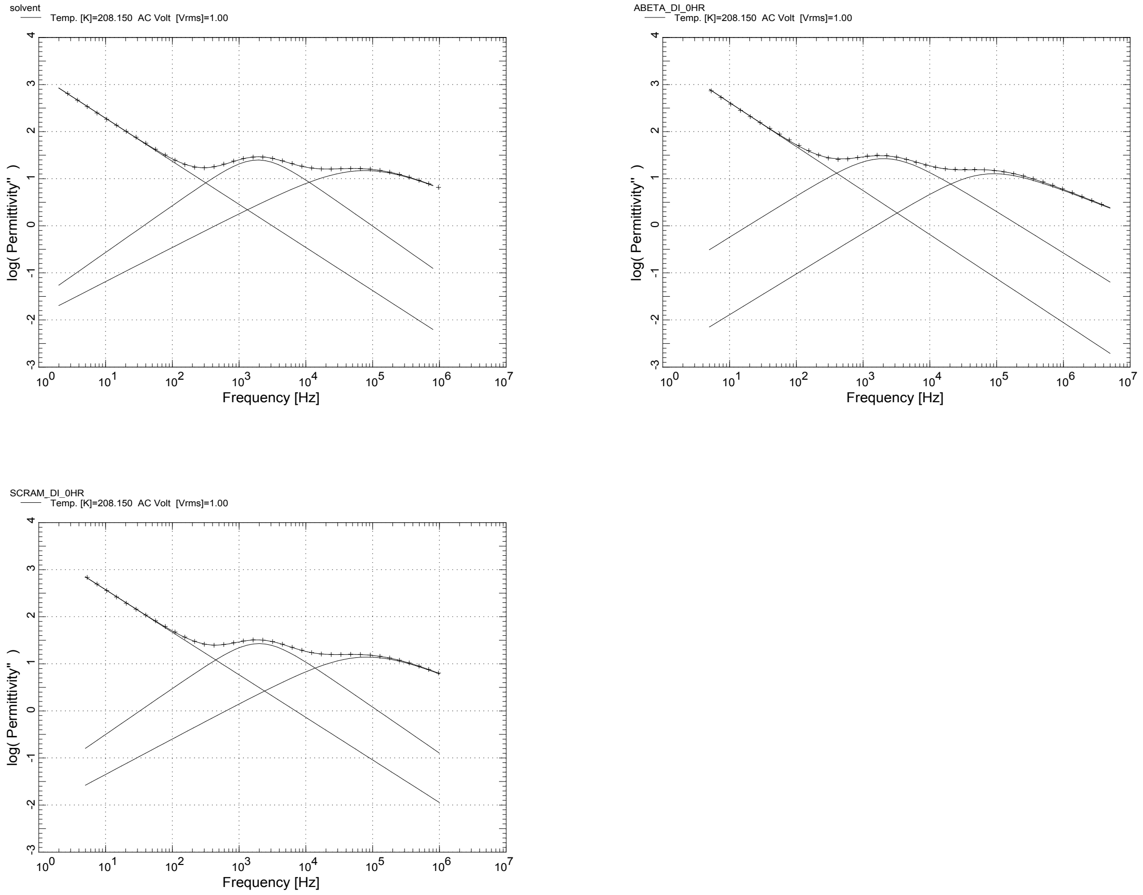

Figure 4.15: **Curve fitting of imaginary part of the permittivity data using the WinFIT program of the solvent, $A\beta_{1-42}$, and $A\beta_{42-1}$ at 208K.** A large, low frequency DC conductivity is fit with a power law. The β-relaxation process at around 10^3 Hz is fit with a Cole-Davidson function and the α-relaxation process at around 10^5 Hz is fit with a Havriliak-Negami function. The RMSD of the fits are 0.045, 0.009, and 0.013, respectively.

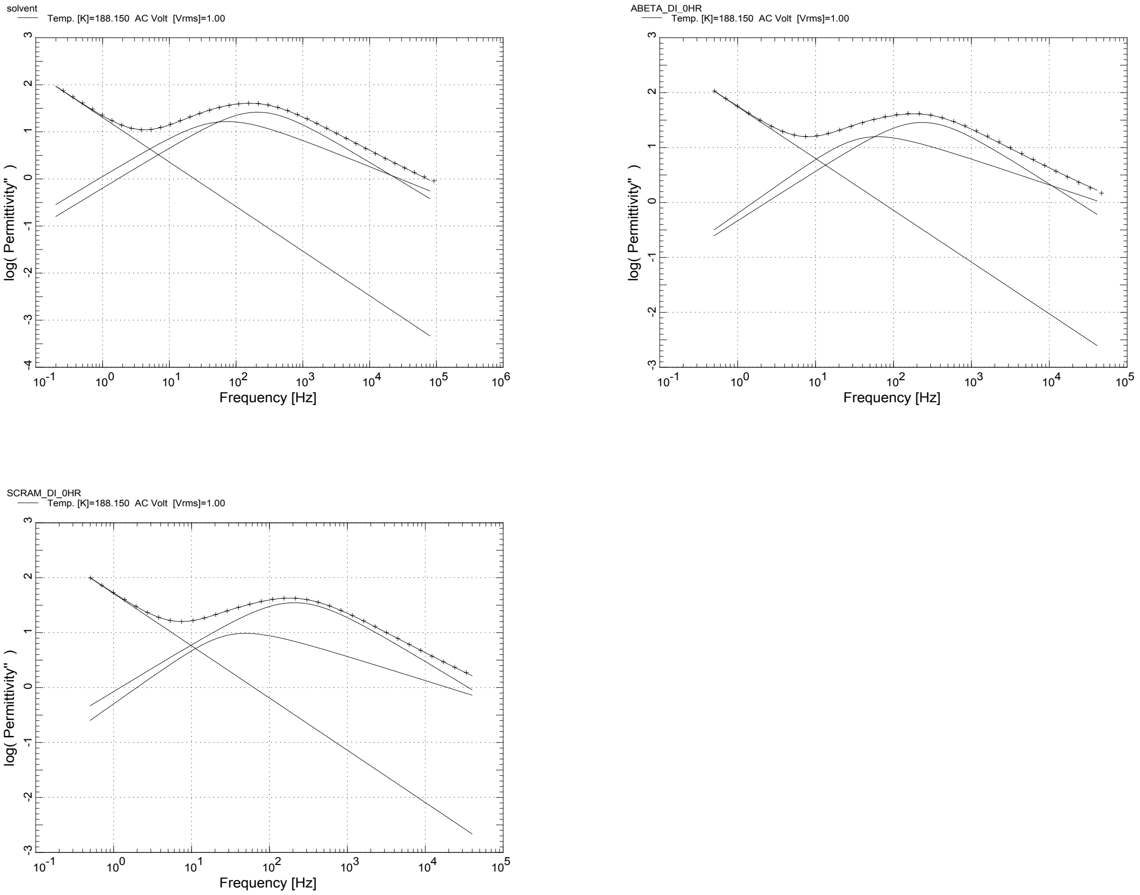

Figure 4.16: **Curve fitting of imaginary part of the permittivity data using the WinFIT program of the solvent, $A\beta_{1-42}$, and $A\beta_{42-1}$ at 188K.** A large, low frequency DC conductivity is fit with a power law. The β-relaxation process at around 10^3 Hz is fit with a Cole-Davidson function and the α-relaxation process at around 10^1 Hz is fit with a Havriliak-Negami function. Here, the α process has crossed over to slower than β relaxation times. The RMSD of the fits are 0.008, 0.011, and 0.013, respectively.

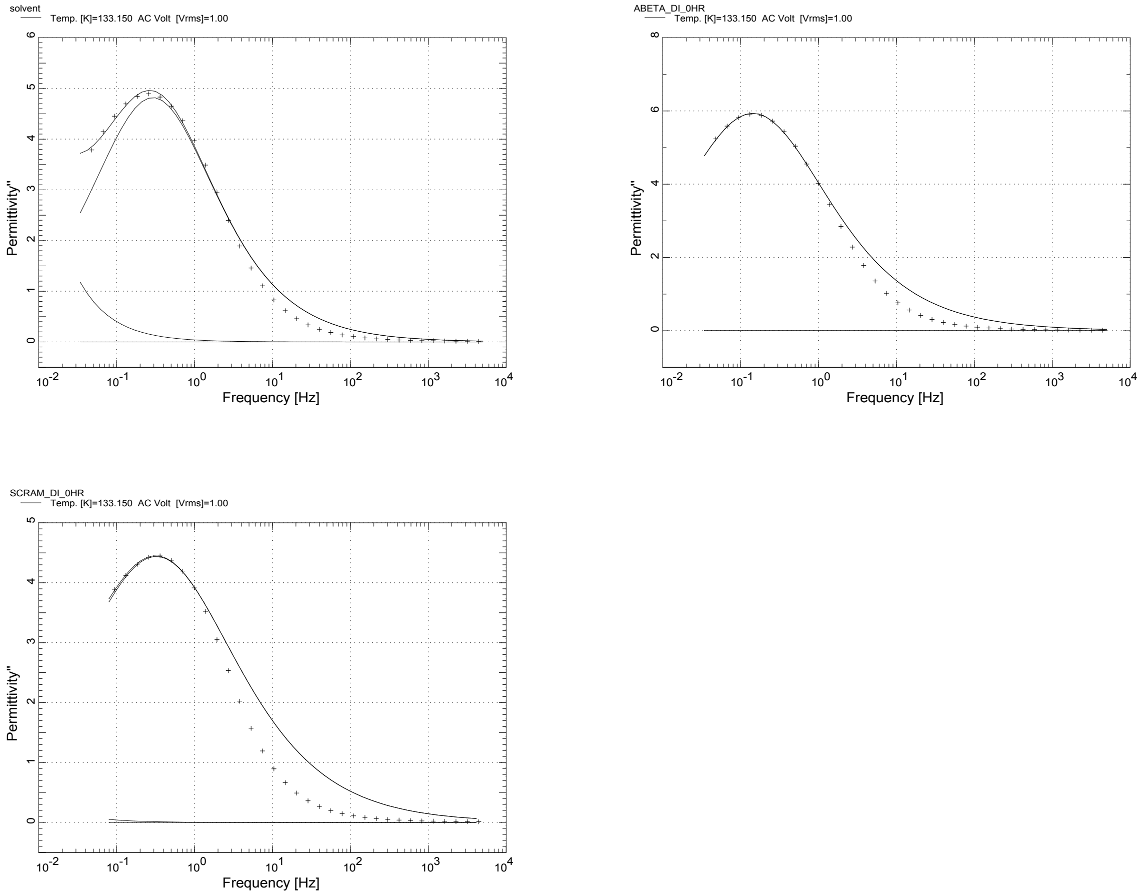

Figure 4.17: **Curve fitting of the imaginary part of the permittivity data using the WinFIT program of the solvent, $A\beta_{1-42}$, and $A\beta_{42-1}$ at 133K.** A small, very low frequency DC conductivity is fit with a power law. The β-relaxation process at around 1 Hz is fit with a Cole-Davidson function and the α-relaxation process is not observed. The RMSD of the fits are 0.092, 0.123, and 0.082, respectively.

The maximum frequency, f_{max} of ε'' of both the α- and β-relaxation processes were determined from the model function curve fitting of the permittivity data at all temperatures. Arrhenius plots of f_{max} versus inverse temperature, 1000/T were created for each process. The β-relaxation process follows a linear, or Arrhenius behavior throughout the temperature range. The α-relaxation process follows a slight non-linear Vogel-Fulcher-Tammann (VFT)-type behavior that is expected in glass-forming solvents such as glycerol (Figures 4.18 and 4.19). Activation energies for the β process and glass-forming fragilities for the α process were determined from the Arrhenius and VFT analysis and tabulated in Tables 4.1 and 4.2. The activation energies for $A\beta_{1-42}$ are close to the value of 23 kJ/mol obtained by Kusumoto et al. from measurements of $A\beta_{1-40}$ using the quasi-electric light scattering (QLS) method [149].

	time	A	B	E_A (kJ/mol)		*time*	A	B	E_A (kJ/mol)
Aβ_{1-42}	0hr	10.4	1.491	28.5	Aβ_{42-1}	0hr	9.64	1.341	25.7
	8hr	9.07	1.360	26.0		8hr	10.2	1.458	28.3
	24hr	9.99	1.421	27.2		24hr	10.4	1.473	28.2
solvent		9.87	1.394	26.7	solvent		9.87	1.394	26.7

Table 4.1: Parameters of the linear fits to the β-relaxation measurements of $\log(f_{max}(T))$ of the form $A + BT$.

	time	$\log f_\infty$	D	T_0 (K)		*time*	$\log f_\infty$	D	T_0 (K)
Aβ_{1-42}	0hr	20	20	88	Aβ_{42-1}	0hr	20	20	89
	8hr	20	21	87		8hr	20	19	90
	24hr	20	20	90		24hr	20	21	86
solvent		20	21	88	solvent		20	21	88

Table 4.2: Parameters of the VFT fits to the α-relaxation measurements of $f_{max}(T)$ of the form $\log(f_{max}) = \log(f_\infty(T)) - \frac{DT_0}{T-T_0}$

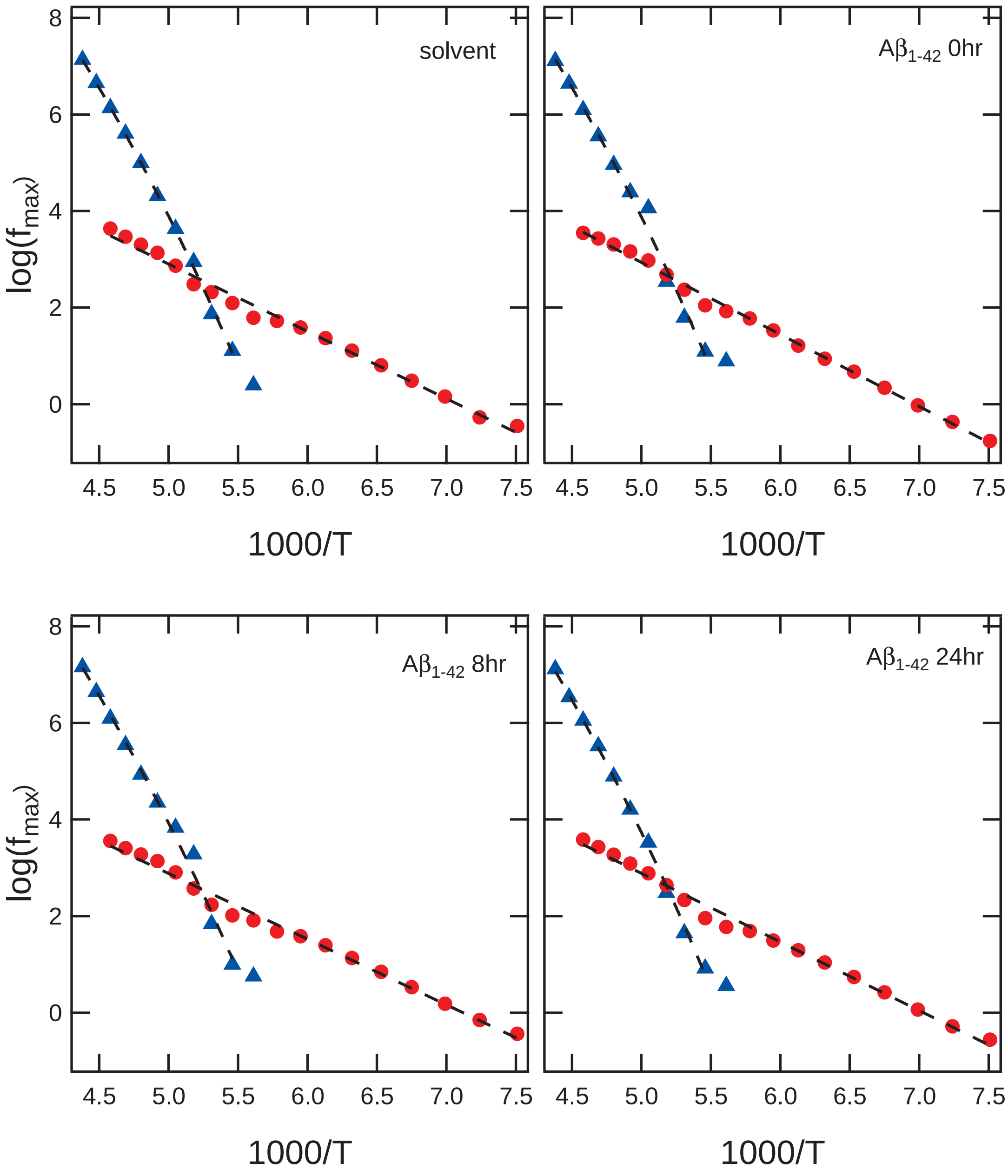

Figure 4.18: **Arrhenius plots of f_{max} versus inverse temperature for $A\beta_{1-42}$ over time.** The α-relaxation process follows a VFT behavior whereas the β-relaxation process follows an Arrhenius, or linear behavior. The α-process departs from the VFT curvature at low temperature.

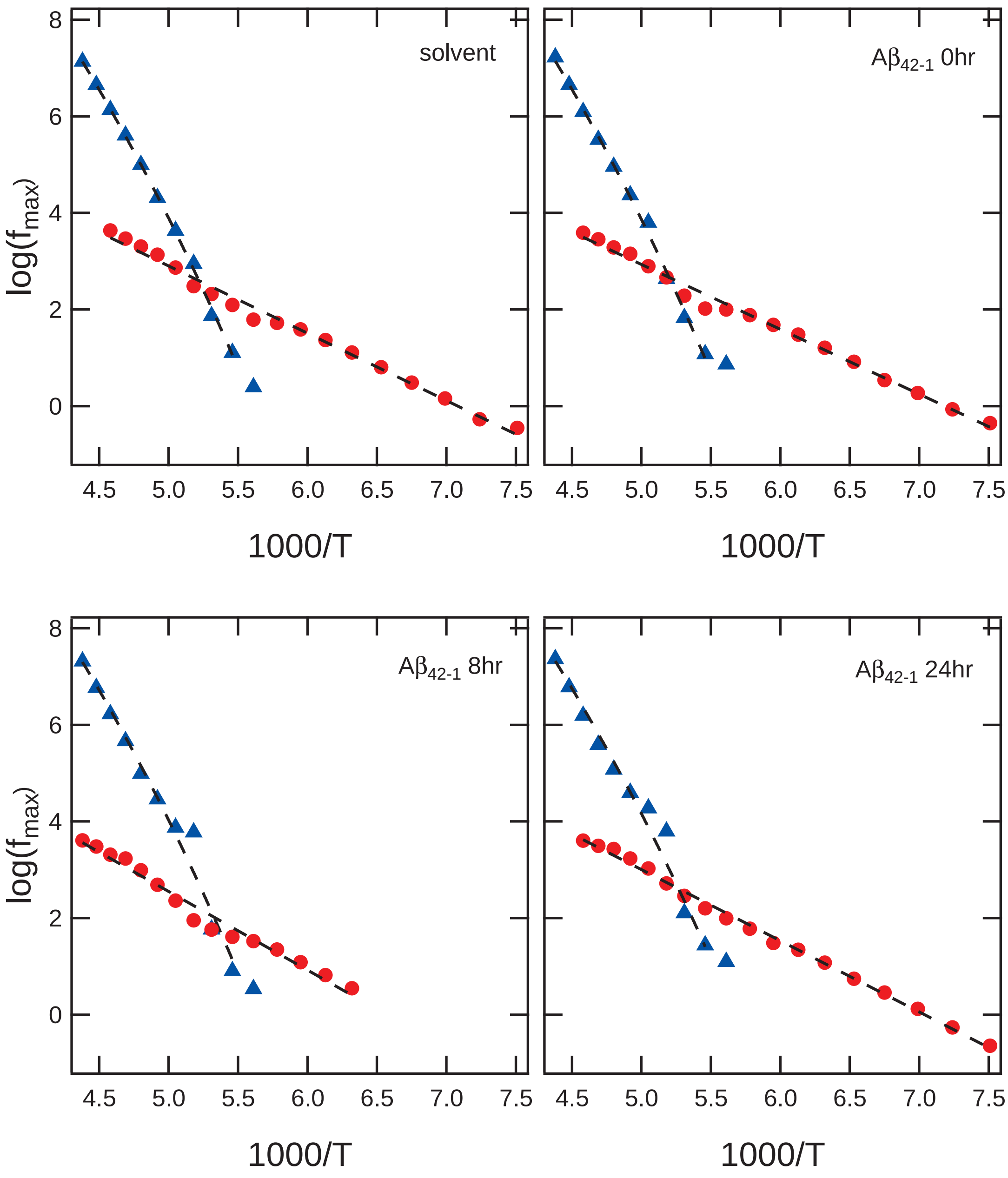

Figure 4.19: **Arrhenius plots of f_{max} versus inverse temperature for scrambled $A\beta_{42-1}$ over time.** The α-relaxation process follows a VFT behavior whereas the β-relaxation process follows an Arrhenius, or linear behavior. The α-process departs from the VFT curvature at low temperature.

Onsager described the enhancement of permanent dipoles by polarization of the environment, or reaction field [150]. Here, the dielectric strength ($\Delta\varepsilon$) is related to the dipole moment (μ) by:

$$\Delta\varepsilon = \frac{1}{3\varepsilon_0} F \frac{\mu^2}{k_B T} \frac{N}{V} \tag{4.2}$$

where N/V is the volume density of dipoles and F is a correction for the reaction field. Kirkwood and Fr$\ddot{o}$hlich further extended the theory for interacting dipoles by introducing a factor, g with g<1 for anti-parallel dipoles and g>1 for parallel dipoles:

$$\Delta\varepsilon = \frac{1}{3\varepsilon_0} F g \frac{\mu^2}{k_B T} \frac{N}{V} \tag{4.3}$$

From this equation, it is evident that the dielectric strength is proportional to the dipole moment squared.

The macroscopic resulting dipole moment of a protein solution can present structural information about the aggregates. The α-helix and random coils will give a significant contribution to the dipole moment [151, 130]. If β-sheets form, the dipole moment should decrease for anti-parallel conformations and remain relatively strong for parallel arrangements. Figure 4.20 shows that over time, $A\beta_{1-42}$ first has an increase, then decreases in the dielectric strength as fibril formation progresses, whereas the non-amyloidogenic $A\beta_{42-1}$ does not change over time. Studies using FTIR have indicated that the structure of the $A\beta_{1-42}$ displays an anti-parallel β-sheet [152, 153]. This is in agreement with our results showing a decrease in the dielectric strength, and thus, the dipole moment as fibrils form. The initial increase in dipole moment could be an indication of a high concentration of oligomers, which are known to form circular micelles [154]. A circular form round present an alignment of dipoles that would have additive dipole moments.

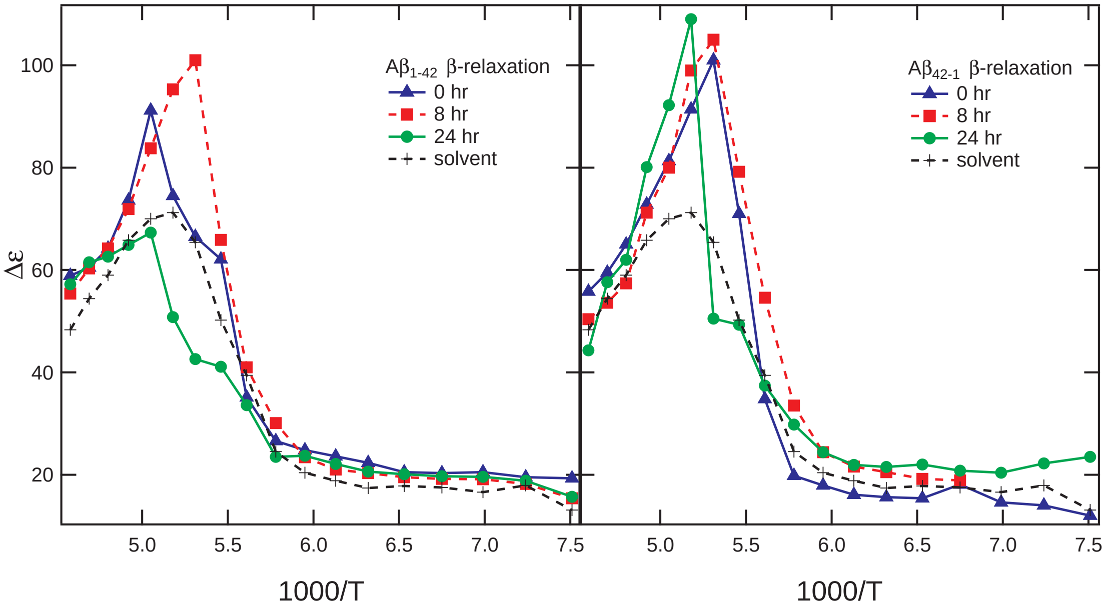

Figure 4.20: **Dielectric strength, $\Delta\varepsilon$ of the β-relaxation for $A\beta_{1-42}$ and $A\beta_{42-1}$ versus inverse temperature.** The dielectric strength for the $A\beta_{1-42}$ solution first increases, then deceases to values less than the solvent. The dielectric strength of $A\beta_{42-1}$ continued to increase over time. The decrease in dielectric strength indicates that the $A\beta_{1-42}$ displays an anti-parallel β-sheet conformation.

4.3.2 Studies of Human and Rat Islet Amyloid Polypeptide

The dielectric spectra of human (hIAPP) and rat (rIAPP) islet amyloid polypeptide and the solvent show two relaxation processes (α and β) and low-frequency DC conductivity below 228K, depicted in Figure 4.21. At temperatures above 228K, the relaxation processes are at frequencies above the range of the Alpha-A Analyzer and the conductivity dominates the spectra. The fast, α-relaxation process is clearly observed at 228K at a frequency of approximately 10^7 Hz in both the real and imaginary parts of the permittivity. The slower β-relaxation process is easily observed at approximately 10^4 Hz at 228K.

With decreasing temperature the peaks of the α- and β-relaxation processes shift towards lower frequency. The α-process shifts faster than the β-process causing the two processes to merge below 203K and eventually cross at approximately 193K as

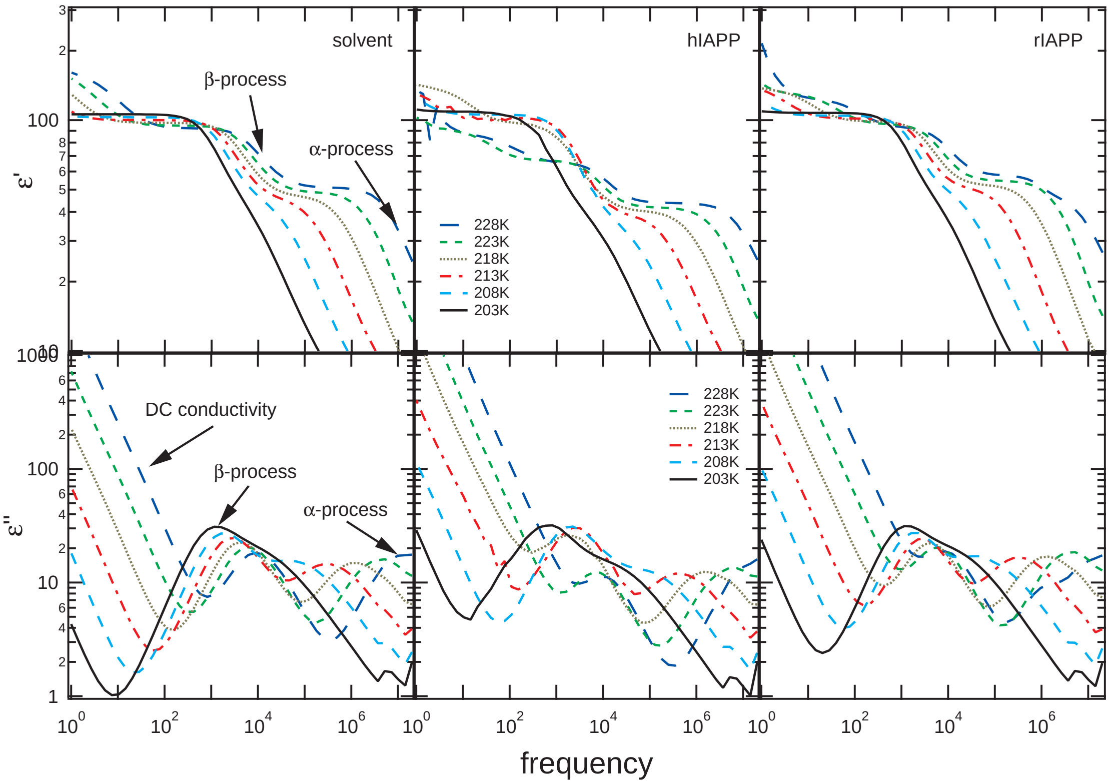

Figure 4.21: **Temperature evolution of the real and imaginary parts of the dielectric permittivity for the solvent, hIAPP, and rIAPP from 228K to 203K.** Two relaxation processes for the real (ε') and imaginary (ε'') parts of the permittivity for the solvent, hIAPP, and rIAPP are observed.

shown in Figure 4.22. The α-process continues to shift to very low frequencies with decreasing temperature. At around 168K the α-process is out of our measured range. After the crossing of the two processes, the β-relaxation process dominates the dielectric spectra and shifts to approximately 10^{-2}-10^0 Hz at 133K, depending on the analyte (Figure 4.23). The DC conductivity has decreased in magnitude and also shifted to low frequency below the measured range at temperatures under 158K.

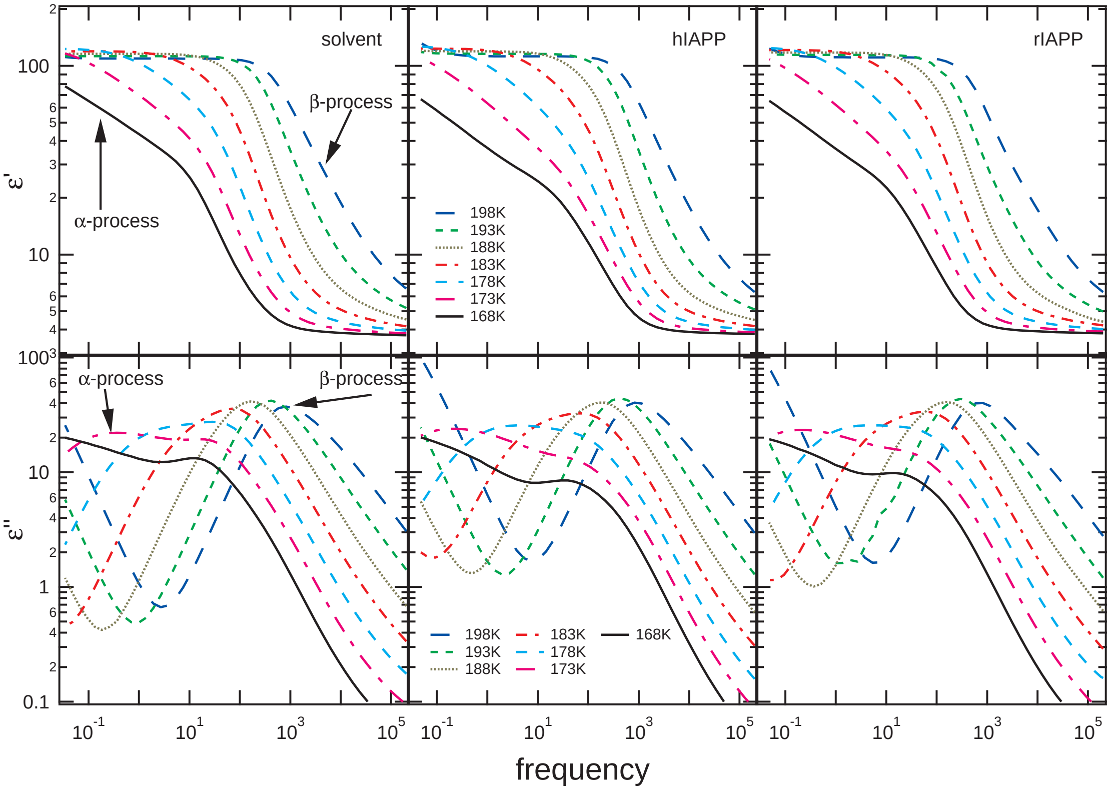

Figure 4.22: **Temperature evolution of the real and imaginary parts of the dielectric permittivity for the solvent, hIAPP, and rIAPP from 198K to 168K.** The α-relaxation process rapidly shifts to lower frequency with decreasing temperature. In the range of 198K to 188K the two processes cross to where the α-relaxation is at lower frequency than the β-relaxation process at temperatures of 183K and below.

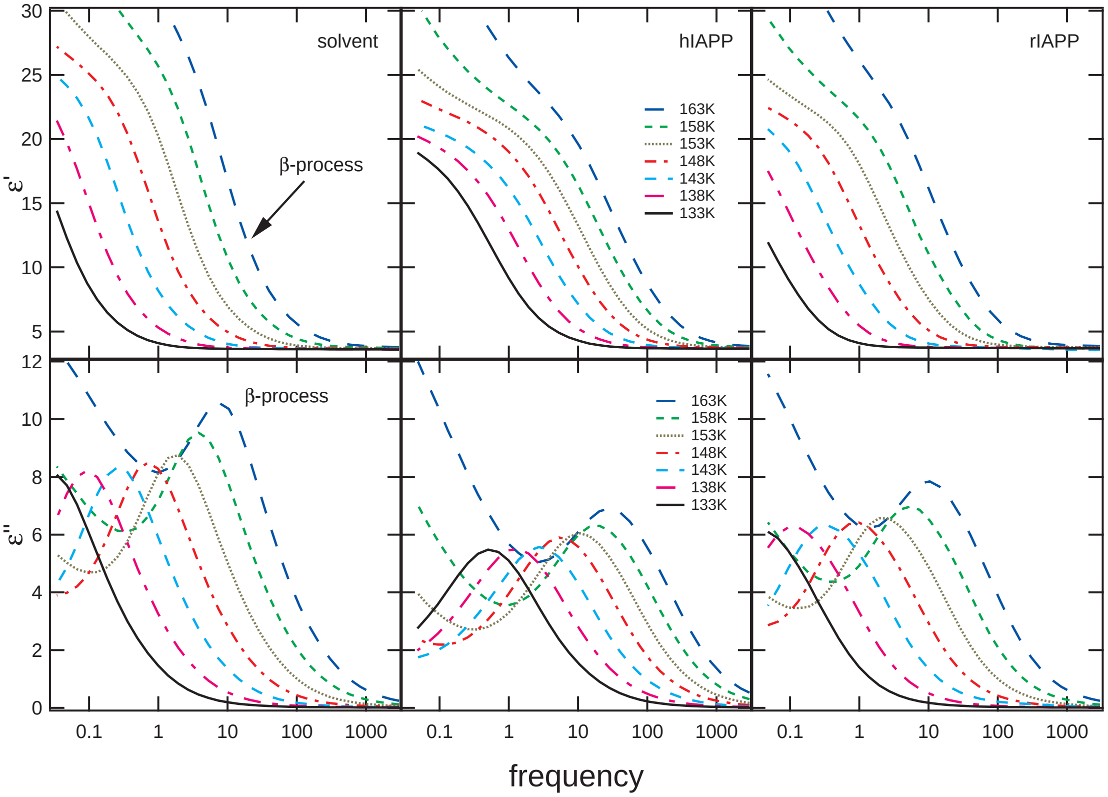

Figure 4.23: **Temperature evolution of the real and imaginary parts of the dielectric permittivity for the solvent, hIAPP, and rIAPP from 163K to 133K.** The β-relaxation process dominates below the crossing temperature and continues to slow to under 1 Hz. The DC conductivity has reduced in magnitude to outside the measured range below 158K.

Permittivity data for hIAPP and rIAPP were plotted against the solvent to compare the time-evolution of dielectric signal. Data were collected after 0, 24, 48, and 120 hours of incubation at room temperature. The dielectric loss of hIAPP and rIAPP as compared to the solvent over the observable temperature range 228K-133K is shown in Figures 4.24 - 4.33.

The magnitude of the dielectric loss peaks of the rIAPP shifts over time towards the signal of the solvent. Above the α-β relaxation crossing temperature of 193K where the α-process dominates the spectra, the magnitude of rIAPP steadily increases towards the solvent as seen in Figure 4.25. In the crossing region of 193K - 183K where the processes occur at similar frequency, Figures 4.27 and 4.29 show that the dielectric signal of rIAPP in both frequency and magnitude are nearly overlapping with the solvent after 120 hours. At temperatures of 168K and below where the β-process dominates the spectra, the magnitude and peak frequency of rIAPP continues to move toward the signal of the solvent. Figures 4.31 - 4.33 show that the peak frequency of the beta process of rIAPP increases over time for each temperature below 178K.

The magnitude of the dielectric loss peaks of the hIAPP follows a different trend than the rIAPP. Above the α-β relaxation crossing temperature of 193K where the α-process dominates the spectra, the magnitude of hIAPP starts near the solvent but then steadily decreases as seen in Figure 4.24. In the crossing region of 193K - 183K where the processes occur at similar frequency, Figures 4.26 and 4.28 show that the dielectric signal of hIAPP in both frequency and magnitude are nearly overlapping from 0-48 hours, but the permittivity at 120 hours is much less than that of the solvent. Figures 4.30 - 4.32 that at 168K and below where the β-process dominates the spectra, the magnitude of hIAPP increase over time as compared to the solvent. Additionally, the peak frequency of the beta process of hIAPP decreases over time.

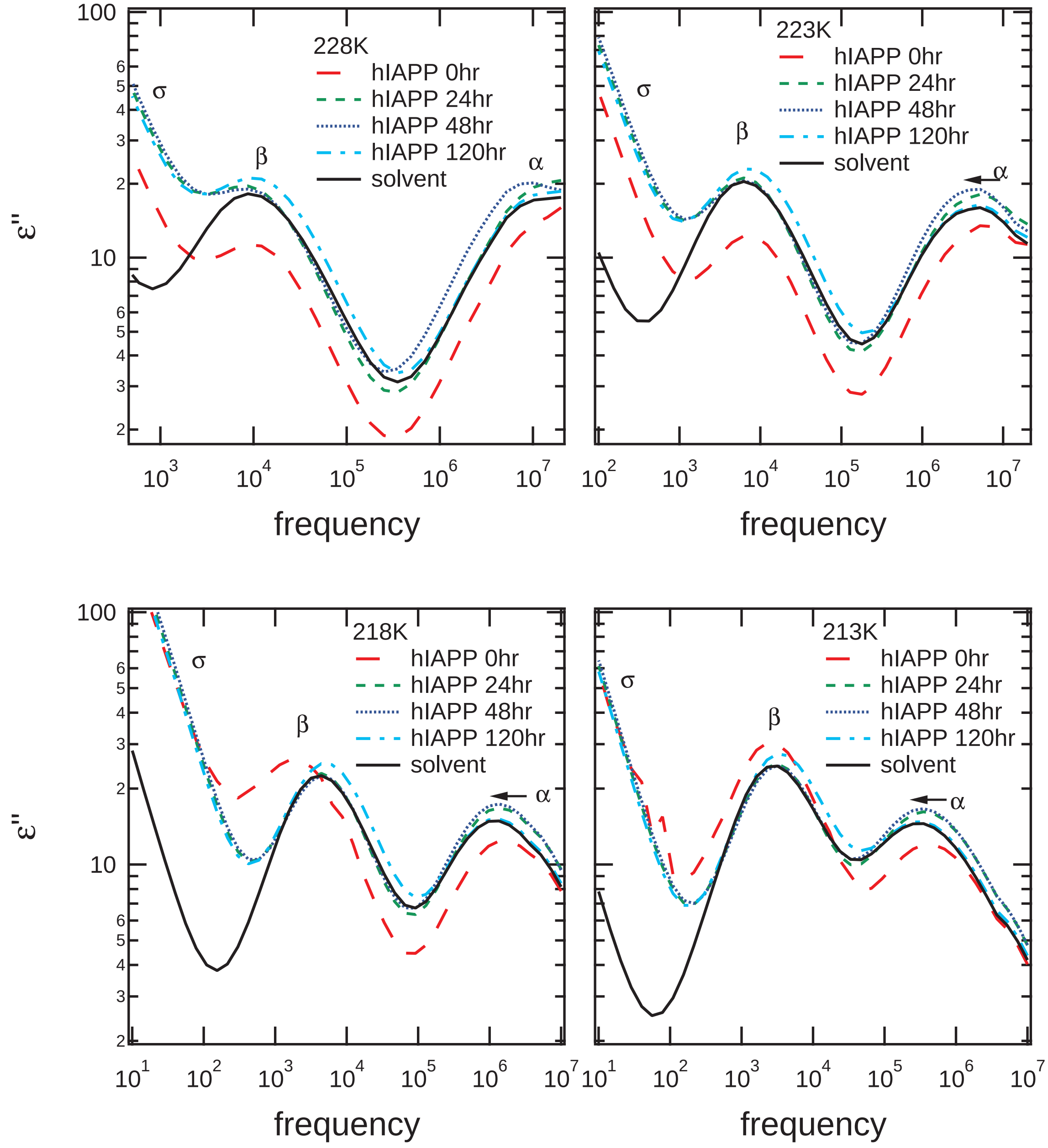

Figure 4.24: **Dielectric loss ε'' as a function of frequency for hIAPP in the range of 228K-213K and incubation periods of 0, 24, 48, and 120 hours.** The arrows depict shifts of the the α-process to slightly lower frequency by approximately a half decade. The conductivity and β-process does show a different behavior for the 0 hour time point, but there is no consistency within this temperature range.

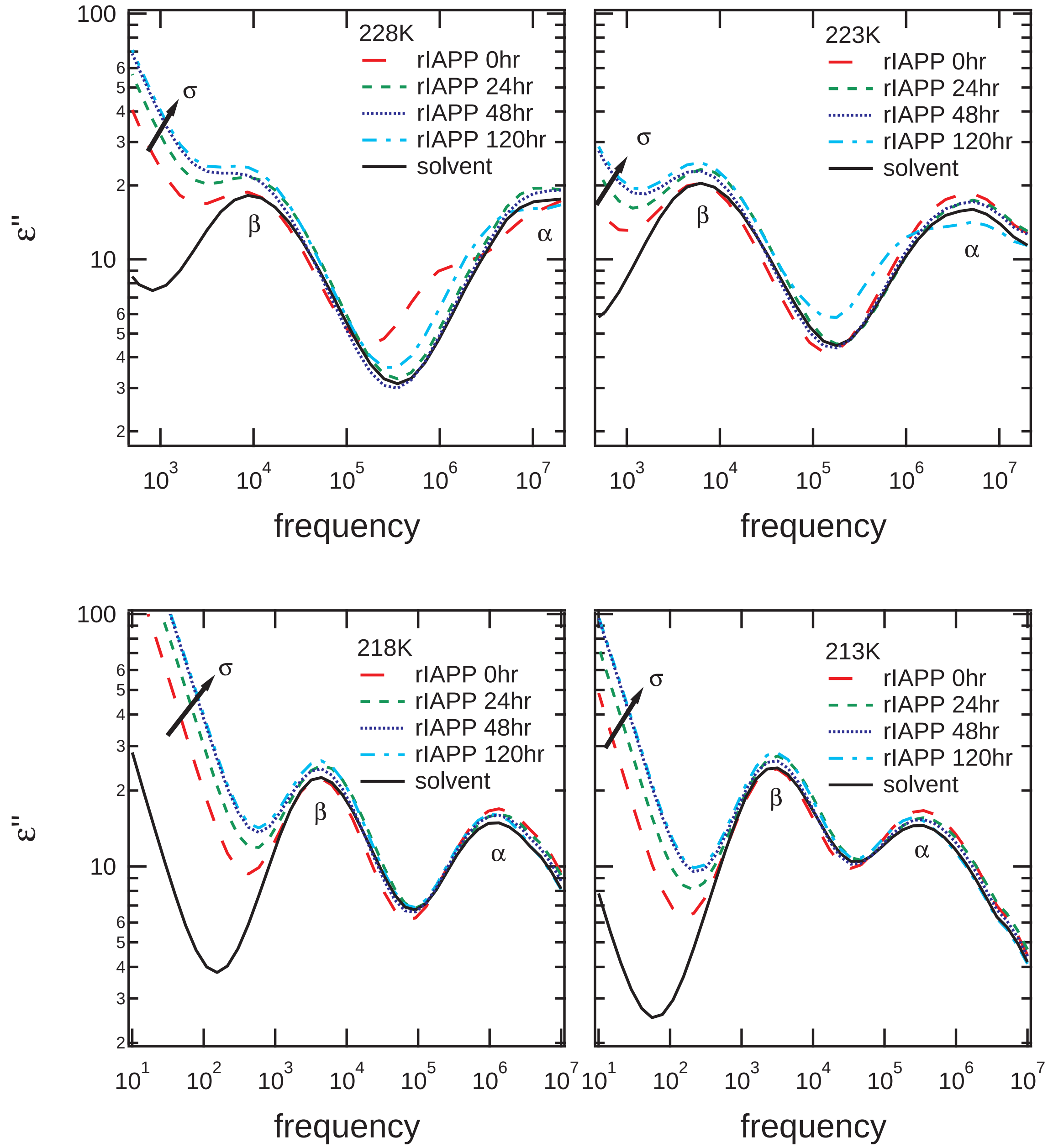

Figure 4.25: **Dielectric loss ε'' as a function of frequency for rIAPP in the range of 228K-213K and incubation periods of 0, 24, 48, and 120 hours.** The arrows show the trend of increasing conductivity over time. This was not observed with hIAPP. The apparent peak increase at the β-process is most likely the result of the change in conductivity and not a process change. There are changes observed in the α-process at 228K and 223K, but without a trend.

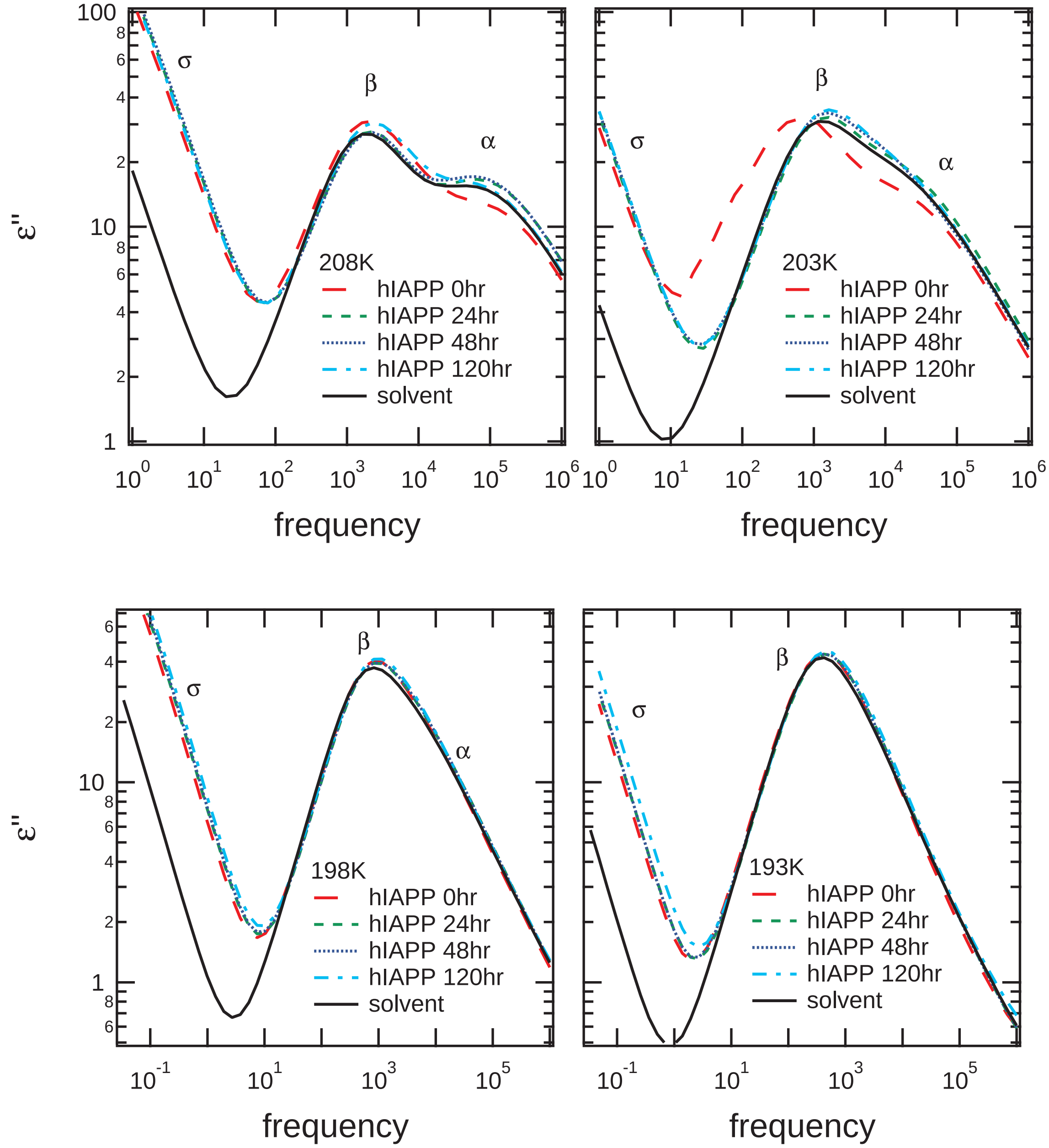

Figure 4.26: **Dielectric loss ε'' as a function of frequency for hIAPP in the range of 208K-193K and incubation periods of 0, 24, 48, and 120 hours.** At 193K, the α-process occurs at near the same frequency as the β-process but with lower magnitude. The conductivity, α-, and β-processes show a different behavior for the 0 hour time point, but it is difficult to determine a time-dependent trend.

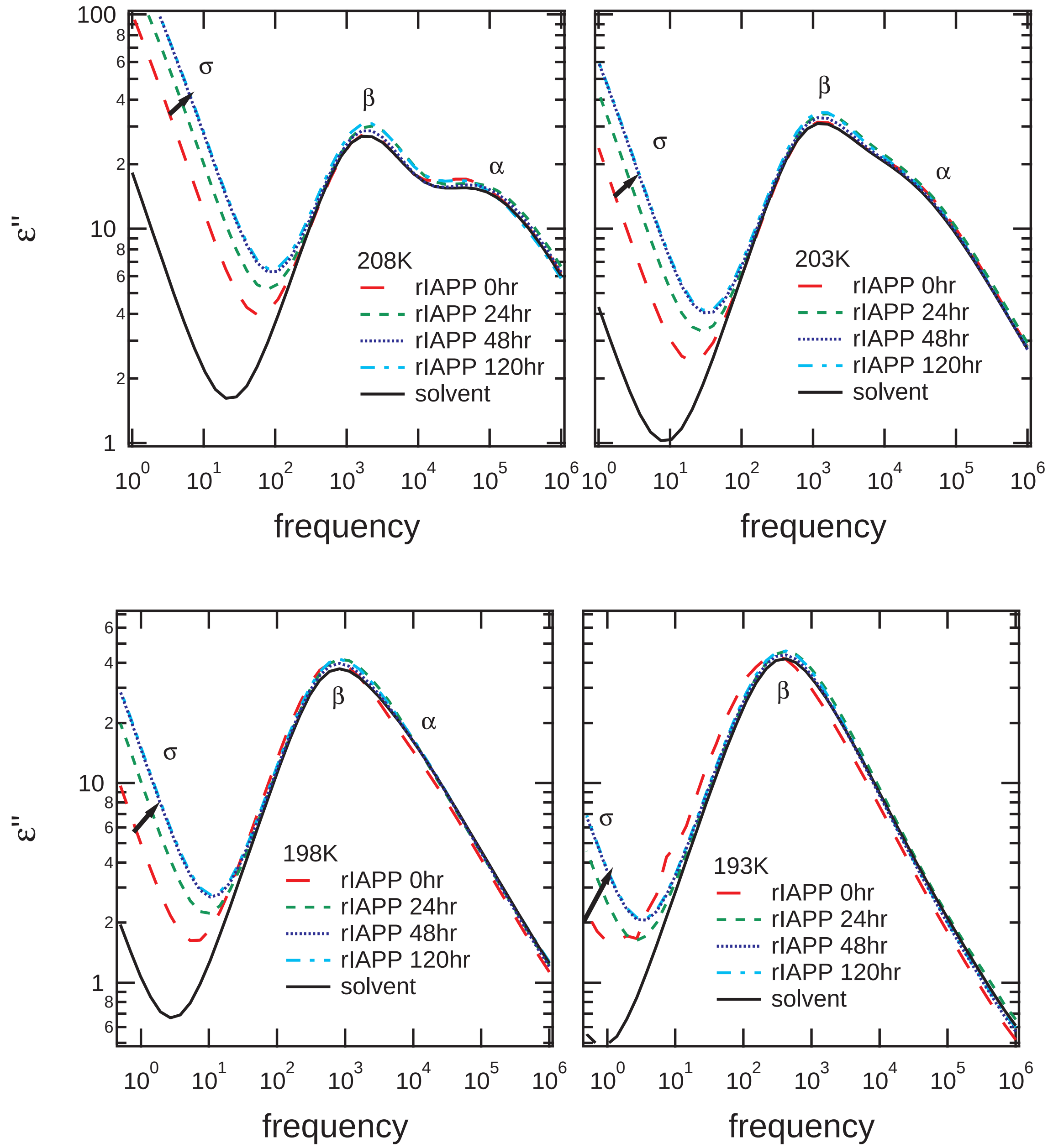

Figure 4.27: **Dielectric loss ε'' as a function of frequency for rIAPP in the range of 208K-193K and incubation periods of 0, 24, 48, and 120 hours.** At 193K, the α-process occurs at near the same frequency as the β-process but with lower magnitude. The arrows show the trend of increasing conductivity over time. This was not observed with hIAPP.

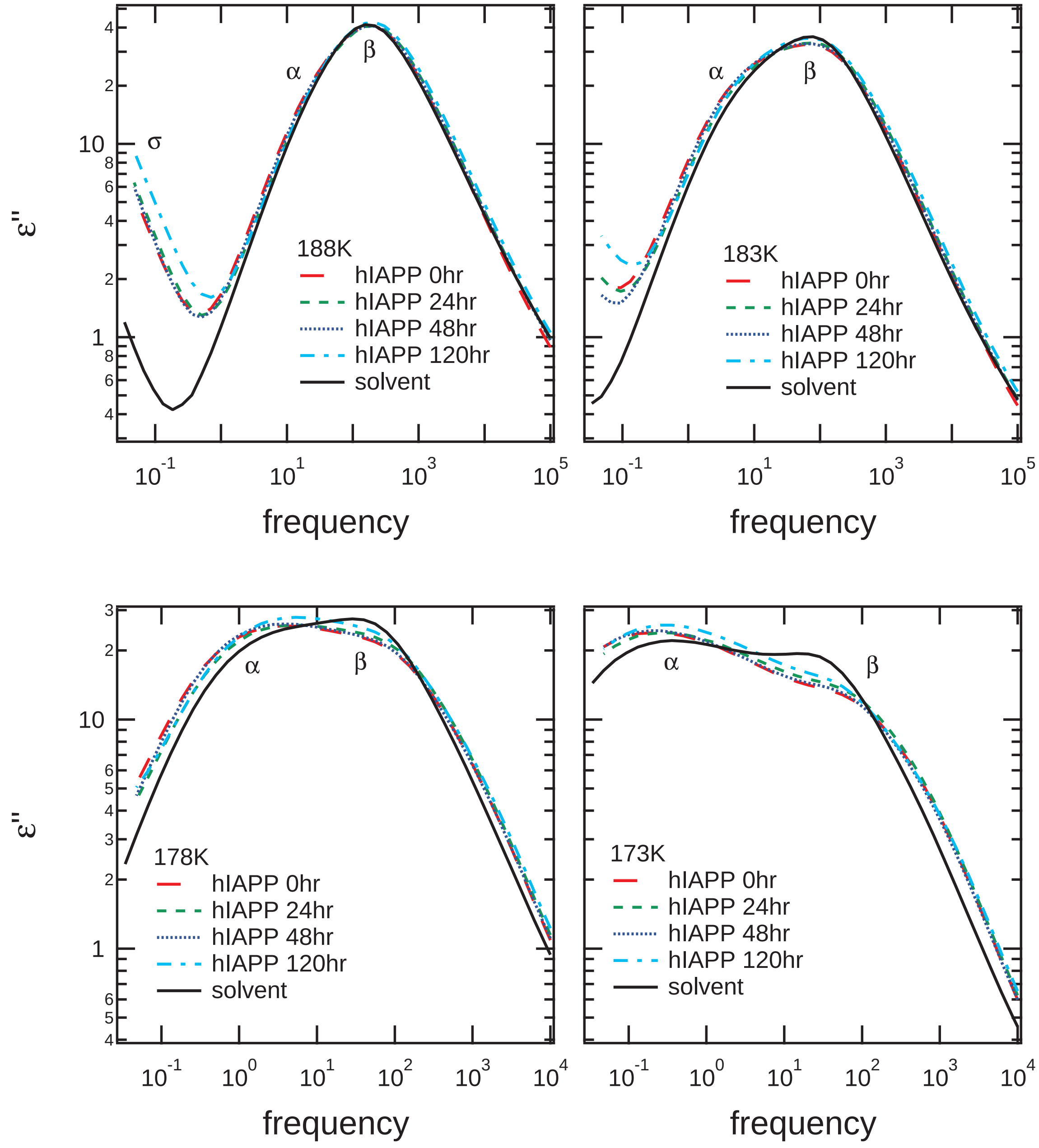

Figure 4.28: **Dielectric loss ε'' as a function of frequency for hIAPP in the range of 183K-168K and incubation periods of 0, 24, 48, and 120 hours.** The α-process has shifted to a lower frequency than the β-process. At 183K and below, the conductivity has been reduced to a point where there is little or no mixing with the processes.

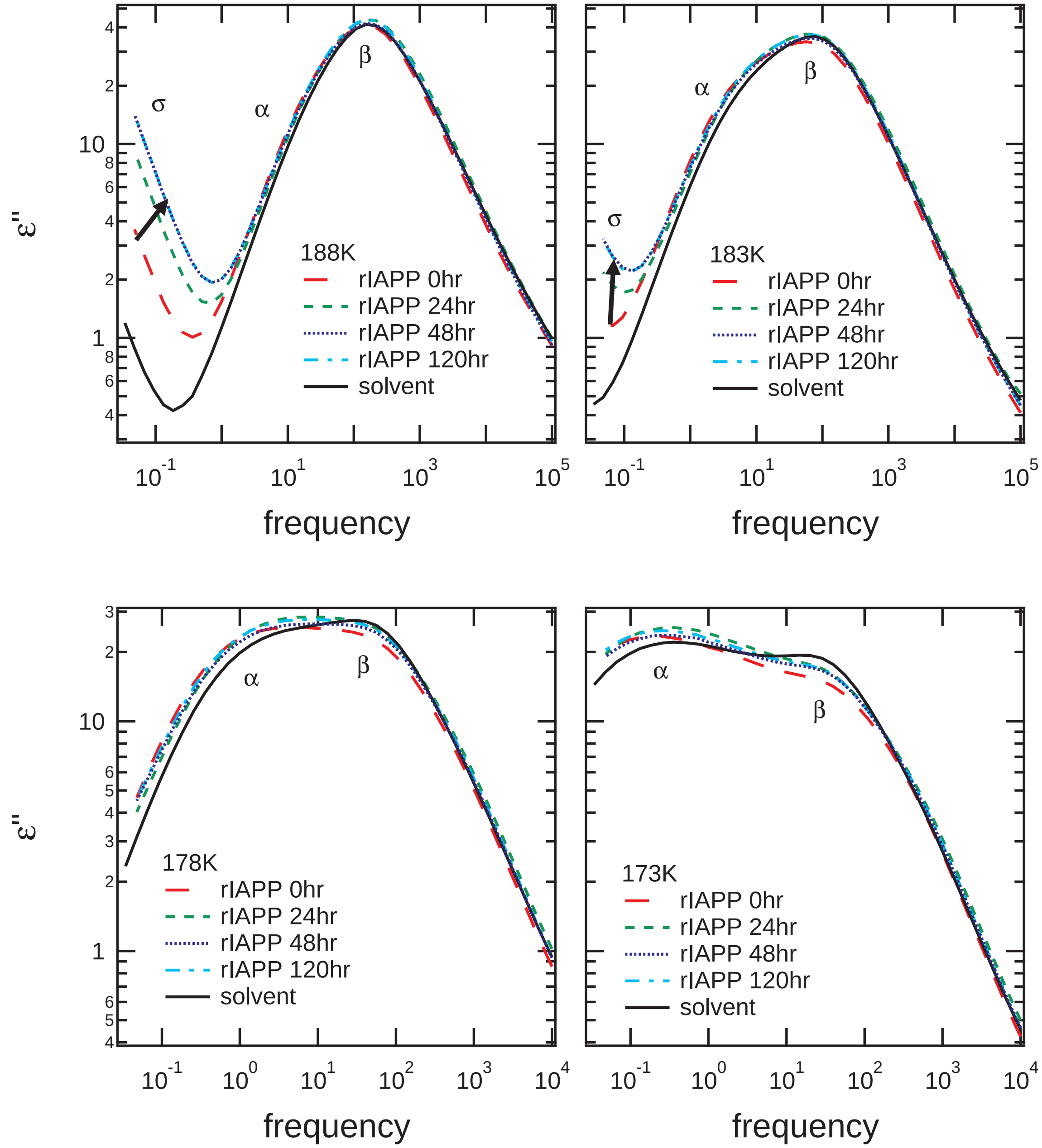

Figure 4.29: **Dielectric loss ε'' as a function of frequency for rIAPP in the range of 188K-173K and incubation periods of 0, 24, 48, and 120 hours.** The α-process has shifted to a lower frequency than the β-process. The arrows show the trend of increasing conductivity over time. This was not observed with hIAPP.

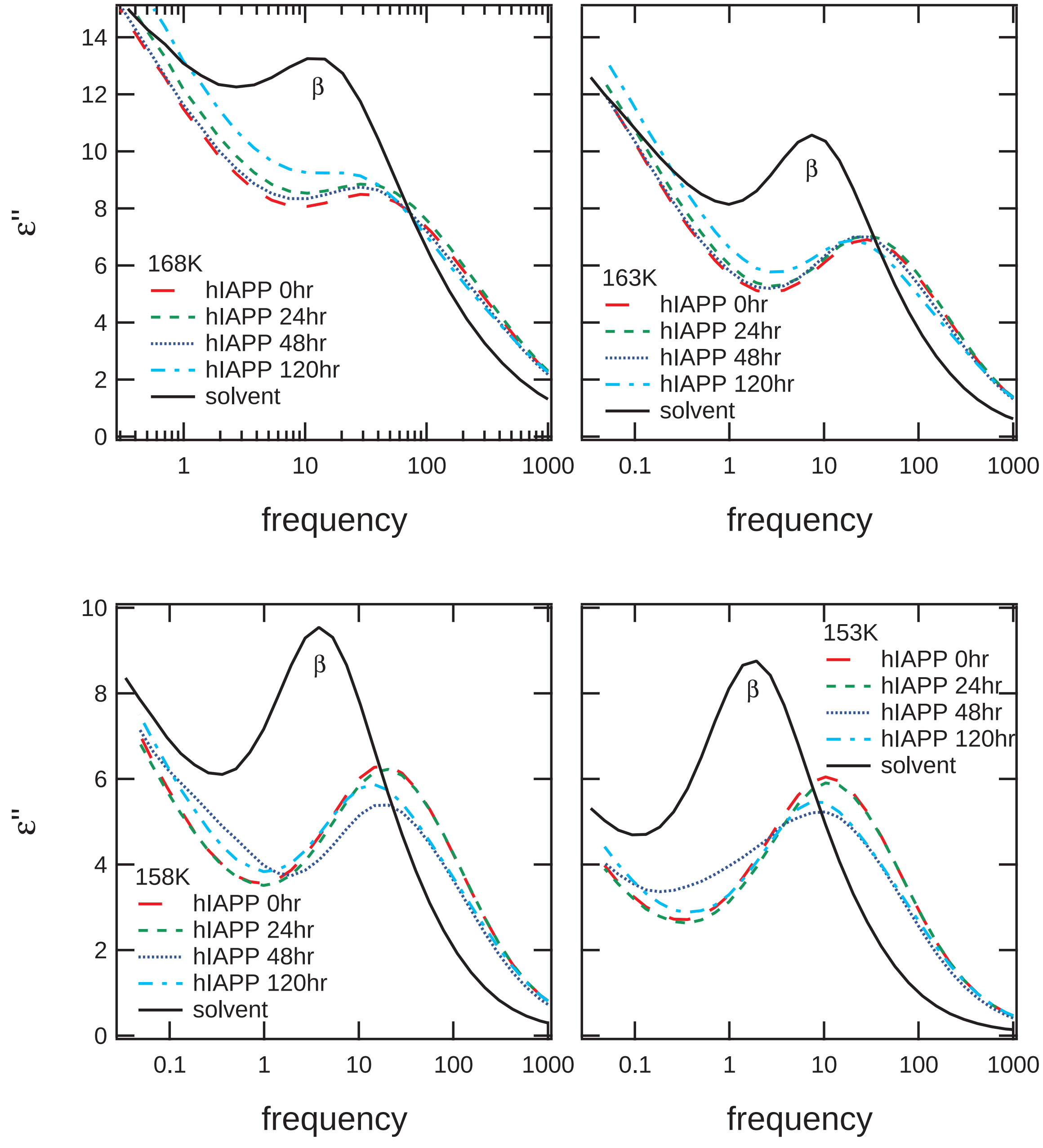

Figure 4.30: **Dielectric loss ε'' as a function of frequency for hIAPP in the range of 168K-153K and incubation periods of 0, 24, 48, and 120 hours.** Only the β-process is observed at temperatures below 168K. The peaks of hIAPP have increased in frequency by more than a decade as compared to the solvent. The peaks have shifted to lower magnitude and frequency over time.

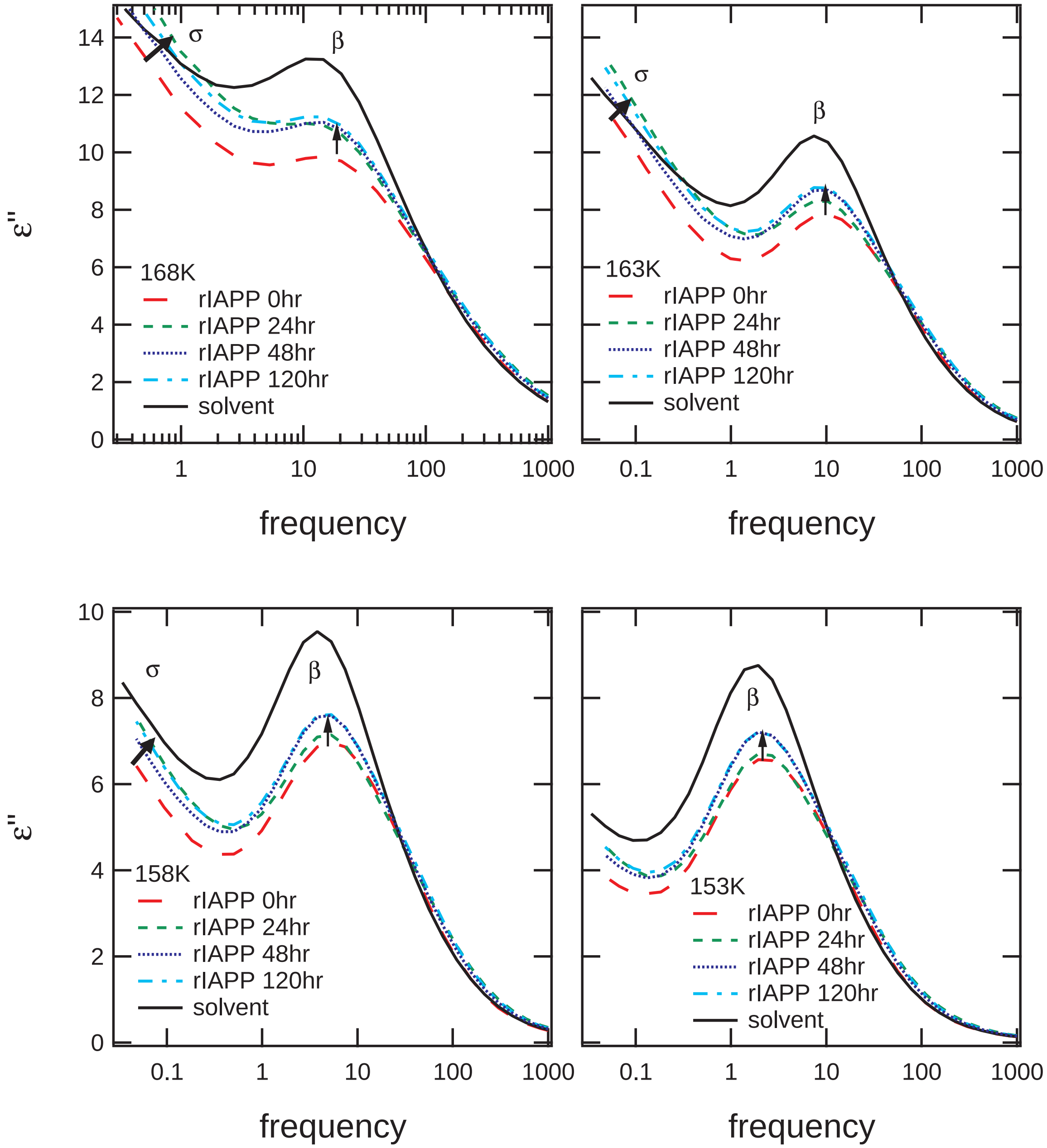

Figure 4.31: **Dielectric loss ε'' as a function of frequency for rIAPP in the range of 168K-153K and incubation periods of 0, 24, 48, and 120 hours.** Only the β-process is observed at temperatures below 158K. The arrows show that the conductivity increases and the β-process peaks shift to higher magnitude over time. This opposite the behavior of hIAPP in the same temperature range. There is no increase in frequency at t = 0hr, where hIAPP displayed a decade shift. The shift in peak position at 168K and 163K may be due to conductivity.

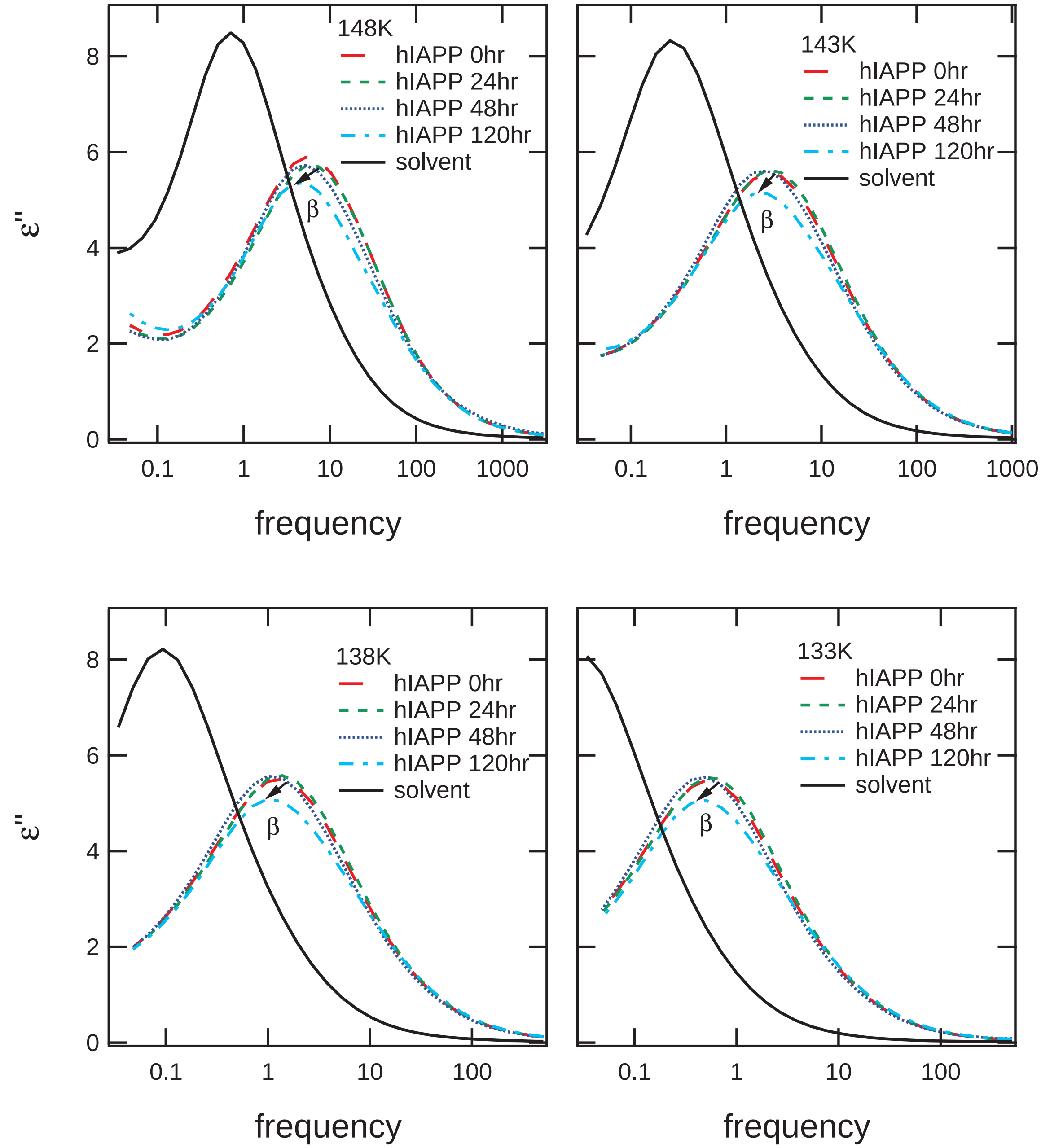

Figure 4.32: **Dielectric loss ε'' as a function of frequency for hIAPP in the range of 148K-133K and incubation periods of 0, 24, 48, and 120 hours.** The arrows depict that the β-process of hIAPP shifts to lower frequency and lower magnitude over time.

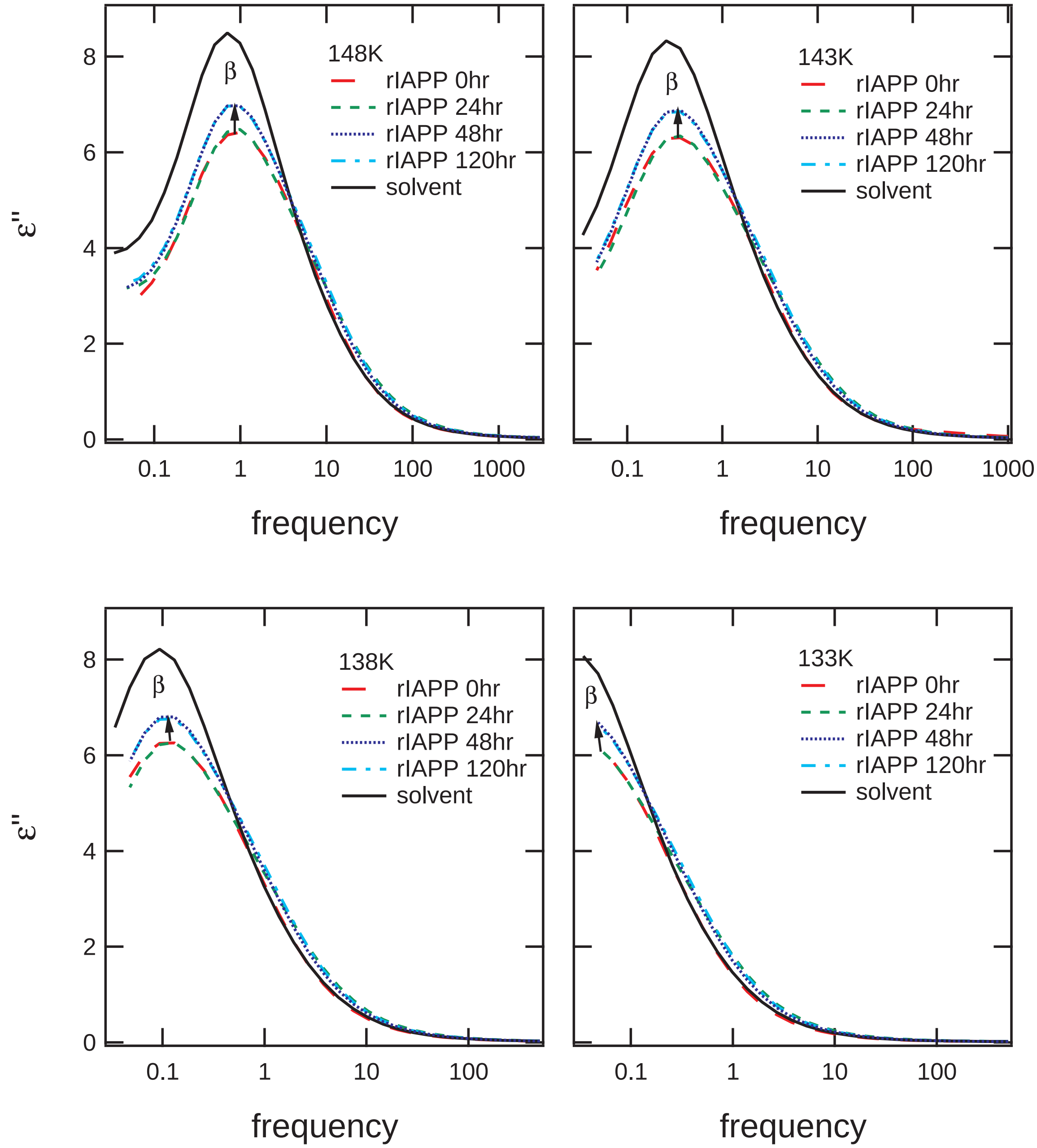

Figure 4.33: **Dielectric loss ε'' as a function of frequency for rIAPP in the range of 148K-133K and incubation periods of 0, 24, 48, and 120 hours.** The arrows depict that the β-process of rIAPP shifts to lower frequency and higher magnitude over time. This opposite the behavior of hIAPP in the same temperature range.

Dielectric permittivity data for hIAPP, rIAPP, and the solvent were modeled using the WinFIT program for each temperature from 223K to 133K and at incubation time points 0, 24, 48, and 120 hours. The β-relaxation process was best fit to a Cole-Davidson function with the β fit parameter remaining relatively constant over the entire temperature range at approximately 0.8. The α-relaxation process demonstrates both symmetric and asymmetric broadening over the observed temperature range with both β and γ spreading parameters changing with temperature.

The α-relaxation process is observed from 223K to 168K, though in the crossing temperatures of 198K to 183K, it overlaps with the β-process. During this temperature range, the β-relaxation process dominates. The β-relaxation process is observed between approximately 208K down to the lowest temperature, 133K. At temperatures above 208K, the DC conductivity dominates the spectra in the region of the β-relaxation. Examples of curve fitting performed at representative temperatures are shown in Figures 4.34 - 4.37.

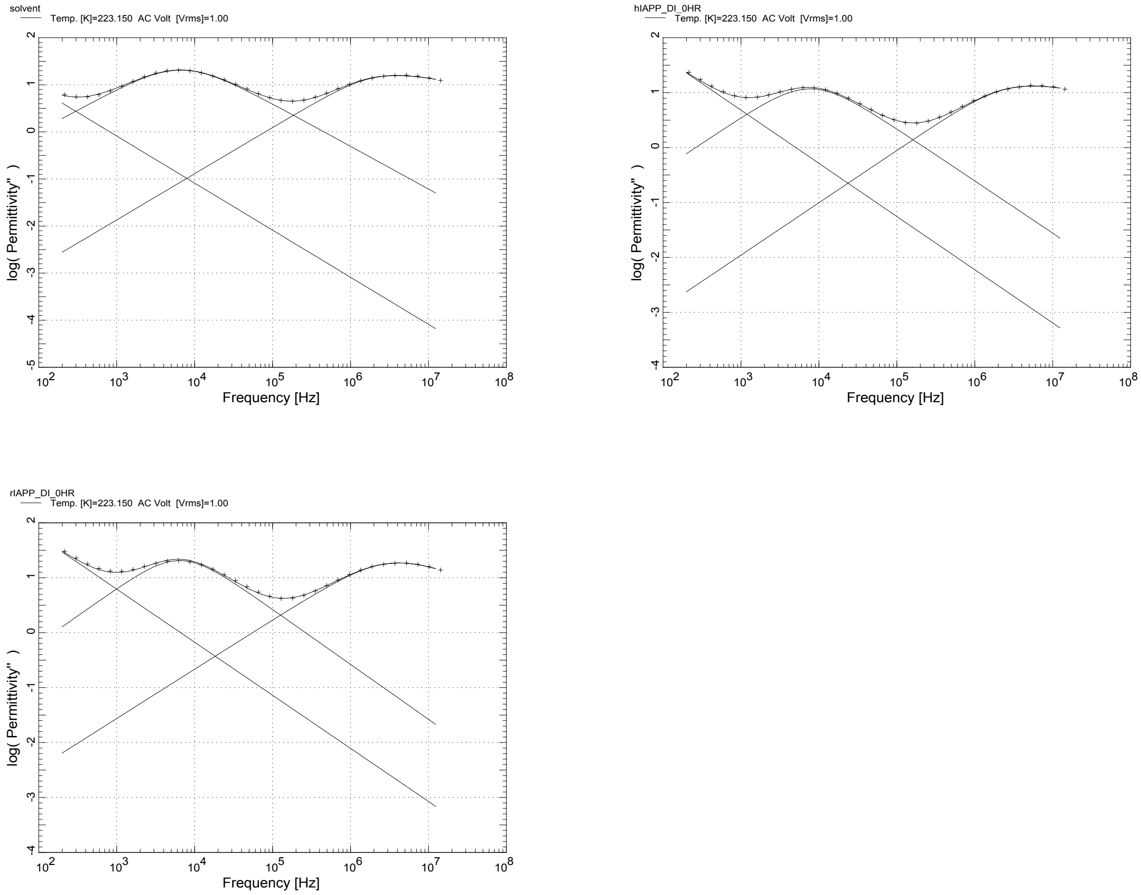

Figure 4.34: **Curve fitting of imaginary part of the permittivity data using the WinFIT program of the solvent, hIAPP, and rIAPP at 223K.** A large, low frequency DC conductivity is fit with a power law. The α-relaxation process at around 10^7 Hz is fit with a Havriliak-Negami function and the β-relaxation function is not observed. The RMSD of the fits are 0.015, 0.005, and 0.016, respectively.

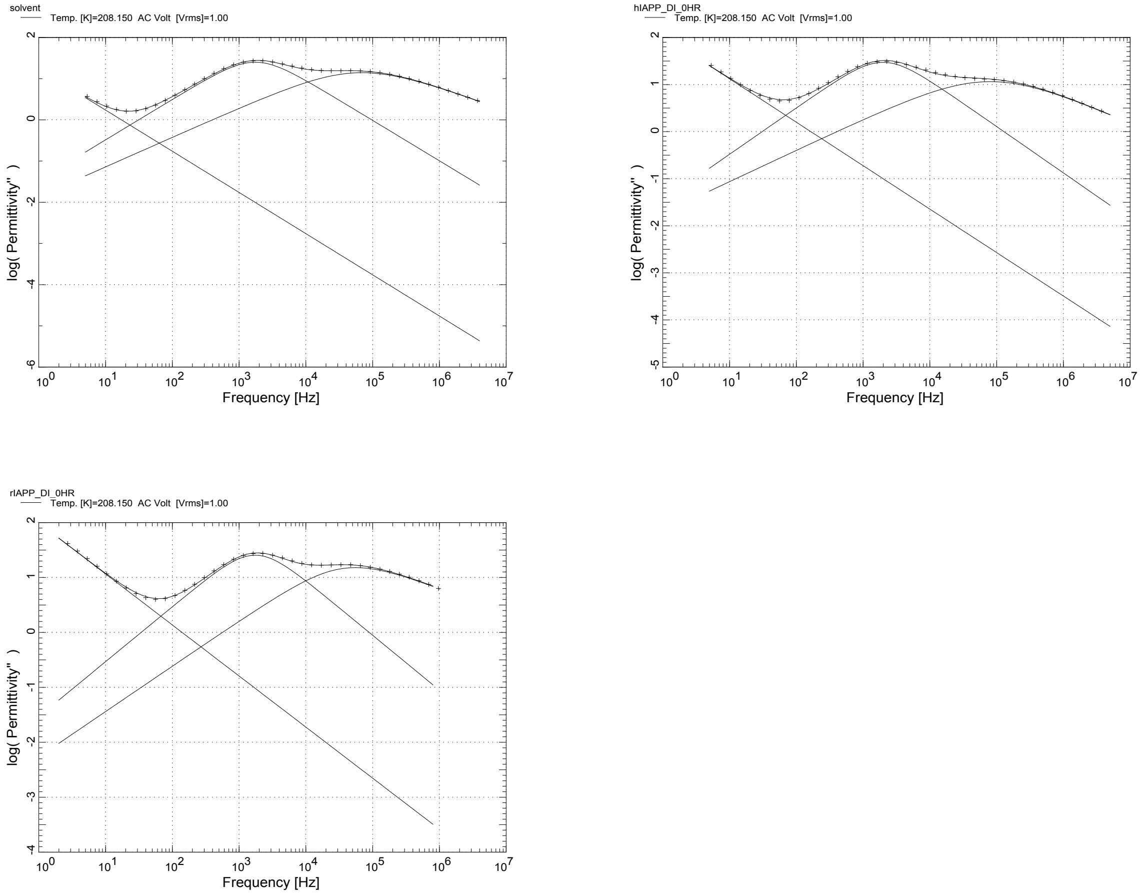

Figure 4.35: **Curve fitting of imaginary part of the permittivity data using the WinFIT program of the solvent, hIAPP, and rIAPP at 208K.** A large, low frequency DC conductivity is fit with a power law. The β-relaxation process at around 10^3 Hz is fit with a Cole-Davidson function and the α-relaxation process at around 10^5 Hz is fit with a Havriliak-Negami function. The RMSD of the fits are 0.027, 0.013, and 0.010, respectively.

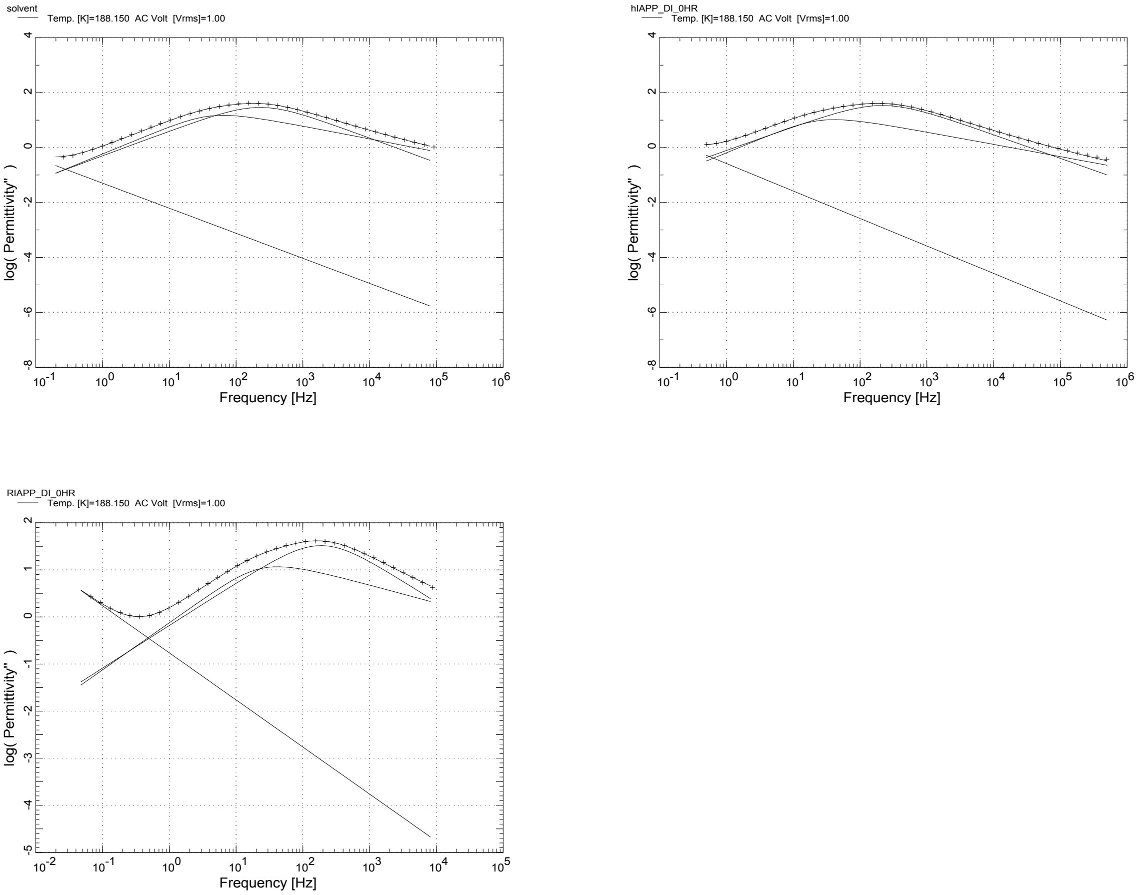

Figure 4.36: **Curve fitting of imaginary part of the permittivity data using the WinFIT program of the solvent, hIAPP, and rIAPP at 188K.** A large, low frequency DC conductivity is fit with a power law. The β-relaxation process at around 10^3 Hz is fit with a Cole-Davidson function and the α-relaxation process at around 10^1 Hz is fit with a Havriliak-Negami function. Here, the α process has crossed over to slower than β relaxation times. The RMSD of the fits are 0.012, 0.004, and 0.043, respectively.

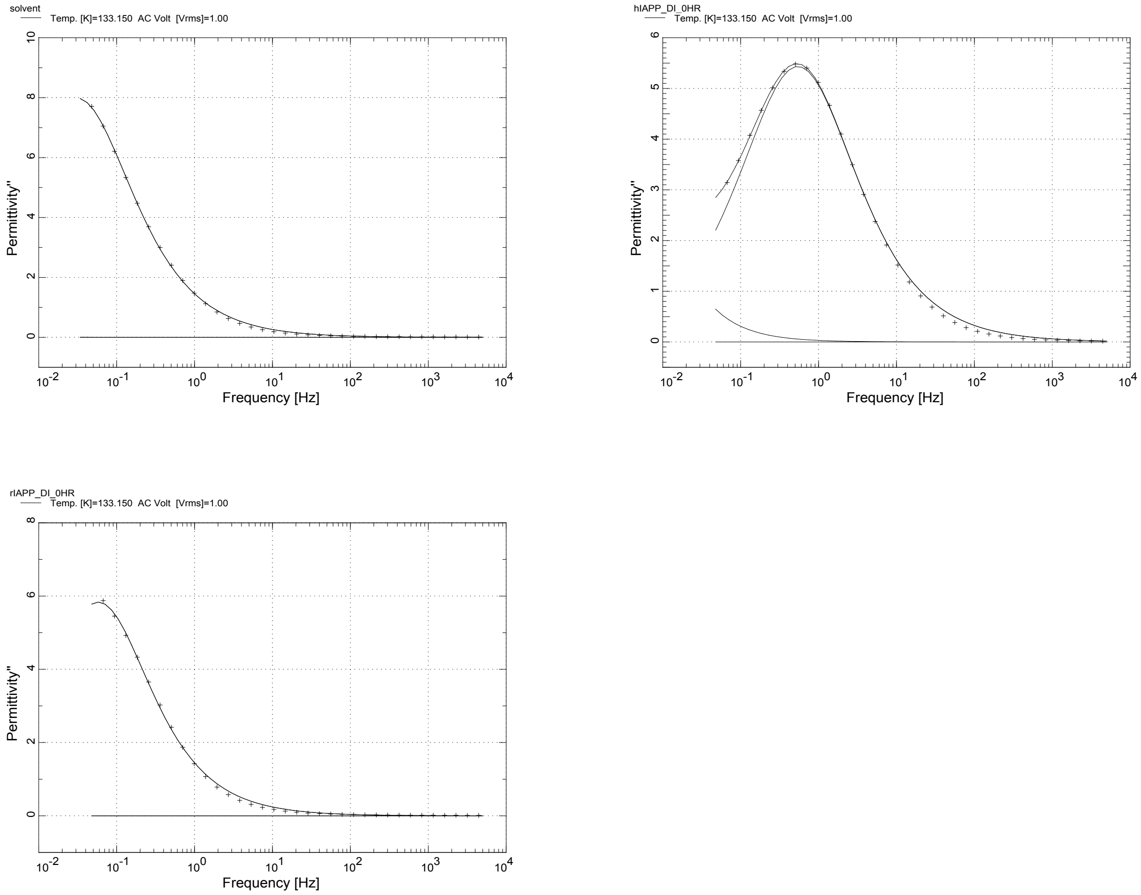

Figure 4.37: **Curve fitting of the imaginary part of the permittivity data using the WinFIT program of the solvent, hIAPP, rIAPP at 133K.** A small, very low frequency DC conductivity is fit with a power law. The β-relaxation process at around 1 Hz is fit with a Cole-Davidson function and the α-relaxation process is not observed. The RMSD of the fits are 0.169, 0.080, and 0.054, respectively.

The maximum frequency, f_{max} of ε'' of both the α- and β-relaxation processes were determined from the model function curve fitting of the permittivity data at all temperatures. Arrhenius plots of f_{max} versus inverse temperature, 1000/T were created for each process. The β-relaxation process follows a linear, or Arrhenius behavior throughout the temperature range. The α-relaxation process follows a slight non-linear Vogel-Fulcher-Tammann (VFT)-type behavior that is expected in glass-forming solvents such as glycerol (Figures 4.38 - 4.40). Activation energies for the β process and glass-forming fragilities for the α process were determined from the Arrhenius and VFT analysis and displayed in Tables 4.3 and 4.4. The activation energies for hIAPP matches the value of 24.4 kJ/mol obtained by Knowles et al. from measurements using the quartz crystal microbalance (QCM) method [155].

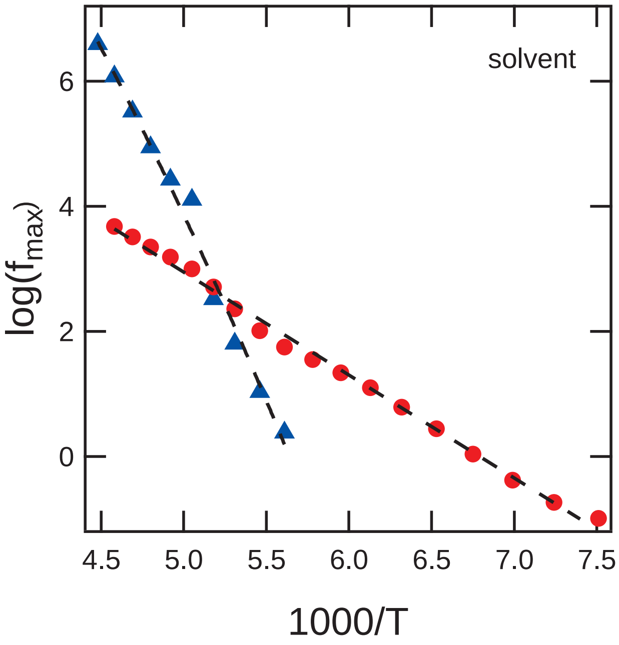

Figure 4.38: **Arrhenius plots of f_{max} versus inverse temperature for solvent over time.** The α-relaxation process follows a VFT behavior whereas the β-relaxation process follows an Arrhenius, or linear behavior.

The structure of hIAPP has been shown by FTIR and NMR to display both parallel and anti-parallel β-sheets [156, 157]. Figure 4.41 shows that over time, hIAPP displayed a series of increases and decreases in the dielectric strength as fibril

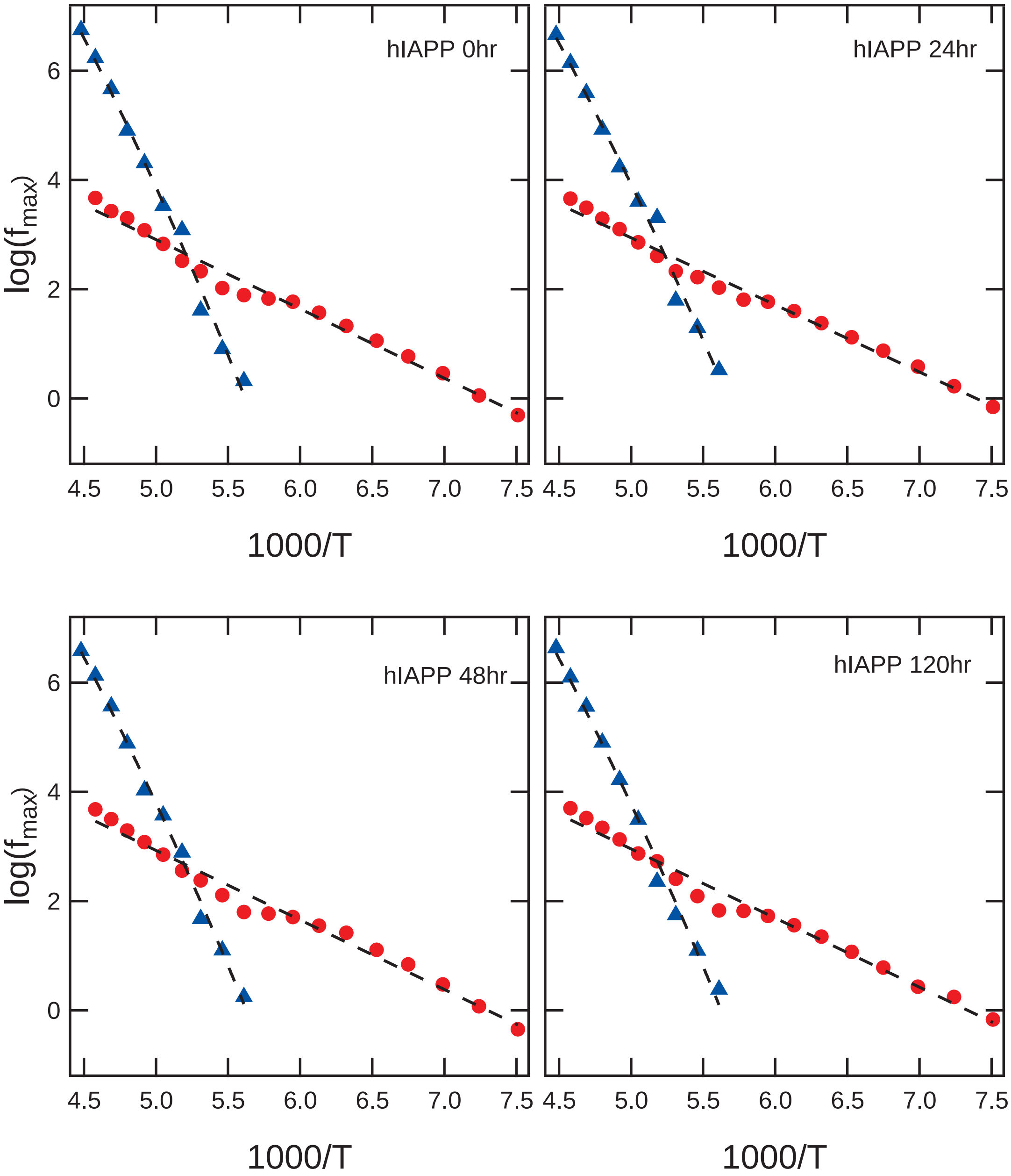

Figure 4.39: **Arrhenius plots of f_{max} versus inverse temperature for hIAPP from 0-120 hours.** The α-relaxation process follows a VFT behavior whereas the β-relaxation process follows an Arrhenius, or linear behavior. The α-process departs from the VFT curvature at low temperature.

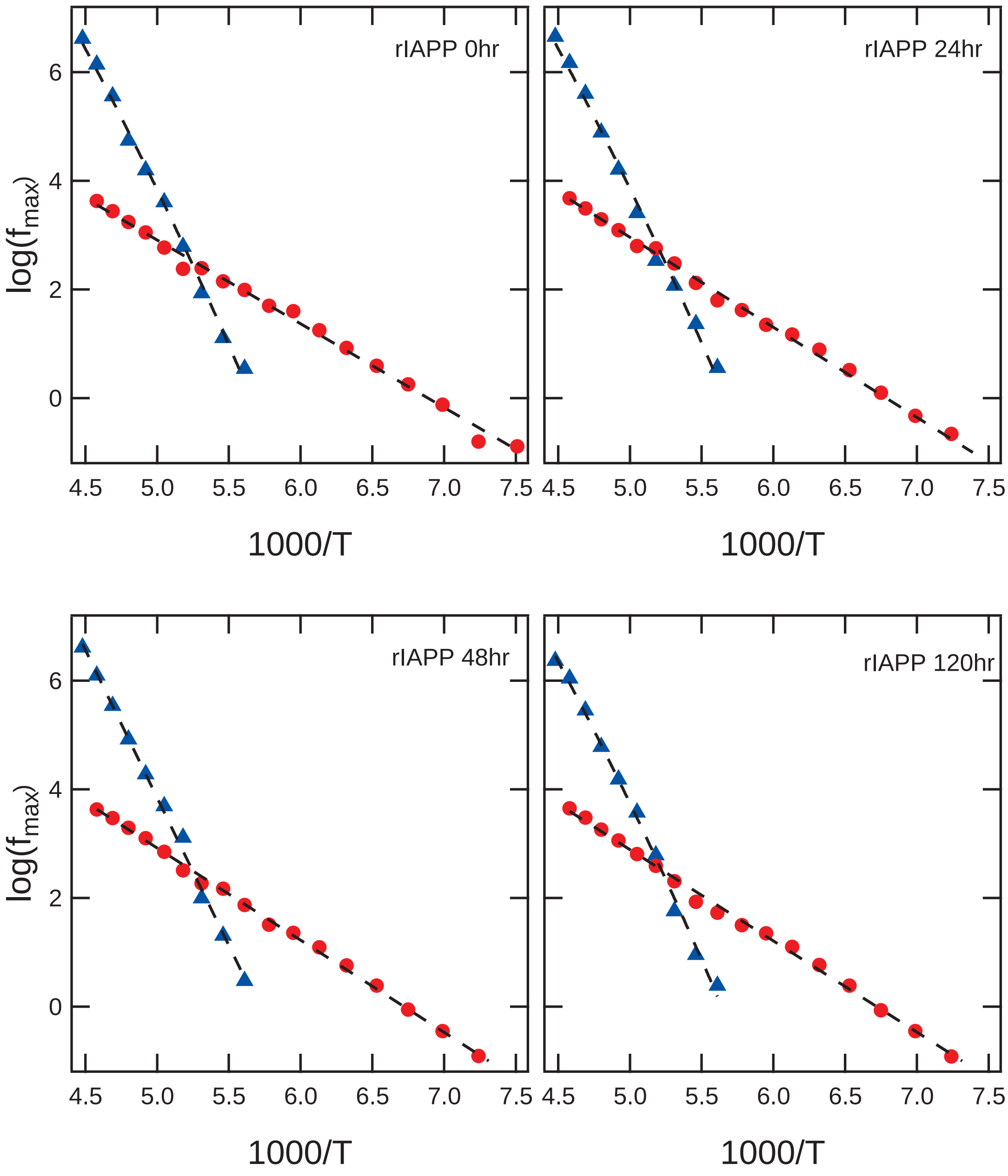

Figure 4.40: **Arrhenius plots of f_{max} versus inverse temperature for rIAPP from 0-120 hours.** The α-relaxation process follows a VFT behavior whereas the β-relaxation process follows an Arrhenius, or linear behavior. The α-process departs from the VFT curvature at low temperature.

	time	A	B	E_A (kJ/mol)		*time*	A	B	E_A (kJ/mol)
hIAPP	0hr	9.25	1.269	24.3	rIAPP	0hr	10.62	1.541	29.5
	24hr	9.09	1.229	23.5		24hr	11.3	1.658	31.7
	48hr	9.29	1.273	24.4		48hr	11.4	1.696	32.4
	120hr	9.28	1.266	24.2		120hr	11.3	1.680	32.2
solvent		11.2	1.646	31.5	solvent		11.2	1.646	31.5

Table 4.3: Parameters of the linear fits to the β-relaxation measurements of $\log(f_{max}(T))$ of the form $A + BT$.

	time	$\log f_\infty$	D	T_0 (K)		*time*	$\log f_\infty$	D	T_0 (K)
hIAPP	0hr	22	30	75	rIAPP	0hr	22	36	67
	24hr	22	36	67		24hr	22	37	66
	48hr	22	33	71		48hr	22	37	66
	120hr	22	34	70		120hr	22	37	67
solvent		22	33	70	solvent		22	33	70

Table 4.4: Parameters of the VFT fits to the α-relaxation measurements of $f_{max}(T)$ of the form $\log(f_{max}) = \log(f_\infty(T)) - \frac{DT_0}{T-T_0}$

formation progresses, whereas the non-amyloidogenic rIAPP increased consistently over time. The increase and decrease cycles for hIAPP may be due to a mixture of both parallel and anti-parallel β-sheet conformations dominating at different phases of the aggregation process. The continuing increase of dipole moment for random-coil aggregation is an explanation for the increasing dielectric strength in rIAPP.

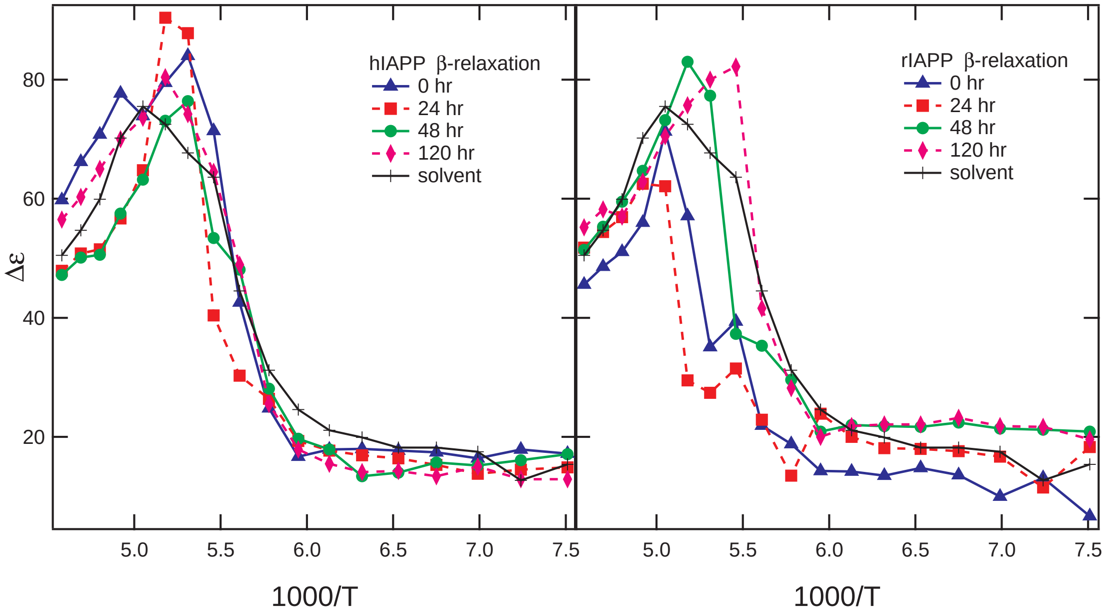

Figure 4.41: **Dielectric strength, $\Delta\varepsilon$ of the β-relaxation for hIAPP and rIAPP versus inverse temperature.** The dielectric strength for the hIAPP solution first increases, then deceases to values less than the solvent. The dielectric strength of rIAPP continued to increase over time. This indicates a mixed grouping of parallel and anti-parallel β-sheets in hIAPP and random-coil aggregation in rIAPP.

4.4 Conclusions

We have demonstrated the dielectric response of $A\beta_{1-42}$, scrambled $A\beta_{42-1}$, hIAPP, and rIAPP in the presence of a deionized water-glycerol solvent. The spectra reveal that these amyloidogenic peptides in their in purified form can be detected and differentiated from their non-amyloidogenic analogs using dielectric relaxation spectroscopy.

Studies at low temperature reveal that the β-process displays a decrease in the dielectric loss, ε'' for both amyloidogenic $A\beta_{1-42}$ and hIAPP and an increase for non-amyloidogenic $A\beta_{42-1}$ and rIAPP. This may point to an increase in fraction of structured water over time associated with the amyloidogenic peptides during β-sheet formation. The trend observed in the non-amyloidogenic peptides reflects that a random aggregation lacks the large fraction of structured water that is contained in a organized β-sheet.

It is notable that the scrambled $A\beta_{42-1}$ increased in ε'' beyond the solvent. This may be a result of the dissociated ions from the NH_4OH solution contributing to the overall dielectric strength. This would probably also be the case with $A\beta_{1-42}$, which may be the cause of such a small shift in ε'' compared to the other peptides. This may also be the reason why there is only a small frequency shift with $A\beta_{1-42}$ where the shift in hIAPP is quite large (2 decades) as compared to the solvent and rIAPP.

To demonstrate agreement with the measurement method and the fitting functions, data analyses of pure glycerol and 50% by weight glycerol-water are presented in Figure 4.43 in comparison with results from the literature. The α-relaxation times of pure glycerol is in agreement with data from Sudo et al. [158] and Kremer [63]. Relaxation times of both α- and β-relaxations for glycerol-water mixtures of 45% (Jansson) [142] and 47% (Hayashi) [78] are in close agreement with our data for 50% glycerol.

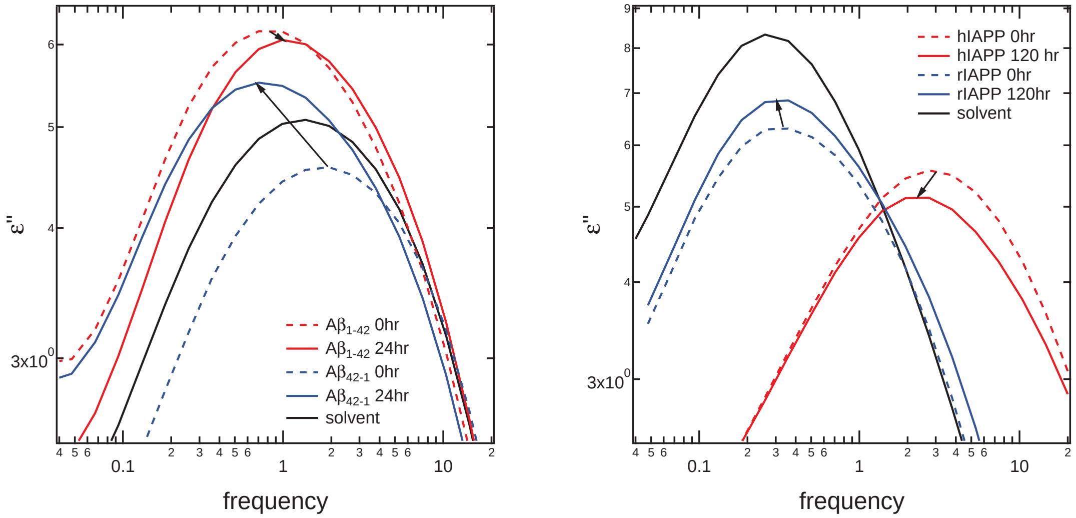

Figure 4.42: Plots of the β-relaxation peak shift at 143K for $A\beta_{1-42}/A\beta_{42-1}$ and hIAPP/rIAPP as compared to the solvent.

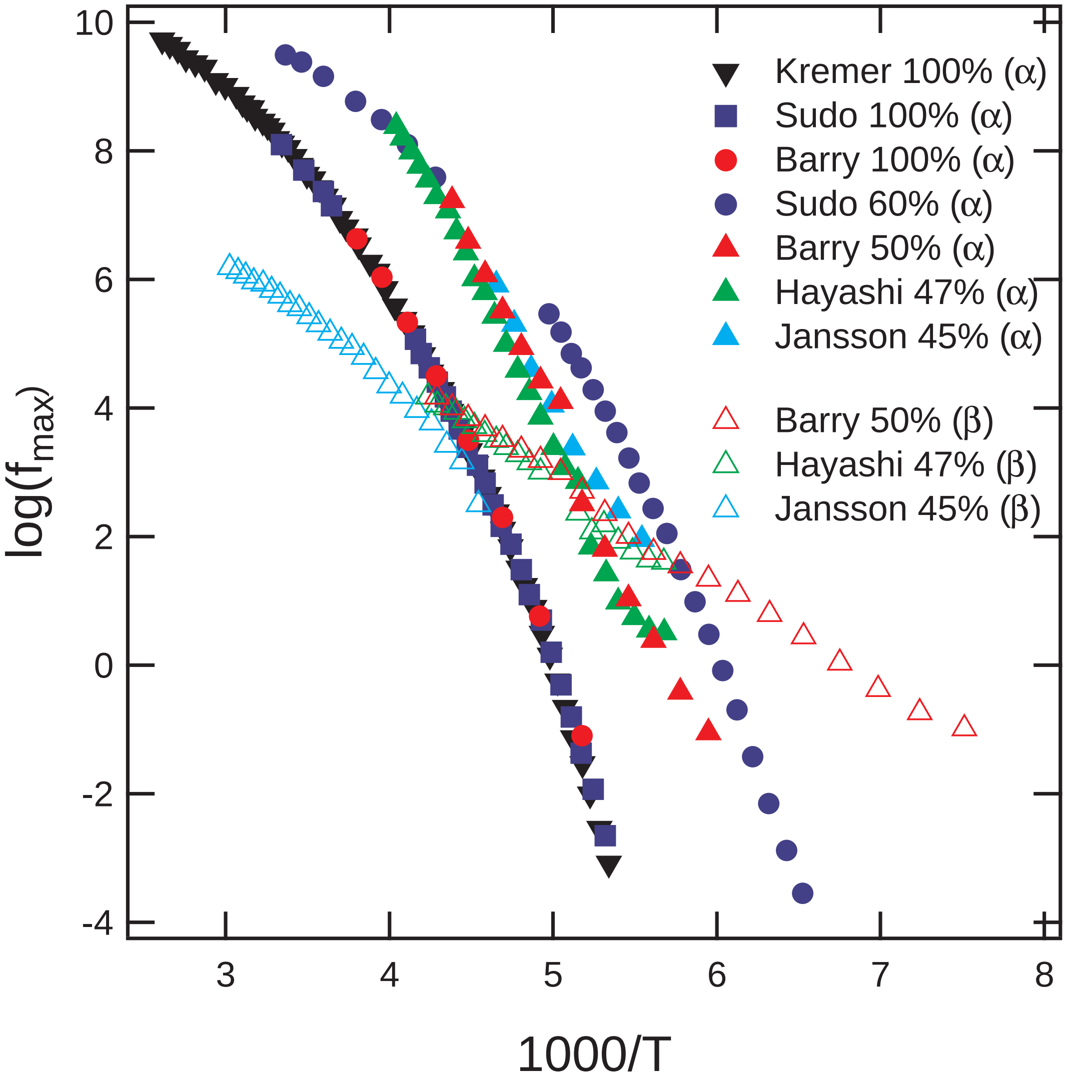

Figure 4.43: **Arrhenius plots of f_{max} versus inverse temperature for pure glycerol and glycerol-water mixtures of approximately 50-50% by weight [63, 158, 142, 78].** The glycerol-water mixtures display both α- and β-relaxation processes. Only the α process appears in pure glycerol.

In Table 4.5, we present activation energies from a selection of small, aggregating peptides in solution. These include silk fibroin [130], $A\beta_{1-40}$ [149], chymotrypsin inhibitor 2 (CI2) [149, 159], phage λ repressor [149, 160, 161], SH3 domain of spectrin [149, 162, 163], the C-terminal fragment(4156) from protein GB1 [149, 164], and insulin [155]. Interestingly, the activation energies for these peptides are within the same order of magnitude, yet each have a distinctive value.

peptide	E_A (kJ/mol)	structure
silk fibroin	27	α,β
$A\beta_{1-40}$	23	β
CI2	31.2	α,β
λ repressor	16.1	α
SH3	9.5	β
GB1	11.6	β-hairpin
insulin	24.4	β

Table 4.5: Activation energies for various small, aggregating peptides

Studies of the dielectric strength over a range of temperatures and incubation times show that determination of β-sheet conformation by dielectric spectroscopy is in agreement with previous studies done using FTIR and solid state NMR. The $A\beta_{1-42}$ displayed anti-parallel characteristics and the hIAPP displayed both parallel and anti-parallel signatures. The non-amyloidogenic peptides produced dipole moments that would be consistent with random coil or non-aggregating proteins.

The use of deionized water as a buffer is informative in that the amount of interfering substances is kept at a minimum. However, deionized water is not representative of native fluids that harbor amyloidogenic peptides. A continuation of this work in bovine serum albumin (BSA) will aid in simulation of more *in vivo*-like conditions. This also may provide a more favorable environment for aggregation and bring the analysis closer to realistic, diagnostic conditions. Additionally, exclusion of NH_4OH in the study of $A\beta_{1-42}$ and scrambled $A\beta_{42-1}$ should be explored.

Chapter 5

Dielectric Studies of Amyloidogenic Peptides in BSA Buffer at Low Temperature

5.1 Overview

In the previous chapter we demonstrated that amyloidogenic peptides $A\beta_{1-42}$ and hIAPP have differentiating dielectric response than that of their non-amyloidogenic analogs in the presence of deionized water-glycerol buffer. Amyloidogenic peptides *in vivo* are naturally found suspended in biological fluids, such as serum. Complex biologic fluids, such as serum contain a number of substances including proteins, electrolytes, hormones, and antibodies that will each have their own interaction with a dielectric signal.

In this chapter, dielectric spectroscopy data and analysis is presented for the same two amyloidogenic peptides and their non-amyloidogenic analogs in a bovine serum albumin (BSA) buffer. BSA was chosen as a buffer to demonstrate dielectric measurements in the presence of heterogenous fluid that simulates *in vivo*-like conditions.

Measurements were performed from room temperature down to cryogenic temperature in order to study relaxation kinetics. Trends of dielectric spectra as a function of incubation time and temperature are explored within.

5.2 Sample Preparation and Data Collection

Lyophilized peptides were obtained from AnaSpec, Inc in quantities of 0.5 mg and 1.0 mg. The vials were stored at approximately -20°C until the time of reconstitution. Bovine serum albumin (BSA) from Sigma was used to dilute and rehydrate the peptides to a concentration of approximately 100μM. The samples were then mixed by repeated inversion of the vials and set to incubate for 0, 8, 24, 48, or 120 hours at room temperature in a 2mL sterile microconical tube. A separate sample was prepared for each time point. Glycerol, 99% minimum from Sigma was then added to a final concentration of 50μM peptide in 50%-50% by weight BSA-glycerol solvent. The samples were again mixed by repeated inversion of the vials. Each sample was then placed in the Novocontrol BDS 1307 stainless steel sample cell.

Data were collected using the Novocontrol Alpha-A Analyzer and Quatro Cryosystem in gain phase measurement mode with an AC probing voltage of 1.000 V_{RMS}. A liquid nitrogen cryostat was used to control temperature from 283K down to 133K at 5K intervals. We selected 60 data points in a frequency range from $2.00 \times 10^7 - 4.78 \times 10^{-2}$ Hz, spaced evenly in a logarithmic scale. Data for each temperature point was collected in duplicate to ensure temperature stabilization and mitigate thermal hysteresis. The second, temperature stabilized duplicates were used for analysis.

5.3 Results and Discussions

5.3.1 Studies of $A\beta_{1-42}$ and Scrambled $A\beta_{42-1}$

The dielectric spectra of $A\beta_{1-42}$, scrambled $A\beta_{42-1}$, and the solvent shows two relaxation processes (α and β) and low-frequency DC conductivity below 223K, depicted in Figure 5.1. At temperatures above 223K, the relaxation processes are either at frequencies above the range of the Alpha-A Analyzer or the conductivity dominates the spectra. The fast, α-relaxation process is clearly observed at 223K at a frequency of approximately 10^7 Hz in both the real and imaginary parts of the permittivity. The slower β-relaxation process is not easily observed until about 208K or 203K in the imaginary part of the permittivity but can be seen in the real part at 223K. At 203K, we determine that the β-relaxation occurs at 10^3 Hz and we estimate that it occurs at approximately 10^4 Hz at 223K.

With decreasing temperature the peaks of the α- and β-relaxation processes shift towards lower frequency. The α-process shifts faster than the β-process causing the two processes to merge below 203K and eventually cross at approximately 193K as shown in Figure 5.2. The α-process continues to shift to very low frequencies with decreasing temperature. At around 168K the α-process shifts to frequencies higher than our measured range. After the crossing of the two processes, the β-relaxation process dominates the dielectric spectra and shifts to approximately 1 Hz at 133K (Figure 5.3). Below 158K, the DC conductivity has decreased in magnitude and also shifted to frequency below the measured range.

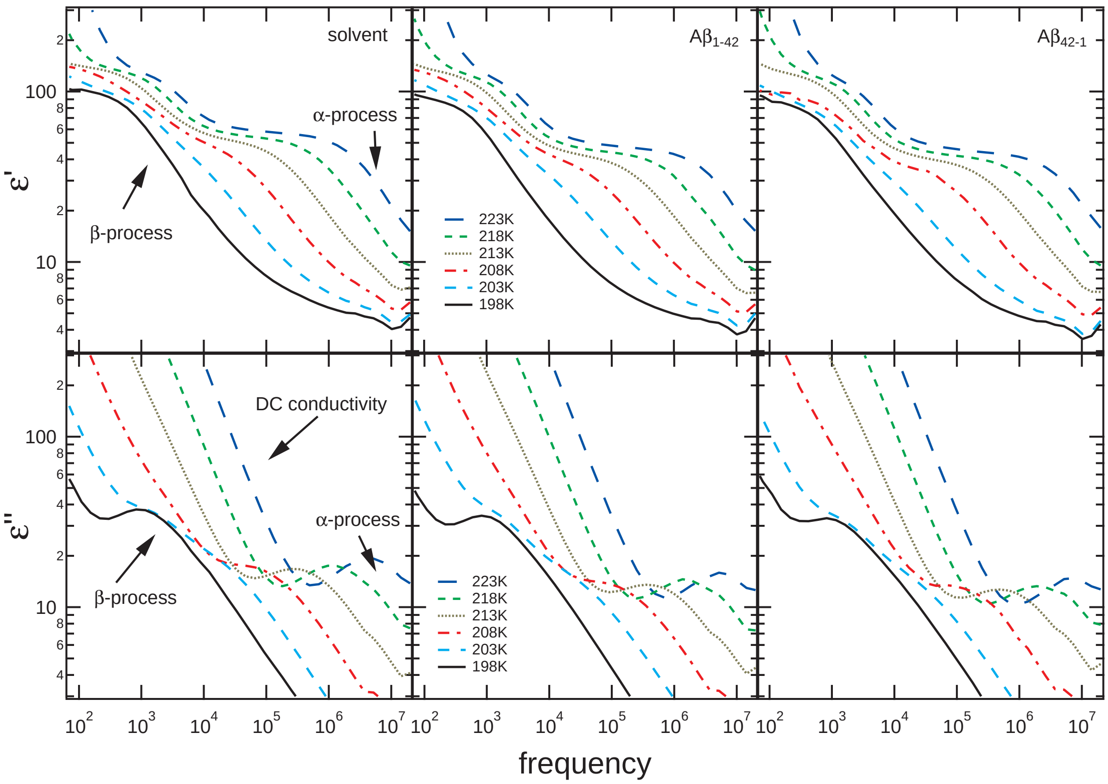

Figure 5.1: **Temperature evolution of the real and imaginary parts of the dielectric permittivity for the solvent, $A\beta_{1-42}$, and $A\beta_{42-1}$ from 223K to 198K.** Two relaxation processes for the real (ε') and imaginary (ε'') parts of the permittivity for the solvent, $A\beta_{1-42}$, and scrambled $A\beta_{42-1}$ are observed.

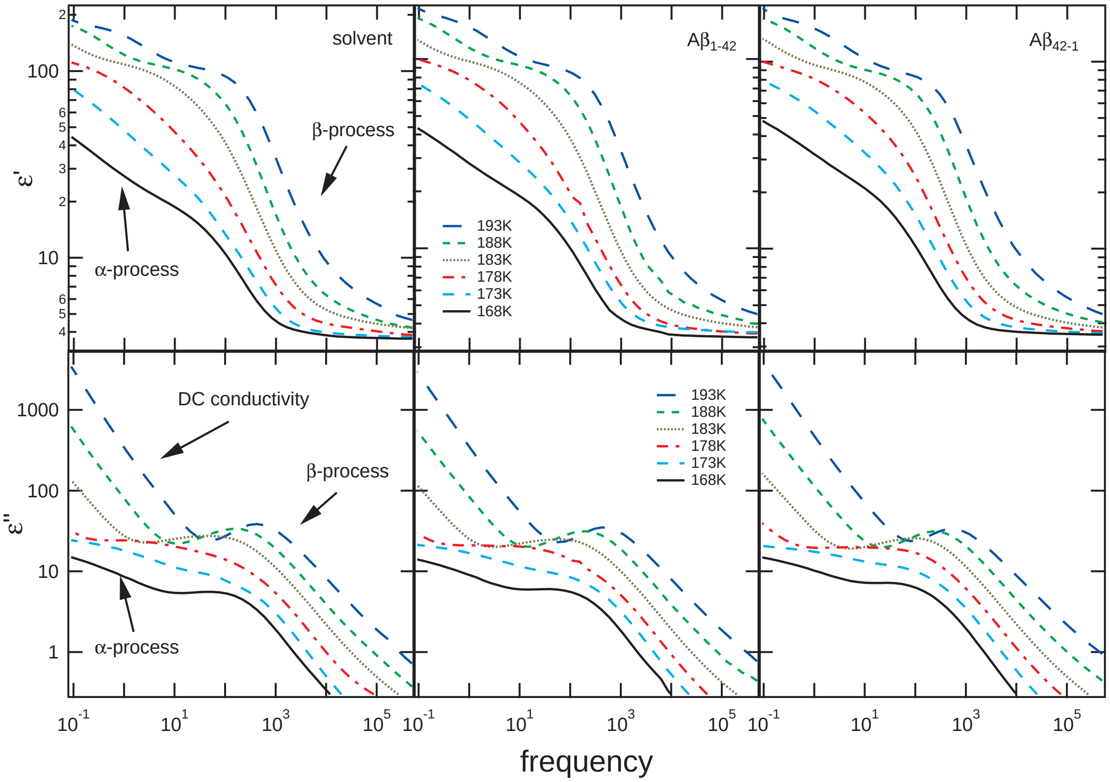

Figure 5.2: **Temperature evolution of the real and imaginary parts of the dielectric permittivity for the solvent,$A\beta_{1-42}$, and $A\beta_{42-1}$ from 193K to 168K.** The α-relaxation process rapidly shifts to lower frequency with decreasing temperature. In the range of 193K to 188K the two processes cross where the α-relaxation is at lower frequency than the β-relaxation process at temperatures of 183K and below.

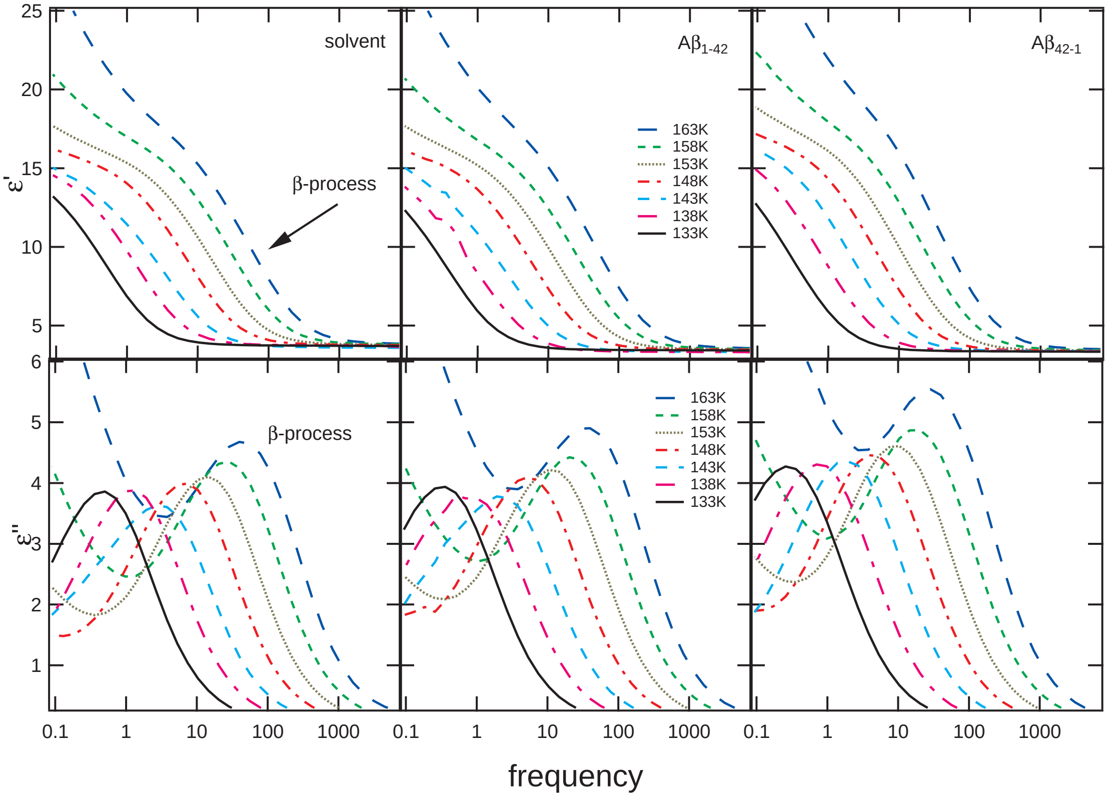

Figure 5.3: **Temperature evolution of the real and imaginary parts of the dielectric permittivity for the solvent, $A\beta_{1-42}$, and $A\beta_{42-1}$ from 163K to 133K.** The β-relaxation process dominates below the crossing temperature and continues to slow to under 1 Hz. The DC conductivity has reduced in magnitude to outside the measured range below 158K.

Permittivity data for $A\beta_{1-42}$ and scrambled $A\beta_{42-1}$ were plotted against the solvent to compare the time-evolution of dielectric signal. Data were collected after 0, 8, and 24 hours of incubation at room temperature. The dielectric loss of $A\beta_{1-42}$ and $A\beta_{42-1}$ as compared to the solvent over the observable temperature range 223K-133K is shown in Figures 5.4 - 5.13.

Above the α-β relaxation crossing temperature of 193K where the α-process dominates the spectra, the magnitude of the dielectric loss peaks of $A\beta_{42-1}$ decreases over time and is less than the solvent, as seen in Figure 5.5. In the crossing region of 193K - 183K where the processes occur at similar frequency, Figures 5.7 and 5.9 show that the trend continues with steady decreasing of the peak magnitude over time. At temperatures of 168K and below where the β-process dominates the spectra, the magnitude of $A\beta_{42-1}$ starts above the solvent, then continues to decrease to a point less than that of the solvent after 24 hours, as shown in Figures 5.9 - 5.13. The peak frequency of the β-process has a slight increase over time towards the solvent in temperatures less than 168K.

The magnitude of the dielectric loss peaks of the $A\beta_{1-42}$ follows a different trend than the $A\beta_{42-1}$. Above the α-β relaxation crossing temperature of 193K where the α-process dominates the spectra, the magnitude of $A\beta_{1-42}$ starts near the solvent from 0-8 hours but then jumps below that of the solvent at 24 hours as seen in Figure 5.4. In the crossing region of 193K - 183K where the processes occur at similar frequency, Figures 5.6 and 5.8 show that the dielectric signal of $A\beta_{1-42}$ is slightly higher in magnitude from 0-8 hours, but again at 24 hours it is much less than that of the solvent. At temperatures of 168K and below where the β-process dominates the spectra, the magnitude of $A\beta_{1-42}$ decreases over time as compared to the solvent as shown in Figures 5.8 - 5.12. Additionally, the peak frequency of the beta process of $A\beta_{1-42}$ slightly increases towards the solvent over time.

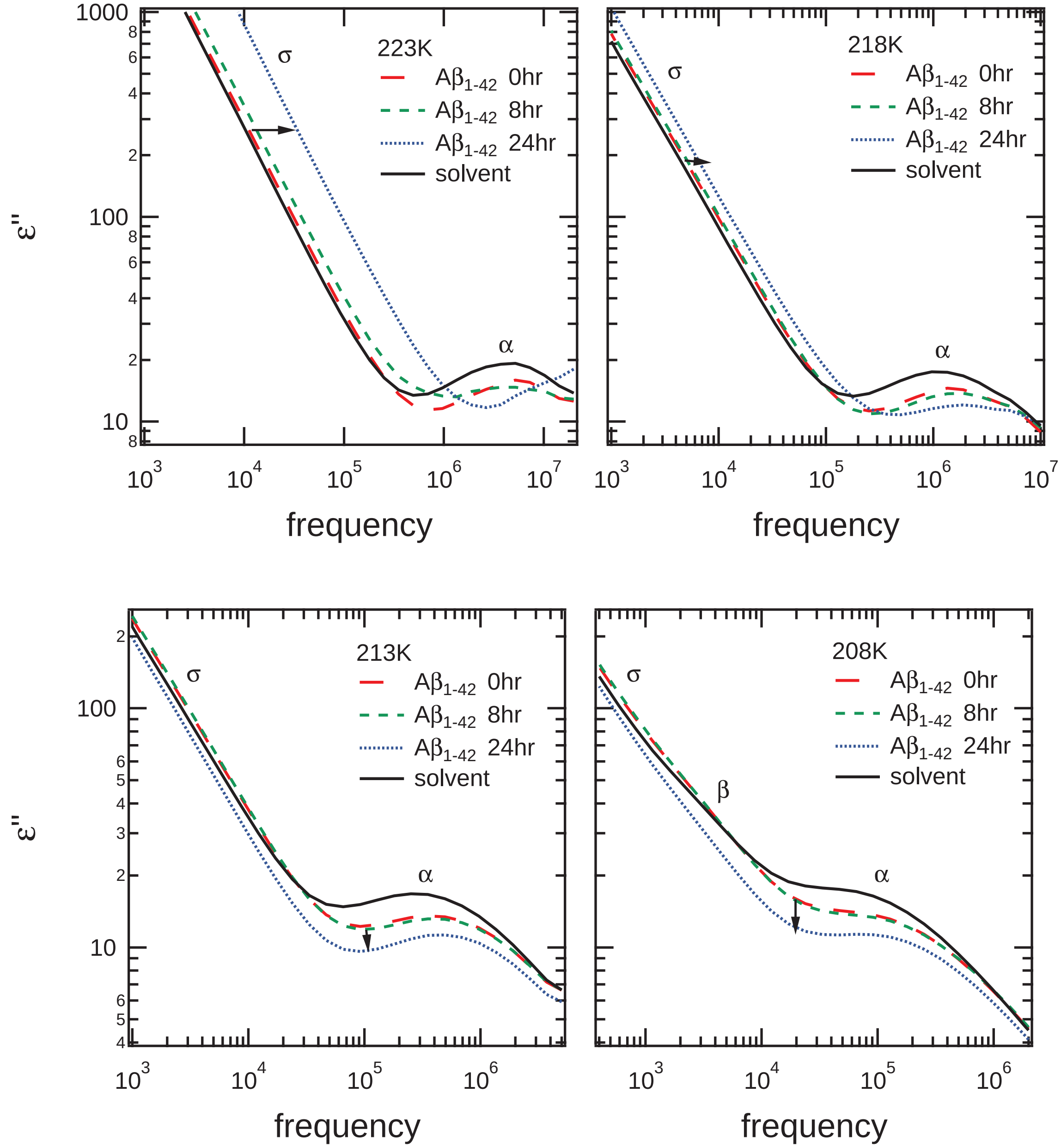

Figure 5.4: **Dielectric loss ε'' as a function of frequency for $A\beta_{1-42}$ in the range of 223K-208K and incubation periods of 0, 8, and 24 hours.** At temperatures above 208K, the β-relaxation process is masked by the conductivity, σ. The arrows depict a decrease in magnitude of ε'', due to the decrease in σ over time. The spectra shows a shift towards higher frequency at 223K, but does not appear to follow a trend.

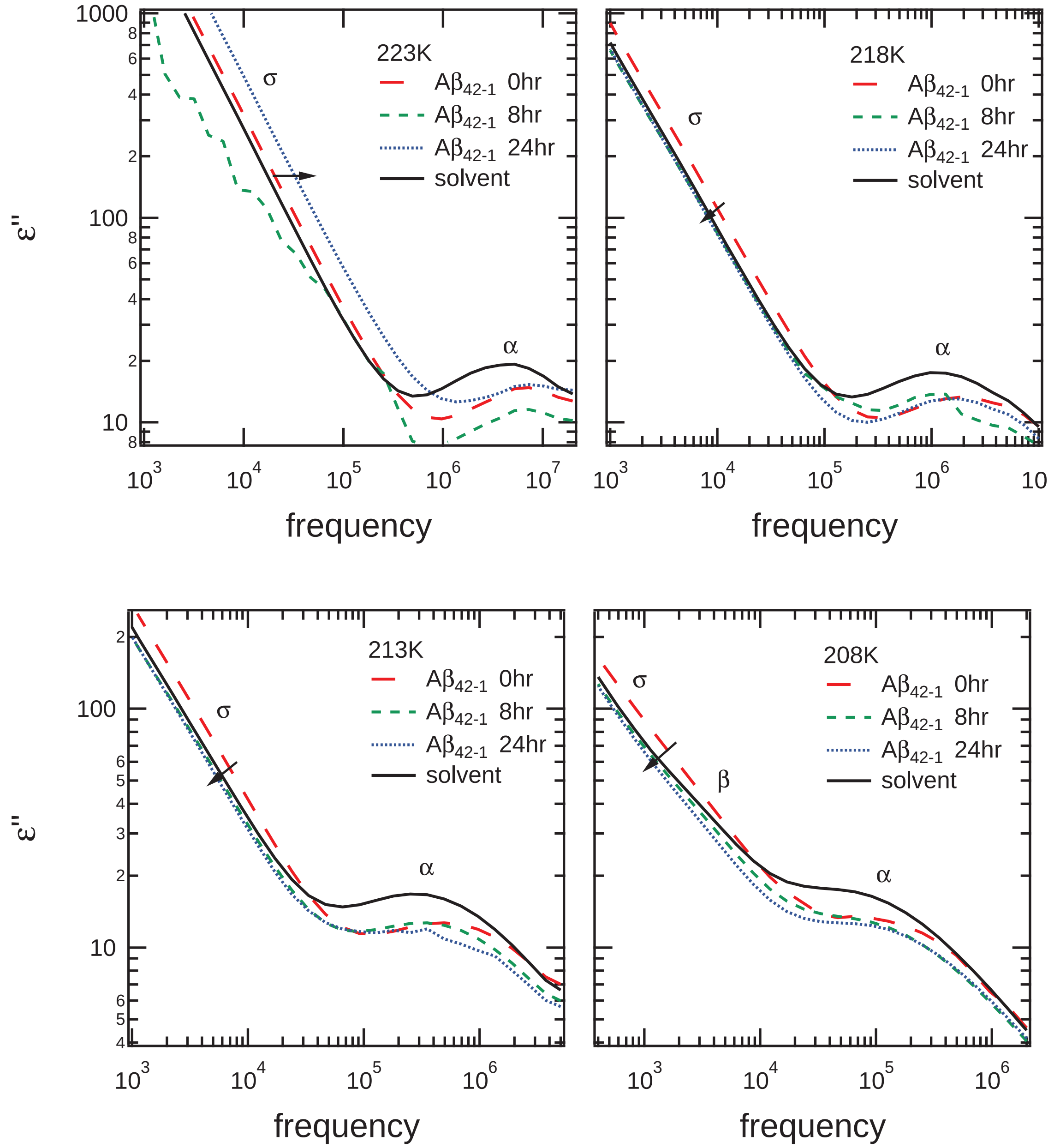

Figure 5.5: **Dielectric loss ε'' as a function of frequency for scrambled $A\beta_{42-1}$ in the range of 223K-208K and incubation periods of 0, 8, and 24 hours.** At temperatures above 208K, the β-relaxation process is masked by the conductivity, σ. The arrows depict a small decrease in magnitude of ε'', due to the decrease in σ over time. As with $A\beta_{1-42}$, the spectra shows a shift towards higher frequency at 223K, but does not appear to follow a trend.

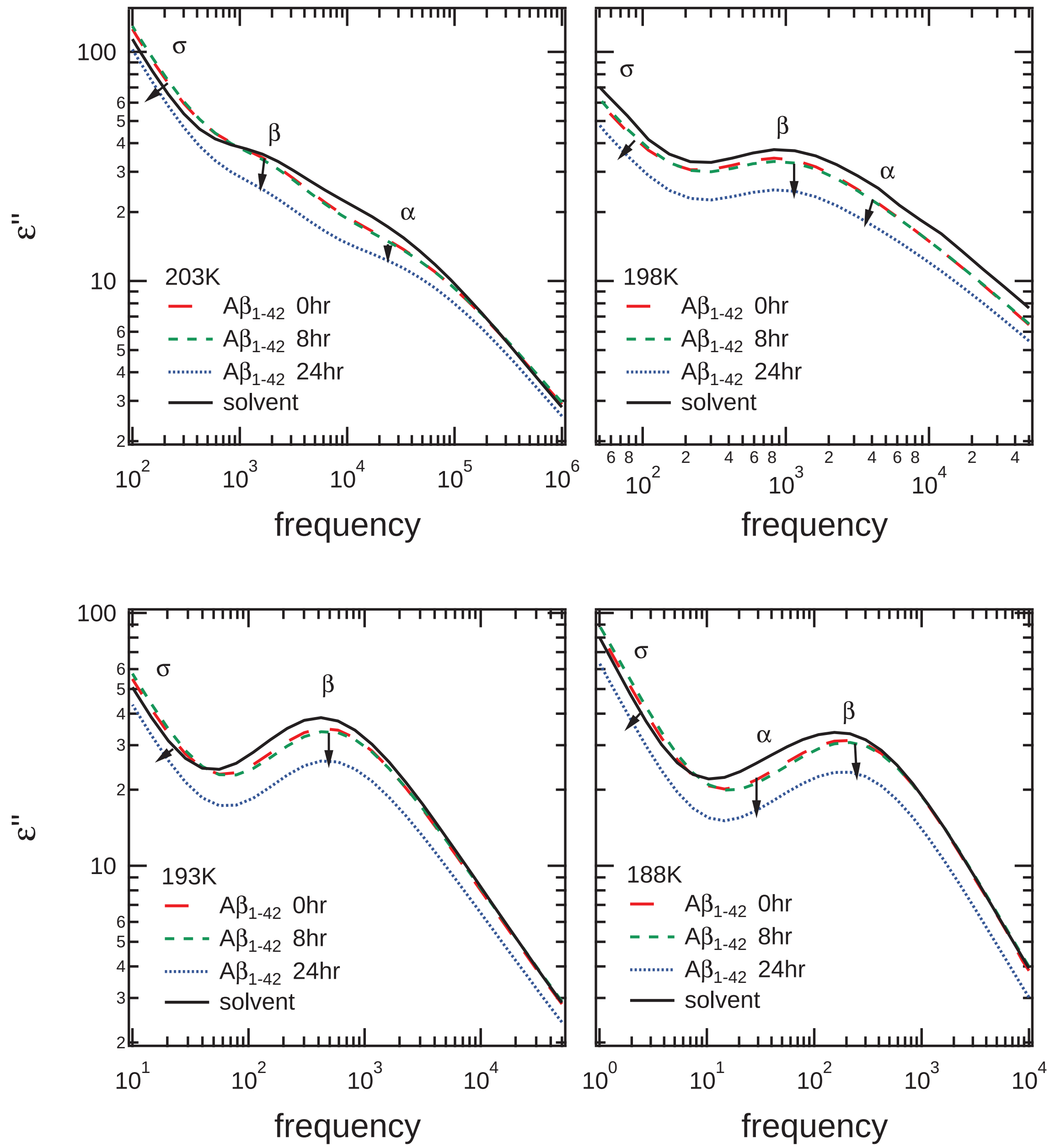

Figure 5.6: **Dielectric loss ε'' as a function of frequency for $A\beta_{1-42}$ in the range of 203K-188K and incubation periods of 0, 8, and 24 hours.** At 193K, the α-process occurs at near the same frequency as the β-process but with lower magnitude. The arrows show a shift in magnitude of ε'' across the spectra due to the conductivity, σ.

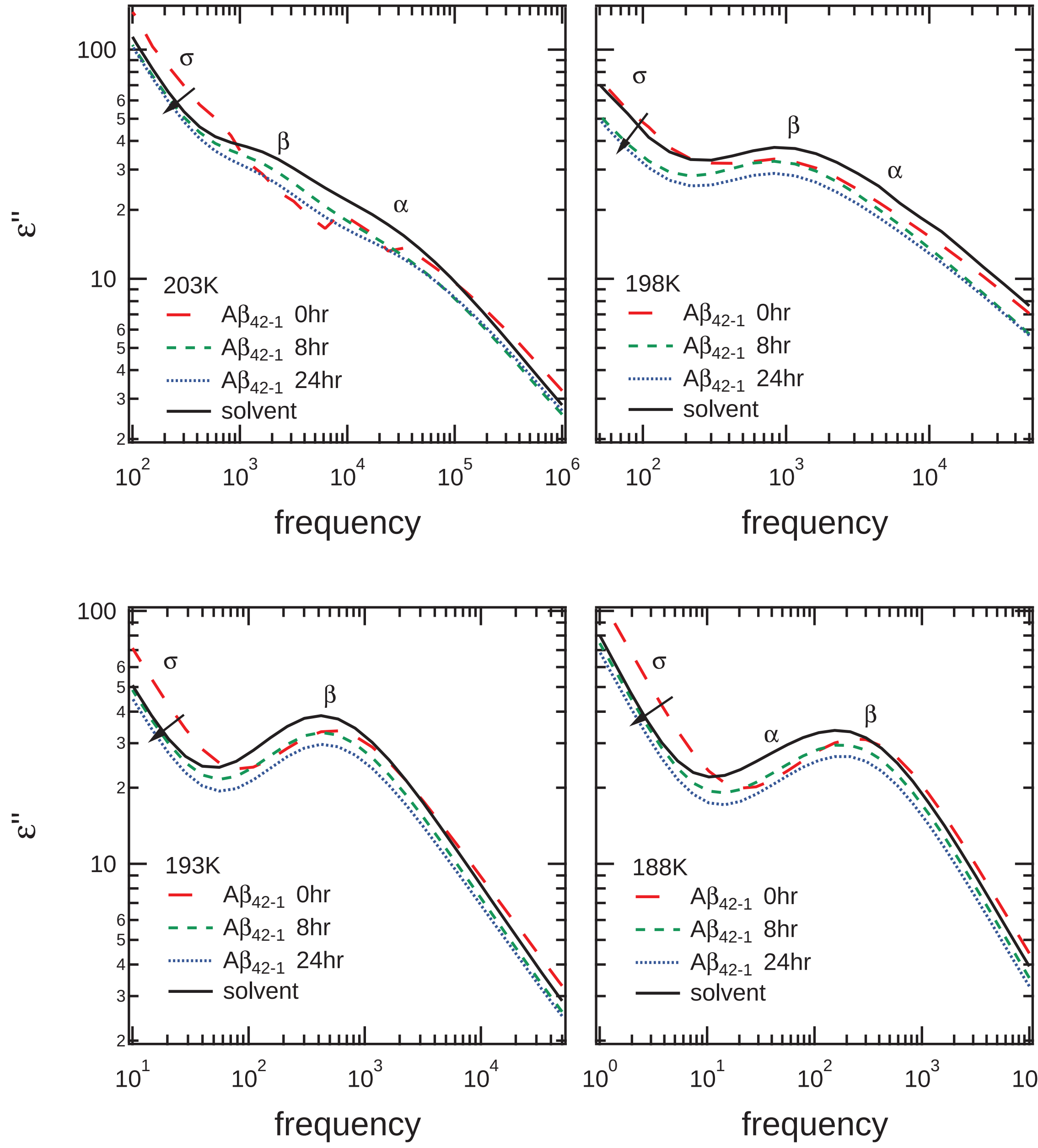

Figure 5.7: **Dielectric loss ε'' as a function of frequency for scrambled $A\beta_{42-1}$ in the range of 203K-188K and incubation periods of 0, 8, and 24 hours.** At 193K, the α-process occurs at near the same frequency as the β-process but with lower magnitude. The arrows show a shift in magnitude of ε'' across the spectra due to the conductivity, σ.

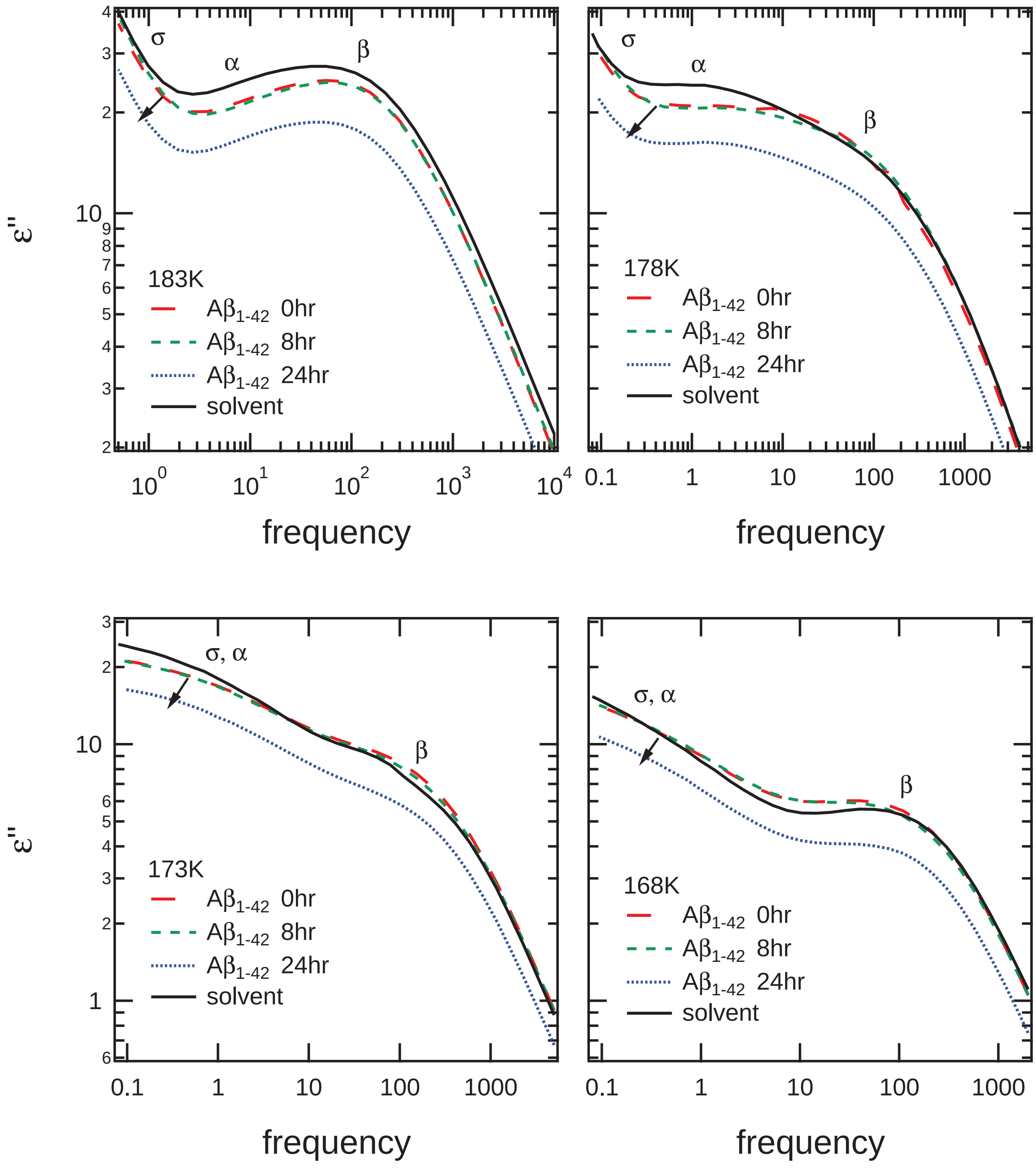

Figure 5.8: **Dielectric loss ε'' as a function of frequency for $A\beta_{1-42}$ in the range of 183K-168K and incubation periods of 0, 8, and 24 hours.** In the range of 183K-168K, there is significant mixing between σ, α-, and β-processes.

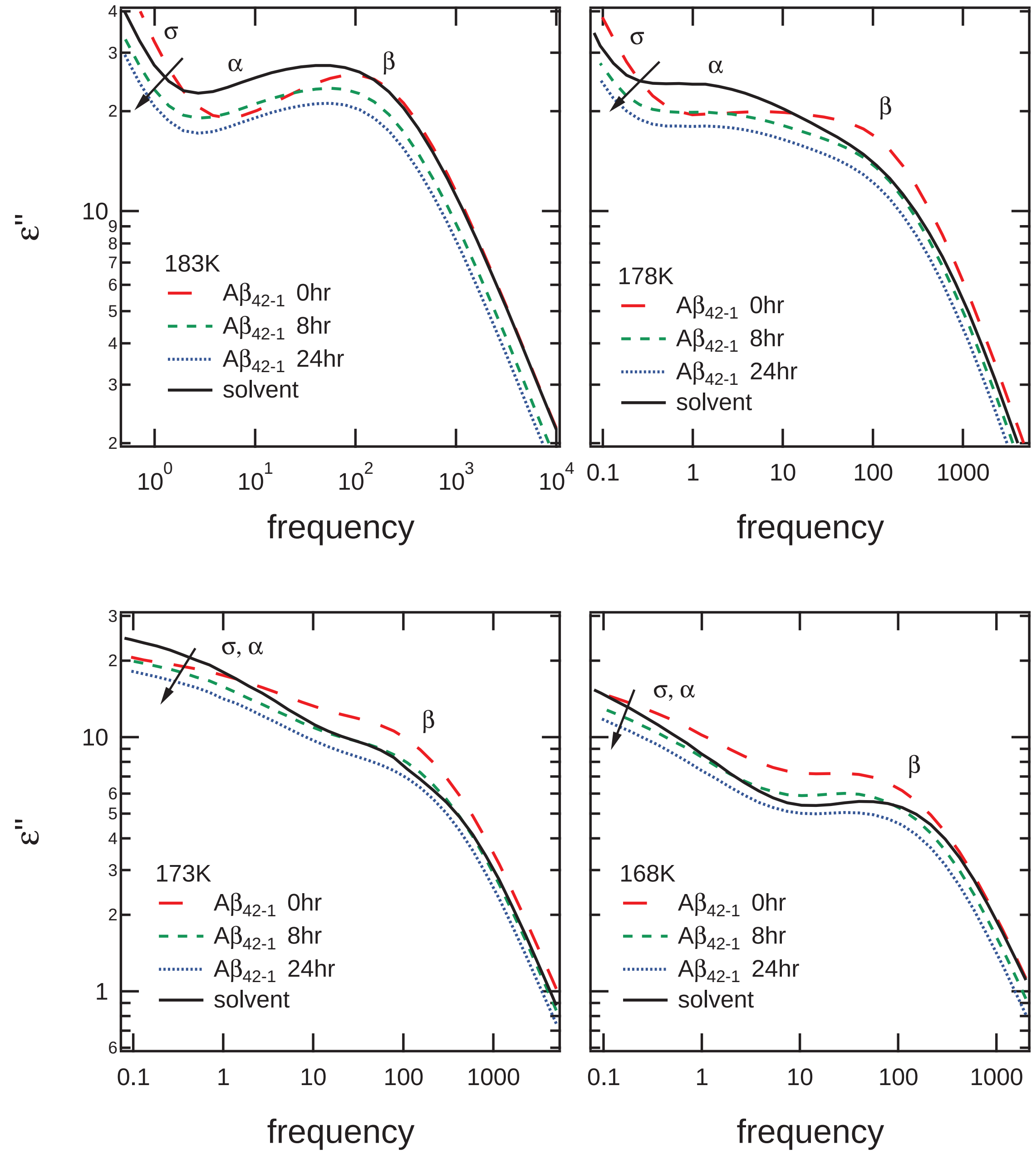

Figure 5.9: **Dielectric loss ε'' as a function of frequency for scrambled** $A\beta_{42-1}$ **in the range of 183K-168K and incubation periods of 0, 8, and 24 hours.** In the range of 183K-168K, there is significant mixing between σ, α-, and β-processes. Trends in this range are due to changes in conductivity, σ.

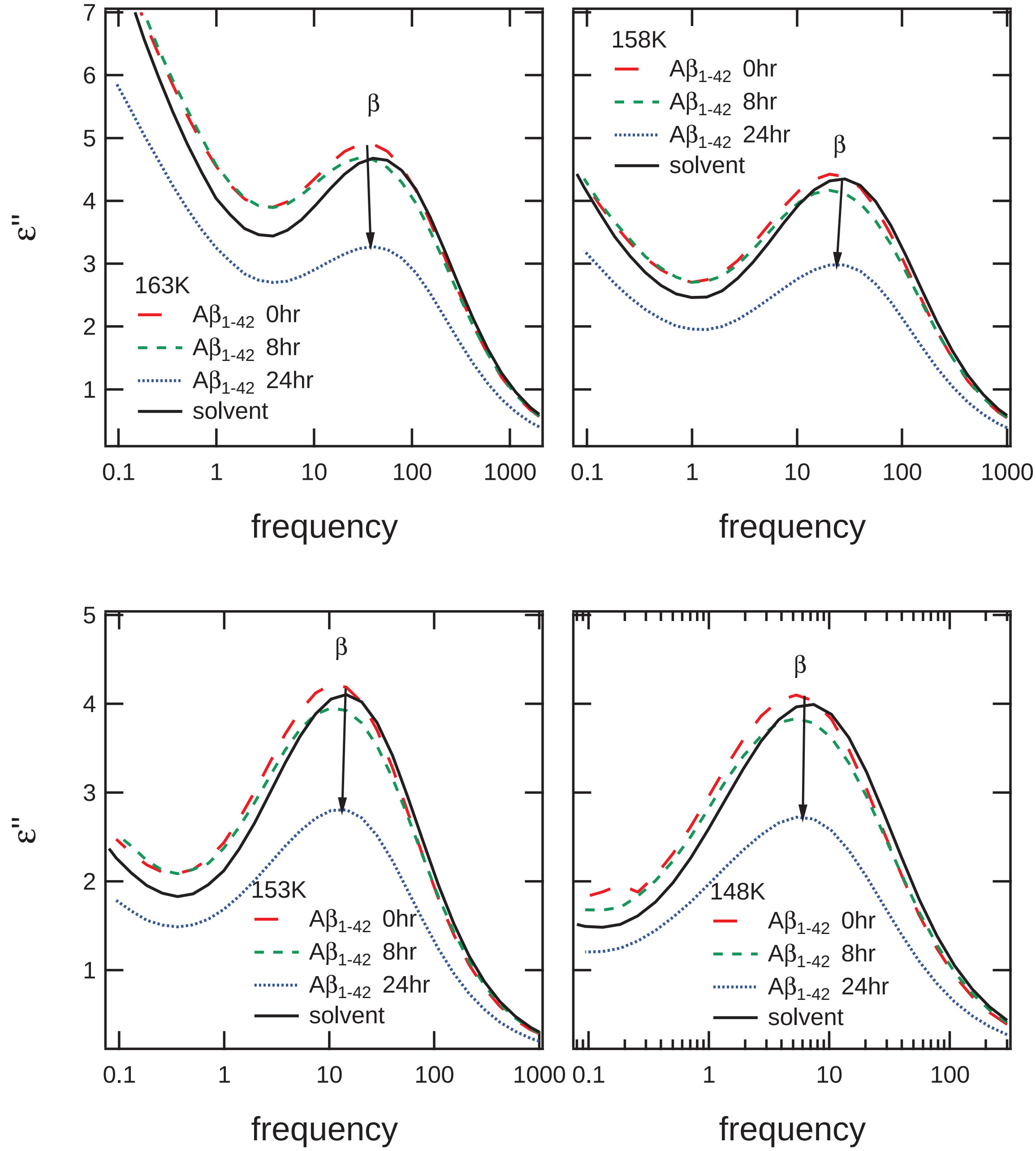

Figure 5.10: **Dielectric loss ε'' as a function of frequency for $A\beta_{1-42}$ in the range of 163K-148K and incubation periods of 0, 8, and 24 hours.** At 158K, the conductivity, σ and the α-process are substantially separated from the β process. At 158K and below, the β-relaxation peak in ε'' trends to lower magnitude and lower frequency over time.

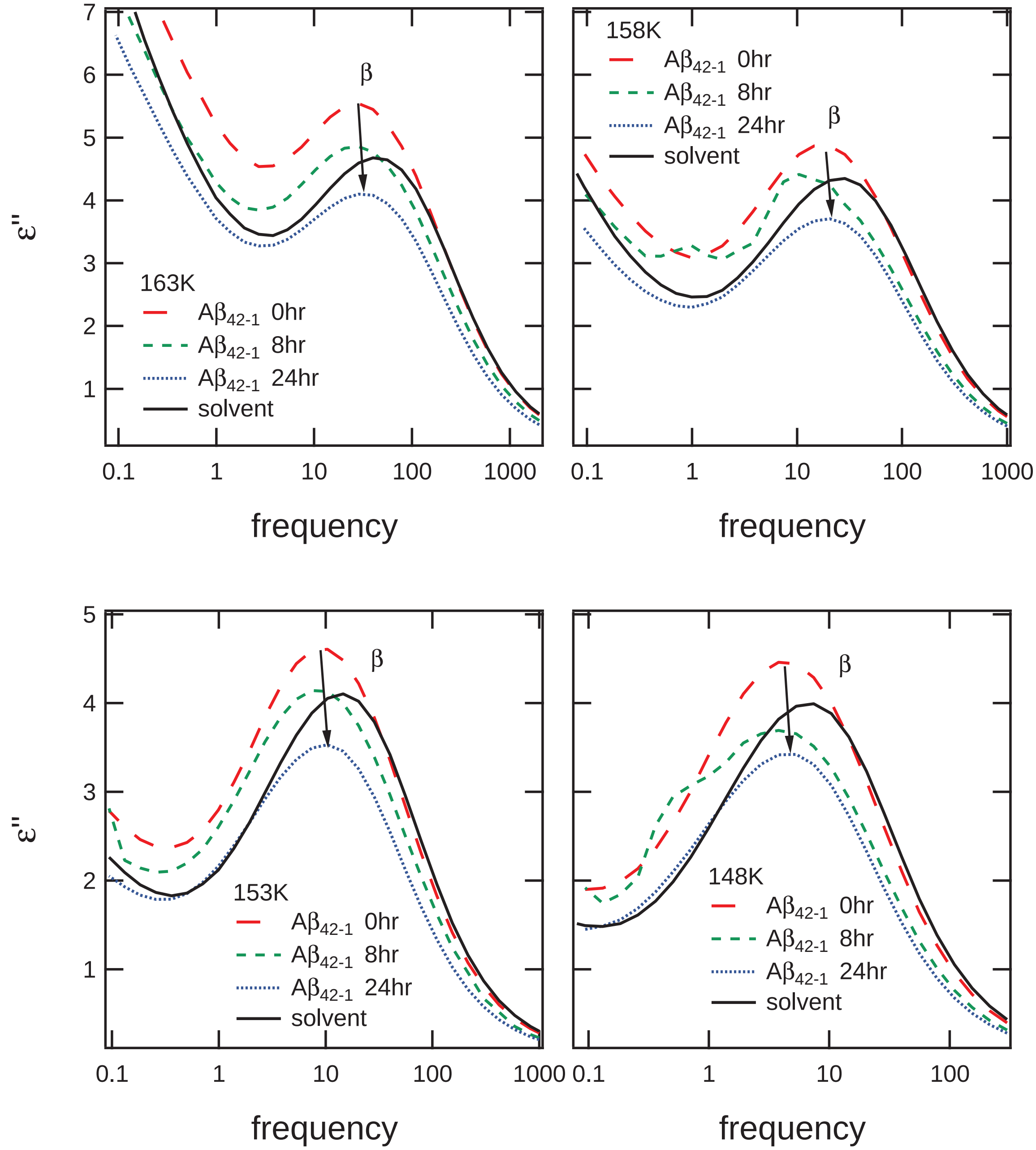

Figure 5.11: **Dielectric loss ε'' as a function of frequency for scrambled $A\beta_{42-1}$ in the range of 163K-148K and incubation periods of 0, 8, and 24 hours.** At 163K, the conductivity, σ and the α-process are substantially separated from the β process. At 158K and below, the β-relaxation peak in ε'' trends to lower magnitude but unlike $A\beta_{1-42}$, the peak shifts towards higher frequency over time.

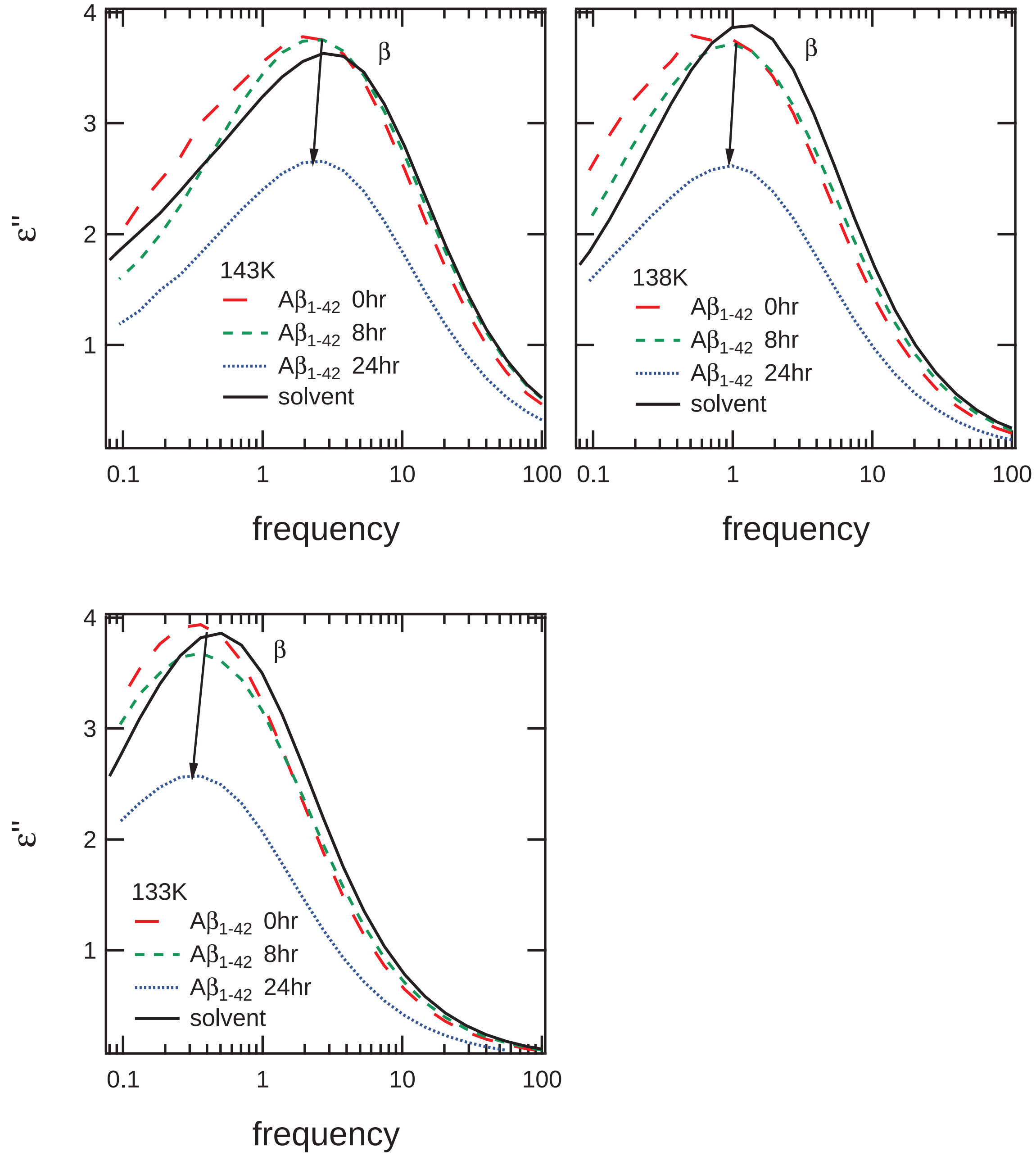

Figure 5.12: **Dielectric loss ε'' as a function of frequency for $A\beta_{1-42}$ in the range of 143K-133K and incubation periods of 0, 8, and 24 hours.** The β-relaxation peak in ε'' trends to lower magnitude and lower frequency over time.

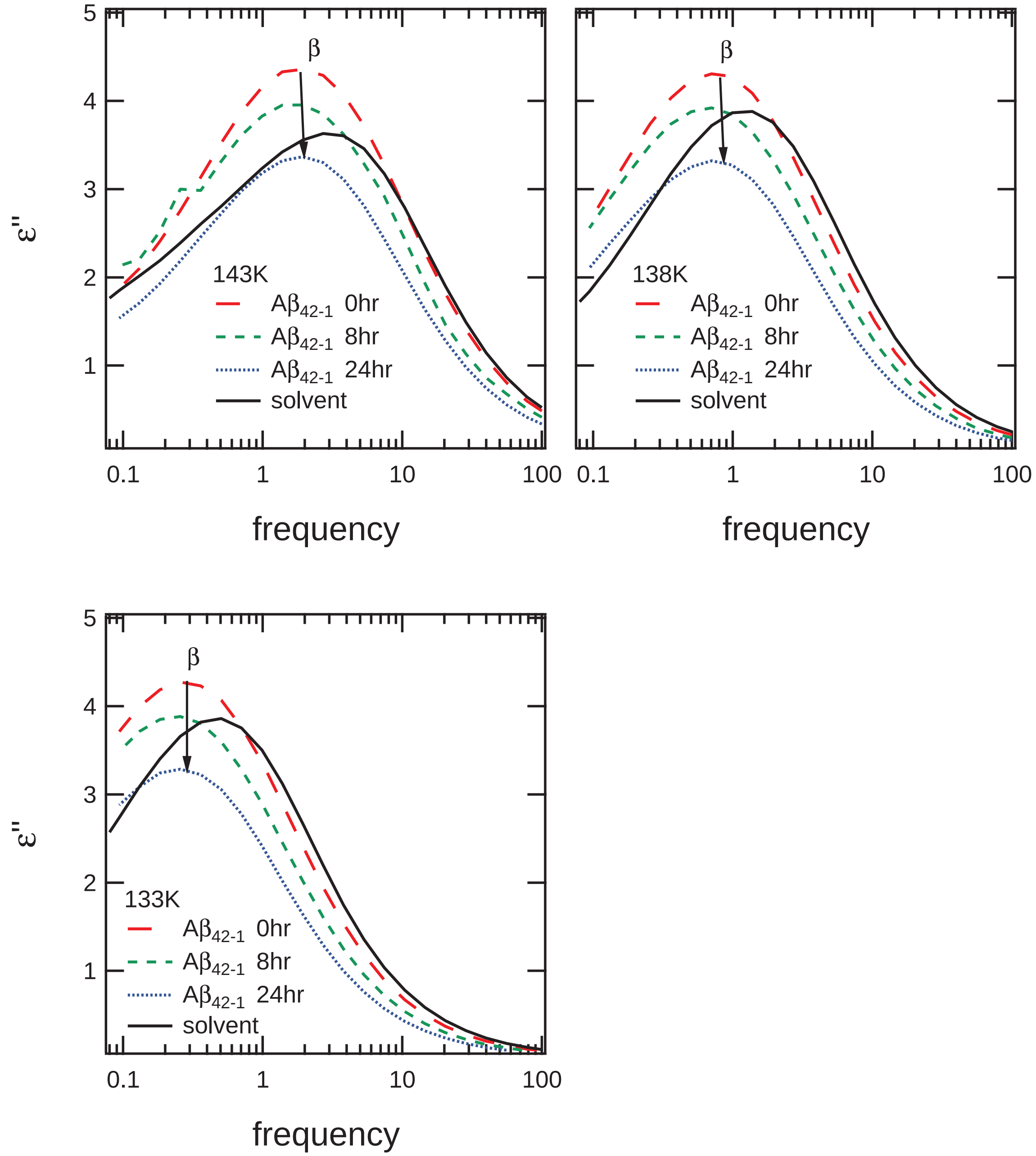

Figure 5.13: **Dielectric loss ε'' as a function of frequency for scrambled $A\beta_{42-1}$ in the range of 143K-133K and incubation periods of 0, 8, and 24 hours.** The β-relaxation peak in ε'' trends to lower magnitude but unlike $A\beta_{1-42}$, the peak shifts towards higher frequency over time.

Dielectric permittivity data for $A\beta_{1-42}$, scrambled $A\beta_{42-1}$, and the solvent were modeled using the WinFIT program for each temperature from 223K to 133K and at incubation time points 0, 8, and 24 hours. The β-relaxation process was best-fit using a Cole-Davidson function with the broadening parameter, β remaining relatively constant over the entire temperature range at approximately 0.8. The α-relaxation process demonstrates both symmetric and asymmetric broadening over the observed temperature range with both β and γ spreading parameters changing with temperature.

The α-relaxation process is observed from 223K to 168K, though in the crossing temperatures of 198K to 183K, it overlaps with the β-process. During this temperature range, the β-relaxation process dominates. The β-relaxation process is observed between approximately 208K down to the lowest temperature, 133K. At temperatures above 208K, the DC conductivity dominates the spectra in the region of the β-relaxation. Examples of curve fitting performed at representative temperatures are shown in Figures 5.14 - 5.17. Figure 5.17 shows a clear β-relaxation process with a high-frequency excess wing for very low temperatures.

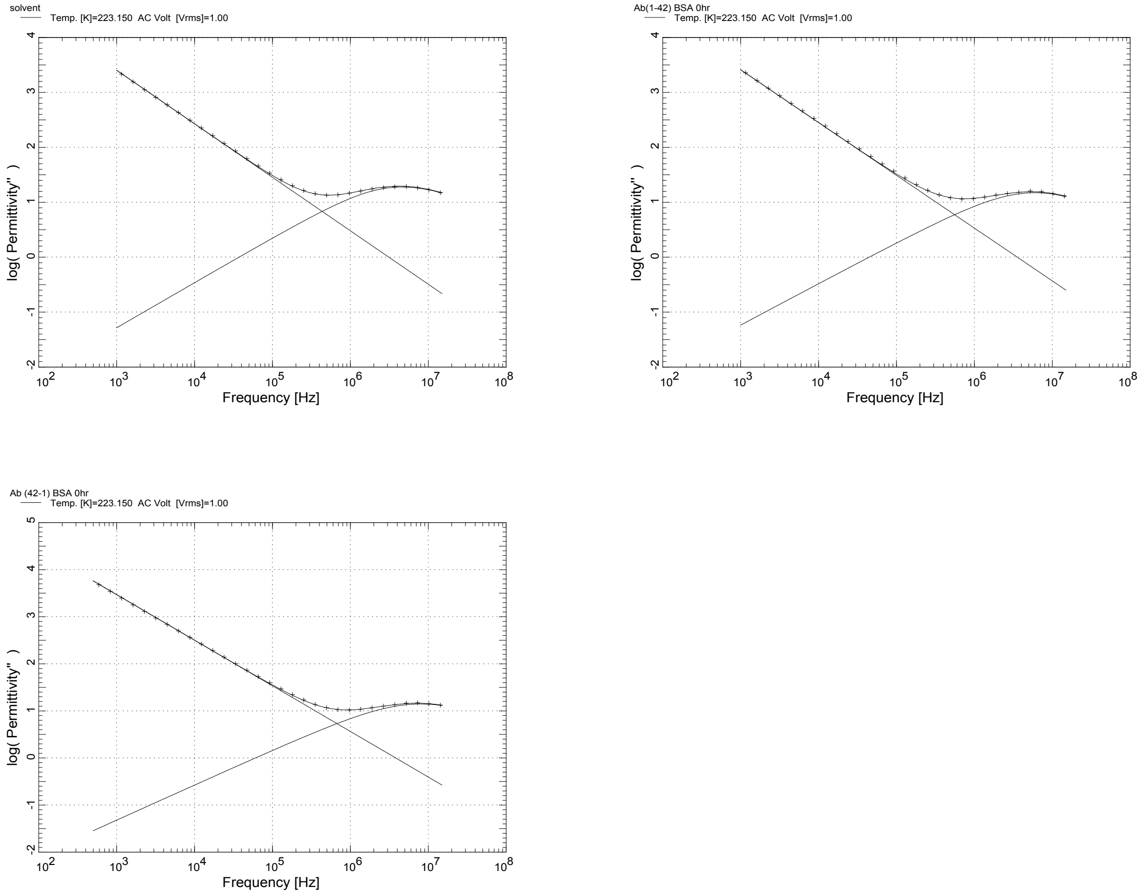

Figure 5.14: **Curve fitting of imaginary part of the permittivity data using the WinFIT program of the solvent, $A\beta_{1-42}$, and $A\beta_{42-1}$ at 223K.** A large, low frequency DC conductivity is fit with a power law. The α-relaxation process at around 10^7 Hz is fit with a Havriliak-Negami function. The β-relaxation function is not observed. The root-mean-square deviation (RMSD) of the fits are 0.015, 0.030, and 0.088, respectively.

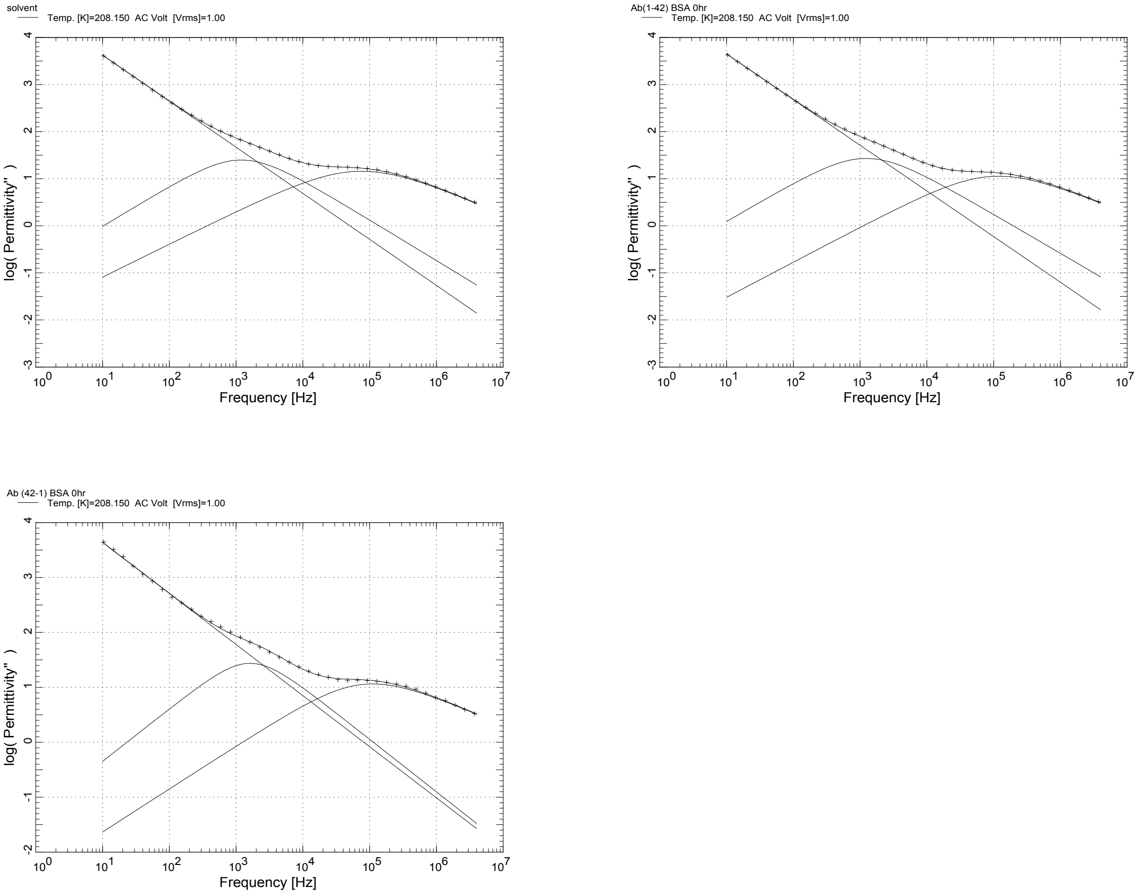

Figure 5.15: **Curve fitting of imaginary part of the permittivity data using the WinFIT program of the solvent, $A\beta_{1-42}$, and $A\beta_{42-1}$ at 208K.** A large, low frequency DC conductivity is fit with a power law. The β-relaxation process at around 10^3 Hz is fit with a Cole-Davidson function and the α-relaxation process at around 10^5 Hz is fit with a Havriliak-Negami function. The RMSD of the fits are 0.018, 0.005, and 0.012, respectively.

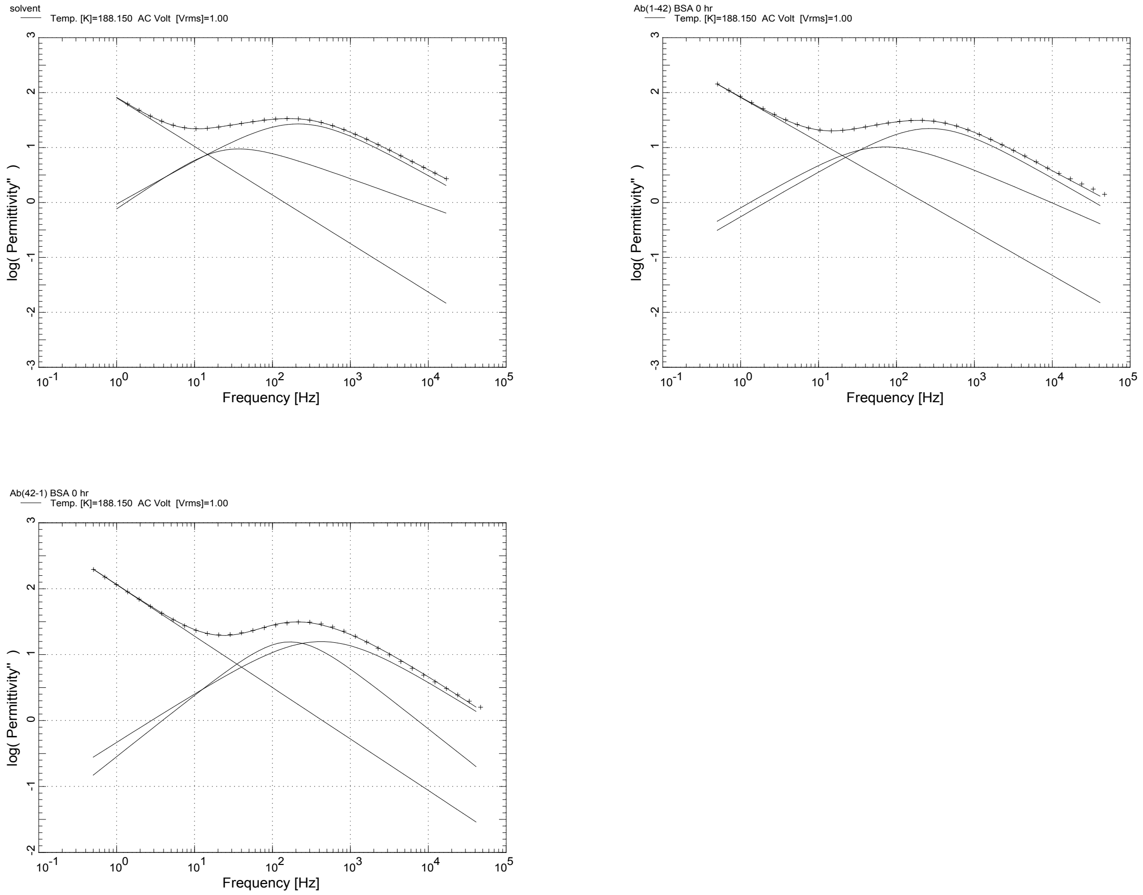

Figure 5.16: **Curve fitting of imaginary part of the permittivity data using the WinFIT program of the solvent, $A\beta_{1-42}$, and $A\beta_{42-1}$ at 188K.** A large, low frequency DC conductivity is fit with a power law. The β-relaxation process at around 10^3 Hz is fit with a Cole-Davidson function and the α-relaxation process at around 10^1 Hz is fit with a Havriliak-Negami function. Here, the α process has crossed over to slower than β relaxation times. The RMSD of the fits are 0.001, 0.019, and 0.017, respectively.

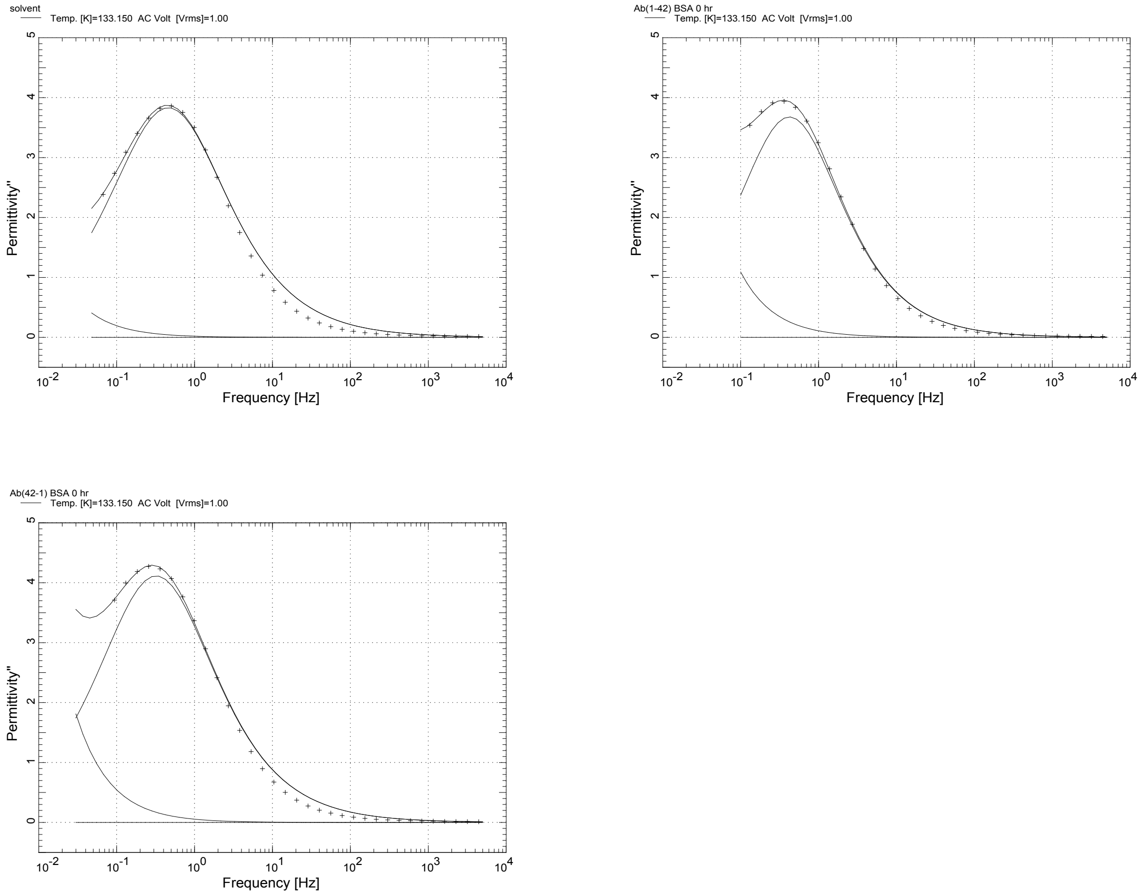

Figure 5.17: **Curve fitting of the imaginary part of the permittivity data using the WinFIT program of the solvent, $A\beta_{1-42}$, and $A\beta_{42-1}$ at 133K.** A small, very low frequency DC conductivity is fit with a power law. The β-relaxation process at around 1 Hz is fit with a Cole-Davidson function and the α-relaxation process is not observed. The RMSD of the fits are 0.073, 0.042, and 0.006, respectively.

The maximum frequency, f_{max} of ε'' of both the α- and β-relaxation processes were determined from the model function curve fitting of the permittivity data at all temperatures. Arrhenius plots of f_{max} versus inverse temperature, 1000/T were created for each process. The β-relaxation process follows a linear, or Arrhenius behavior throughout the temperature range. The α-relaxation process follows a slight non-linear Vogel-Fulcher-Tammann (VFT)-type behavior that is expected in glass-forming solvents such as glycerol (Figures 5.18 and 5.19). Activation energies for the β process and glass-forming fragilities for the α process were determined from the Arrhenius and VFT analysis and presented in Tables 5.1 and 5.2.

	time	A	B	E_A (kJ/mol)		*time*	A	B	E_A (kJ/mol)
Aβ_{1-42}	0hr	9.13	1.250	23.9	Aβ_{42-1}	0hr	9.95	1.392	26.6
	8hr	9.53	1.311	25.1		8hr	9.76	1.367	26.1
	24hr	9.59	1.321	25.3		24hr	9.91	1.380	26.4
solvent		9.18	1.245	23.8	solvent		9.18	1.245	23.8

Table 5.1: Parameters of the linear fits to the β-relaxation measurements of $\log(f_{max}(T))$ of the form $A + BT$.

	time	$\log f_\infty$	D	T_0 (K)		*time*	$\log f_\infty$	D	T_0 (K)
Aβ_{1-42}	0hr	22	35	68	Aβ_{42-1}	0hr	22	30	74
	8hr	22	30	75		8hr	22	29	77
	24hr	22	25	83		24hr	22	27	80
solvent		22	31	74	solvent		22	31	74

Table 5.2: Parameters of the VFT fits to the α-relaxation measurements of $f_{max}(T)$ of the form $\log(f_{max}) = \log(f_\infty(T)) - \frac{DT_0}{T-T_0}$

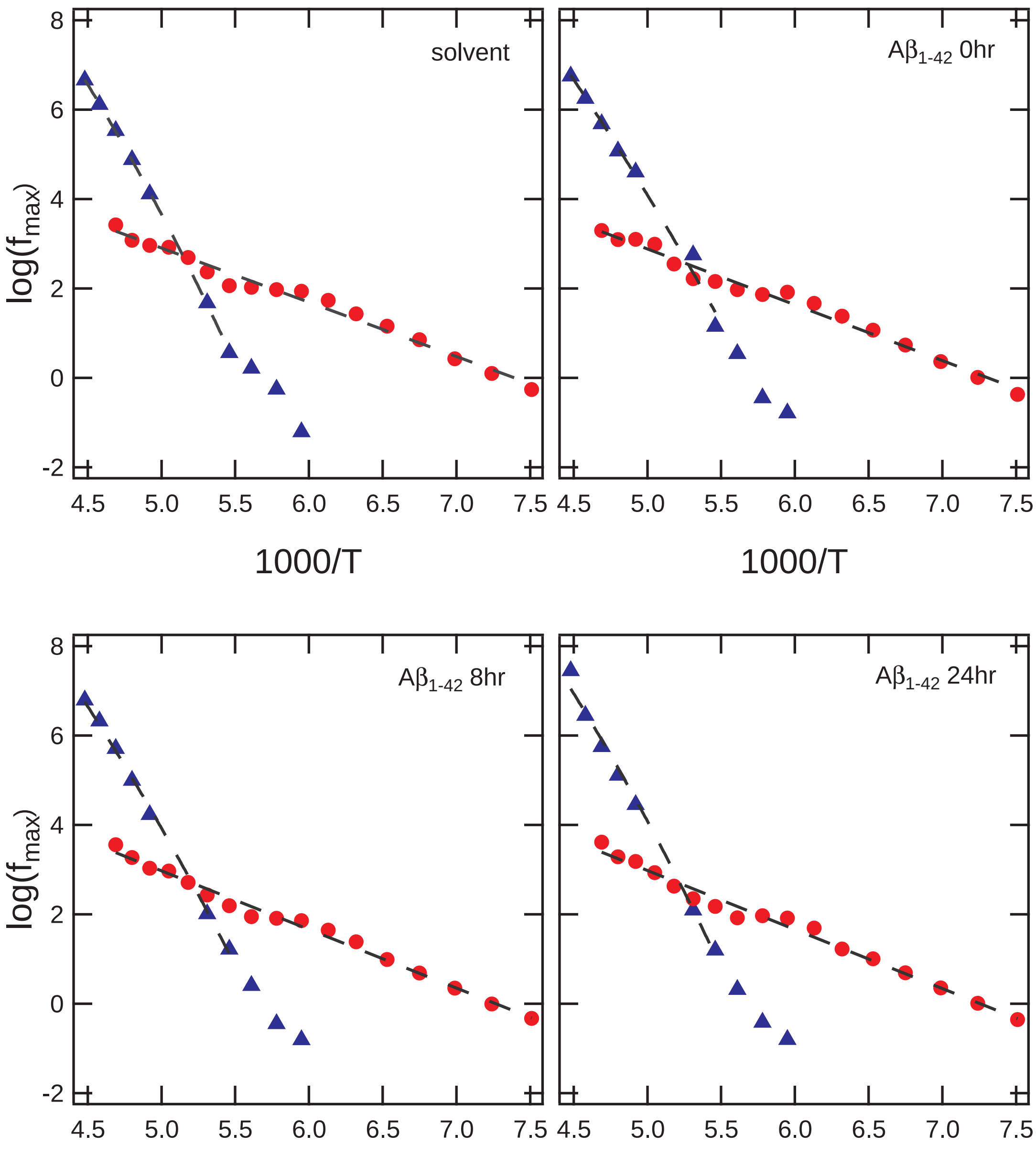

Figure 5.18: **Arrhenius plots of f_{max} versus inverse temperature for $A\beta_{1-42}$ over time.** The α-relaxation process follows a VFT behavior whereas the β-relaxation process follows an Arrhenius, or linear behavior. The α-process departs from the VFT curvature at low temperature.

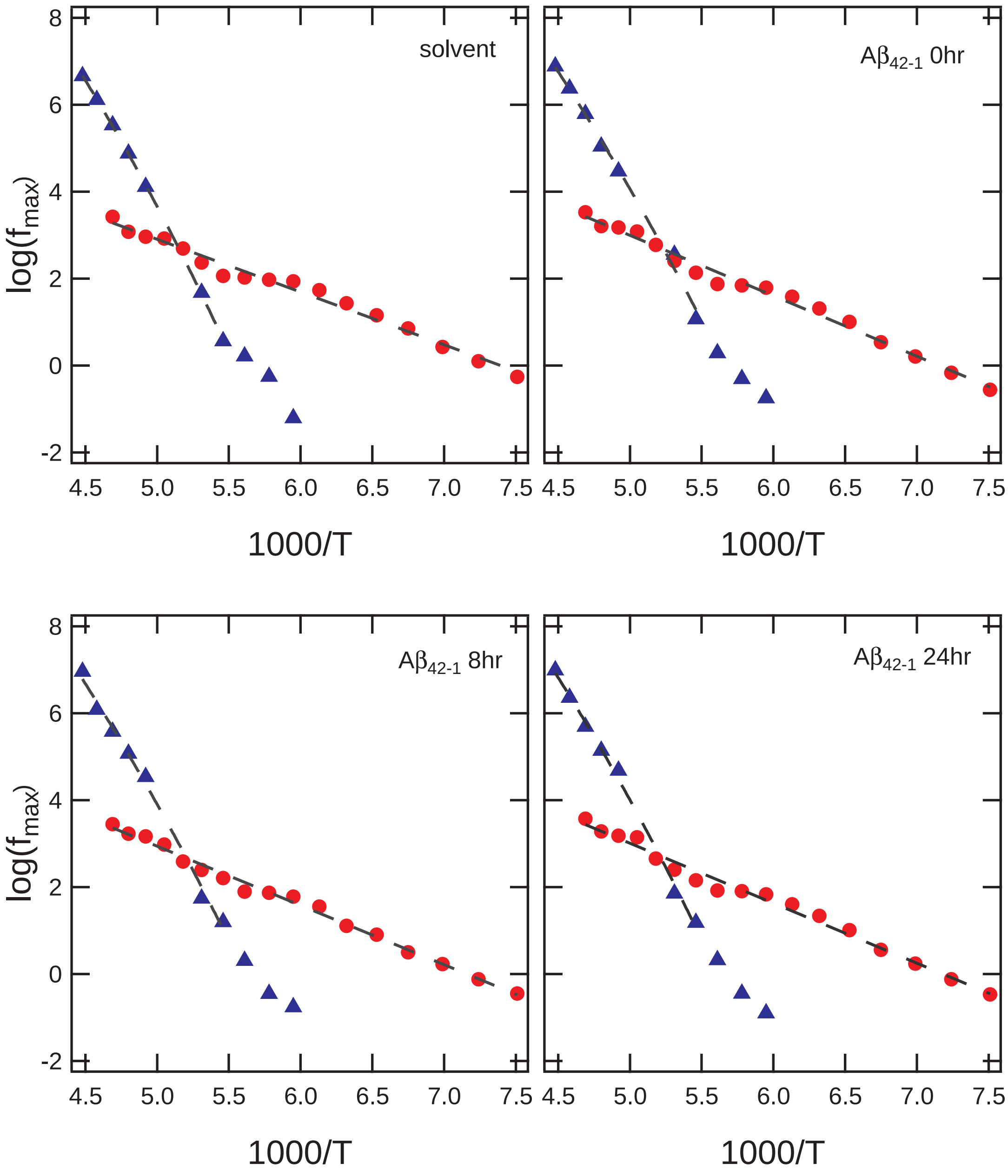

Figure 5.19: **Arrhenius plots of f_{max} versus inverse temperature for scrambled $A\beta_{42-1}$ over time.** The α-relaxation process follows a VFT behavior whereas the β-relaxation process follows an Arrhenius, or linear behavior. The α-process departs from the VFT curvature at low temperature.

The α-relaxation process for $A\beta_{1-42}$, scrambled $A\beta_{42-1}$, and the solvent display VFT behavior down to 183K. Below 183K, the curvature of the VFT changes where the temperature dependence of f_{max} would be better approximated by another VFT or different empirical fit function. Studies have shown that two or more temperature-dependent fit functions may be necessary to describe the behavior of the α-relaxation of glass formers such as glycerol [63, 165]. The departure of the VFT behavior occurs at approximately the glass transition of glycerol, indicating that the change in temperature dependance may be due to the phase change. Whereas the α-relaxation process is representative of large scale structural fluctuations in the solvent, it is conceivable that a phase transition could change the temperature dependance of the relaxation rate.

Studies of the dielectric strength of $A\beta_{1-42}$ and $A\beta_{42-1}$ in serum confirm the studies done in deionized water. Figure 5.20 shows that over time, $A\beta_{1-42}$ decreased in the dielectric strength as fibril formation progressed. The non-amyloidogenic $A\beta_{42-1}$ did not change over time. Unlike the deionized water buffer, the $A\beta_{1-42}$ did not show any increase in dielctric strength after 8 hours of incubation. Walton et al. showed using immunochemistry that 50μM $A\beta_{1-42}$ in a BSA buffer possesses significant concentrations of oligomers and fibrils after just 3 hours of incubation at room temperature [111]. The serum, which is closer to in vivo biological conditions, may be causing a more rapid aggregation of the $A\beta_{1-42}$. A study to look for intermediary dielectric strength increases for shorter incubation times, such as 1, 2, or 4 hours may help confirm this.

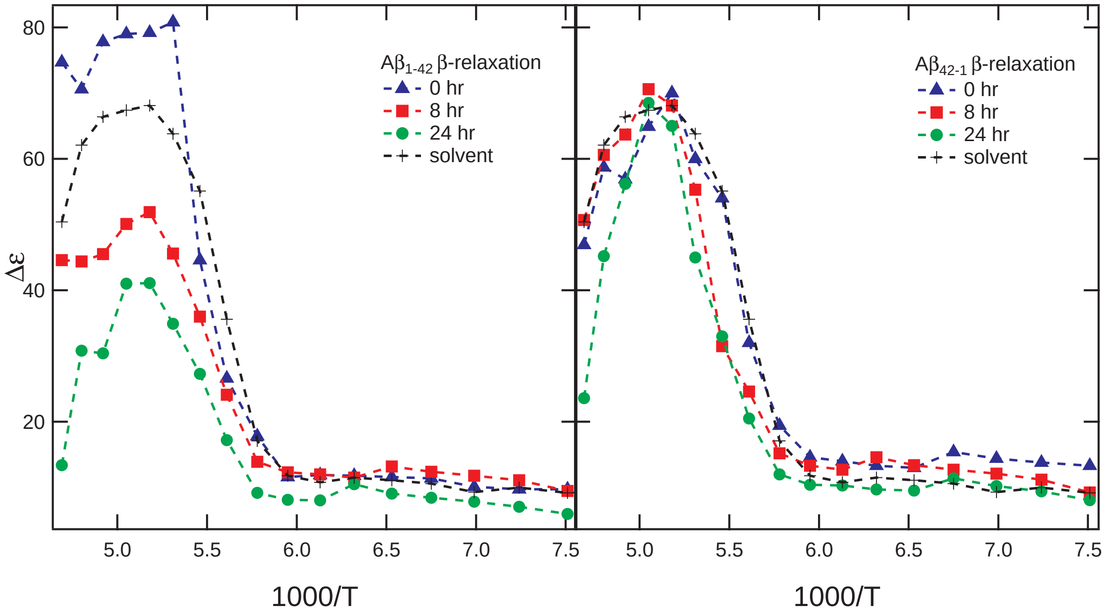

Figure 5.20: **Dielectric strength, $\Delta\varepsilon$ of the β-relaxation for $A\beta_{1-42}$ and $A\beta_{42-1}$ versus inverse temperature.** The dielectric strength for the $A\beta_{1-42}$ solution deceases to values less than the solvent over time. The decrease in dielectric strength indicates an anti-parallel β-sheet confirmation. The dielectric strength of $A\beta_{42-1}$ does not change and remains similar to the profile of the solvent.

5.3.2 Human and Rat Islet Amyloid Polypeptide

The dielectric spectra of human (hIAPP) and rat (rIAPP) islet amyloid polypeptide and the solvent show two relaxation processes (α and β) and low-frequency DC conductivity below 223K, depicted in Figure 5.21. At temperatures above 223K, the relaxation processes are either at frequencies above the range of the Alpha-A Analyzer or the conductivity dominates the spectra. The fast, α-relaxation process is clearly observed at 223K at a frequency of approximately 10^7 Hz in both the real and imaginary parts of the permittivity. The slower β-relaxation process is not easily observed until about 208K or 203K in the imaginary part of the permittivity but can be seen in the real part at 223K. At 203K, we determine that the β-relaxation occurs at 10^3 Hz and we estimate that it occurs at approximately 10^4 Hz at 223K.

With decreasing temperature the peaks of the α- and β-relaxation processes shift towards lower frequency. The α-process shifts faster than the β-process causing the two processes to merge below 203K and eventually cross at approximately 193K as shown in Figure 5.22. The α-process continues to shift to very low frequencies with decreasing temperature. At around 168K the α-process shifts to frequencies higher than our measured range. After the crossing of the two processes, the β-relaxation process dominates the dielectric spectra and shifts to approximately 1 Hz at 133K (Figure 5.23). Below 158K, the DC conductivity has decreased in magnitude and also shifted to frequency below the measured range.

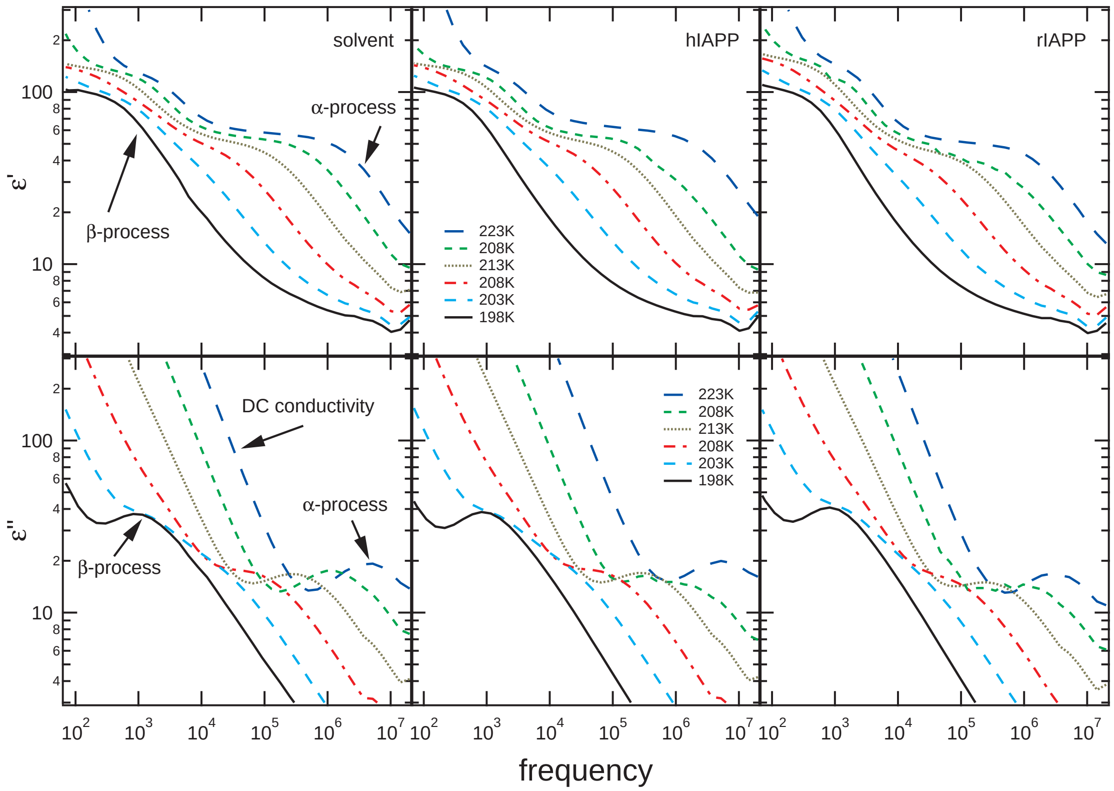

Figure 5.21: **Temperature evolution of the real and imaginary parts of the dielectric permittivity for the solvent, hIAPP, and rIAPP from 223K to 198K.** Two relaxation processes for the real (ε') and imaginary (ε'') parts of the permittivity for the solvent, hIAPP, and rIAPP are observed.

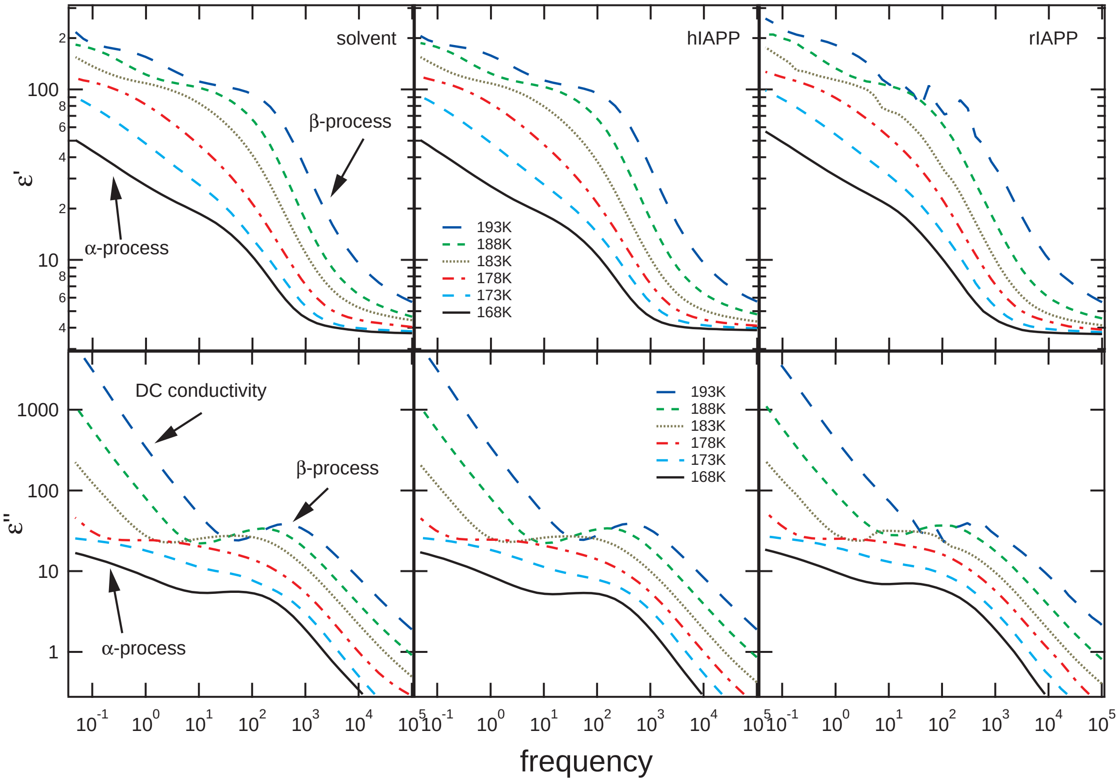

Figure 5.22: **Temperature evolution of the real and imaginary parts of the dielectric permittivity for the solvent, hIAPP, and rIAPP from 193K to 168K.** The α-relaxation process rapidly shifts to lower frequency with decreasing temperature. In the range of 193K to 188K the two processes cross to where the α-relaxation is at lower frequency than the β-relaxation process at temperatures of 183K and below.

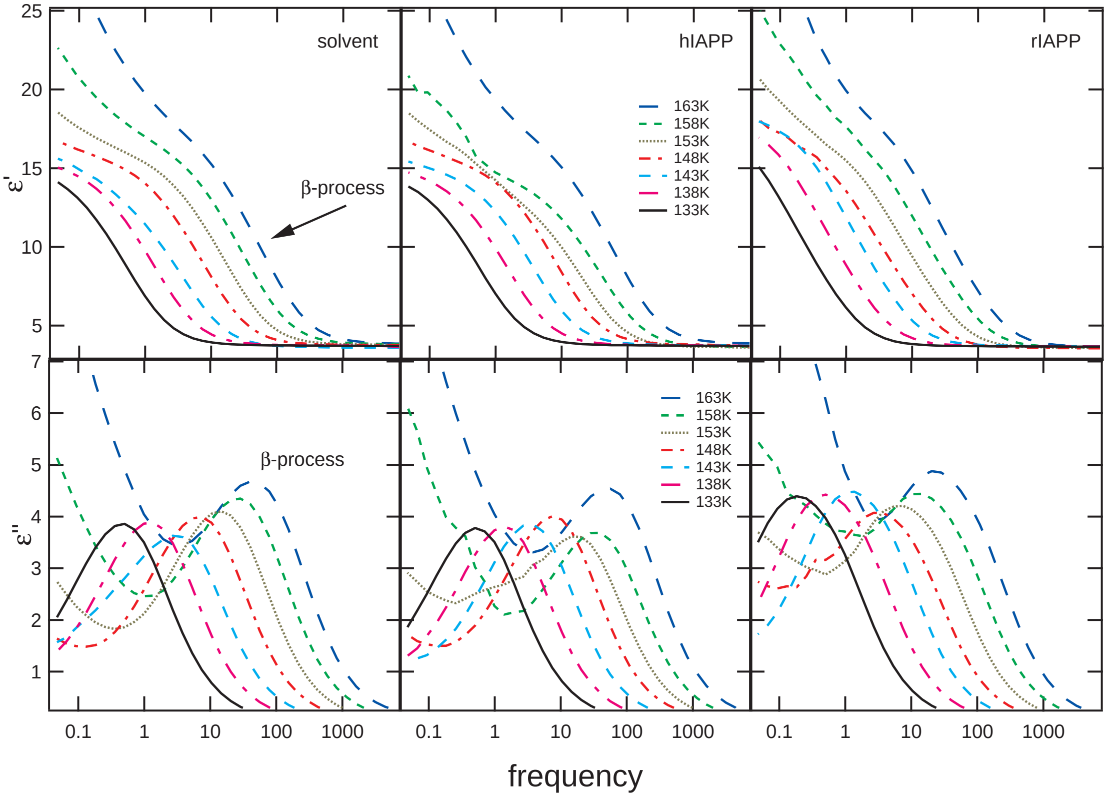

Figure 5.23: **Temperature evolution of the real and imaginary parts of the dielectric permittivity for the solvent, hIAPP, and rIAPP from 163K to 133K.** The β-relaxation process dominates below the crossing temperature and continues to slow to under 1 Hz. The DC conductivity has reduced in magnitude to outside the measured range below 158K.

Permittivity data for hIAPP and rIAPP were plotted against the solvent to compare the time-evolution of dielectric signal. Data were collected after 0, 24, 48, and 120 hours of incubation at room temperature. The dielectric loss of hIAPP and rIAPP as compared to the solvent over the observable temperature range 223K-133K is shown in Figures 5.24 - 5.33.

The magnitude dielectric loss peaks of the rIAPP shifts over time towards the signal of the solvent. Above the α-β relaxation crossing temperature of 193K where the α-process dominates the spectra, the magnitude of the dielectric loss of rIAPP steadily increases towards the solvent as seen in Figure 5.25. In the crossing region of 193K - 183K where the processes occur at similar frequency, Figures 5.27 and 5.29 show that the dielectric signal of rIAPP in both frequency and magnitude are nearly overlapping with the solvent after 120 hours. At temperatures of 168K and below where the β-process dominates the spectra, the magnitude and peak frequency of rIAPP continues to move toward the signal of the solvent. Figures 5.29 - 5.33 show that the peak frequency of the beta process of rIAPP increases over time for each temperature below 178K.

The magnitude of the dielectric loss peaks of the hIAPP follows a different trend than the rIAPP. Above the α-β relaxation crossing temperature of 193K where the α-process dominates the spectra, the magnitude of hIAPP starts near the solvent but then steadily decreases as seen in Figure 5.24. In the crossing region of 193K - 183K where the processes occur at similar frequency, Figures 5.26 and 5.28 show that the dielectric signal of hIAPP in both frequency and magnitude are nearly overlapping from 0-48 hours, but the permittivity at 120 hours is much less than that of the solvent. At temperatures of 168K and below where the β-process dominates the spectra, the magnitude of hIAPP increase over time as compared to the solvent as shown in Figures 5.28 - 5.32. Additionally, the peak frequency of the beta process of hIAPP decreases over time.

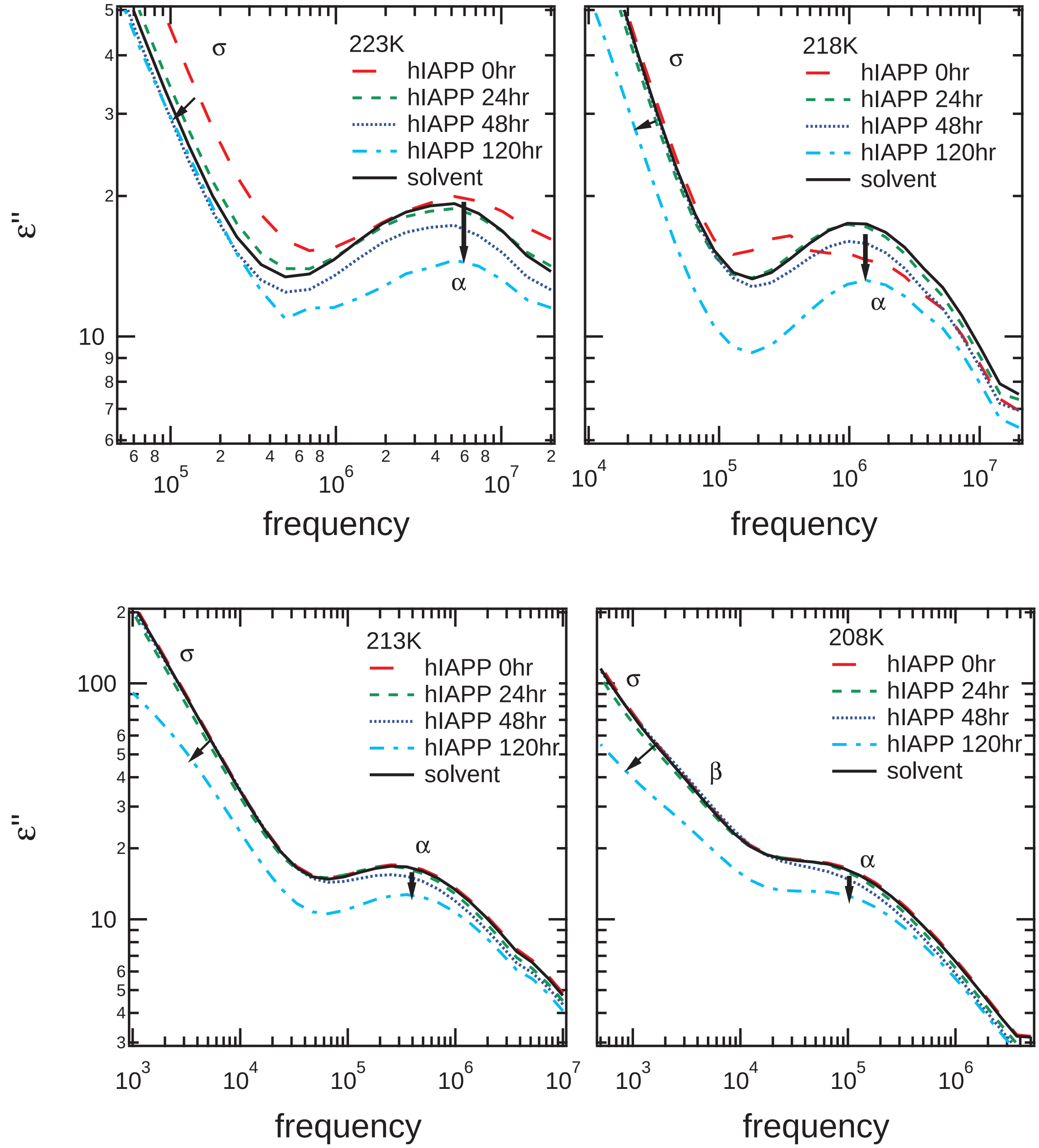

Figure 5.24: **Dielectric loss ε'' as a function of frequency for hIAPP in the range of 223K-208K and incubation periods of 0, 24, 48, and 120 hours.** At temperatures above 208K, the β-relaxation process is masked by the conductivity, σ. The arrows depict a decrease in magnitude of ε'', due to the decrease in σ over time. The α-relaxation peak shows a shift at 223K and 218K at 0 hours, but does not appear to follow a trend.

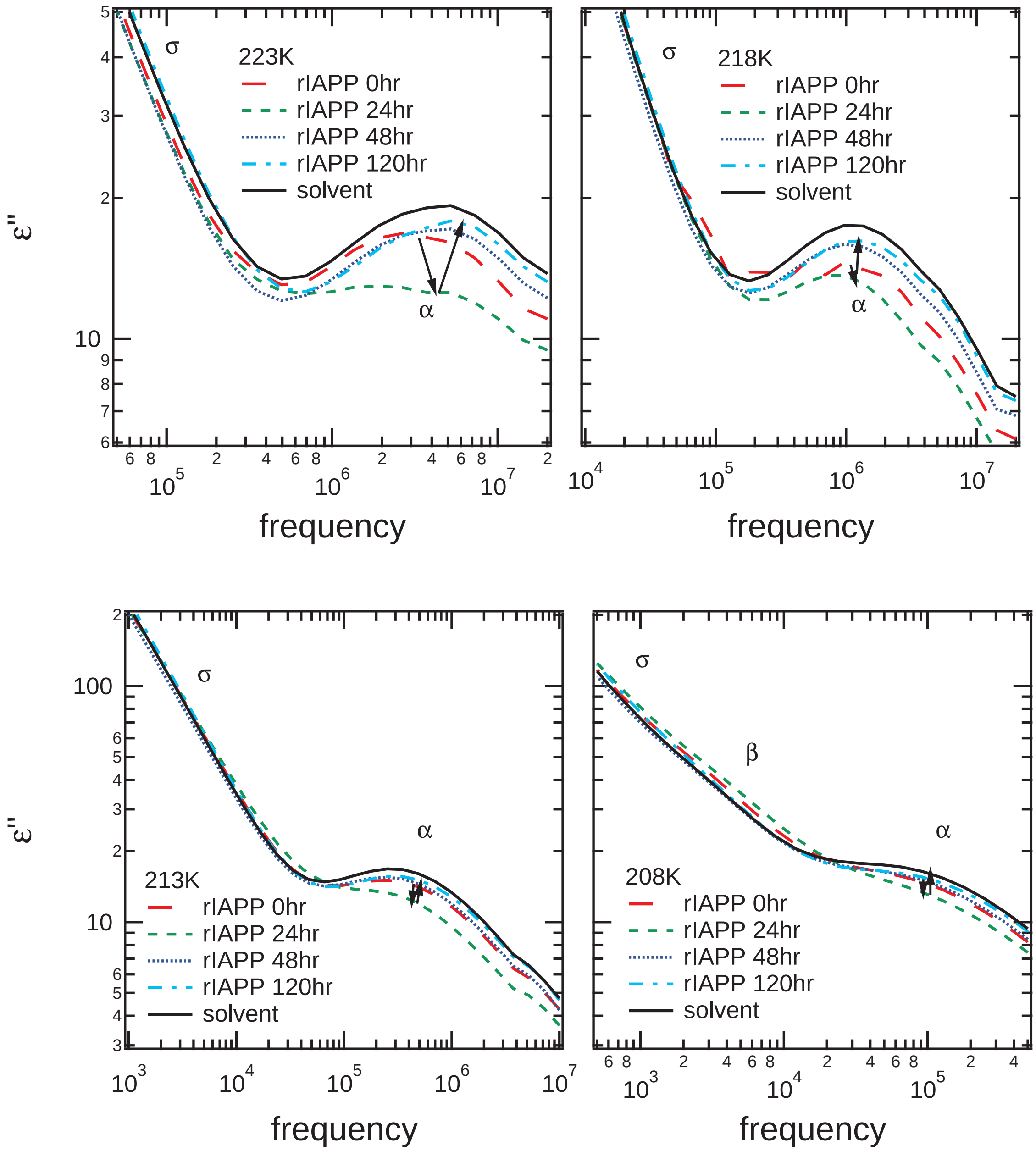

Figure 5.25: **Dielectric loss ε'' as a function of frequency for rIAPP in the range of 223K-208K and incubation periods of 0, 24, 48, and 120 hours.** At temperatures above 208K, the β-relaxation process is masked by the conductivity, σ. The arrows depict an apparent shift in the α-relaxation process first to lower magnitude and frequency, then higher magnitude and frequency. This differs in behavior to hIAPP in the same temperature range.

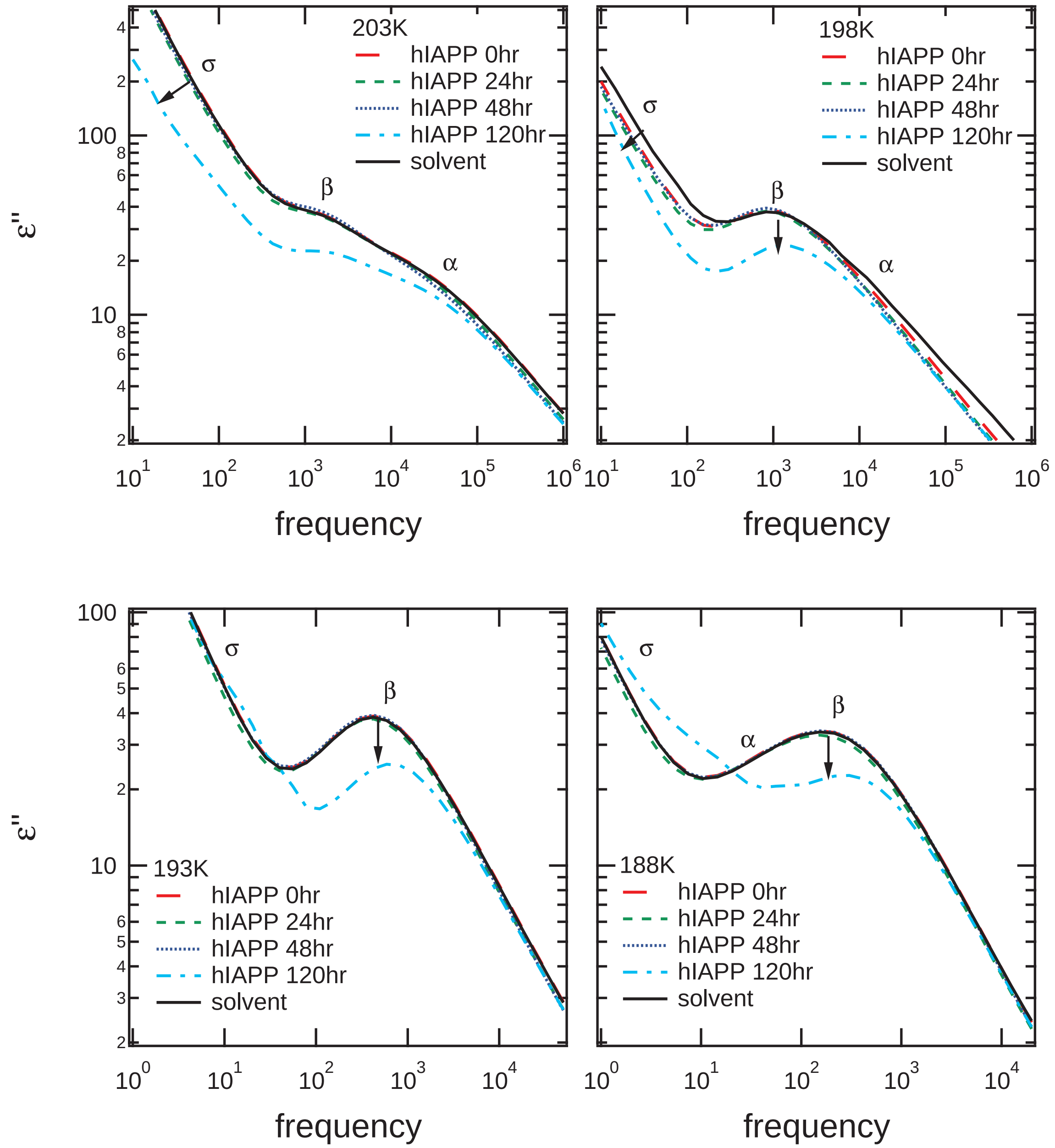

Figure 5.26: **Dielectric loss ε'' as a function of frequency for hIAPP in the range of 203K-188K and incubation periods of 0, 24, 48, and 120 hours.** At 193K, the α-process occurs at near the same frequency as the β-process but with lower magnitude. The arrows depict trends of the conductivity, σ to lower magnitude at 203K and 198K, however trends in the permittivity at 193K and 188K appear to be due to relaxation processes.

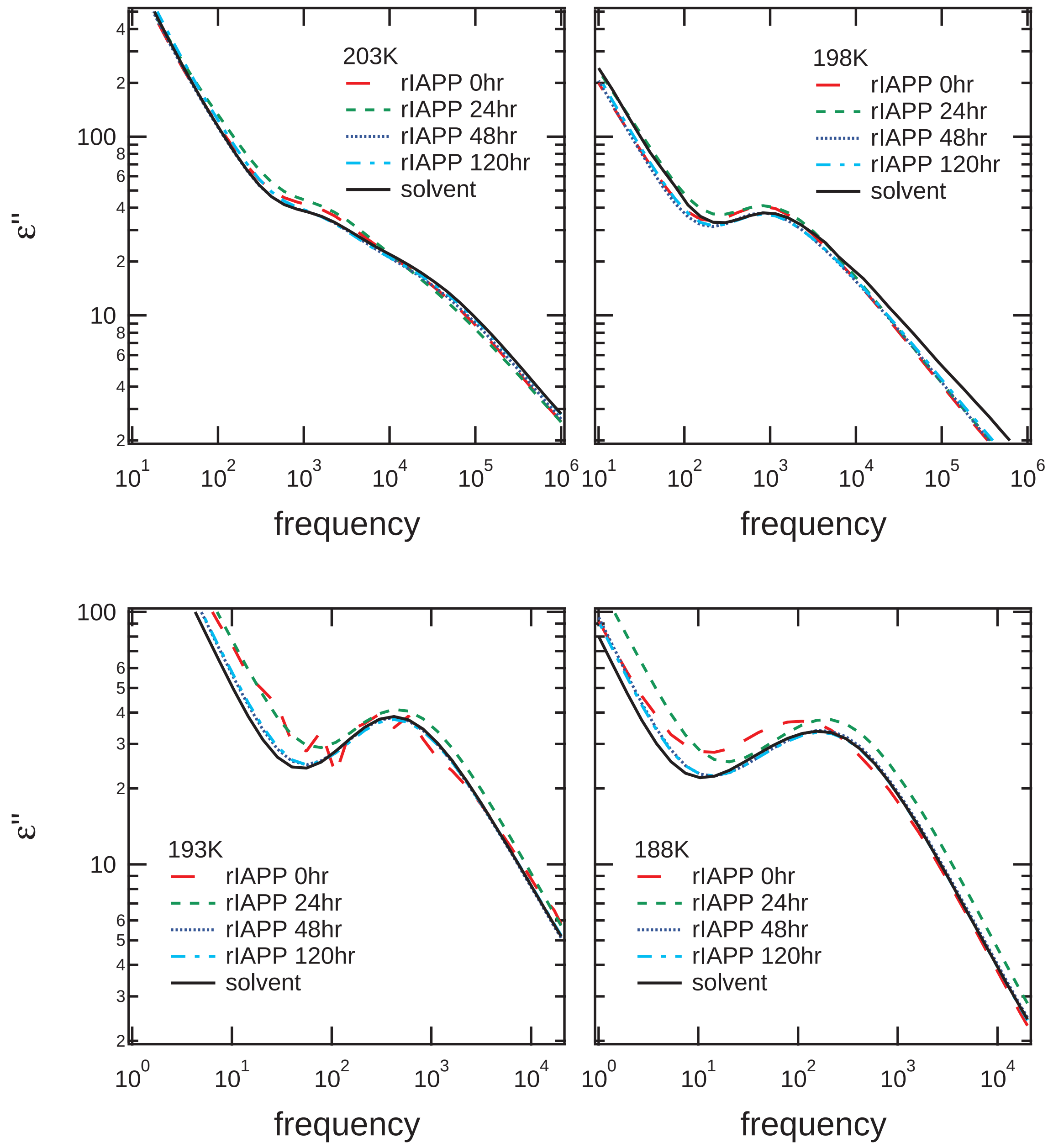

Figure 5.27: **Dielectric loss ε'' as a function of frequency for rIAPP in the range of 203K-188K and incubation periods of 0, 24, 48, and 120 hours.** At 193K, the α-process occurs at near the same frequency as the β-process but with lower magnitude. At 193K and 188K, there are some shifts in the the conductivity, σ, but it does not appear to follow a trend over time.

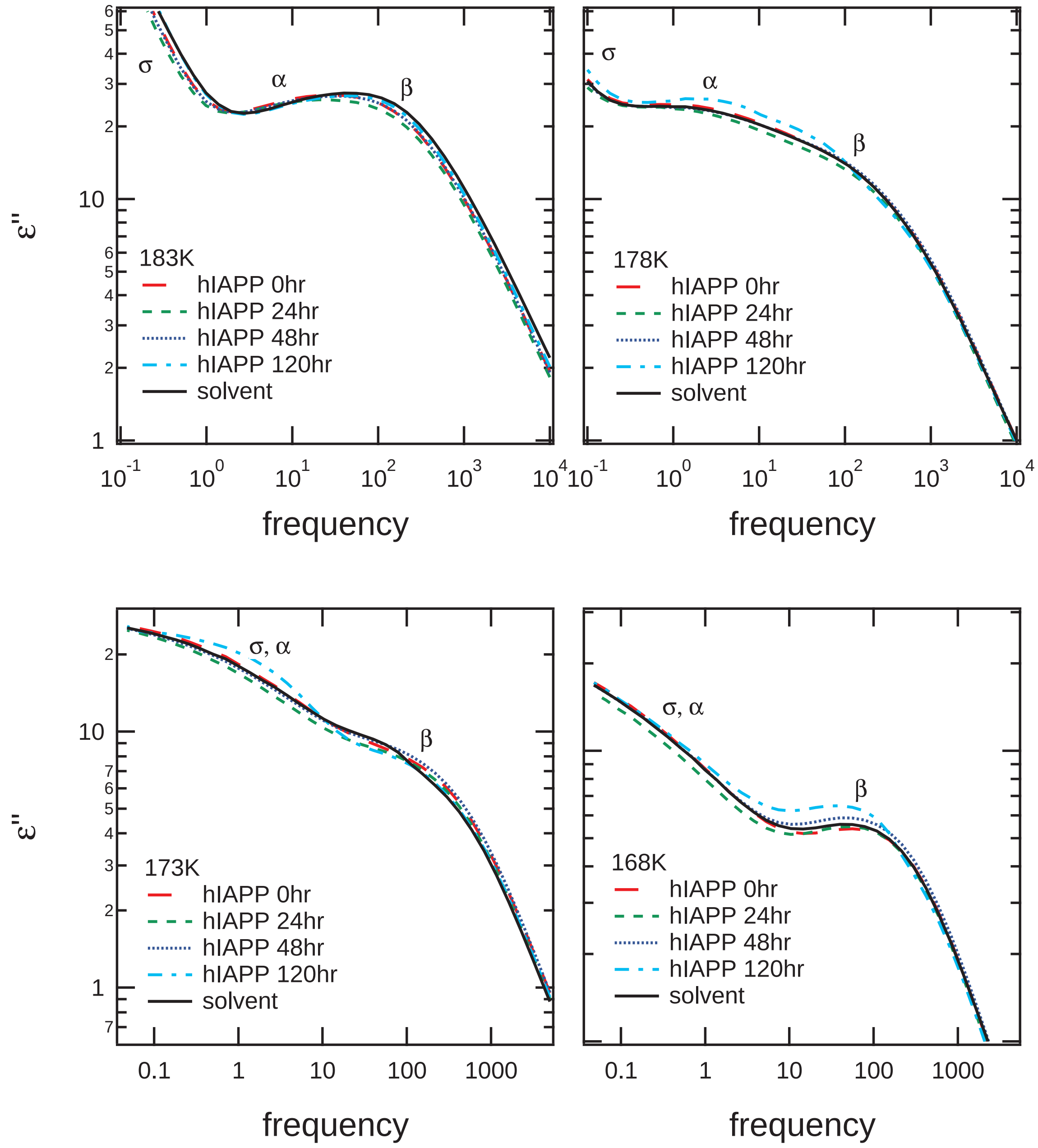

Figure 5.28: **Dielectric loss ε'' as a function of frequency for hIAPP in the range of 183K-168K and incubation periods of 0, 24, 48, and 120 hours.** In the range of 183K-168K, there is significant mixing between σ, α-, and β-processes. Trends in this range are indeterminate.

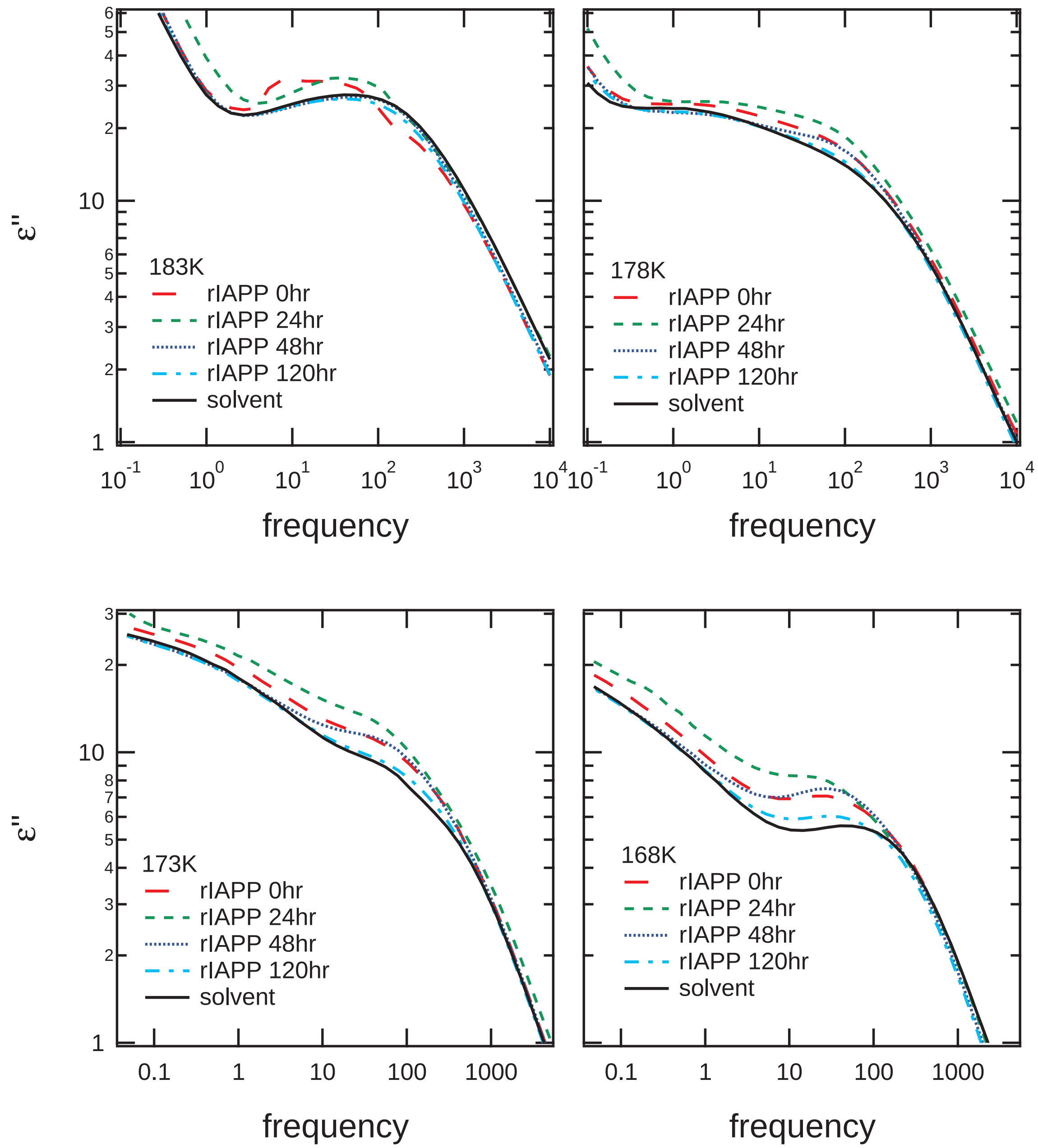

Figure 5.29: **Dielectric loss ε'' as a function of frequency for rIAPP in the range of 183K-168K and incubation periods of 0, 24, 48, and 120 hours.** In the range of 183K-168K, there is significant mixing between σ, α-, and β-processes. Trends in this range are indeterminate.

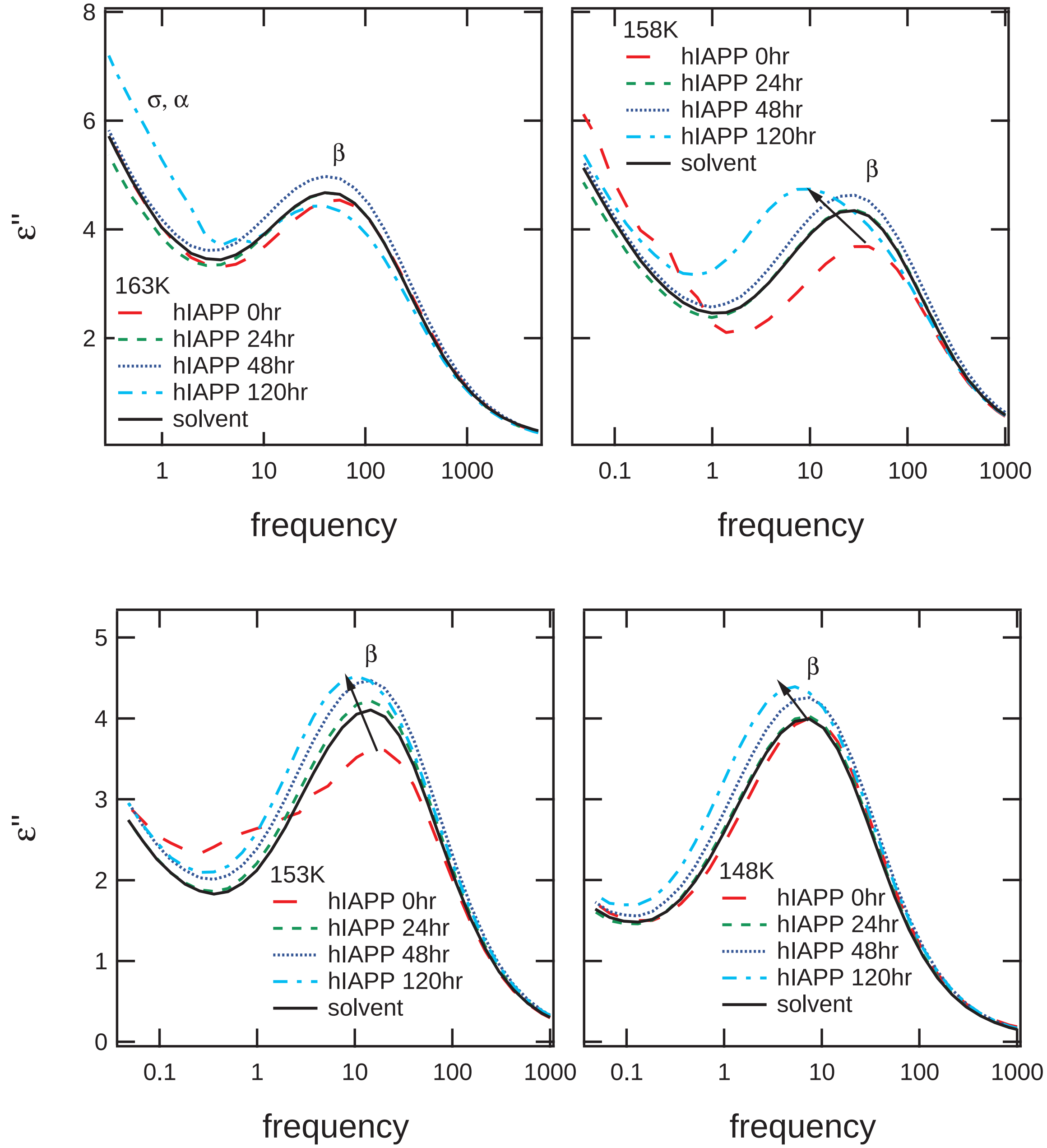

Figure 5.30: **Dielectric loss ε'' as a function of frequency for hIAPP in the range of 163K-148K and incubation periods of 0, 24, 48, and 120 hours.** At 158K, the conductivity, σ and the α-process are substantially separated from the β process. At 158K and below, the β-relaxation peak in ε'' trends to higher magnitude and lower frequency over time.

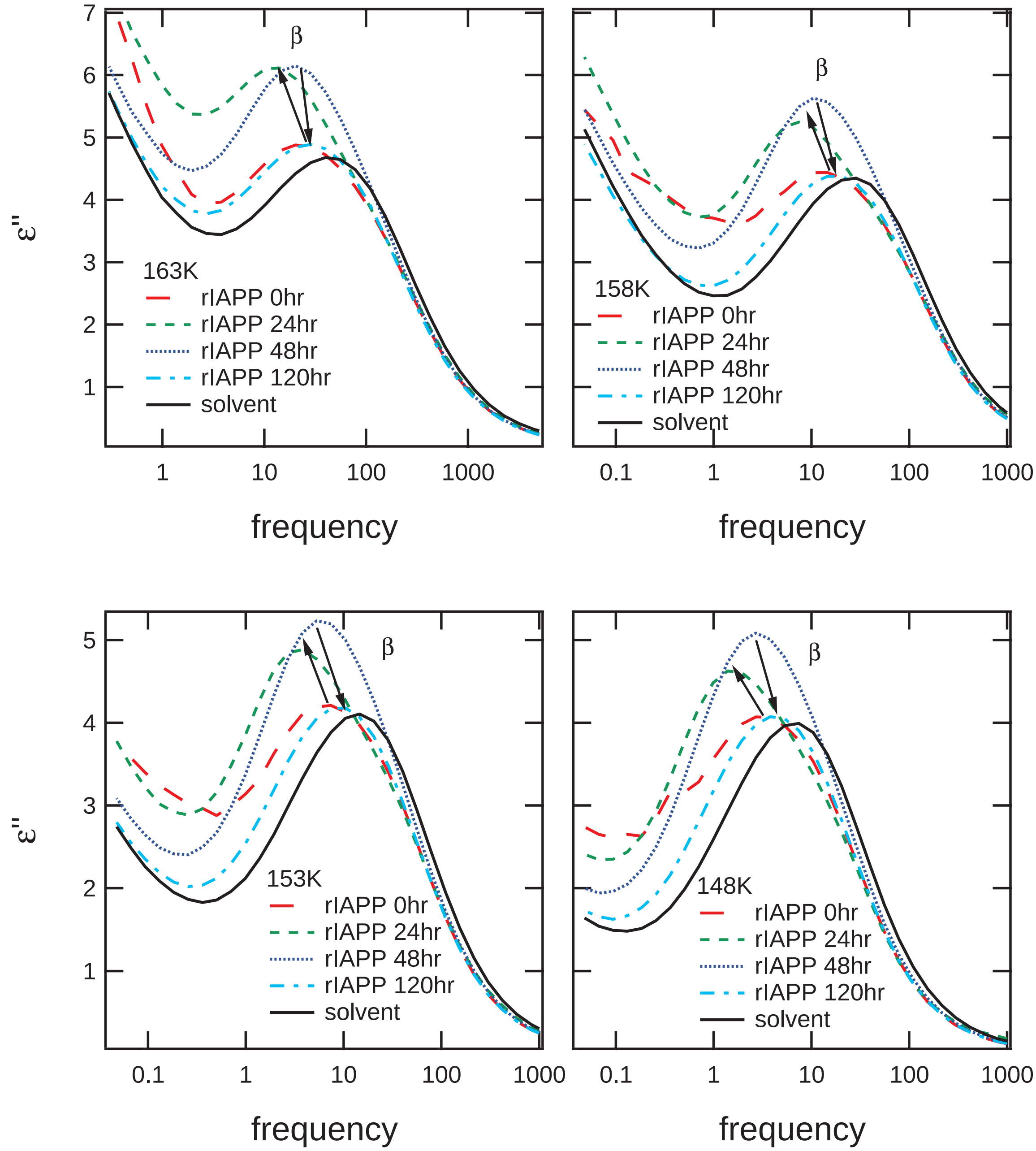

Figure 5.31: **Dielectric loss ε'' as a function of frequency for rIAPP in the range of 163K-148K and incubation periods of 0, 24, 48, and 120 hours.** At 158K, the conductivity, σ and the α-process are substantially separated from the β process. At 158K and below, the β-relaxation peak first shifts to lower frequency and higher magnitude, then shifts to higher frequency and lower magnitude towards the spectra of the solvent. This differs in behavior from that of hIAPP in the same temperature range.

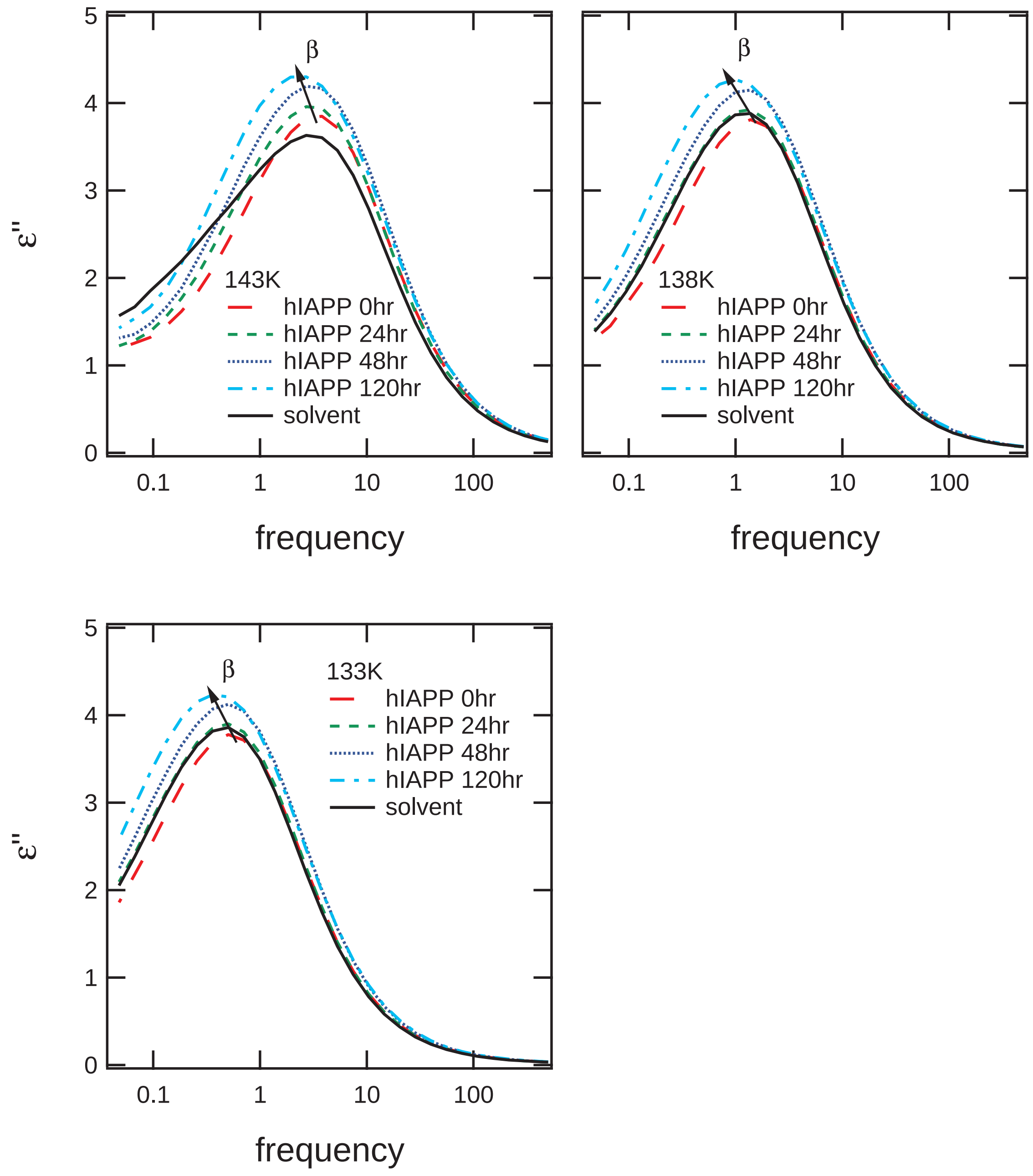

Figure 5.32: **Dielectric loss ε'' as a function of frequency for hIAPP in the range of 143K-133K and incubation periods of 0, 24, 48, and 120 hours.** The β-relaxation peak in ε'' trends to higher magnitude and lower frequency over time.

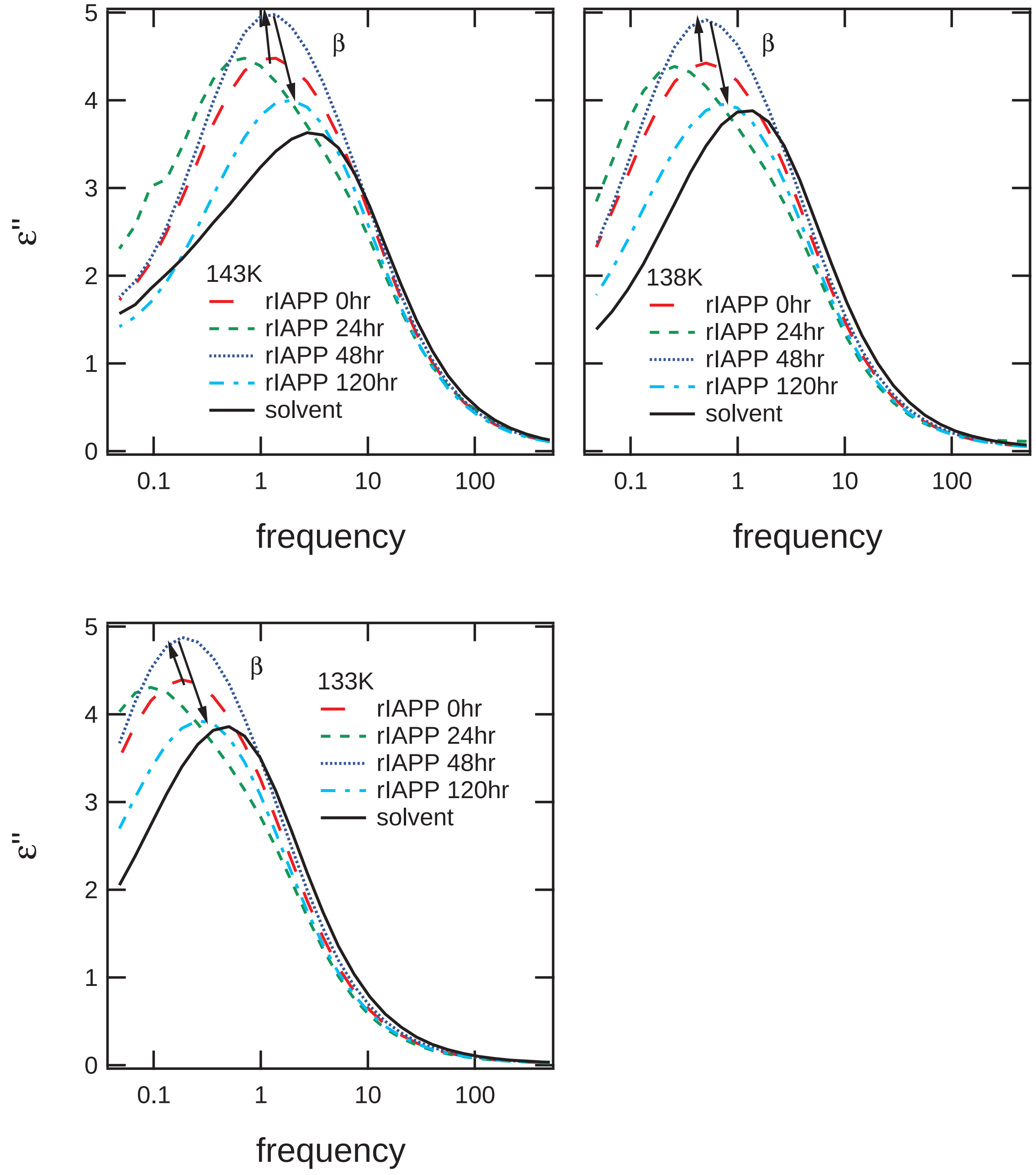

Figure 5.33: **Dielectric loss ε'' as a function of frequency for rIAPP in the range of 143K-133K and incubation periods of 0, 24, 48, and 120 hours.** The β-relaxation peak first shifts to lower frequency and higher magnitude, then shifts to higher frequency and lower magnitude towards the spectra of the solvent. This differs in behavior from that of hIAPP in the same temperature range.

Dielectric permittivity data for hIAPP, rIAPP, and the solvent were modeled using the WinFIT program for each temperature from 223K to 133K and at incubation time points 0, 24, 48, and 120 hours. The β-relaxation process is best-fit to a Cole-Davidson with the symmetric broadening parameter, β remaining relatively constant over the entire temperature range at approximately 0.8. The α-relaxation process demonstrates both symmetric and asymmetric broadening over the observed temperature range with both β and γ spreading parameters changing with temperature.

The α-relaxation process is observed from 223K to 168K, though in the crossing temperatures of 198K to 183K, it overlaps with the β-process. During this temperature range, the β-relaxation process dominates. The β-relaxation process is observed between approximately 208K down to the lowest temperature, 133K. At temperatures above 208K, the DC conductivity dominates the spectra in the region of the β-relaxation. Examples of curve fitting performed at representative temperatures are shown in Figures 5.34 - 5.37.

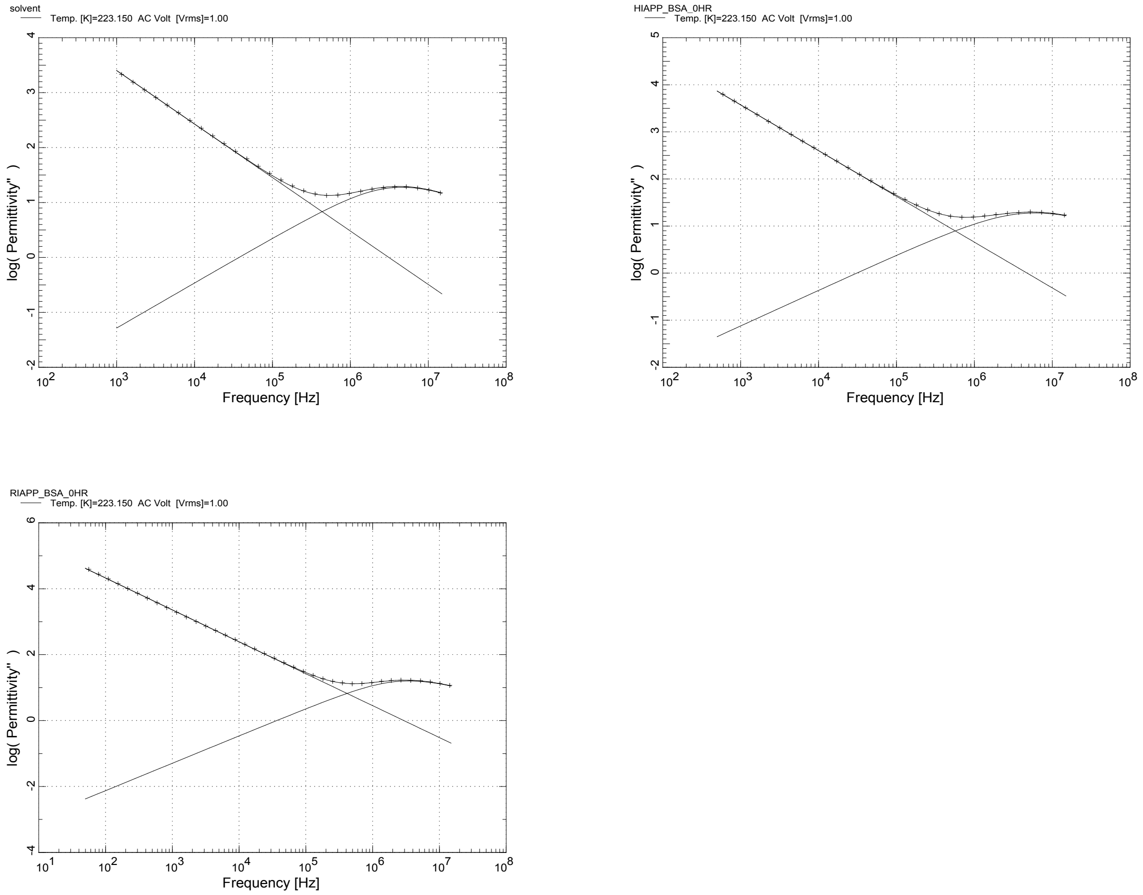

Figure 5.34: **Curve fitting of imaginary part of the permittivity data using the WinFIT program of the solvent, hIAPP, and rIAPP at 223K.** A large, low frequency DC conductivity is fit with a power law. The α-relaxation process at around 10^7 Hz is fit with a Havriliak-Negami function. The β-relaxation function is not observed. The RMSD of the fits are 0.015, 0.016, and 0.034, respectively.

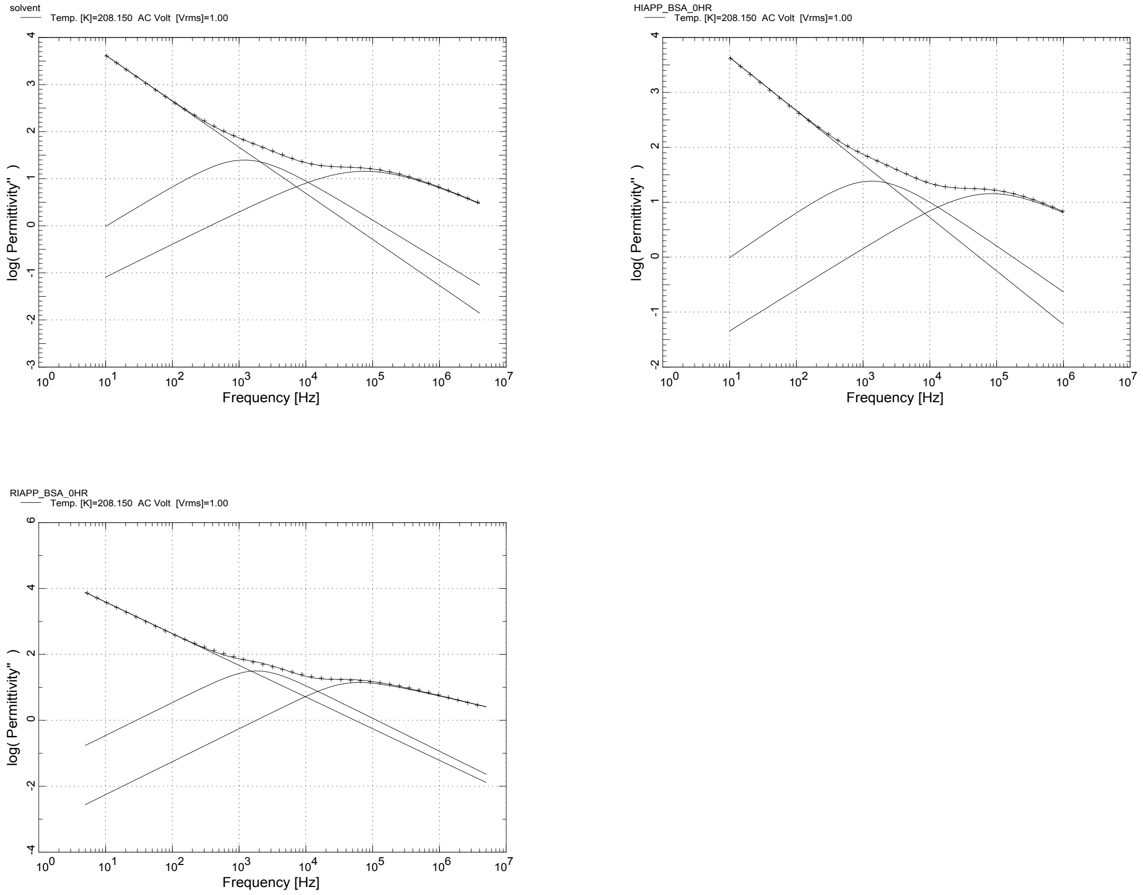

Figure 5.35: **Curve fitting of imaginary part of the permittivity data using the WinFIT program of the solvent, hIAPP, and rIAPP at 208K.** A large, low frequency DC conductivity is fit with a power law. The β-relaxation process at around 10^3 Hz is fit with a Cole-Davidson function and the α-relaxation process at around 10^5 Hz is fit with a Havriliak-Negami function. The RMSD of the fits are 0.018, 0.007, and 0.020, respectively.

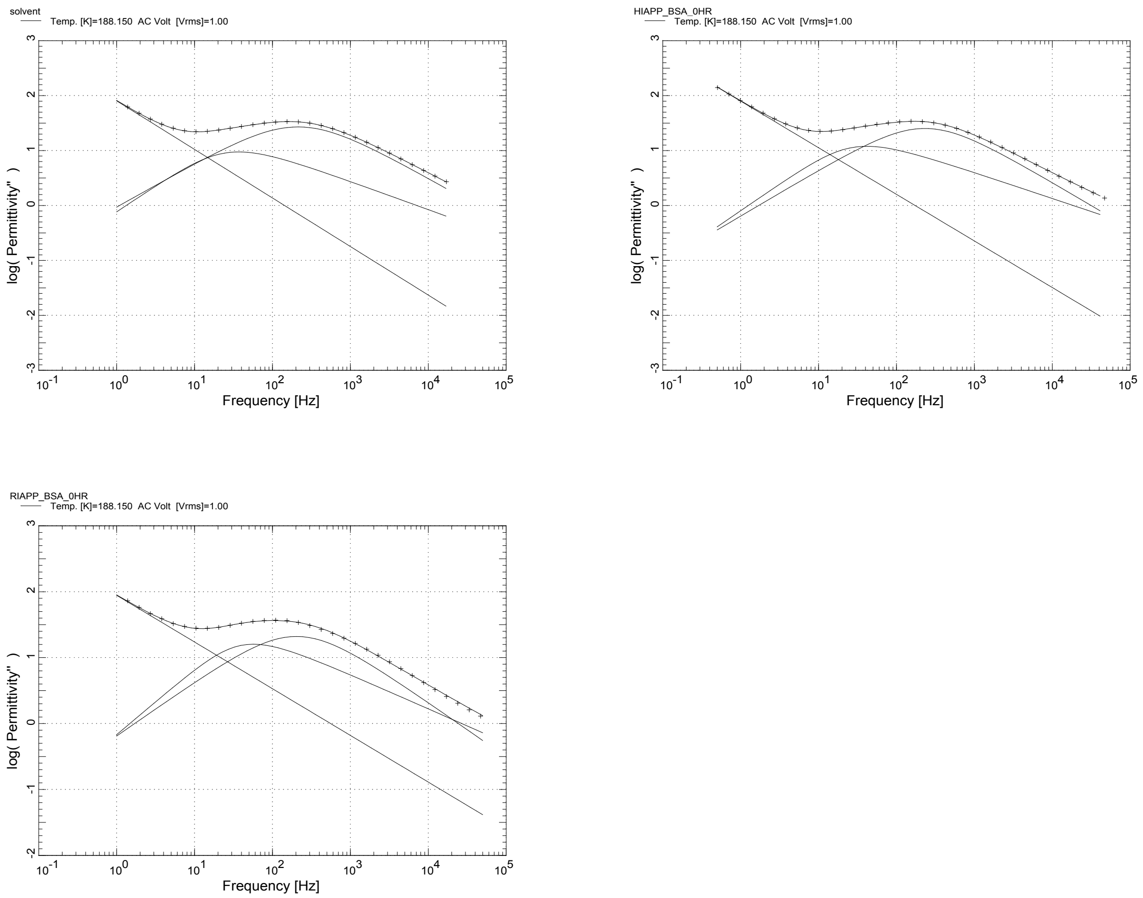

Figure 5.36: **Curve fitting of imaginary part of the permittivity data using the WinFIT program of the solvent, hIAPP, and rIAPP at 188K.** A large, low frequency DC conductivity is fit with a power law. The β-relaxation process at around 10^3 Hz is fit with a Cole-Davidson function and the α-relaxation process at around 10^1 Hz is fit with a Havriliak-Negami function. Here, the α process has crossed over to slower than β relaxation times. The RMSD of the fits are 0.001, 0.006, and 0.008, respectively.

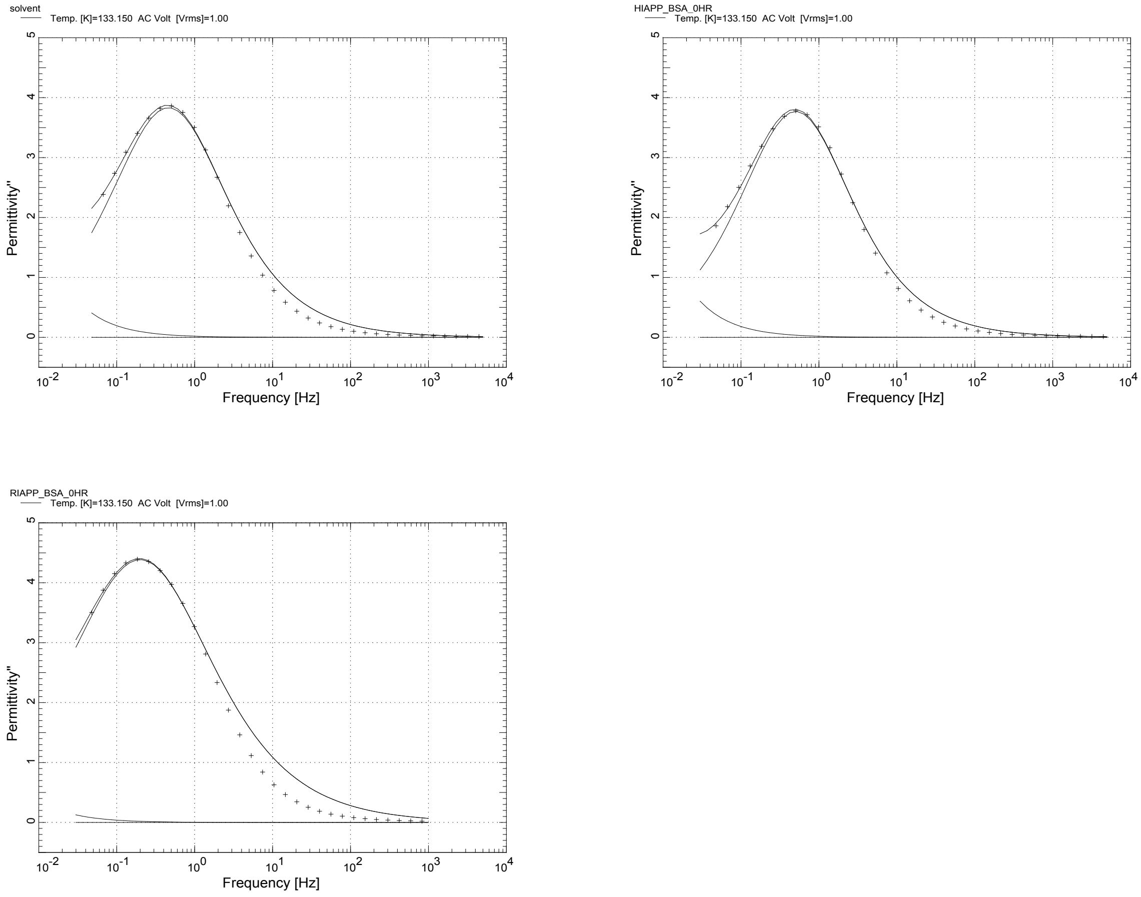

Figure 5.37: **Curve fitting of the imaginary part of the permittivity data using the WinFIT program of the solvent, hIAPP, rIAPP at 133K.** A small, very low frequency DC conductivity is fit with a power law. The β-relaxation process at around 1 Hz is fit with a Cole-Davidson function and the α-relaxation process is not observed. The RMSD of the fits are 0.073, 0.090, and 0.035, respectively.

The maximum frequency, f_{max} of ε'' of both the α- and β-relaxation processes were determined from the model function curve fitting of the permittivity data at all temperatures. Arrhenius plots of f_{max} versus inverse temperature, 1000/T were created for each process. The β-relaxation process follows a linear, or Arrhenius behavior throughout the temperature range. The α-relaxation process follows a slight non-linear Vogel-Fulcher-Tammann (VFT)-type behavior that is expected in glass-forming solvents such as glycerol (Figures 5.38 - 5.40). Activation energies for the β process and glass-forming fragilities for the α process were determined from the Arrhenius and VFT analysis and presented in Tables 5.3 and 5.4.

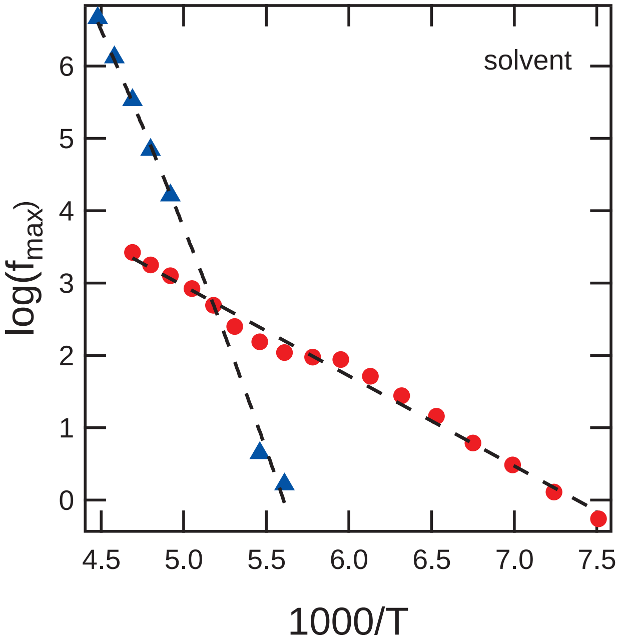

Figure 5.38: **Arrhenius plots of f_{max} versus inverse temperature for solvent over time.** The α-relaxation process follows a VFT behavior whereas the β-relaxation process follows an Arrhenius, or linear behavior.

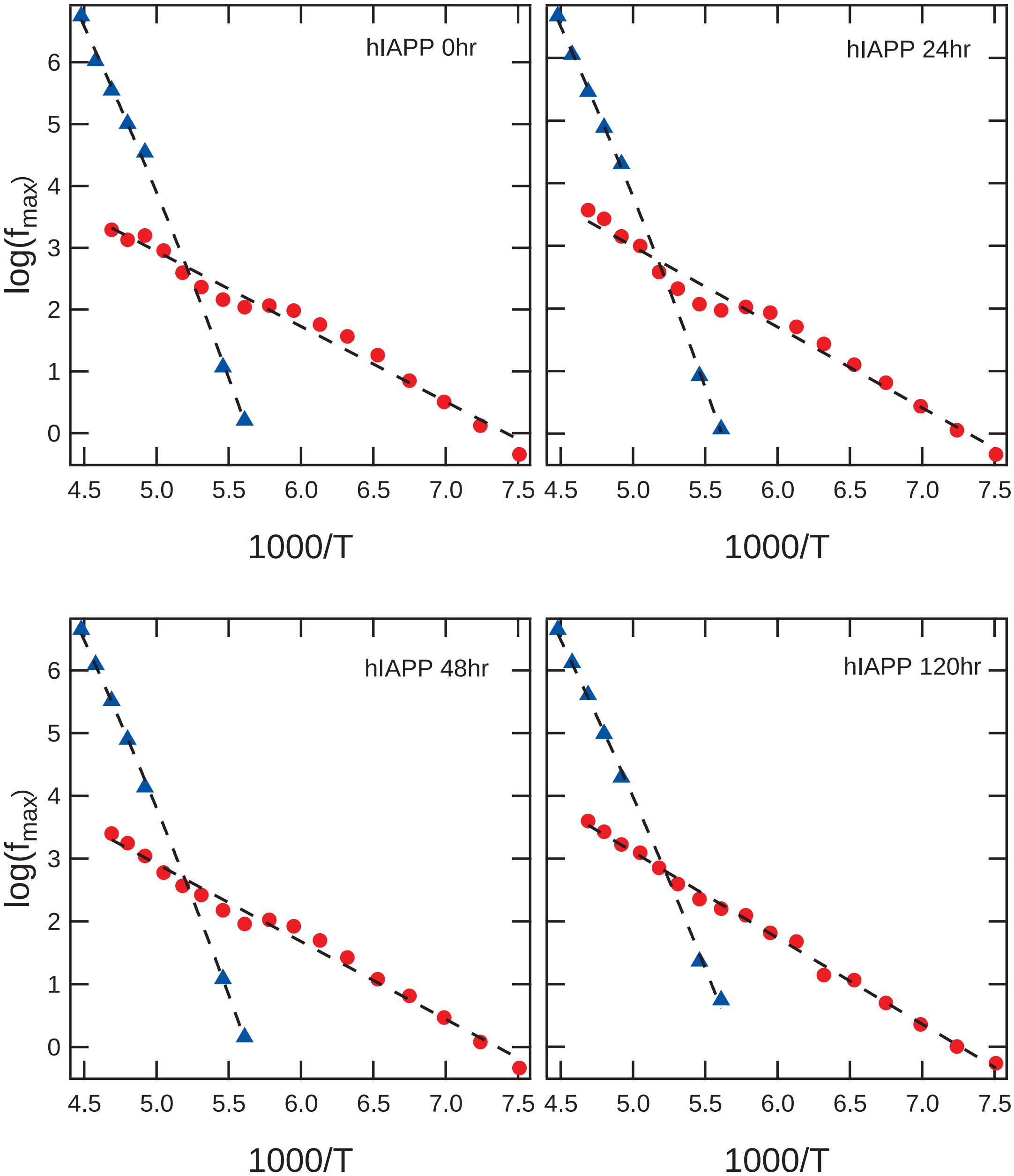

Figure 5.39: **Arrhenius plots of f_{max} versus inverse temperature for hIAPP from 0-120 hours.** The α-relaxation process follows a VFT behavior whereas the β-relaxation process follows an Arrhenius, or linear behavior. The α-process departs from the VFT curvature at low temperature.

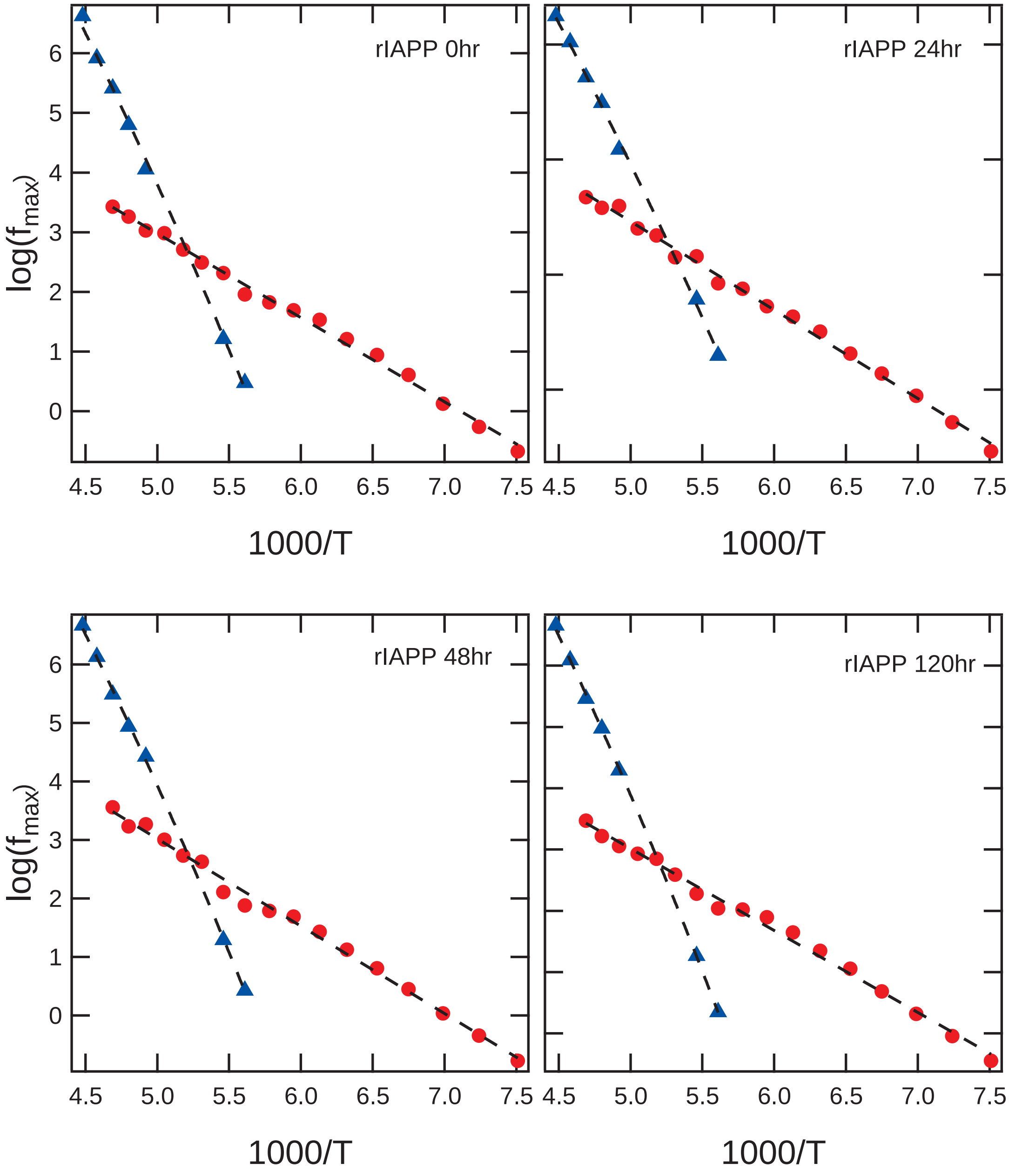

Figure 5.40: **Arrhenius plots of f_{max} versus inverse temperature for rIAPP from 0-120 hours.** The α-relaxation process follows a VFT behavior whereas the β-relaxation process follows an Arrhenius, or linear behavior. The α-process departs from the VFT curvature at low temperature.

	time	A	B	E_A (kJ/mol)		*time*	A	B	E_A (kJ/mol)
hIAPP	0hr	9.02	1.216	23.3	rIAPP	0hr	10.0	1.412	27.0
	24hr	9.44	1.289	24.7		24hr	10.6	1.540	29.5
	48hr	9.10	1.237	23.7		48hr	10.5	1.494	28.6
	120hr	9.97	1.373	26.3		120hr	9.70	1.338	25.6
solvent		9.18	1.245	23.8	solvent		9.18	1.245	23.8

Table 5.3: Parameters of the linear fits to the β-relaxation measurements of $\log(f_{max}(T))$ of the form $A + BT$.

	time	$\log f_\infty$	D	T_0 (K)		*time*	$\log f_\infty$	D	T_0 (K)
hIAPP	0hr	22	32	72	rIAPP	0hr	22	40	63
	24hr	22	32	73		24hr	22	44	59
	48hr	22	33	71		48hr	22	36	67
	120hr	22	40	62		120hr	22	35	69
solvent		22	31	74	solvent		22	31	74

Table 5.4: Parameters of the VFT fits to the α-relaxation measurements of $f_{max}(T)$ of the form $\log(f_{max}) = \log(f_\infty(T)) - \frac{DT_0}{T-T_0}$

The α-relaxation process for hIAPP, rIAPP, and the solvent display VFT behavior down to 183K. Below 183K, the curvature of the VFT changes where the temperature dependance of f_{max} would be better approximated by another VFT or different empirical fit function. Studies have shown that two or more temperature-dependent fit functions may be necessary to describe the behavior of the α-relaxation of glass formers such as glycerol [63, 165]. The departure of the VFT behavior occurs at approximately the glass transition of glycerol, indicating that the change in temperature dependance may be due to the phase change. Whereas the α-relaxation process is representative of large scale structural fluctuations in the solvent, it is conceivable that a phase transition could change the temperature dependance of the relaxation rate.

Studies of the dielectric strength of hIAPP and rIAPP in serum confirm the studies done in deionized water. Figure 5.41 shows that over time, hIAPP displayed a series of increases and decreases in the dielectric strength as fibril formation progresses, with a final dielectric strength much less than the solvent at 120 hours. The non-amyloidogenic rIAPP did not change over time. The increase and decrease cycles for hIAPP may be due to a mixture of both parallel and anti-parallel β-sheet conformations dominating at different phases of the aggregation process, but here we see a final state that would appear to be anti-parallel in nature.

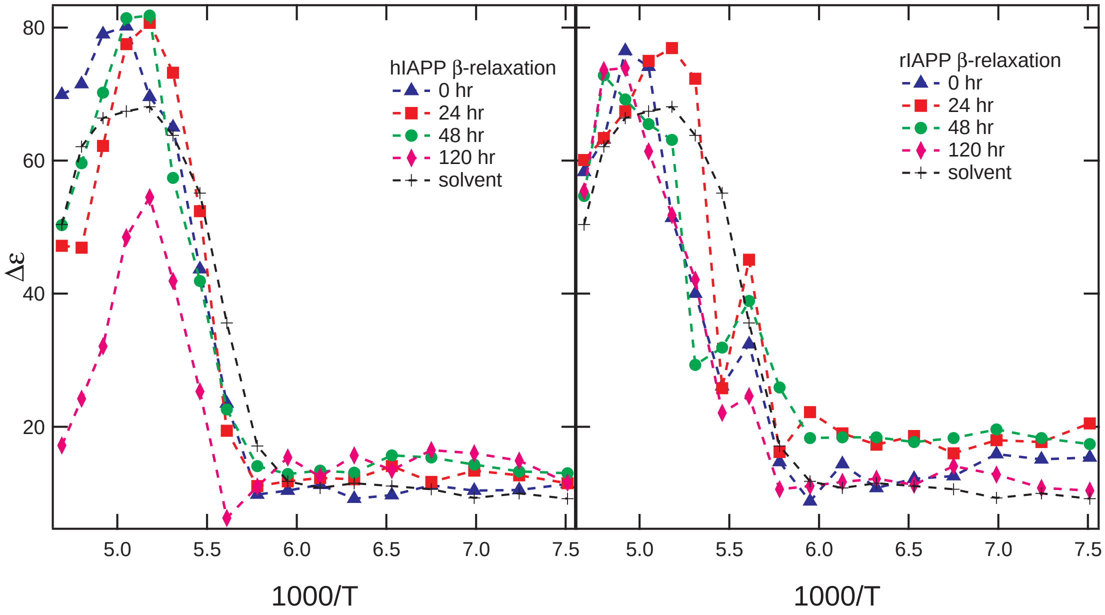

Figure 5.41: **Dielectric strength, $\Delta\varepsilon$ of the β-relaxation for hIAPP and rIAPP versus inverse temperature.** The dielectric strength for the hIAPP solution remains relatively constant for the first 48 hours, then deceases to values less than the solvent after 120 hours of incubation. This may be an indication that the final aggregated state of hIAPP in serum is an anti-parallel β-sheet. The dielectric strength of rIAPP was similar to the solvent for all time points. This is a similar $\Delta\varepsilon$ behavior of $A\beta_{1-42}$ and $A\beta 42-1$ observed for the same solvent.

5.4 Conclusions

We have demonstrated the dielectric response of $A\beta_{1-42}$, scrambled $A\beta_{42-1}$, hIAPP, and rIAPP in the presence of a BSA-glycerol solvent. The spectra reveal that these amyloidogenic peptides can be detected and differentiated from their non-amyloidogenic analogs in the presence of other proteins and biological substances, similar to *in vivo* conditions. This is a crucial step in demonstrating the viability of using dielectric relaxation spectroscopy as a tool for detecting amyloidogenic peptides in biological fluids, such as blood serum.

Studies at low temperature reveal that the β-process displays a characteristic "red-shift" in the permittivity in both $A\beta_{1-42}$ and hIAPP that is not observed in $A\beta_{42-1}$ and rIAPP (see Figure 5.42). Theory predicts that this red-shift occurs due to a hinderance of the rotational motion of molecular dipoles in structured, biological water [64, 166]. This restructuring of the hydrogen bond network as a result of hydrophobic interactions causes a reduction in the hydrogen bond exchange. We also observed the red-shift in the hIAPP measurements in deionized water (see Figure 4.42) but not previously in $A\beta_{1-42}$.

Studies of the dielectric strength over a range of temperatures and incubation times show that determination of β-sheet conformation by dielectric spectroscopy is in agreement with previous studies done using FTIR and solid state NMR. The $A\beta_{1-42}$ displayed anti-parallel characteristics and the hIAPP displayed both parallel and anti-parallel signatures. The non-amyloidogenic peptides produced dipole moments that would be consistent with random coil or non-aggregating proteins.

The change in dielectric strength of the peptides in serum is a further extension to the information presented in deionized water buffer. Both $A\beta_{1-42}$ and hIAPP displayed a decrease in the dielectric strength from start to final time points. The $A\beta_{1-42}$ displayed a larger decrease and in shorter time, indicating that $A\beta_{1-42}$ may form oligomers and fibrils faster than hIAPP. The lack of changing dielectric strength

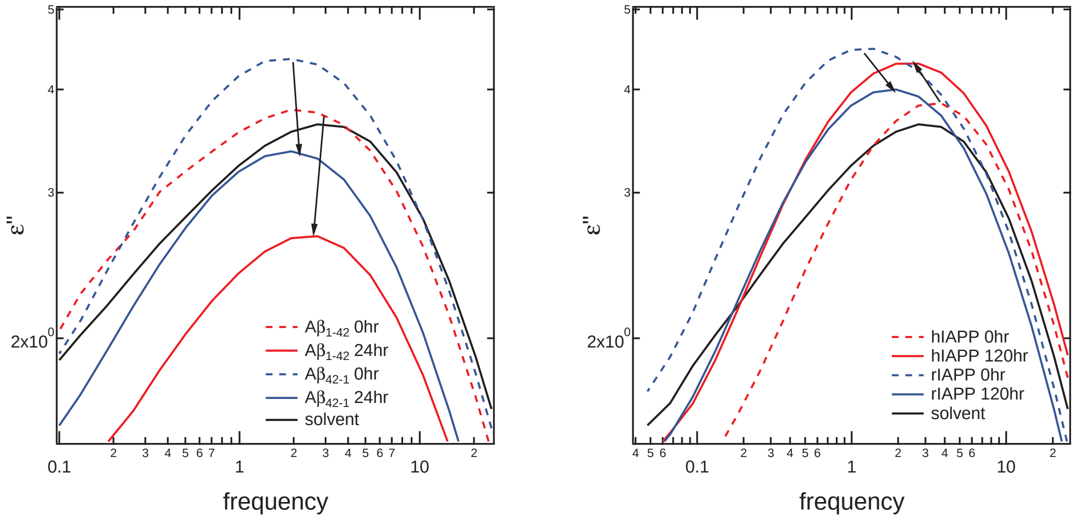

Figure 5.42: **Plots of the β-relaxation peak shift at 143K for $A\beta_{1-42}/A\beta_{42-1}$ and hIAPP/rIAPP as compared to the solvent.** The amyloidogenic peptides demonstrate a characteristic ”red- shift” towards tower frequencies, indicating an increase in structured water.

for both non-amyloidogenic peptides $A\beta_{42-1}$ and rIAPP was expected for a random aggregation of protein lacking a β-sheet.

Chapter 6

Conclusion

6.1 General Conclusions

At present, there is no unequivocal method for the early detection for amyloid-related diseases such as Alzheimer's and Type II Diabetes. Although it was long believed that amyloidogenic diseases were caused by highly organized fibrillar aggregates, recent theory and experiment has shown that the soluble oligomer forms of these peptides are the most toxic form. Amyloid oligomers circulate freely through bodily fluids [18, 17, 16] and thus, detection of soluble amyloid aggregates might represent the best strategy for early detection. Although there have been several attempts to develop diagnostic methods based on the detection of amyloidogenic oligomers, there is an absence of a widely-accepted and deterministic approach.

The work presented in this thesis has focussed on the studies of amyloidogenic peptides using dielectric relaxation spectroscopy (DRS). Dielectric measurements performed over a broadband of frequencies (10^{-2}-10^{7}), temperature ranges from 133K-300K, and incubation times up to 7 days has revealed patterns that may be used to classify these peptides in various media.

Amyloidogenic peptides amyloid beta ($A\beta_{1-42}$) and human islet amyloid polypeptide (hIAPP) were used as analytes in these studies, with their non-amyloidogenic analogs, scrambled $A\beta_{42-1}$ and rat islet amyloid polypeptide (rIAPP) as controls. These amyloidogenic peptides are known to aggregate into well-ordered fibrillar structures, namely the β-sheet conformation. Our hypothesis is that structural changes during the fibrillization process causes a re-ordering of water molecules due to the hydrophobicity of exposed amino acids. This re-ordering of water can be observed in the protein-solvent relaxations using DRS.

Studies of the peptides at room temperature revealed that there is a large contribution to the conductivity and space-charge polarization due to the heterogeneity of the peptide-solvent mixture. The dielectric modulus formalism was used to reveal changes in the conductivity relaxation peaks between amyloidogenic and non-amyloidogenic peptides over time.

The dielectric response of the peptides in a deionized water-glycerol solvent revealed that amyloidogenic peptides in their in purified (non-*in vivo*-like) form can be detected and differentiated from their non-amyloidogenic analogs. Studies at low temperature revealed that the β-process displayed a decrease in the dielectric loss, ε'' for both amyloidogenic $A\beta_{1-42}$ and hIAPP and an increase for non-amyloidogenic $A\beta_{42-1}$ and rIAPP. This may point to an increase in fraction of structured water over time associated with the amyloidogenic peptides during β-sheet formation. The trend observed in the non-amyloidogenic peptides reflects that a random aggregation lacks the large fraction of structured water that is contained in a organized β-sheet.

The dielectric response of the peptides in the presence of a BSA-glycerol solvent revealed that these amyloidogenic peptides can be detected and differentiated from their non-amyloidogenic analogs in the presence of other proteins and biological substances, similar to *in vivo* conditions. This is a crucial step in demonstrating the viability of using dielectric relaxation spectroscopy as a tool for detecting amyloidogenic peptides in biological fluids, such as blood serum. Studies at low temperature revealed that the β-process displays a characteristic "red-shift" in the permittivity in both $A\beta_{1-42}$ and hIAPP that is not observed in $A\beta_{42-1}$ and rIAPP (see Figure 5.42). Theory predicts that this red-shift occurs due to a hinderance of the rotational motion of molecular dipoles in structured, biological water [64, 166]. This restructuring of the hydrogen bond network as a result of hydrophobic interactions causes a reduction in the hydrogen bond exchange. We also observed the red-shift in the hIAPP measurements in deionized water (see Figure 4.42) but not previously in $A\beta_{1-42}$.

Analysis of the dielectric strength showed that the macroscopic dipole moment of the amyloidogenic protein-solvent solutions changed over time in a different manner than the non-amyloidogenic peptides. The decreasing dipole moment upon fibril formation of $A\beta_{1-42}$ in both deionized water and serum buffers confirms the results found by FTIR and solid state NMR that the structure is comprised of anti-parallel β-sheets. The intermediate increase in dipole moment of $A\beta_{1-42}$ in DI buffer may be indicative of a high fraction of oligomers. Oligomers of $A\beta_{1-42}$ form a reverse micelle that should display a net increase in the dipole moment. The collective dipole moment of $A\beta_{1-42}$ at different incubation times could be used to determine the domination aggregate species, whether monomer, oligomer, or fibril forms. The varying dipole moment of hIAPP over time may be due to a mixture of both parallel and anti-parallel sheets, as published in the literature from FTIR and NMR studies. The non-amyloidogenic peptides either increased in collective dipole moment or did not change at all. This would indicate that if any aggregation occurred, it may be α-helix or random coil.

We note that the limits of sensitivity of DRS as a tool to study amyloidogenic peptides has not yet been tested. Serum concentration of β-amyloid in Alzheimer's patients has been found on the order of 100 nM (nanomolar) [167] and concentrations of IAPP in Type II Diabetes has been found on the order of 10pM (picomolar) [168].

Future work to determine the detectable limit of amyloidogenic peptides using DRS is an important examination.

Recent theory suggests that protein motions are slaved to solvent fluctuations [58, 59]. Studies of solvent relaxation processes yield insight into protein fluctuations, structure, and function. Measurements of the time evolution and relaxation kinetics of α- and β-relaxation processes allow us to model dielectric permittivity to the various phases of fibril formation. We demonstrated that amyloidogenic peptides, in general, move towards lower activation energy, confirming that the fibrillar state is thermodynamically favorable and stable. The observation that the amyloidogenic peptides displayed a lower activation energy as compared to their non-amyloidogenic analogs would indicate a higher fraction of structured water in the amyloid β-sheet.

6.2 Future Direction

This work demonstrates that studies of the time evolution of dielectric permittivity by use of dielectric relaxation spectroscopy can reveal differences between amyloidogenic peptides and their non-amyloidogenic analogs. The following is an outline a suggested plan for further work to develop a method for using DRS as a tool for detecting toxic pre-amyloid aggregates in patient samples.

6.2.1 Expansion of DRS Methods

Measurements we have performed thus far have only begun to explore the dielectric properties of amyloidogenic peptides. Thermal studies to examine the dielectric response during heating, as well as cooling would show if there are reversible processes and any hysteresis effects. Additionally, thermal quenching techniques can be implored to rapidly freeze the system to study particular phases. Other input parameters, such as the driving AC electric field, V_0 for the DRS measurements can be varied to study a dependency on the strength of the field. A study of the dielectric response as a function of the applied electric field could give further insight into deformation polarization effects.

6.2.2 Miniaturized sample cell

Broadband dielectric relaxation spectroscopy is an important tool to study molecular dynamics in broad temperature and frequency ranges. It has the additional advantage that the sensitivity of the measurement increases with decrease sample thickness [169]. Using nano-scale components, information about single molecules and molecular assemblies is an attainable goal [170]. For example, Kremer et al. used 10nm gap sizes to probe the molecular dynamics of polymers and suggest this method as a tool for studying nano-biophysics [169]. A continuation of this work using a sample cell with micrometer or nanometer gap size may lead to additional information about the dielectric behavior of amyloidogenic peptides by exploring their microscopic behavior.

6.2.3 Amyloid fibril inhibitors

Since detection of soluble, pre-fibrillar amyloid structures is the end-goal for a diagnostic test, there is a desire to definitively correlate the dielectric signal with various stages of oligomerization and fibril growth. Several small molecules have been identified that inhibit the formation of amyloid fibrils from monomers [171, 172, 173, 174]. These inhibitors can be used *in vitro* to stop the aggregation process at the different phases of fibril formation. From this, one can classify dielectric spectra with each particular phase. Further insight into fibril formation rates and possibly quantitative measurements of pre-amyloid oligomers may be possible by using these inhibitors.

6.2.4 Complementary analysis tools

A number of measurement and analysis tools have been used in the study of amyloidogenic peptides and their aggregates (see Section 1.6). Electron microscopy (EM) and atomic force microscopy (AFM) are possible choices for confirmatory tools to correlate dielectric spectra with phases of fibril formation. EM can be used to show the presence of pre-fibrillar oligomers at various concentrations, incubation times, and buffers. Both EM and AFM can be used to image the size and shape of amyloid fibrils to verify the end-point of fibril formation.

6.2.5 Serum studies

The studies we have performed thus far have been on purified peptides placed in a solution of deionized water or bovine serum albumin (BSA). A continuation of this work would be to obtain serum samples from transgenic mice models that are known to have various stages of clinical Type II diabetes and Alzheimer's disease. Use of the pathogenic murine models and known controls can be used to correlate a quantitative measurement of pre-amyloid oligomers in blood-serum media. A further continuation would be to perform the same experiments using human serum of clinical and non-clinical donors.

Bibliography

[1] Life expectancy. `http://en.wikipedia.org/wiki/Life_expectancy`. Accessed: 09/03/2013.

[2] Liesi E. Hebert, Jennifer Weuve, Paul A. Scherr, and Denis A. Evans. Alzheimer disease in the United States (2010–2050) estimated using the 2010 census. *Neurology*, 2013.

[3] Alzhiemer's association. `http://www.alz.org`. Accessed: 24/09/2012.

[4] Alzheimer's Association. 2012 alzheimer's disease facts and figures. *Alzheimer's and dementia the journal of the Alzheimer's Association*, 6(2):131–168, 2012.

[5] American diabetes association. `http://www.diabetes.org`. Accessed: 24/09/2012.

[6] Center for Disease Control and Prevention. 2011 national diabetes fact sheet. 2011.

[7] Claudio Soto. Protein misfolding and disease; protein refolding and therapy. *FEBS Letters*, 498(2-3):204 – 207, 2001. ¡ce:title¿Lisbon Special Issue¡/ce:title¿.

[8] Christopher M. Dobson. The structural basis of protein folding and its links with human disease. *Philosophical Transactions of the Royal Society of London. Series B: Biological Sciences*, 356(1406):133–145, 2001.

[9] Christopher M. Dobson. Protein misfolding, evolution and disease. *Trends in Biochemical Sciences*, 24(9):329 – 332, 1999.

[10] George G. Glenner and Caine W. Wong. Alzheimer's disease: Initial report of the purification and characterization of a novel cerebrovascular amyloid protein. *Biochemical and Biophysical Research Communications*, 120(3):885 – 890, 1984.

[11] Dennis J. Selkoe. Alzheimer's disease genes, proteins, and therapy. *Physiological Reviews*, 81(2):741–766, 2001.

[12] Magdalena Anguiano, Richard J. Nowak, and Peter T. Lansbury. Protofibrillar islet amyloid polypeptide permeabilizes synthetic vesicles by a pore-like mechanism that may be relevant to type ii diabetes. *Biochemistry*, 41(38):11338–11343, 2002. PMID: 12234175.

[13] Byron Caughey and Peter T. Lansbury. Protofibrils, pores, fibrils, and neurodegeneration: Separating the responsible protein aggregates from the innocent bystanders*. *Annual Review of Neuroscience*, 26(1):267–298, 2003.

[14] Marina D. Kirkitadze, Gal Bitan, and David B. Teplow. Paradigm shifts in alzheimer's disease and other neurodegenerative disorders: The emerging role of oligomeric assemblies. *Journal of Neuroscience Research*, 69(5):567–577, 2002.

[15] Kelly A. Conway, Seung-Jae Lee, Jean-Christophe Rochet, Tomas T. Ding, Robin E. Williamson, and Peter T. Lansbury. Acceleration of oligomerization, not fibrillization, is a shared property of both a-synuclein mutations linked to early-onset parkinson's disease: Implications for pathogenesis and therapy. *Proceedings of the National Academy of Sciences*, 97(2):571–576, 2000.

[16] Rakez Kayed, Elizabeth Head, Jennifer L. Thompson, Theresa M. McIntire, Saskia C. Milton, Carl W. Cotman, and Charles G. Glabe. Common structure of soluble amyloid oligomers implies common mechanism of pathogenesis. *Science*, 300(5618):486–489, 2003.

[17] Alex E. Roher, Jerome Baudry, Michael O. Chaney, Yu-Min Kuo, W.Blaine Stine, and Mark R. Emmerling. Oligomerization and fibril assembly of the amyloid-beta protein. *Biochimica et Biophysica Acta (BBA) - Molecular Basis of Disease*, 1502(1):31 – 43, 2000.

[18] Dennis J. Selkoe. Physiological production of the beta-amyloid protein and the mechanism of alzheimer's disease. *Trends in Neurosciences*, 16(10):403 – 409, 1993.

[19] Rainulf A. Stelzmann, H. Norman Schnitzlein, and F. Reed Murtagh. An english translation of alzheimer's 1907 paper, uber eine eigenartige erkankung der hirnrinde. *Clinical Anatomy*, 8(6):429–431, 1995.

[20] Dominic M. Walsh, Aleksey Lomakin, George B. Benedek, Margaret M. Condron, and David B. Teplow. Amyloid beta-protein fibrillogenesis. *Journal of Biological Chemistry*, 272(35):22364–22372, 1997.

[21] S. S. Mirra, A. Heyman, D. McKeel, S. M. Sumi, B. J. Crain, L. M. Brownlee, F. S. Vogel, J. P. Hughes, G. van Belle, and L. Berg. The consortium to establish a registry for alzheimer's disease. *Neurology*, 41(4):479, 1991.

[22] John Hardy and David Allsop. Amyloid deposition as the central event in the aetiology of alzheimer's disease. *Trends in Pharmacological Sciences*, 12(0):383–388, 1991.

[23] Lars O. Tjernberg, Jan Naslund, Fredrik Lindqvist, Jan Johansson, Anders R. Karlstrom, Johan Thyberg, Lars Terenius, and Christer Nordstedt. Arrest of beta-amyloid fibril formation by a pentapeptide ligand. *Journal of Biological Chemistry*, 271(15):8545–8548, 1996.

[24] Salim S. El-Amouri, Hong Zhu, Jin Yu, Robert Marr, Inder M. Verma, and Mark S. Kindy. Neprilysin: An enzyme candidate to slow the progression of alzheimer's disease. *The American Journal of Pathology*, 172(5):1342–1354, 2008.

[25] BA Yankner, LK Duffy, and DA Kirschner. Neurotrophic and neurotoxic effects of amyloid beta protein: reversal by tachykinin neuropeptides. *Science*, 250(4978):279–282, 1990.

[26] N Arispe, E Rojas, and H B Pollard. Alzheimer disease amyloid beta protein forms calcium channels in bilayer membranes: blockade by tromethamine and aluminum. *Proceedings of the National Academy of Sciences*, 90(2):567–571, 1993.

[27] Masahiro Kawahara and Yoichiro Kuroda. Molecular mechanism of neurodegeneration induced by alzheimer's beta-amyloid protein: channel formation and disruption of calcium homeostasis. *Brain Research Bulletin*, 53(4):389–397, 2000.

[28] Jorge Ghiso, Miguel Calero, Etsuro Matsubara, Samuel Governale, Joseph Chuba, Ronald Beavis, Thomas Wisniewski, and Blas Frangione. Alzheimer's soluble amyloid beta is a normal component of human urine. *FEBS Letters*, 408(1):105–108, 1997.

[29] P Westermark, C Wernstedt, E Wilander, D W Hayden, T D O'Brien, and K H Johnson. Amyloid fibrils in human insulinoma and islets of langerhans of the diabetic cat are derived from a neuropeptide-like protein also present in normal islet cells. *Proceedings of the National Academy of Sciences*, 84(11):3881–3885, 1987.

[30] A. Lorenzo and B. A. Yankner. Amyloid fibril toxicity in alzheimer's disease and diabetesa. *Annals of the New York Academy of Sciences*, 777(1):89–95, 1996.

[31] P Westermark, U Engstrom, K H Johnson, G T Westermark, and C Betsholtz. Islet amyloid polypeptide: pinpointing amino acid residues linked to amyloid fibril formation. *Proceedings of the National Academy of Sciences*, 87(13):5036–5040, 1990.

[32] Christer Betsholtz, Lars Christmansson, Ulla Engstram, Frederik Rorsman, Viveka Svensson, Kenneth H. Johnson, and Per Westermark. Sequence divergence in a specific region of islet amyloid polypeptide (iapp) explains differences in islet amyloid formation between species. *FEBS Letters*, 251(1-2):261 – 264, 1989.

[33] M Nishi, S J Chan, S Nagamatsu, G I Bell, and D F Steiner. Conservation of the sequence of islet amyloid polypeptide in five mammals is consistent with

its putative role as an islet hormone. *Proceedings of the National Academy of Sciences*, 86(15):5738–5742, 1989.

[34] Tajib A. Mirzabekov, Meng-chin Lin, and Bruce L. Kagan. Pore formation by the cytotoxic islet amyloid peptide amylin. *Journal of Biological Chemistry*, 271(4):1988–1992, 1996.

[35] Steven E. Kahn. The importance of beta-cell failure in the development and progression of type 2 diabetes. *Journal of Clinical Endocrinology & Metabolism*, 86(9):4047–4058, 2001.

[36] E. Hartter, T. Svoboda, B. Ludvik, M. Schuller, B. Lell, E. Kuenburg, M. Brunnbauer, W. Woloszczuk, and R. Prager. Basal and stimulated plasma levels of pancreatic amylin indicate its co-secretion with insulin in humans. *Diabetologia*, 34:52–54, 1991. 10.1007/BF00404025.

[37] J.M. Berg, J.L. Tymoczko, and L. Stryer. *Biochemistry*. W. H. Freeman, 2006.

[38] R.H. Garrett and C.M. Grisham. *Biochemistry*. Thomson Brooks/Cole, 1999.

[39] I.N. Serdyuk, N.R. Zaccai, and J. Zaccai. *Methods in Molecular Biophysics: Structure, Dynamics, Function*. Cambridge University Press, 2007.

[40] Aphrodite Kapurniotu. Amyloidogenicity and cytotoxicity of islet amyloid polypeptide. *Peptide Science*, 60(6):438–459, 2001.

[41] Mihael H. Polymeropoulos, Christian Lavedan, Elisabeth Leroy, Susan E. Ide, Anindya Dehejia, Amalia Dutra, Brian Pike, Holly Root, Jeffrey Rubenstein, Rebecca Boyer, Edward S. Stenroos, Settara Chandrasekharappa, Aglaia Athanassiadou, Theodore Papapetropoulos, William G. Johnson, Alice M. Lazzarini, Roger C. Duvoisin, Giuseppe Di Iorio, Lawrence I. Golbe, and Robert L. Nussbaum. Mutation in the alpha-synuclein gene identified in families with parkinson's disease. *Science*, 276(5321):2045–2047, 1997.

[42] Yoshio Namba, Masanori Tomonaga, Hiroshi Kawasaki, Eiichi Otomo, and Kazuhiko Ikeda. Apolipoprotein e immunoreactivity in cerebral amyloid deposits and neurofibrillary tangles in alzheimer's disease and kuru plaque amyloid in creutzfeldt-jakob disease. *Brain Research*, 541(1):163 – 166, 1991.

[43] Richard T. Johnson and Clarence J. Gibbs. Creutzfeldt-jakob disease and related transmissible spongiform encephalopathies. *New England Journal of Medicine*, 339(27):1994–2004, 1998.

[44] C. Soto. Alzheimer's and prion disease as disorders of protein conformation: implications for the design of novel therapeutic approaches. *Journal of Molecular Medicine*, 77:412–418, 1999. 10.1007/s001090050371.

[45] C. Soto. Alzheimer's and prion disease as disorders of protein conformation: implications for the design of novel therapeutic approaches. *Journal of Molecular Medicine*, 77:412–418, 1999. 10.1007/s001090050371.

[46] Ehud Gazit. The "correctly folded" state of proteins: Is it a metastable state? *Angewandte Chemie International Edition*, 41(2):257–259, 2002.

[47] Fabrizio Chiti and Christopher M. Dobson. Protein misfolding, functional amyloid, and human disease. *Annual Review of Biochemistry*, 75(1):333–366, 2006.

[48] Stanley B Prusiner, Michael R Scott, Stephen J DeArmond, and Fred E Cohen. Prion protein biology. *Cell*, 93(3):337 – 348, 1998.

[49] Fabrizio Chiti, Paul Webster, Niccola Taddei, Anne Clark, Massimo Stefani, Giampietro Ramponi, and Christopher M. Dobson. Designing conditions for in vitro formation of amyloid protofilaments and fibrils. *Proceedings of the National Academy of Sciences*, 96(7):3590–3594, 1999.

[50] Rainer Jaenicke and Robert Seckler. Protein misassembly in vitro. In David S. Eisenberg Frederic M. Richards and Peter S. Kim, editors, *Protein Misassembly*, volume 50 of *Advances in Protein Chemistry*, pages 1 – C10. Academic Press, 1997.

[51] D A Kirschner, C Abraham, and D J Selkoe. X-ray diffraction from intraneuronal paired helical filaments and extraneuronal amyloid fibers in alzheimer disease indicates cross-beta conformation. *Proceedings of the National Academy of Sciences*, 83(2):503–507, 1986.

[52] Charles G. Glabe. Structural classification of toxic amyloid oligomers. *Journal of Biological Chemistry*, 283(44):29639–29643, 2008.

[53] Fabrizio Chiti, Niccolo Taddei, Fabiana Baroni, Cristina Capanni, Massimo Stefani, Giampietro Ramponi, and Christopher M. Dobson. Kinetic partitioning of protein folding and aggregation. *Nature Structural Biology*, 9(2):137–143, 2003.

[54] Kazuhiro Hasegawa, Itaru Yamaguchi, Saburou Omata, Fumitake Gejyo, and Hironobu Naiki. Interaction between abeta(1-42) and abeta(1-40) in alzheimer's beta-amyloid fibril formation in vitro. *Biochemistry*, 38(47):15514–15521, 1999.

[55] Rebecca Nelson, Michael R. Sawaya, Melinda Balbirnie, Anders O. Madsen, Christian Riekel, Robert Grothe, and David Eisenberg. Structure of the cross-beta spine of amyloid-like fibrils. *Nature*, 435(7043):773–778, 2005.

[56] Aneta T. Petkova, Yoshitaka Ishii, John J. Balbach, Oleg N. Antzutkin, Richard D. Leapman, Frank Delaglio, and Robert Tycko. A structural model for alzheimer's beta-amyloid fibrils based on experimental constraints from solid state nmr. *Proceedings of the National Academy of Sciences*, 99(26):16742–16747, 2002.

[57] P. W. Fenimore, H. Frauenfelder, B. H. McMahon, and F. G. Parak. Slaving: Solvent fluctuations dominate protein dynamics and functions. *Proceedings of the National Academy of Sciences*, 99(25):16047–16051, 2002.

[58] H. Frauenfelder, P. W. Fenimore, G. Chen, and B. H. McMahon. Protein folding is slaved to solvent motions. *Proceedings of the National Academy of Sciences*, 103(42):15469–15472, 2006.

[59] Hans Frauenfelder, Guo Chen, Joel Berendzen, Paul W. Fenimore, Helen Jansson, Benjamin H. McMahon, Izabela R. Stroe, Jan Swenson, and Robert D. Young. A unified model of protein dynamics. *Proceedings of the National Academy of Sciences*, pages 1–6, 2009.

[60] P. W. Fenimore, Hans Frauenfelder, B. H. McMahon, and R. D. Young. Bulk-solvent and hydration-shell fluctuations, similar to alpha- and beta-fluctuations in glasses, control protein motions and functions. *Proceedings of the National Academy of Sciences*, 101(40):14408–14413, 2004.

[61] Vassiliy Lubchenko, Peter G. Wolynes, and Hans Frauenfelder. Mosaic energy landscapes of liquids and the control of protein conformational dynamics by glass-forming solvents. *The Journal of Physical Chemistry B*, 109(15):7488–7499, 2005.

[62] G. Chen, P.W. Fenimore, H. Frauenfelder, F. Mezei, J. Swenson, and R.D. Young. Protein fluctuations explored by inelastic neutron scattering and dielectric relaxation spectroscopy. *Philosophical Magazine*, 88(33-35):3877–3883, 2008.

[63] F. Kremer and A. Schonhals. *Broadband Dielectric Spectroscopy.* Springer, 2003.

[64] Florin Despa. Biological water. *Annals of the New York Academy of Sciences*, 1066(1):1–11, 2006.

[65] Orlando Crescenzi, Simona Tomaselli, Remo Guerrini, Severo Salvadori, Anna M. D'Ursi, Piero Andrea Temussi, and Delia Picone. Solution structure of the alzheimer amyloid beta-peptide (1-42) in an apolar microenvironment. *European Journal of Biochemistry*, 269(22):5642–5648, 2002.

[66] T.M. Nordlund. *Quantitative Understanding of Biosystems: An Introduction to Biophysics.* Taylor & Francis, 2010.

[67] G D Rose and R Wolfenden. Hydrogen bonding, hydrophobicity, packing, and protein folding. *Annual Review of Biophysics and Biomolecular Structure*, 22(1):381–415, 1993.

[68] F M Richards. Areas, volumes, packing, and protein structure. *Annual Review of Biophysics and Bioengineering*, 6(1):151–176, 1977.

[69] G Otting, E Liepinsh, and K Wuthrich. Protein hydration in aqueous solution. *Science*, 254(5034):974–980, 1991.

[70] J. L. Oncley. Studies of the dielectric properties of protein solutions. i. carboxyhemoglobin1,2. *Journal of the American Chemical Society*, 60(5):1115–1123, 1938.

[71] J. L. Oncley. The investigation of proteins by dielectric measurements. *Chemical Reviews*, 30(3):433–450, 1942.

[72] G.H. Haggis, T.J. Buchanan, and J.B. Hasted. Estimation of protein hydration by dielectric measurements at microwave frequencies. *Nature*, 167:607–608, 1951.

[73] T. J. Buchanan, G. H. Haggis, J. B. Hasted, and B. G. Robinson. The dielectric estimation of protein hydration. *Proceedings of the Royal Society of London. Series A. Mathematical and Physical Sciences*, 213(1114):379–391, 1952.

[74] R Pethig. Protein-water interactions determined by dielectric methods. *Annual Review of Physical Chemistry*, 43(1):177–205, 1992.

[75] H. Frauenfelder, S.S. Chan, W.S. Chan, R.H. Austin, C.E. Schulz, G.U. Nienhaus, and R.D. Young. *The Physics of Proteins: An Introduction to Biological Physics and Molecular Biophysics*. Biological and Medical Physics, Biomedical Engineering. Springer, 2010.

[76] Ranko Richert. Heterogeneous dynamics in liquids: fluctuations in space and time. *Journal of Physics: Condensed Matter*, 14(23):R703, 2002.

[77] K. L. Ngai and M. Paluch. Classification of secondary relaxation in glass-formers based on dynamic properties. *The Journal of Chemical Physics*, 120(2):857–873, 2004.

[78] Yoshihito Hayashi, Alexander Puzenko, and Yuri Feldman. Slow and fast dynamics in glycerol-water mixtures. *Journal of Non-Crystalline Solids*, 352(42-49):4696–4703, 2006. Proceedings of the 5th International Discussion Meeting on Relaxations in Complex Systems: 5th International Discussion Meeting on Relaxations in Complex Systems.

[79] S. Capaccioli, K. L. Ngai, and N. Shinyashiki. The johari-goldstein beta-relaxation of water. *The Journal of Physical Chemistry B*, 111(28):8197–8209, 2007. PMID: 17585798.

[80] Andrea Mandanici, Wei Huang, Maria Cutroni, and Ranko Richert. Dynamics of glass-forming liquids. xii. dielectric study of primary and secondary relaxations in ethylcyclohexane. *The Journal of Chemical Physics*, 128(12):124505, 2008.

[81] Gyan P. Johari and Martin Goldstein. Viscous liquids and the glass transition. ii. secondary relaxations in glasses of rigid molecules. *The Journal of Chemical Physics*, 53(6):2372–2388, 1970.

[82] Nilashis Nandi and Biman Bagchi. Dielectric relaxation of biological water. *The Journal of Physical Chemistry B*, 101(50):10954–10961, 1997.

[83] Nilashis Nandi, Kankan Bhattacharyya, and Biman Bagchi. Dielectric relaxation and solvation dynamics of water in complex chemical and biological systems. *Chemical Reviews*, 100(6):2013–2046, 2000.

[84] Udo Kaatze. Dielectric spectroscopy of aqueous solutions. hydration phenomena and hydrogen-bonded networks. *Journal of Molecular Liquids*, 56(0):95 – 115, 1993.

[85] D A Kirschner, H Inouye, L K Duffy, A Sinclair, M Lind, and D J Selkoe. Synthetic peptide homologous to beta protein from alzheimer disease forms amyloid-like fibrils in vitro. *Proceedings of the National Academy of Sciences*, 84(19):6953–6957, 1987.

[86] Yeonho Choi, Soongweon Hong, Taewook Kang, and Luke P. Lee. Noninvasive real-time monitoring of amyloid-beta fibrillization via simultaneous label-free dielectric relaxation spectroscopy and dark-field imaging. *The Journal of Physical Chemistry C*, 113(33):14587–14590, 2009.

[87] G. G. Glenner, D. L. Page, and E. D. Eanes. The relation of the properties of congo red-stained amyoid fibrils to the beta-conformation. *Journal of Histochemistry & Cytochemistry*, 20(10):821–826, 1972.

[88] H. Puchtler, F. Sweat, and M. LeVine. On the binding of congo red by amyloid. *Journal of Histochemistry & Cytochemistry*, 10(3):355–364, 1962.

[89] Harry Levine. Thioflavine t interaction with synthetic alzheimer's disease beta-amyloid peptides: Detection of amyloid aggregation in solution. *Protein Science*, 2(3):404–410, 1993.

[90] Y C Kudva, C Mueske, P C Butler, and N L Eberhardt. A novel assay in vitro of human islet amyloid polypeptide amyloidogenesis and effects of insulin secretory vesicle peptides on amyloid formation. *Biochem. J.*, 331(3):809–813, 1998.

[91] Harry LeVine III. Quantification of beta-sheet amyloid fibril structures with thioflavin t. In Ronald Wetzel, editor, *Amyloid, Prions, and Other Protein Aggregates*, volume 309 of *Methods in Enzymology*, pages 274 – 284. Academic Press, 1999.

[92] Leslie S. Wolfe, Matthew F. Calabrese, Abhinav Nath, Dorottya V. Blaho, Andrew D. Miranker, and Yong Xiong. Protein-induced photophysical changes

to the amyloid indicator dye thioflavin t. *Proceedings of the National Academy of Sciences*, 2010.

[93] A Lomakin, D S Chung, G B Benedek, D A Kirschner, and D B Teplow. On the nucleation and growth of amyloid beta-protein fibrils: detection of nuclei and quantitation of rate constants. *Proceedings of the National Academy of Sciences*, 93(3):1125–1129, 1996.

[94] Michael R. Nichols, Melissa A. Moss, Dana Kim Reed, Wen-Lang Lin, Rajendrani Mukhopadhyay, Jan H. Hoh, and Terrone L. Rosenberry. Growth of beta-amyloid(1-40) protofibrils by monomer elongation and lateral association. characterization of distinct products by light scattering and atomic force microscopy. *Biochemistry*, 41(19):6115–6127, 2002. PMID: 11994007.

[95] Ronit Azriel and Ehud Gazit. Analysis of the minimal amyloid-forming fragment of the islet amyloid polypeptide. *Journal of Biological Chemistry*, 276(36):34156–34161, 2001.

[96] C.L. Shen, G.L. Scott, F. Merchant, and R.M. Murphy. Light scattering analysis of fibril growth from the amino-terminal fragment beta(128) of beta-amyloid peptide. *Biophysical Journal*, 65(6):2383 – 2395, 1993.

[97] A.S. Cohen and S.E. Calkin. Electron microscopic observations on a fibrous component in amyloid of diverse origins. *Nature*, 183(4669):1202–1203, 1959.

[98] Tsuranobu Shirahama and Alan S. Cohen. High-resolution electron microscopic analysis of the amyloid fibril. *The Journal of Cell Biology*, 33(3):679–708, 1967.

[99] Jose L. Jimenez, J.Inaki Guijarro, Elena Orlova, Jesus Zurdo, Christopher M. Dobson, Margaret Sunde, and Helen R. Saibil. Cryo-electron microscopy structure of an sh3 amyloid fibril and model of the molecular packing. *Embo J*, 18(4):815–821, 1999.

[100] O. Sumner Makin and Louise C. Serpell. Structural characterisation of islet amyloid polypeptide fibrils. *Journal of Molecular Biology*, 335(5):1279 – 1288, 2004.

[101] George G. Glenner, E. David Eanes, and Clayton A. Wiley. Amyloid fibrils formed from a segment of the pancreatic islet amyloid protein. *Biochemical and Biophysical Research Communications*, 155(2):608 – 614, 1988.

[102] Margaret Sunde, Louise C Serpell, Mark Bartlam, Paul E Fraser, Mark B Pepys, and Colin C.F Blake. Common core structure of amyloid fibrils by synchrotron x-ray diffraction. *Journal of Molecular Biology*, 273(3):729 – 739, 1997.

[103] Margaret Sunde and Colin Blake. The structure of amyloid fibrils by electron microscopy and x-ray diffraction. In David S. Eisenberg Frederic M. Richards and Peter S. Kim, editors, *Protein Misassembly*, volume 50 of *Advances in Protein Chemistry*, pages 123–159. Academic Press, 1997.

[104] O. Sumner Makin and Louise C. Serpell. X-ray diffraction studies of amyloid structure. In Einar M. Sigurdsson and John M. Walker, editors, *Amyloid Proteins*, volume 299 of *Methods in Molecular Biology*, pages 67–80. Humana Press, 2005. 10.1385/1-59259-874-9:067.

[105] W. B. Stine, S. W. Snyder, U. S. Ladror, W. S. Wade, M. F. Miller, T. J. Perun, T. F. Holzman, and G. A. Krafft. The nanometer-scale structure of amyloid-beta visualized by atomic force microscopy. *Journal of Protein Chemistry*, 15:193–203, 1996. 10.1007/BF01887400.

[106] James D. Harper, Charles M. Lieber, and Peter T. Lansbury. Atomic force microscopic imaging of seeded fibril formation and fibril branching by the alzheimer's disease amyloid-beta protein. *Chem Bio*, 4(12):951–959, 1997.

[107] H.K.L Blackley, G.H.W Sanders, M.C Davies, C.J Roberts, S.J.B Tendler, and M.J Wilkinson. In-situ atomic force microscopy study of beta-amyloid fibrillization. *Journal of Molecular Biology*, 298(5):833–840, 2000.

[108] Aaron K. Chamberlain, Cait E. MacPhee, Jesus Zurdo, Ludmilla A. Morozova-Roche, H. Allen O. Hill, Christopher M. Dobson, and Jason J. Davis. Ultrastructural organization of amyloid fibrils by atomic force microscopy. *Biophysical Journal*, 79(6):3282 – 3293, 2000.

[109] Thorsten Luhrs, Christiane Ritter, Marc Adrian, Dominique Riek-Loher, Bernd Bohrmann, Heinz Dobeli, David Schubert, and Roland Riek. 3d structure of alzheimer's amyloid-beta(142) fibrils. *Proceedings of the National Academy of Sciences*, 102(48):17342–17347, 2005.

[110] Robert Tycko. Insights into the amyloid folding problem from solid-state nmr. *Biochemistry*, 42(11):3151–3159, 2003.

[111] J.H. Walton, R.S. Berry, and F. Despa. Amyloid oligomer formation probed by water proton magnetic resonance spectroscopy. *Biophysical Journal*, 100(9):2302 – 2308, 2011.

[112] D.J. Griffiths. *Introduction to Electrodynamics*. Prentice Hall, 1999.

[113] Yuri Feldman, Alexander Puzenko, and Yaroslav Ryabov. *Dielectric Relaxation Phenomena in Complex Materials*, pages 1–125. John Wiley & Sons, Inc., 2005.

[114] A. Serghei, M. Tress, J. R. Sangoro, and F. Kremer. Electrode polarization and charge transport at solid interfaces. *Phys. Rev. B*, 80:184301, Nov 2009.

[115] Dielectric spectroscopy. `http://en.wikipedia.org/wiki/Dielectric_spectroscopy`. Accessed: 24/09/2012.

[116] H. Frohlich. *Theory of Dielectrics; Dielectric Constant and Dielectric Loss*. Monographs on the physics and chemistry of materials. Clarendon Press, 1949.

[117] J.D. Jackson. *Classical Electrodynamics*. Wiley, 1998.

[118] P.J.W. Debye. *Polar Molecules*. Chemical Catalog Company, 1929.

[119] Kenneth S. Cole and Robert H. Cole. Dispersion and absorption in dielectrics i. alternating current characteristics. *The Journal of Chemical Physics*, 9(4):341–351, 1941.

[120] D. W. Davidson and R. H. Cole. Dielectric relaxation in glycerine. *The Journal of Chemical Physics*, 18(10):1417–1417, 1950.

[121] D. W. Davidson and R. H. Cole. Dielectric relaxation in glycerol, propylene glycol, and n-propanol. *The Journal of Chemical Physics*, 19(12):1484–1490, 1951.

[122] S. Havriliak and S. Negami. A complex plane analysis of alpha-dispersions in some polymer systems. *Journal of Polymer Science Part C: Polymer Symposia*, 14(1):99–117, 1966.

[123] S. Havriliak and S. Negami. A complex plane representation of dielectric and mechanical relaxation processes in some polymers. *Polymer*, 8(0):161–210, 1967.

[124] R. Diaz-Calleja. Comment on the maximum in the loss permittivity for the havriliak-negami equation. *Macromolecules*, 33(24):8924–8924, 2000.

[125] Ranko Richert and Hermann Wagner. The dielectric modulus: relaxation versus retardation. *Solid State Ionics*, 105(1-4):167–173, 1998.

[126] G. M Tsangaris, G. C Psarras, and N Kouloumbi. Electric modulus and interfacial polarization in composite polymeric systems. *Journal of Materials Science*, 33:2027–2037, 1998. 10.1023/A:1004398514901.

[127] Jovan Mijovic, Yu Bian, Richard A. Gross, and Bo Chen. Dynamics of proteins in hydrated state and in solution as studied by dielectric relaxation spectroscopy. *Macromolecules*, 38(26):10812–10819, 2005.

[128] R El Moznine, G Smith, E Polygalov, P M Suherman, and J Broadhead. Dielectric properties of residual water in amorphous lyophilized mixtures of sugar and drug. *Journal of Physics D: Applied Physics*, 36(4):330, 2003.

[129] Alfredo Bello, Estrella Laredo, and Mario Grimau. Comparison of analysis of dielectric spectra of pcl in the e* and the m* formalism. *Journal of Non-Crystalline Solids*, 353(47-51):4283–4287, 2007.

[130] Lei Yu, Xiao Hu, David Kaplan, and Peggy Cebe. Dielectric relaxation spectroscopy of hydrated and dehydrated silk fibroin cast from aqueous solution. *Biomacromolecules*, 11(10):2766–2775, 2010.

[131] S. Arrhenius. Uber die reaktionsgeschwindigkeit der inversion von rohrzucker durch sauren. *Physikalische Zeitschrift*, 4:226, 1889.

[132] H. Vogel. *Physikalische Zeitschrift*, 22:645, 1921.

[133] Gordon S. Fulcher. Analysis of recent measurements of the viscosity of glasses. *Journal of the American Ceramic Society*, 8(6):339–355, 1925.

[134] G. Tammann and W. Hesse. Die abhangigkeit der viscositat von der temperatur bie unterkuhlten flussigkeiten. *Zeitschrift fur anorganische und allgemeine Chemie*, 156(1):245–257, 1926.

[135] C A Angell. The old problems of glass and the glass transition, and the many new twists. *Proceedings of the National Academy of Sciences*, 92(15):6675–6682, 1995.

[136] C. A. Angell. Liquid fragility and the glass transition in water and aqueous solutions. *Chemical Reviews*, 102(8):2627–2650, 2002.

[137] Novocontrol. *Alpha-A Analyzer User's Manual.* Novocontrol Technologies, 2.9 edition, 2009.

[138] Y. Hayashi, A. Guitina, and Y. Feldman. Low frequency liquid sample holder: Three electrode type. *Dielectrics Newsletter*, (21):6–7, 2005.

[139] Autumn M. Klein, Neil W. Kowall, and Robert J. Ferrante. Neurotoxicity and oxidative damage of beta amyloid 1-42 versus beta amyloid 1-40 in the mouse cerebral cortex. *Annals of the New York Academy of Sciences*, 893(1):314–320, 1999.

[140] Andisheh Abedini and Daniel P. Raleigh. Destabilization of human iapp amyloid fibrils by proline mutations outside of the putative amyloidogenic domain: Is there a critical amyloidogenic domain in human iapp? *Journal of Molecular Biology*, 355(2):274 – 281, 2006.

[141] R. Bergman. General susceptibility functions for relaxations in disordered systems. *Journal of Applied Physics*, 88(3):1356–1365, 2000.

[142] H. Jansson and J. Swenson. The protein glass transition as measured by dielectric spectroscopy and differential scanning calorimetry. *Biochimica et Biophysica Acta (BBA) Proteins and Proteomics*, 1804(1):20–26, 2010. Includes Special Section: Protein-Water Interactions¿.

[143] Florin Despa, Ariel Fernandez, L.Ridgway Scott, and R.Stephen Berry. Hydration profiles of amyloidogenic molecular structures. *Journal of Biological Physics*, 34:577–590, 2008.

[144] Alfonso De Simone, Guy G. Dodson, Chandra S. Verma, Adriana Zagari, and Franca Fraternali. Prion and water: Tight and dynamical hydration sites have a key role in structural stability. *Proceedings of the National Academy of Sciences of the United States of America*, 102(21):7535–7540, 2005.

[145] Ariel Fernndez, Jozsef Kardos, L. Ridgway Scott, Yuji Goto, and R. Stephen Berry. Structural defects and the diagnosis of amyloidogenic propensity. *Proceedings of the National Academy of Sciences*, 100(11):6446–6451, 2003.

[146] Joseph T. Jarrett, Elizabeth P. Berger, and Peter T. Lansbury. The carboxy terminus of the .beta. amyloid protein is critical for the seeding of amyloid formation: Implications for the pathogenesis of alzheimer's disease. *Biochemistry*, 32(18):4693–4697, 1993. PMID: 8490014.

[147] Elizabeth Rhoades, Jayant Agarwal, and Ari Gafni. Aggregation of an amyloidogenic fragment of human islet amyloid polypeptide. *Biochimica et Biophysica Acta (BBA) - Protein Structure and Molecular Enzymology*, 1476(2):230 – 238, 2000.

[148] Paul K. Dixon, Lei Wu, Sidney R. Nagel, Bruce D. Williams, and John P. Carini. Scaling in the relaxation of supercooled liquids. *Phys. Rev. Lett.*, 65:1108–1111, Aug 1990.

[149] Yoko Kusumoto, Aleksey Lomakin, David B. Teplow, and George B. Benedek. Temperature dependence of amyloid beta-protein fibrillization. *Proceedings of the National Academy of Sciences*, 95(21):12277–12282, 1998.

[150] Lars Onsager. Electric moments of molecules in liquids. *Journal of the American Chemical Society*, 58(8):1486–1493, 1936.

[151] Wim G. J. Hol, Louis M. Halie, and Christian Sander. Dipoles of the alpha-helix and beta-sheet: their role in protein folding. *NAture*, 294(5841):532–536, 1981.

[152] Sorin Luca, Wai-Ming Yau, Richard Leapman, and Robert Tycko. Peptide conformation and supramolecular organization in amylin fibrils: Constraints from solid-state nmr. *Biochemistry*, 46(47):13505–13522, 2007. PMID: 17979302.

[153] Emilie Cerf, Rabia Sarroukh, Shiori Tamamizu-Kato, Leonid Breydo, Sylvie Derclaye, Yves F. Dufrene, Vasanthy Narayanaswami, Erik Goormaghtigh, Jean-Marie Ruysschaert, and Vincent Raussens. Antiparallel beta-sheet: a signature structure of the oligomeric amyloid beta-peptide. *Biochemical Journal*, 421(3):415–423, 2009.

[154] Mahiuddin Ahmed, Judianne Davis, Darryl Aucoin, Takeshi Sato, Shivani Ahuja, Saburo Aimoto, James I Elliott, William E Van Nostrand, and Steven O Smith. Structural conversion of neurotoxic amyloid-beta 1-42 oligomers to fibrils. *Nature Structural and Molecular Biology*, 17(5):561–567, 2010.

[155] Tuomas P. J. Knowles, Wenmiao Shu, Glyn L. Devlin, Sarah Meehan, Stefan Auer, Christopher M. Dobson, and Mark E. Welland. Kinetics and thermodynamics of amyloid formation from direct measurements of fluctuations in fibril mass. *Proceedings of the National Academy of Sciences*, 104(24):10016–10021, 2007.

[156] Ted T. Ashburn, Michele Auger, and Peter T. Lansbury. The structural basis of pancreatic amyloid formation: isotope-edited spectroscopy in the solid state. *Journal of the American Chemical Society*, 114(2):790–791, 1992.

[157] Janet M. Griffiths, Ted T. Ashburn, Michele Auger, Philip R. Costa, Robert G. Griffin, and Peter T. Lansbury. Rotational resonance solid-state nmr elucidates a structural model of pancreatic amyloid. *Journal of the American Chemical Society*, 117(12):3539–3546, 1995.

[158] Seiichi Sudo, Mayumi Shimomura, Naoki Shinyashiki, and Shin Yagihara. Broadband dielectric study of alpha-beta separation for supercooled glycerol-water mixtures. *Journal of Non-Crystalline Solids*, 307-310(0):356 – 363, 2002.

[159] Sophie E. Jackson and Alan R. Fersht. Folding of chymotrypsin inhibitor 2. 1. evidence for a two-state transition. *Biochemistry*, 30(43):10428–10435, 1991.

[160] G S Huang and T G Oas. Submillisecond folding of monomeric lambda repressor. *Proceedings of the National Academy of Sciences*, 92(15):6878–6882, 1995.

[161] Michelle L. Scalley, Qian Yi, Hongdi Gu, Ashley McCormack, John R. Yates, and David Baker. Kinetics of folding of the igg binding domain of peptostreptoccocal protein l. *Biochemistry*, 36(11):3373–3382, 1997.

[162] A. R. Viguera, J. C. Martinez, V. V. Filimonov, P. L. Mateo, and L. Serrano. Thermodynamic and kinetic analysis of the sh3 domain of spectrin shows a two-state folding transition. *Biochemistry*, 33(8):2142–2150, 1994.

[163] V. Munoz, P. A. Thompson, J. Hofrichter, and W. A. Eaton. Folding dynamics and mechanism of beta-hairpin formation. *Nature*, 390:196–199, 1998.

[164] David B. Teplow. Structural and kinetic features of amyloid beta-protein fibrillogenesis. *Amyloid*, 5(2):121–142, 1998. PMID: 9686307.

[165] F. Stickel, E. W. Fischer, and R. Richert. Dynamics of glass-forming liquids. i. temperature-derivative analysis of dielectric relaxation data. *The Journal of Chemical Physics*, 102(15):6251–6257, 1995.

[166] Florin Despa, Ariel Fernandez, and R. Stephen Berry. Dielectric modulation of biological water. *Phys. Rev. Lett.*, 93:228104, Nov 2004.

[167] Alex E. Roher, Chera L. Esh, Tyler A. Kokjohn, Eduardo M. Castano, Gregory D. Van Vickle, Walter M. Kalback, R. Lyle Patton, Dean C. Luehrs, Ian D. Daugs, Yu-Min Kuo, Mark R. Emmerling, Holly Soares, Joseph F. Quinn, Jeffrey Kaye, Donald J. Connor, Nina B. Silverberg, Charles H. Adler, James D. Seward, Thomas G. Beach, and Marwan N. Sabbagh. Amyloid beta peptides in human plasma and tissues and their significance for alzheimer's disease. *Alzheimer's and Dementia*, 5(1):18–29, 2009.

[168] S. Makimattila, M. S. Fineman, and H. Yki-Jarvinen. Deficiency of total and nonglycosylated amylin in plasma characterizes subjects with impaired glucose tolerance and type 2 diabetes. *Journal of Clinical Endocrinology & Metabolism*, 85(8):2822–2827, 2000.

[169] F. Kremer, A. Serghei, J.R. Sangoro, M. Tress, and E.U. Mapesa. Broadband dielectric spectroscopy in nano-(bio)-physics. In *Electrical Insulation and Dielectric Phenomena, 2009. CEIDP '09. IEEE Conference on*, pages 1–6, oct. 2009.

[170] A. Serghei and F. Kremer. Broadband dielectric studies on the interfacial dynamics enabled by use of nanostructured electrodes. *Review of Scientific Instruments*, 79(2):026101, 2008.

[171] Tadato Ban, Masaru Hoshino, Satoshi Takahashi, Daizo Hamada, Kazuhiro Hasegawa, Hironobu Naiki, and Yuji Goto. Direct observation of abeta amyloid fibril growth and inhibition. *Journal of Molecular Biology*, 344(3):757 – 767, 2004.

[172] T. Hamaguchi, K. Ono, and M. Yamada. Anti-amyloidogenic therapies: strategies for prevention and treatment of alzheimer's disease. *Cellular and Molecular Life Sciences CMLS*, 63:1538–1552, 2006.

[173] Harry Levine. Small molecule inhibitors of abeta assembly. *Amyloid*, 14(3):185–197, 2007.

[174] Mark A. Findeis. Approaches to discovery and characterization of inhibitors of amyloid beta-peptide polymerization. *Biochimica et Biophysica Acta (BBA) - Molecular Basis of Disease*, 1502(1):76–84, 2000.